

DPhil Thesis

The Temperature Dependence of Plasticity in Molybdenum

Author

Katherine P.E. Plummer

Supervised by

Professor David Armstrong

and Professor Steve Roberts

May 2019



Preface

This thesis describes works carried out by the author in the Department of Materials, University of Oxford, from October 2012 to May 2019 under the supervision of Prof. David E.J. Armstrong and Prof. Steve G. Roberts. No part of this thesis has been previously submitted for a degree at this or any other university. The work of other authors has been drawn upon and has been referenced and acknowledged in the text. A list of references is given at the end of the thesis. Some work from this thesis has been reported at the following conferences:

Conferences

- ECI Nanomechanics 2015, Albufeira, Portugal - poster presentation
- MSE 2014, Darmstadt, Germany - verbal presentation
- UNTF 2014, Oxford, UK - verbal presentation

Abstract

The Temperature Dependence of Plasticity in Molybdenum

A Thesis Submitted for the Degree of Doctor of Philosophy

K.P.E.F. Plummer

Lincoln College

Trinity Term 2019

This thesis aims to add to the knowledge of the mechanical properties of molybdenum, with particular emphasis on the temperature and size dependence of plasticity. The experimental findings of this thesis will help to build a picture of the small scale properties of Mo for future studies on irradiated thin layers.

Bulk scale microhardness testing of [001] orientated single crystal Mo from -196 to 872°C formed a basis for a size-dependent nanoindentation study from -31 to 800°C and maximum loads from 2 to 300mN. The size dependent behaviour was consistent with the approach of BCC metals to FCC behaviour upon heating due to the thermal activation of the kink pair mechanism, as the size dependence increased up to the knee temperature to the level expected of an FCC metal. A strain gradient plasticity model was used with success above the knee temperature, but was not suitable at lower temperatures. It is proposed that two different mechanisms act to control the characteristic length scale of indentation above and below the knee temperature.

Bulk scale four point bend tests were carried out on single crystal Mo from -165 to 328°C with sample edges parallel to {001} to provide a comparison with microcantilever bend tests with the same crystallographic orientation from -30 to 571°C. The microscale tests showed much higher flow stresses at all temperatures. This is most likely due to the high strain gradients imposed on the smaller scale bend specimens, although a further experiment covering a range of beam widths would be necessary to explore this area further.

Additionally, polycrystalline samples were annealed until cold work was observed to decrease significantly and tested from -40 to 522°C. These samples had very similar behaviour to the single crystal samples, but reduced flow stresses compared to a previous study on unannealed samples, suggesting the grain growth and reduced cold work measured by EBSD were responsible.

Acknowledgments

Writing this thesis was more difficult than I ever imagined when I first signed up. I have so many people to thank for both technical help and amazing support. I have wonderful memories of the Oxford Materials Dept, St Edmund Hall, Lincoln College and the City of Oxford, and have made life-long friends.

Dave and Steve - thank you for seeing me all the way through from first year of undergrad to the end of my DPhil. I have learned so much from both of you.

Adrian and Ged from Micromaterials - thanks for all your help with the hot nanoindenter.

James G - thanks for showing me the ropes on many different instruments.

Hamid - thank you for your excellent help with PECS.

Gabriella, Greg, Gareth, Graham and the rest of the EM team - thanks for teaching me to use the microscopes and running to my aid so many times.

Karen, Marion and Rebecca - you have all been so helpful.

James H, Christian B, Chris B, Chris H, Mike G, Ele G and Stella P - thanks for helping me with various things and so many great coffee breaks. I will miss G&Ds.

Anna K and Helen P - what would Erica do?

Kris B, Junnan J, Bo-Shiuan L, Aidan R, Francesco F, Robbie A, Glenn J, Jack H and Edd R - thanks for cheering up the latter years in the office.

Katherine - thanks for making me run a marathon with you. It helped so much with the DPhil mindset. Linda and Imogen - thanks for all your support (and distractions when required).

The Fairhursts - I wrote a large portion of this in the dining room at the Schloss. Thanks for the encouragement (especially Merle, although you can be a little scary when shouting at me from behind).

My family - you have been very patient. Thanks for all the encouragement and for all the many things you have done to help me.

Sean - you have helped me so much, from teaching me metallographic preparation to proof reading my thesis, and putting up with me during the write up. You really are the best.

Glossary of Abbreviations

4PB	four point bend
AFM	atomic force microscope
BCC	body centred cubic
CBN	cubic boron nitride
CFC	carbon fibre composite
CCFE	Culham Centre for Fusion Energy
CNC	computer numerical control
CRSS	critical resolved shear stress
CSM	continuous stiffness measurement
CVN	Charpy v-notch
DBT(T)	ductile-brittle transition (temperature)
DD	dislocation dynamics
DEMO	demonstration reactor
(HR)EBSD	(high resolution) electron back scattered diffraction
EDM	electric discharge machining
ELM	edge localised mode
DIC	digital image correlation
FCC	face centred cubic
FEG	field emission gun
FEA	finite element method
FIB	focussed ion beam
GND	geometrically necessary dislocation
IPF	inverse pole figure
ITER	International Thermonuclear Experimental Reactor
JET	Joint European Torus
LEFM	linear elastic fracture mechanics
MEMS	microelectromechanical system
NET	Next European Torus
ODS	oxide dispersion strengthened
PECS	precision etching and coating system
PFC	plasma facing component
PID	proportional integral derivative
PX	polycrystal
ROI	region of interest
SBT	simple beam theory
SEM	scanning electron microscopy
SSD	statistically stored dislocation
SX	single crystal
TEM	transition electron microscopy
TRISE	Temperature and Rate Indentation Size Effects

Contents

1 Literature Review **1**

1.1 Molybdenum for Fusion Power . . . 1

1.2 Deformation Mechanisms of BCC Metals . . . 7

1.2.1 Dislocation Dynamics . . . 7

1.2.1.1 Core Polarisation . . . 9

1.2.1.2 Temperature Dependent Deformation . . . 9

1.2.1.3 The Kink-Pair Mechanism and Cross-Slip . . . 12

1.2.1.4 Tension-Compression Asymmetry . . . 15

1.2.1.5 Summary . . . 15

1.2.2 The Ductile-Brittle Transition . . . 16

1.2.2.1 Defining T_{DBT} . . . 19

1.2.3 Mo Recrystallisation . . . 19

1.2.4 Elastic Constants of Mo . . . 22

1.3 Investigation of Temperature-Dependent Plasticity in BCC Metals . . . 25

1.3.1 Macro-testing . . . 25

1.3.1.1 Three- and Four-Point-Bend Testing . . . 26

1.3.2 Micro- and Nano-Testing . . . 29

1.3.2.1 Microindentation . . . 29

1.3.2.2 Nanoindentation . . . 37

1.3.2.3 Hot and Cold Nanoindentation . . . 39

1.3.2.4 Indentation Size Effect . . . 44

1.3.2.5 Micromechanical Testing . . . 47

1.3.2.6 Hot and Cold Micromechanics . . . 50

1.3.2.7 Micromechanical Size Effect . . . 52

1.3.2.8 In-Situ Measurements . . . 57

1.3.2.9 Effects of FIB Milling . . . 57

1.4 Summary . . . 58

1.5 Research Goals . . . 59

1.6 Chapter Summary . . . 59

2 Materials and Sample Preparation **61**

2.1 Single crystal Mo . . . 61

2.2 Polycrystalline Mo . . . 61

2.2.1 Annealing Polycrystalline Molybdenum . . . 65

3 Microhardness Testing **72**

3.1 Microhardness Testing . . . 72

3.1.1 Method 1: Temperature range 20 to 880°C, under vacuum . . . 73

3.1.2 Method 2: Temperature range 20 to 350°C, hot air gun . . . 74

3.1.3 Method 3: Temperature range −179 to 20°C, liquid nitrogen submersion 74

3.2 Indentation Area Measurement . . . 75

3.2.1 Meyer Hardness . . . 77

3.2.1.1 Converting Meyer Hardness to Vickers Hardness . . . 77

3.2.2 Thermal Expansion Correction . . . 78

3.2.2.1 Thermal Expansion of Molybdenum . . . 79

3.3 Elastic Recovery . . . 80

3.4 Milman Plasticity Parameter . . . 82

3.5 Results . . . 85

3.5.1 Indentation Area . . . 85

3.5.2 Meyer Hardness . . . 85

3.5.3 Indentation Micrographs . . . 87

3.5.4 Elastic Recovery . . . 91

3.5.5 Milman Plasticity Parameter . . . 94

3.6 Discussion . . . 95

4 Nanoindentation **97**

4.1 High and Low Temperature Nanoindentation . . . 97

4.1.1 Load and Displacement Control . . . 97

4.1.2 Imaging . . . 98

4.1.3 Sample Mounting . . . 99

4.1.4 Cold Stage . . . 99

4.1.5 Hot stage . . . 101

4.1.5.1 Oxidation . . . 101

4.1.5.2 Tip Material . . . 101

4.1.5.3 Thermal Drift . . . 102

4.2 Experimental Method . . . 104

4.2.1 Nanoindentation Data Analysis . . . 106

4.2.1.1 Area of a Nanoindentation . . . 106

4.2.2 Area Function Calibration . . . 109

4.2.2.1 Elastic Modulus . . . 110

4.2.2.2 Hardness . . . 111

4.3 Results . . . 113
4.3.1 Load-Displacement Data . . . 113
4.3.2 Hardness-Temperature Behaviour at One Load . . . 113
4.3.3 The Effect of Temperature on the Size Effect . . . 116
4.3.4 Low Depth Softening . . . 118
4.3.5 Strain Gradient Plasticity Model . . . 119
4.3.6 Power Law Model . . . 127
4.3.7 Elastic Recovery . . . 130
4.4 Discussion . . . 132

5 Four Point Bend Testing **136**
5.1 Samples . . . 138
5.2 Data Analysis . . . 139
5.2.0.1 Defining the yield point . . . 141
5.2.1 Simple Beam Theory . . . 141
5.2.1.1 Stress . . . 141
5.2.1.2 Strain . . . 142
5.3 Results . . . 143
5.3.1 Polycrystalline Samples . . . 143
5.3.2 Single Crystal Samples . . . 143
5.3.3 Comparison of Single Crystal and Polycrystalline Results . . . 146
5.3.4 Graph Characteristics . . . 146
5.4 Discussion . . . 151

6 Micromechanical Testing **153**
6.1 Micromechanical Bend Testing . . . 153
6.1.1 Focussed Ion Beam . . . 153
6.1.2 Microcantilever Preparation . . . 153
6.1.3 Experimental Method . . . 157
6.2 Data Analysis . . . 158
6.2.1 Simple Beam Theory . . . 158
6.2.2 Finite Element Analysis . . . 161
6.3 Results . . . 163
6.3.1 Load-Displacement Graph Characteristics . . . 163
6.3.2 Yield Behaviour . . . 166
6.3.2.1 Defining the yield point . . . 166

6.4 Discussion 167

7 Overall Discussion **170**

7.1 Thermal Dependence of Flow Stress 170

7.1.1 Estimation of Flow Stress at Absolute Zero 175

7.2 Activation Energy for Deformation 178

8 Future Work **185**

1 Literature Review

1.1 Molybdenum for Fusion Power

Fusion power has attracted great interest due to its potential as a major power source for the mid-21st century onwards, due to an increase in global demand for clean, low-carbon energy sources. There are significant challenges faced by the materials community in the design of a fusion reactor, and this provides one of the limiting factors in the development of fusion power plants. A considerable amount of work has been dedicated to developing suitable structural materials for the divertor, which is situated along the bottom of the vacuum vessel, shown in figure 1. It extracts heat and helium ash — both products of the fusion reaction — and other impurities from the plasma, acting as an exhaust system [1].

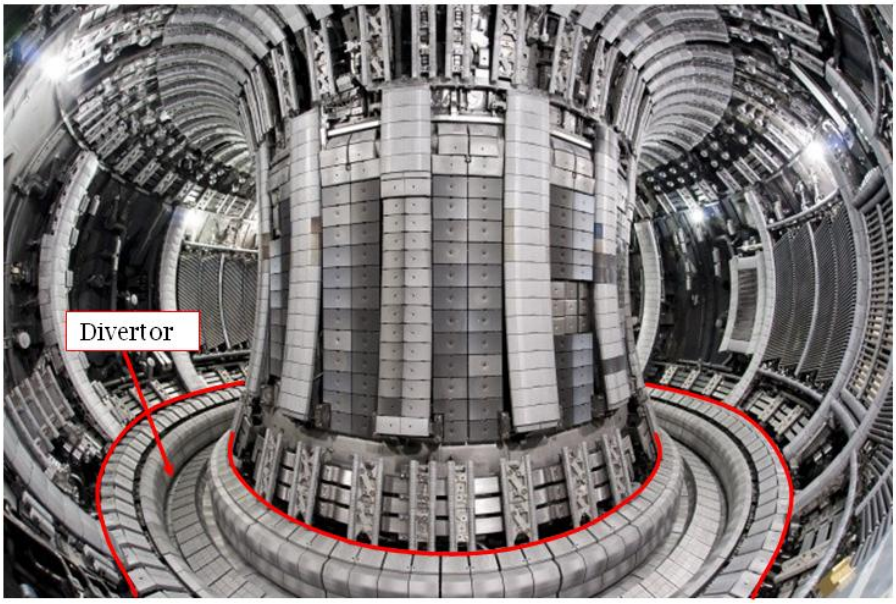


Figure 1: The vacuum chamber in JET, Culham (UK). The divertor is highlighted in red [2].

The divertor is exposed to some of the most extreme conditions in the fusion reactor as a result of interaction with the plasma, in terms of neutron damage (3–30 displacements per atom per year (dpa year $^{-1}$)), high mechanical and thermal loads (1390°C at the divertor [3], rising during fluctuations). As a plasma-facing component it is directly exposed to a high flux of energetic particles (including hydrogen and helium ions) [4]. The neutron flux in the divertor region of NET (the Next European Torus) was reported to be approximately $2x10^{14}ncm^{-2}s^{-1}$ (neutrons per cm^2 per second) [3]. ITER's planned neutron fluence is 0.5 dpa/yr and DEMO's divertor components should experience a neutron fluence of 20 dpa per year [5]. The large increase between ITER and DEMO is due to the fact that ITER is a demonstration of the technological and scientific feasibility of fusion energy, whereas DEMO will bring fusion energy research to the threshold of a prototype fusion reactor.[6]

The effect of energetic neutrons on the performance of divertor components is an important issue for ITER and future fusion devices. Neutron interactions with targets lead to knock-on ions (secondary displacements) that then cause displacement damage (forming dislocations, interstitials, voids and vacancies in the crystal lattice).[7] The net effect is either swelling (metals and ceramics) or shrinkage (carbon fibre composites, CFCs) and a change in the thermal conductivity of materials and mechanical properties. If material thermal conductivity is reduced, the temperature profile throughout the thickness of the protection material will be affected. Consequently, the temperature at which the material sustains neutron damage increases with time [3] and leads to a reduction in the power handling capabilities.

In the divertor there are two critical components, the inner and outer divertor targets, where plasma is allowed to touch the plasma-facing material, resulting in surface heat loads in the range of 10 to 20 MWm^{-2} [8]. The ITER divertor is expected to meet the requirements of 1000 cycles of 10 MWm^{-2} for 400s and 100 transient cycles of 20MWm^{-2} for 10s, even after irradiation corresponding to about 10 years of full performance plasma operation [8].

Contact with the plasma brings additional complications, such as electromagnetic radiation, sputtering erosion and plasma disruptions and instabilities in the plasma edge such as ELM (edge localised mode) events [9]. These are periodic disturbances of the plasma periphery that occur in tokamaks.[10]

The choice of material for the divertor is complex. The outer portion of the divertor contains armour tiles connected to a coolant substrate. A high thermal conductivity and high melting point are required to channel heat away quickly and avoid melting upon contact with the plasma. Finding a material that can cope with this as well as a constant high heat flux restricts the choice to refractory metals such as tungsten and molybdenum, and graphite in the form of carbon fibre composites (CFCs) [9].

The large fluctuations in temperature during a heat pulse in the fusion reactor cause large variations in stress. If these stresses exceed the divertor material's yield stress, plastic deformation will occur. In a study on the use of tungsten material for the ITER divertor, Hirai et al. carried out elastic-plastic finite element analysis to understand the stress and strain in tungsten monoblocks at the loaded surface of the divertor [11].

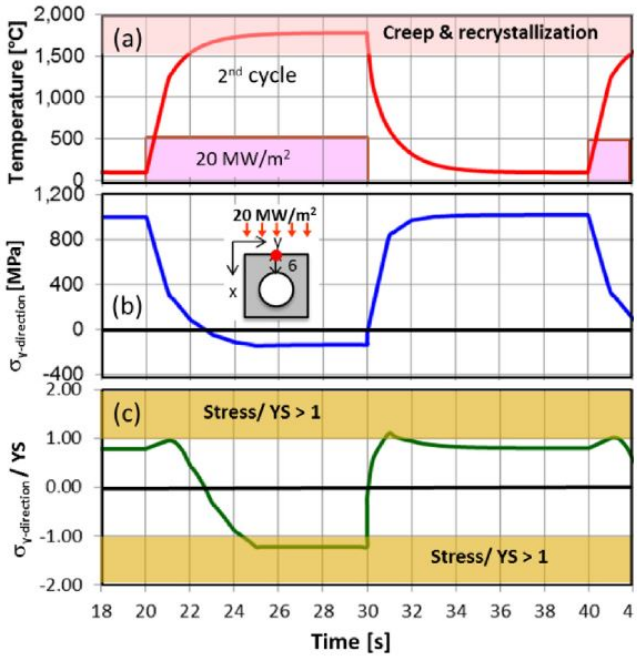


Figure 2: Time evolution of (a) surface temperature, (b) stress in y-direction, (c) stress in y-direction normalised by yield strength, at middle of W monoblock loaded surface as indicated in the sketch [11].

Figure 2 shows the calculated time evolution of surface temperature, stress in the y-direction and stress in the y-direction normalised by yield stress at the middle of a W monoblock loaded surface. This plastic strain due to compressive stress would cause the material to experience progressive deformation or thermal fatigue, as well as creep dmage and degradation due to recrystallisation. The mechanical properties of divertor materials must be sufficiently resistant to fatigue and creep, by control of microstructure and composite structure, to restrict this effect [11]. Additionally, the material itself must have a high yield stress. The precise value of this yield stress depends on the geometry of the divertor components, such as the use of multi-layered materials.

The first wall and divertor of a reacting fusion device, facing the plasma, is subjected to a surface flux of particles and heat in addition to the volume effect of irradiation damage. Taking this into account, out of the four candidate materials (beryllium, carbon, molybdenum and tungsten), tungsten is considered to hold the best long-term promise by CCFE [2].

Sputtering erosion further influences divertor material selection. Individual, very energetic plasma particles can approach the target and sputter away divertor material. A high sputtering rate is extremely undesirable; it reduces component lifetime and introduces impurities into the plasma. Sputtering threshold (the ion energy required to sputter one atom) must be high, decreasing sputtering rate.

Figure 3 shows the relationship between sputter yield and deuteron energy for different plasma-

facing candidate materials. Carbon sputters at lower energy and at a higher loss than molybdenum or tungsten. This alone would eliminate graphite as a possible divertor material. However, there are other factors influencing both divertor design and the structural material used [9].

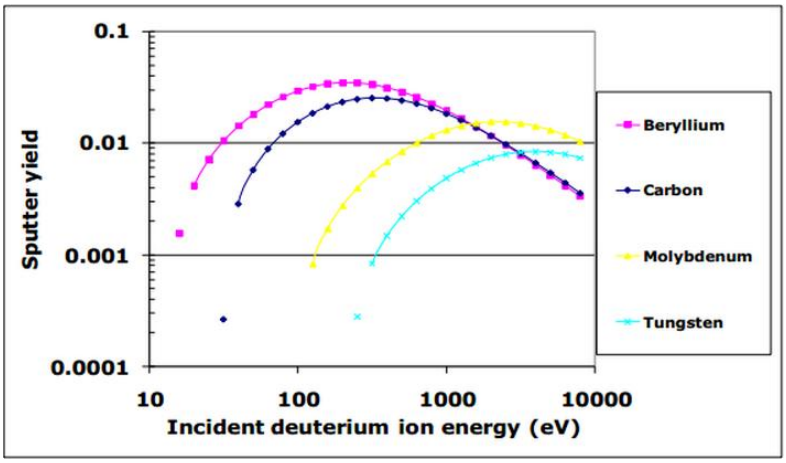


Figure 3: The relationship between sputter yield and deuteron energy for plasma-facing candidate materials. Carbon sputters at lower energy and at a higher loss than molybdenum or tungsten [12].

Plasma impurity introduction is another important consideration. Once sputtered, an atom of divertor material will release electrons into the plasma, causing energy loss by Bremsstrahlung. This acts to cool the plasma, reducing efficiency. High Z materials release more electrons ($W = 74$, $Mo = 42$, $C = 6$) so the cooling effect is more pronounced [13].

The tritium inventory of an experimental fusion reactor (the total quantity of tritium allowed on site at any one time) is determined by a broad range of factors such as plasma physics parameters and component design. However, most importantly for material selection, tritium retention in divertor materials, especially those that are carbon-based, has an impact on the total quantity of tritium on site. Due to safety concerns and associated imposed limits, designers try to minimise this inventory as far as possible [14].

Molybdenum and molybdenum alloys were among the first materials suggested for use as divertor and other structures in fusion reactors [15]. The mechanical properties of molybdenum often have values that lie between those of tungsten and graphite; its sputtering rate is lower than C but higher than W, and is lower Z than tungsten (Z=42 rather than 74), presenting less of a threat to the plasma when atoms are eventually released. Importantly, it is also tougher than W, making the manufacturing process less complex and giving Mo components better mechanical properties in the reactor; this specific property is the focus of this research.

Molybdenum is disadvantaged compared to tungsten due to its lower melting point (2642°C). However, there is a very large drawback in the form of high activation, where Mo atoms transmute into long-lived radioactive waste in the form of technetium-99 that has a half-life of 211000

years [16] - as neutrons move through the components in fusion reactors they interact with the atoms of the material, producing new variants of atoms ('nuclides'), some of which are radioactive. Figure 4 shows a model of the concentration of Mo transmutation products in atomic parts per million after three years in DEMO [12].

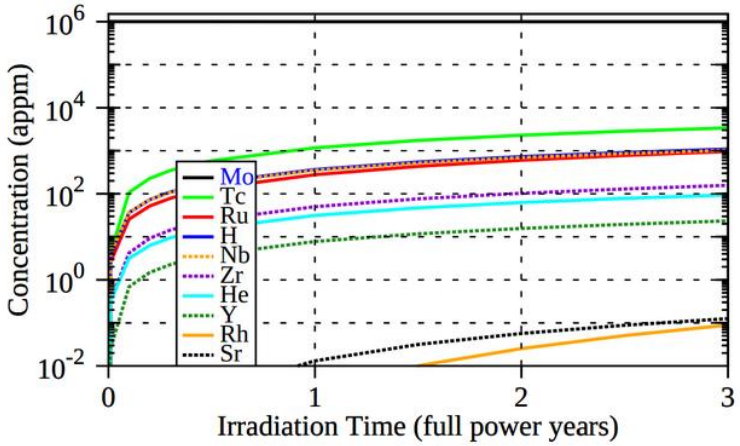


Figure 4: A model of Mo transmutation under DEMO divertor armour conditions showing the concentration of transmutation products in atomic parts per million over the course of three years [12].

Neutron-induced transmutation of materials in a D/T fusion power plant gives rise to the potential for long-term activation. To ensure that the attractive safety and environmental characteristics of fusion power are not degraded, careful design choices are necessary. An aim of optimising power plant design must be to minimise both the level of activation and the total volume of active material that might ultimately be categorised as waste requiring disposal. Materials selection is central to this optimisation [17]. Generally, fusion reactors are only designed to contain low activation elements (W, Fe, Cr, Ta, C, Si and V) to prevent long-lived waste, but if these materials alone prove to be unsuitable from an engineering point of view some sacrifices may have to be made.

One practical application for this tool could be in the selection of materials for the inner lining of tokamak fusion reactors. At JET, and the forthcoming international fusion project ITER, beryllium and tungsten are favoured. However, others could be more effective when the time comes to build commercial fusion power stations.

Molybdenum is one alternative metal that has previously been considered; it is easier to manufacture than tungsten and less brittle (Mo has a ductility of 0.01-0.45 [18] (strain to failure in tension), W has a ductility of 0.01-0.25 [19]). It has, however, been discounted because it remains highly active for a long time. Plasma disruptions and instabilities can occur in the plasma edge, such as edge localised modes (ELM) events. These local events can cause large thermal shock, subjecting the local area to high strain rates. Changes in power during these

events can reach 24MW during a large ELM [20].

If target materials are too brittle to withstand these conditions, cracks form during contact with the plasma, potentially leading to a catastrophic failure in the divertor (as higher ductility retards crack propagation). Although high yield stress is often sacrificed when toughness is sought after, an increase in ductility will allow a larger safety margin. An understanding is required of the mechanisms controlling the ductile-brittle transition and its strain-rate dependence in Mo before further consideration for applications in the fusion reactor.

This DPhil project, a very small part of the wider research movement into molybdenum for fusion applications, will investigate the dependence on temperature and strain rate of the flow behaviour of molybdenum.

1.2 Deformation Mechanisms of BCC Metals

An understanding of the mechanisms responsible for the high temperature dependence of plasticity (and its influence on the ductile-brittle transition) in body centred cubic metals is necessary before details are given of experimental research. This section covers the mechanisms responsible for this behaviour, starting at the atomic scale of the dislocation core and working through various important dislocation mechanisms, and finally outlining fracture mechanics and extrinsic factors that might have an influence on this transition.

1.2.1 Dislocation Dynamics

Molybdenum is a group VI transition metal with refractory properties. It has a body centred cubic (BCC) crystal structure as shown in figure 5.

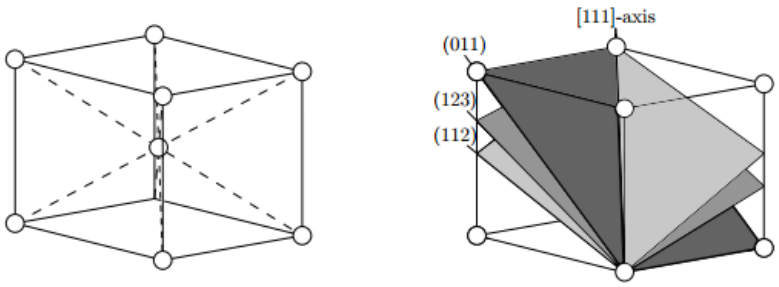


Figure 5: Schematic diagram of a BCC unit cell (left) and the three slip planes available for slip (right). The [111] axis is common to all three planes [21].

Schmid's law, derived from tensile tests on cadmium single crystals, was one of the first derived quantitative laws of crystal plasticity [22]. It states that extensive plastic deformation by slip will set in when the resolved shear stress in the active slip system reaches a critical value (critical shear stress, τ_0). For a given temperature T and rate of resolved plastic shear strain $\dot{\varepsilon}_{pl}$, extensive plastic deformation sets in at the axial stress τ_{axial} at which the resolved shear stress τ:

$$\tau = \tau_{axial} cos\phi cos\lambda \tag{1}$$

reaches a critical value τ_0. ϕ is the angle between the slip plane normal and applied axial force, and λ is the angle between slip direction and applied force, as shown in figure 6.

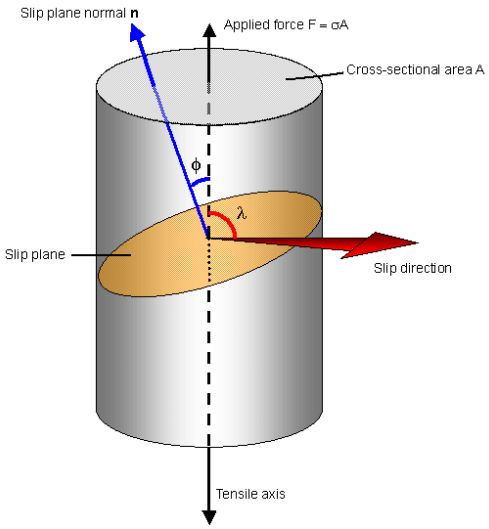


Figure 6: Schematic diagram showing the angles involved in Schmid's law - ϕ is the angle between the applied force and the slip plane normal, λ is the angle between the applied force and the slip direction [23].

In general, a BCC metal will deform by nucleation and movement of dislocations when an external stress is applied, unless temperatures are particularly low and strain rates high, when twinning may occur. Slip in BCC metals occurs in close-packed directions; the Burgers vector for unit slip is $a/2 < 111 >$, as shown in figure 7

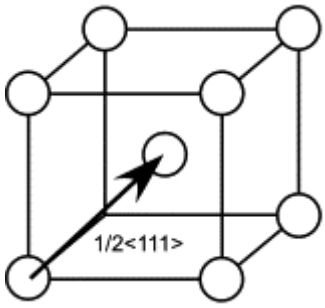


Figure 7: Burgers vector for $a/2 < 111 >$ unit slip shown by the arrow [24].

At low temperature (a few degrees Kelvin), slip has been shown to take place on {110} planes in high purity refractory BCC metals, obeying Schmid's law[25]. However, upon heating, the operating slip planes are not exclusively those with the densest packing ({110} planes in BCC metals), but on slip planes {110}, {112} and {123}, with all slip systems intersecting the $< 111 >$ axis, as shown in figure 5. The common $< 111 >$ direction is identical to the Burgers vector, so that screw dislocations lie along this common axis. This makes BCC metals susceptible to cross-slip, leaving wavy slip lines on the sample surface after deformation. Since τ_0 cannot be expected to be the same for all slip planes, Schmid's law becomes difficult to apply.

1.2.1.1 Core Polarisation The screw dislocation axis in BCC metals, $< 111 >$, has a 3-fold symmetry, and as such, has a tendency to spread in three directions on either a {110} or a {112} plane [26]:

$$\frac{1}{2}[111] \rightarrow \frac{1}{6}[111] + \frac{1}{6}[111] + \frac{1}{6}[111] \tag{2}$$

This is shown in figure 8 [27].

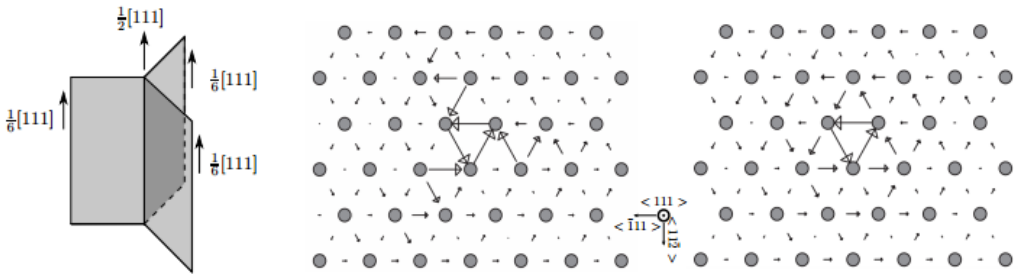
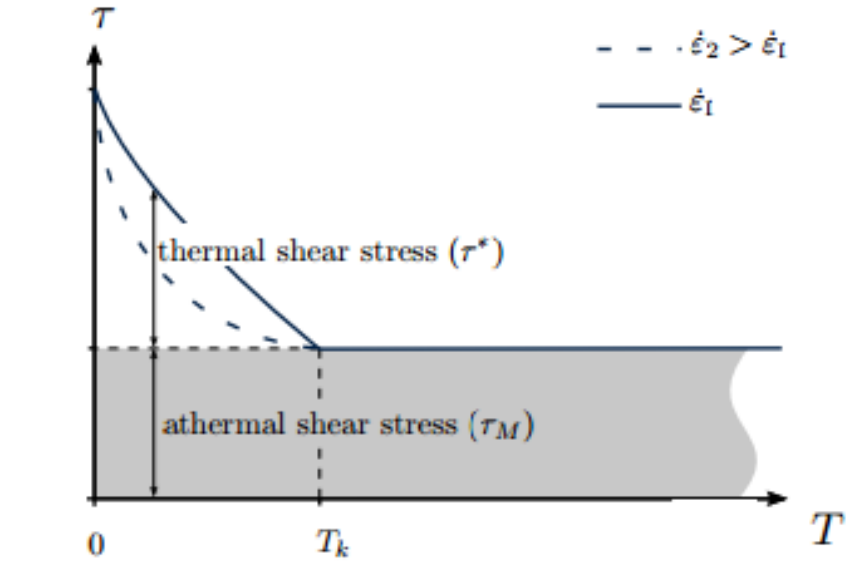


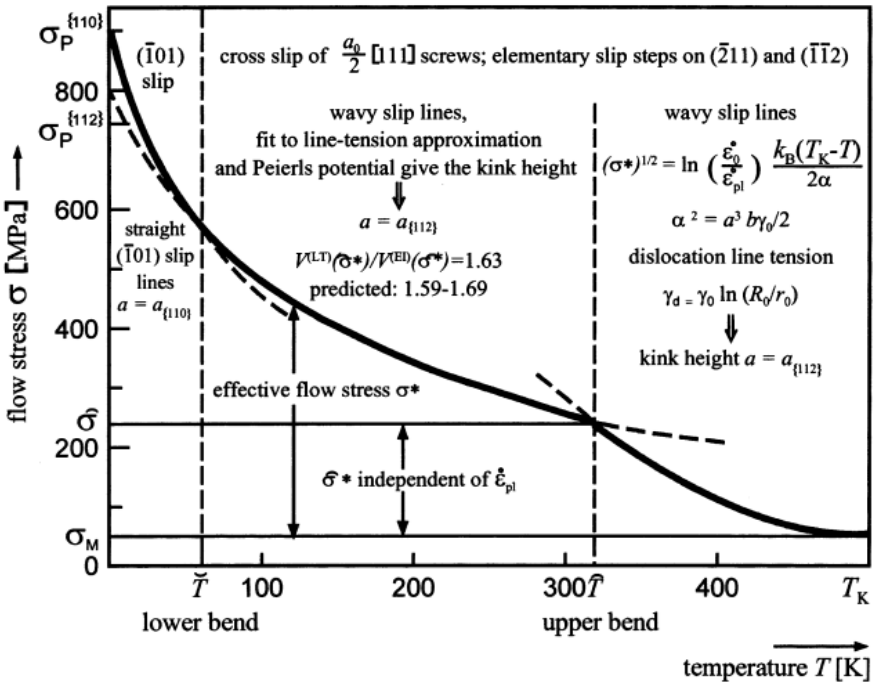
Figure 8: (a) Schematic representation of the $\frac{1}{2}[111]$ screw dislocation core spread into three planes. (b) degenerated or polarised core (c) non-degenerated or non-polarised core. The projection is perpendicular to the [111] dislocation line. The relative replacement of the atoms is described by the arrows between them [27]

This spreading increases the resistance to motion of the screw dislocation by raising its Peierls potential (lattice friction stress) far above that of the edge dislocation. Dissimilarly to FCC "dissociation" into partial dislocations, no stacking fault is formed in ambient conditions [28, 29]. Instead, the dislocation is "polarised" into fractional dislocations, so named due to the breakdown in symmetry. As shown by Vitek [30] by the use of atomistic simulations, this polarisation is non-planar, and so for this purpose, screw dislocations may be described as having a non-planar core. As first proposed by Hirsch in 1960 [25], there is a need for screw dislocations in BCC metals to overcome this large Peierls potential by thermal activation before they are fully mobile, and only then can macroscopic slip occur. This special role of screw dislocations in BCC metals leads to a strong temperature-dependence of macroplasticity.

1.2.1.2 Temperature Dependent Deformation The yield and flow stresses of BCC metals undergo a marked increase below a critical temperature, the knee temperature T_K, which is on the order of $0.2\mathrm{T}_m$ [25] (where T_m is the absolute melting temperature) [31]. The typical graph of flow stress versus temperature for BCC metals is shown in figure 9a and the responsible mechanisms are shown in greater detail in figure 9b; flow-stress–temperature relationship of high-purity bcc metals (schematic). Numerical statements refer to ultrapure Mo single crystals with plastic shear-strain rate equal to $8.6 \times 10^4 s^1$. The lower bend, upper bend and knee temperature (T_K) are all shown [25].



[a]



[b]

Figure 9: (a) Shear stress variation with strain rate and temperature for BCC metals, showing strong dependence below T_K and a plateau above T_K once dislocations are thermally activated and the kink-pair mechanism takes effect [21]. (b) Seeger's graph conveys the same idea but the responsible mechanisms are shown in greater detail; flow-stress–temperature relationship of high-purity bcc metals (schematic). Numerical statements refer to ultrapure Mo single crystals with plastic shear-strain rate equal to $8.6 \times 10^4 s^1$. The lower bend, upper bend and knee temperature (T_K) are all shown [25].

This temperature dependence has been recognised for decades but the understanding of the relationship between temperature and critical stress became more comprehensive alongside the development of dislocation dynamics. Hollang et al. [32] performed a detailed study of the T-dependence of stress-strain curves compared with the T-dependence of flow stress, looking

at ultrapure Mo crystals with initial Schmid factor of 0.5 for $< 110 > \{110\}$ slip. From plastic strains of 0.1 and above, they found the T-dependent part of the flow stress (the "effective" stress) to be completely controlled by the mobility of the screw dislocations. This behaviour is shown in figure 10.

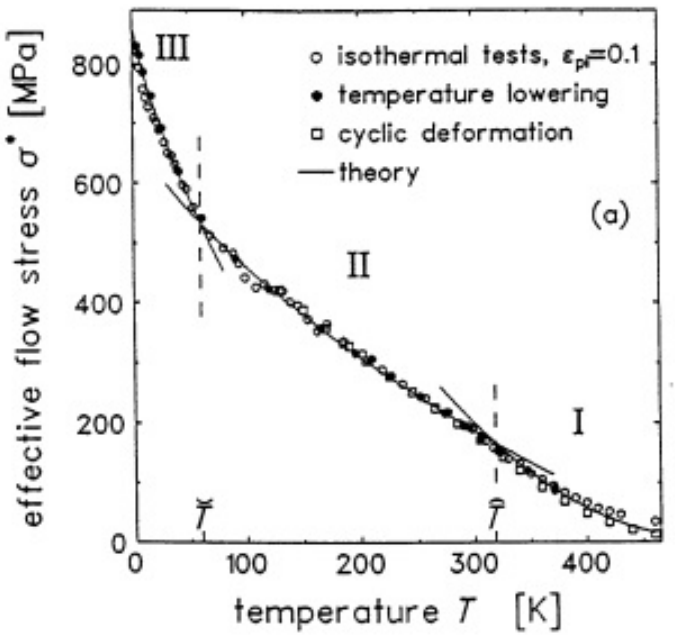


Figure 10: Temperature dependence of flow stress from [32]. Comparison of three experimenal techniques (isothermal measurements, temperature-lowering tests and cyclic-deformation). The full lines represent fits to the theory ([32] and [33]).

It is now understood that the thermally-dependent region below T_K is restricted by the mobility of screw dislocations, hence the high thermal and strain rate dependence. Below T_K, stress-strain curves of BCC metals characteristically show a microstrain region. In this regime [34, 35], long $a/2 < 111 >$ screw dislocation segments are drawn out, accompanied by the gradual elimination of non-screw dislocations. Consequently, the mobility of screw dislocations below T_K is much lower than for non-screw dislocations with the same Burgers vector **b**; dislocation mobility, rather than dislocation density, is the rate-controlling factor of plastic strain rate [25].

As the metal is heated, a thermally-activated mechanism (called the "kink-pair" - section 1.2.1.3) reduces the critical stress required to move a screw dislocation until screw and edge dislocations are equally mobile at T_K. The athermal region, corresponding to flow stress, is dominated by classical strengthening mechanisms such as work hardening, precipiate hardening and grain boundary strengthening.

A graph of critical stress vs temperature will therefore be composed of two parts, thermal τ^*

and athermal τ_M, which are linked by the following equation:

$$\tau = \tau^* + \tau_M \tag{3}$$

The two distinct regions of this behaviour are shown in figure 9a [21]. In his 2001 review on anomalous slip in BCC metals [25], Seeger presented a useful and complete summary of the various active mechanisms leading to the changes in critical stress. These are shown in figure 9b.

Hollang et al. [33] found the knee temperature of ultra pure single crystal Mo undergoing tension to be approximately 450K. Above this knee temperature, the flow stress remained at the strain rate-independent value of 53MPa. The strain rate independence indicates that under these conditions, thermally activated processes no longer contribute to the flow stress.

53MPa was, therefore, taken as the athermal component of flow stress in this case. It was assumed to be constant over the entire temperature range above the knee temperature because the thermal dependence of the elastic moduli of Mo is negligible compared with the steep increase of flow stress with decreasing temperature below the knee.

This thermal dependence of slip in BCC metals manifests itself in a transition from ductile to brittle behaviour upon cooling a specimen, and this is affected by the loading rate and mode. Further detail of the ductile-brittle transition will be covered in Section 1.2.2.

1.2.1.3 The Kink-Pair Mechanism and Cross-Slip The dominant slip mechanism of screw dislocations in BCC metals is the 'kink-pair mechanism' [36] as its energy barrier for dislocation movement is much lower than for the movement of a whole dislocation line. The mechanism is thermally-activated and initiated by the thermal fluctuation of small groups of atoms. These stages are outlined in figure 11.

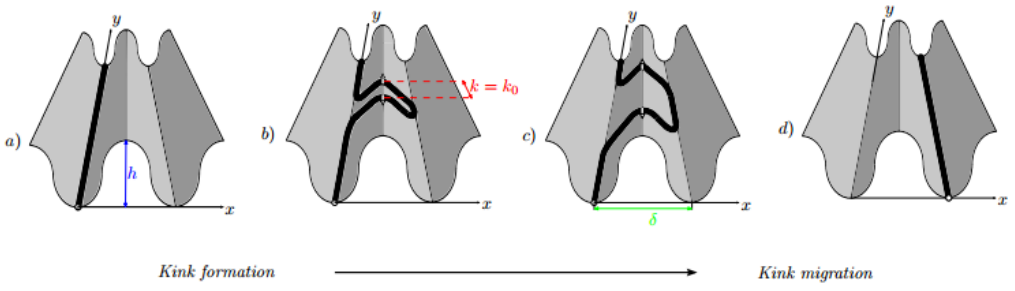


Figure 11: Kink-pair mechanism: thermal activation of dislocation glide, which allows the dislocation line to pass from one stable position to the next at finite temperature [21].

1. Kink-pair formation: thermal fluctuations cause the movement of a few core atoms (figure

11a/b)

2. Kink migration: if the distance between two kinks is above a critical value k_0, the pair (mobile edge dislocation segments) are driven apart by shear stress [37] (figure 11c)

3. Eventually the segments have fully separated and slip by one Burgers vector has occurred (figure 11d)

Figure 12 shows an example of atomistic simulation of a kink-pair.[38] It is important to note here that due to its magnetic nature, iron can behave slightly differently from other BCC metals, but the initial atomistic form of a kink-pair is of the same form (an image of a non-magnetic BCC metal could not be found).

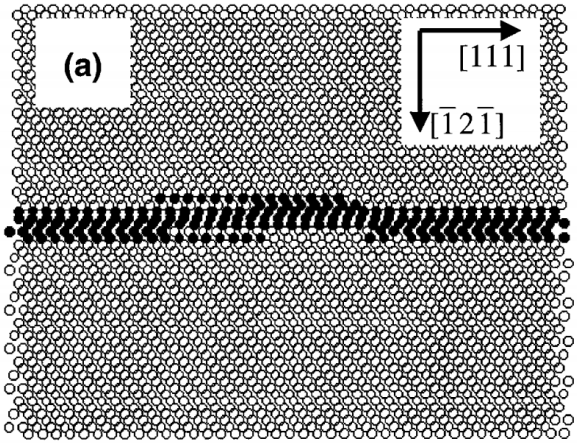


Figure 12: Atomistic simulation of a dislocation jump in BCC iron showing a kink-pair. (Saddle configuration of the BnApB kink-pair in a $\frac{1}{2} < 111 >$ screw dislocation at 320MPa. The filled atoms have energy <4.22eV, and so they trace out the dislocation line.)[38]

The thermal activation energy required to overcome the Peierls barrier of height h is affected by the dislocation core size; the non-planar polarisation of the $\frac{1}{2}[111]$ screw dislocation core in this case raises the Peierls barrier.

The existence of the kink-pair mechanism also gives a good explanation for the prevalence of cross-slip in BCC metals. When BCC crystals undergo plastic deformation, the slip planes are often noncrystallographic. Ngan's atomistic simulation on the activation pathway of dislocation jumps in BCC iron showed that the main reason for BCC crystals to exhibit this phenomenon is that one type of kink pair has significantly lower energy than all the other types on the same slip plane [38]. Dislocation motion cannot continue on the same slip plane, and the dislocation has to cross slip onto an intersecting slip plane after each atomic jump so in the long run, the average slip plane would be zigzag and noncrystallographic. They also found that kink spacing decreases with applied stress. This implies several different activation energies may be seen if several types of kink exist, but this was not observed in tungsten experiments performed by

Giannattasio et al. [39]. The rate of kink-pair formation controls plastic strain rate, rather than their migration. According to Seeger's theory of kink-pair formation [40], the thermal component of a resolved shear stress σ^* exerts a repulsive force on the kinks which decreases the value of $2H_K$ An effective kink-pair formation enthalpy $H_{KP}(\sigma^*)$, which can be identified with the activation enthalpy for screw dislocation motion, can then be written as [41]:

$$H_{KP}(\sigma^*) = 2H_K - 2\alpha\sigma^* \tag{4}$$

with $\alpha = (a^3 b\gamma_0/2)^{1/2}$, where a is the distance between two adjacent Peierls valleys connected by a kink in a dislocation with Burgers vector b and γ_0 is the pre-factor in the logarithmic expression of the dislocation line tension [42].

BCC metals behave according to Schmid's law below the lower bend temperature shown in figure 9 with slip occurring on {110} slip planes, but above this temperature, slip also occurs on {211} and {321} planes (as already discussed on page 8) [25].

Another way of considering this behaviour is by calculating the period of the Peierl's potential on each slip plane, which determines the kink height. The kink height is the distance between two Peierls valleys connected by kinks. For a dislocation running along $< 111 >$, the Peierls potential has the period:

$$a_{\{110\}} = (2/3)^{1/2} a_0 \tag{5}$$

$$a_{\{211\}} = 2^{1/2} a_0 = 3^{1/2} a_{\{110\}} \tag{6}$$

$$a_{\{321\}} = (8/3)^{1/2} a_0 = 2a_{\{110\}} \tag{7}$$

for the slip planes {110}, {211} and {321}. It would be expected for the kink height to be equal to equation 5, the separation of the Peierls valleys on the {110} slip planes, as $a_{\{110\}}$ is the shortest kink height in the BCC structure, and the kink-pair formation enthalpy increases with an increasing kink height [43].

In studies performed to calculate the kink height from cyclic deformation experiments by the analysis of the cyclic-deformation data in terms of kink-pair formation [33, 44, 45, 46, 47], all BCC metals investigated disagreed with equation 5 (elementary slip steps on {110} planes) despite all specimens being aligned to favour the $[111]\{\bar{1}01\}$ slip system. However, there was excellent agreement with equation 6 - elementary slip steps on {211} planes. This result was also found for tensile tests [48, 33, 32, 49, 50].

Slip lines are often observed to be wavy and closely correlated to the plane of maximum resolved shear stress, but this does not contradict the idea of elementary {211} slip steps and easy cross-

slip at temperatures between the upper bend temperature and the knee temperature (these are referred to in figure 9) [43, 51].

Detailed slip behaviour studies in BCC transition metals were performed by Garratt-Reed and Taylor (niobium) [52] and Vesely (molybdenum) [53]. Their TEM studies showed dislocations with the $a/2 < 111 >$ Burgers vector predominate, although small numbers of $< 100 >$ type were observed. The $< 100 >$ originated from the interaction of two $a/2 < 111 >$ dislocations: $\frac{a}{2} < 1\bar{1}1 > + \frac{a}{2} < 11\bar{1} > \rightarrow a < 100 >$, which is an energetically favourable reaction.

1.2.1.4 Tension-Compression Asymmetry It is well known that the flow stress of BCC metals can depend on whether the specimen is being tested in tension or compression. Hollang et al. [33] and Seeger et al. [51] reported significant differences exist between stresses attained in compression vs tension for different crystallographic orientations in bulk single crystalline molybdenum. This was explained by the presence of twinning–anti-twinning slip asymmetry and by the motion of non-planar screw dislocation cores in response to the non-glide stress components via atomistic simulations [54, 55].

Groger et al. [56] found that shear stresses perpendicular to the Burgers vector on the glide of $\frac{a}{2} < 111 >$ screw dislocations had an influence on this effect by the use of atomistic modelling. These shear stresses were found to significantly elevate or reduce the critical resolved shear stress in the direction of the Burgers vector needed for the dislocation motion, (the Peierls stress). This occurs because the stresses affect the shape of the dislocation core. This effect may be the reason why slip systems with smaller Schmid factors may often be preferred over that with the largest Schmid factor in BCC metals (the 'Schmid law breakdown').

Being perpendicular to the Burgers vector, these non-glide stress components cannot directly exert a Peach-Koehler force on the dislocation (inducing glide), but by altering the structure of the core, they influence how large stresses exerting the Peach-Koehler force need to be applied for the dislocation to glide. In other words, the induced structural changes of the core modify the Peierls stress [56].

Hollang et al. [33] found the flow stresses in tension and compression began to deviate at temperatures around 65K below the knee temperature in pure Mo single crystals showing (211) glide. The asymmetry showed a similar strain rate dependence to the knee temperature. Similar effects in high-purity molybdenum were also observed by other authors in uniaxial testing [57] as well as in cyclic deformation [58].

1.2.1.5 Summary In BCC metals, edge dislocations are more mobile than screw dislocations at low temperatures ($0.2T_m$) and so the movement of screw dislocations is the rate limiting factor for slip. This is due to the polarisation of screw dislocation cores, which causes an ele-

vated Peierls stress. Movement of screw dislocations via the kink-pair mechanism (initiated by the thermally-activated movement of screw dislocation core atoms between lattice sites) has a lower associated energy than regular slip, hence this is the dominant slip mechanism. Below the critical "knee" temperature, flow stress of a BCC metal is reduced with increasing temperature (and increases with strain rate), as screw dislocation movement is thermally-assisted. This behaviour changes at T_k, above which there is a much lower thermal dependence of critical shear stress, and screw and edge dislocations are equally mobile. In a macroscale context, this translates to brittle behaviour of a BCC metal below the knee temperature, with deformation becoming gradually more ductile as the knee temperature is approached (the "semi-ductile" regime), above which the brittle character has disappeared. However, the knee temperature is not directly equivalent to the ductile-brittle transition temperature.

1.2.2 The Ductile-Brittle Transition

The temperature at which the behaviour of a BCC metal is said to transition from ductile to brittle upon cooling is referred to as the ductile-brittle transition temperature (T_{DBT}). There is no single method of stating the exact temperature at which a material has changed from ductile to brittle, primarily because it occurs over a range of temperature.

At a temperature above T_K, highly pure crystals with directional bonding can be plastically deformed with great reductions in area and their fracture is usually of a ductile nature. At the same time, below this temperature a quasi-brittle or brittle fracture usually occurs. The knee temperature T_K is not the ductile-brittle transition temperature T_{DBT}, but for crystals that are plastic above T_K, a danger of brittle fracture arises below this temperature. In other words, the condition $T_{DBT} < T_K$ is always true [29].

For a given material T_{DBT} is dependent on many factors: strain rate, crystallographic orientation, test geometry, purity, radiation effects, composition and sign of applied stress. All these parameters affect the type and form of operative slip systems, the magnitudes of yield and flow stresses and the shape of stress-strain curves [31]. "DBT graphs" of BCC metals - the variation of energy required for fracture with temperature and strain rate - have a characteristic S-shape, as shown in figure 13.

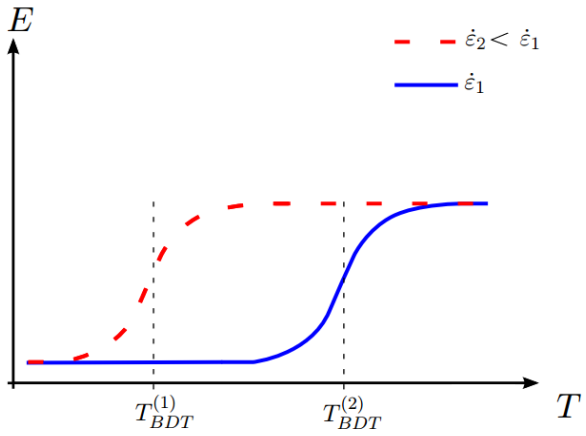


Figure 13: Strain rate and temperature dependence of energy required for fracture (equivalent to fracture toughness) in a typical BCC metal across the DBT range. Redrawn from [21] with a correction of sign error in the original source.

Although it has long been recognised that there is a relationship between the applied strain rate on a sample and its ductile-brittle transition temperature [31], Roberts, Hirsch and Samuels in 1989 [59], [60] were the first to link these two variables by an exact equation. In experiments on pre-cracked single crystal silicon, they found the strain rate $\dot{\varepsilon}$ and transition temperature T_{DBT} to be related via an Arrhenius relationship.

Dislocation velocity $V(\tau, T)$ and activation energy for dislocation mobility ΔE_d are related as follows:

$$V(\tau, T) = V_0(\frac{\tau}{\tau_0})^{m(T)} exp(-\frac{\Delta E_d}{kT}) \tag{8}$$

where V_0 and τ_0 are constants. Sample strain rate and dislocation velocity $V(\tau, T)$ are related:

$$\dot{\varepsilon} = \rho b V(\tau, T) \tag{9}$$

and the substitution of (9) into (8) leads to

$$\dot{\varepsilon} = \rho b V_0(\frac{\tau}{\tau_0})^{m(T)} exp(-\frac{\Delta E_d}{kT}) \tag{10}$$

Experimental study of T_{DBT} and $\dot{\varepsilon}$ by Roberts, Hirsch and Samuels [60] led to the following (very significant) relationship relating the ductility of a specimen's deformation response to a load to temperature, strain rate and geometry:

$$\dot{\varepsilon} = A e^{-\frac{E_{DBT}}{kT_{DBT}}} \tag{11}$$

where A is a constant dependent on loading geometry and specimen material, E_{DBT} is activation energy for the DBT, and k is Boltzmann's constant. Following this, the activation energy

for the DBT was then found to be the same as the activation energy for dislocation motion ($\Delta E_{DBT} = \Delta E_d$) [59] used in equation 10. This implies that the controlling process for the DBT in these materials is dislocation glide in the region near the crack tip (rather than whether dislocations can be nucleated at or near the crack tip) [61].

Experimental confirmation of this equation was found during studies of the DBT in other single-phase materials such as germanium [62] and alumina [63] in the 1980s and has been used in related studies since [64]. Dislocation-dynamics models applied to these materials of slip around crack tips and crack tip shielding can fit experimental results to high accuracy [65]. Similar modelling of BCC materials (W, Fe, V and Mo) has been performed with some success [66],[39]. However, the lack of experimental data on etch pitting techniques (needed to measure dislocation velocity) such as those successfully adopted for semiconductors (e.g. Si, Ge [39] and GaAs [67]) has held up its application to BCC metals [61].

Experimental data showed a value averaging 25 for the ratio $\frac{E_{DBT}}{kT_{DBT}}$, which equals the $\frac{E_{slip}}{kT_{DBT}}$ ratio [68], again confirming that the DBT is controlled by dislocation motion, and for T < T_k as shown in Section 1.2.1.3 by the formation of kink-pairs. The explanation for this number is still unclear.

A summary of E_{DBT} data on the ductile-brittle transition of Mo and other BCC metals is shown in figure 14.

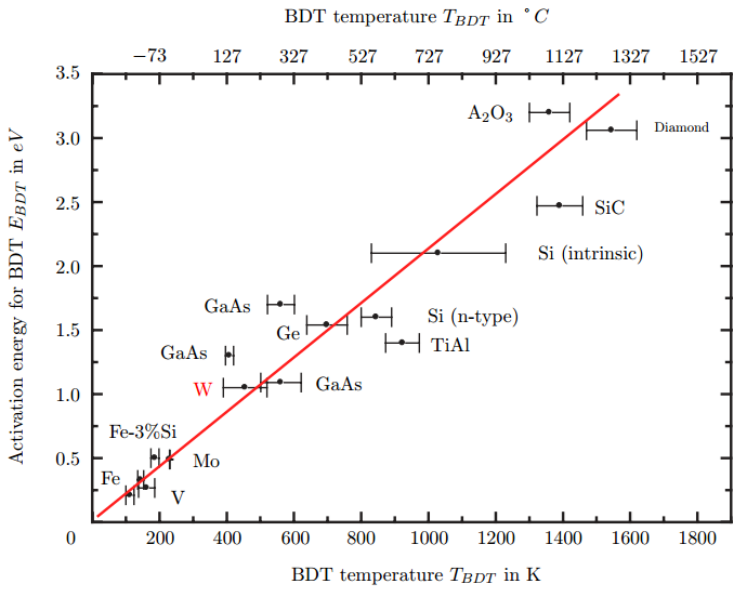


Figure 14: The activation energy for the brittle-ductile transition in different materials plotted as a function of BDT temperature. Data points indicate the average BDT temperature taken within the temperature range investigated. Data for W, V, Fe are from [39]. Other data are from: Si [59], GaAs [69], Ge [62], Al_2O_3 [70], Mo [66], SiC [71], TiAl [72], diamond [29] and Fe-3%Si [73]. Diagram from [39]. The error bars are a result of the strain rate dependence of T_{DBT}.

The values most important to this project are shown in table 1.

Table 1: E_{DBT} values for various BCC metals.

Material	E_{DBT} (eV)	$\frac{E_{DBT}}{kT_{DBT}}$
Mo	0.49	24.77
W	1.05	26.83
V	0.27	19.09
Fe (single)	0.33	27.08
Fe (poly)	0.21	21.80
Fe-3%Si	0.5	31.17

1.2.2.1 Defining $\mathbf{T}_{DBT}$ The transition from ductile to brittle behaviour occurs over a range of temperatures; there is no single specific criterium for defining a transition temperature but energy absorbed, ductility and fracture appearance may all be used to decide T_{DBT} [74].

The ductile-brittle transition and the knee in flow stress vs temperature have almost exclusively been treated as separate entities in the literature, and a search of the literature has found no studies that investigate both properties in detail on the same BCC sample, and a very small number that discuss both the ductile-brittle transition and the flow stress knee - an exception is [75] by Nemeth *et al.*.

As both behaviours are controlled by the enthalpy of kink-pair formation and affected by the same factors such as strain rate and impurity concentration, and there is an important interplay between the elevated flow stress at low temperatures and the increased likelihood of fracture at low temperatures, it is likely that further studies into the plastic behaviour of BCC metals will begin to investigate this area.

1.2.3 Mo Recrystallisation

A material's mechanical properties, such as ductility, hardness, strength and toughness, are strongly influenced by its recrystallisation behaviour, and in the interests of DBT and flow properties research, it is useful to know how this behaviour changes with thermomechanical treatment parameters, as experiments (for example hot nanoindentation) may approach recrystallisation temperatures. A recrystallisation diagram is therefore useful to predict the recrystallised grain size and to gain knowledge about how the recrystallisation temperature depends on the degree of deformation. Until 2009 the only reliable Mo recrystallisation diagram was recorded in the 1960s by Pink [76], but this diagram (figure 15a) does not accurately describe the recrystallisation behaviour of the current quality of technically pure molybdenum and Pink's study neglects to describe the history of the material in question.

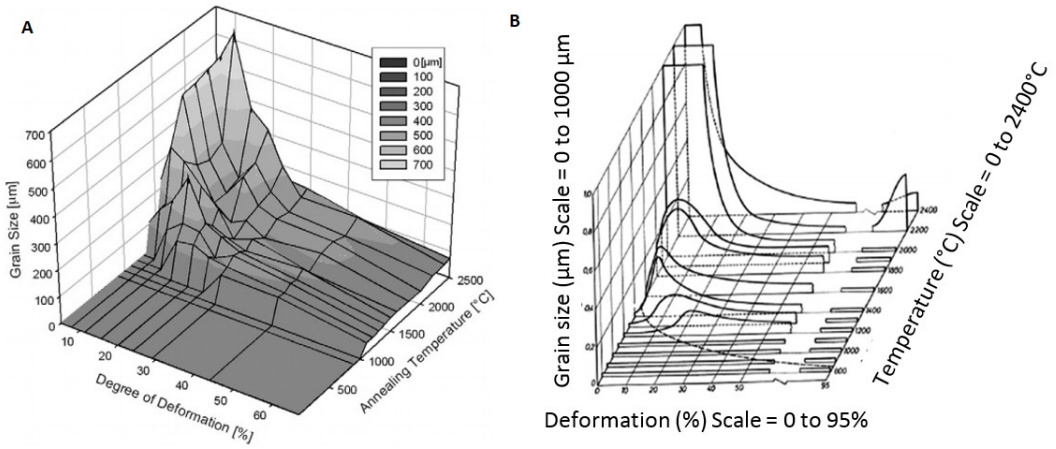


Figure 15: Mo recrystallization diagrams as reported by (A) Pink in 1965 [76] (The deformation was achieved by tension and the annealing time was 30 minutes). and (B) Primig in 2010 [77] (The deformation was achieved by hot rolling and the annealing time was 60 minutes)

Consequently, Primig et al. [77] performed a recrystallisation study (figure 15b) and established a diagram that reflects the static recrystallisation behaviour of current technically pure molybdenum by the means of electron back-scattered diffraction (EBSD) and electron channeling contrast imaging (ECCI) along with light microscopy and hardness testing, as shown in figure 16.

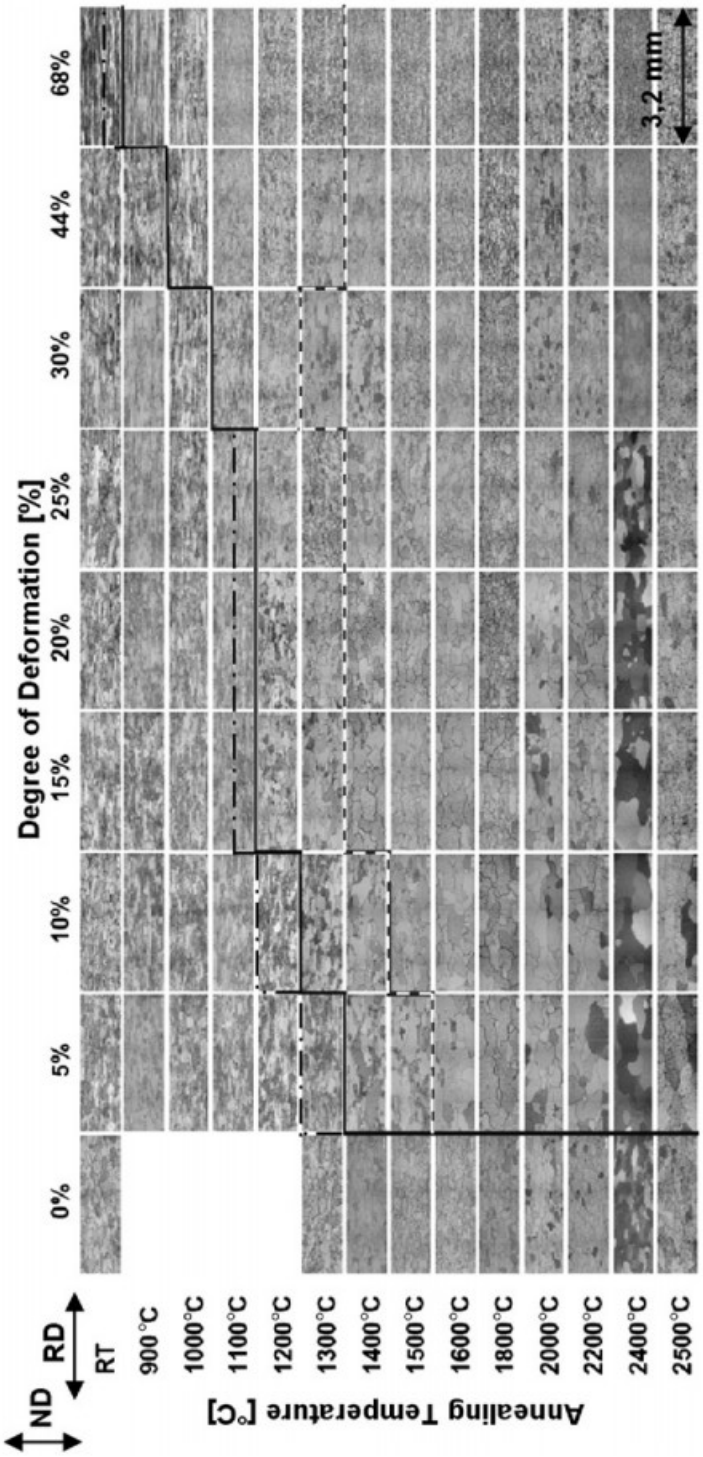


Figure 16: Overview of all differently deformed and subsequently heat-treated Mo sheet specimens from [77]. All images taken on longitudinal cross-sections. Annealing time - 1 hour. Start and end of recrystallisation determined by means of light microscopy are marked by the solid and broken lines, respectively. Start of recrystallisation determined by means of ECCI is marked by the dash–dot line. (RD - rolling direction, ND - direction normal to surface).

Figures 15 and 16 show that the higher the degree of deformation, the lower the recrystallisation temperature, and the first 5% has the greatest effect in reducing this temperature. This

has consequences for the length of the 'athermal' section of the BCC hardness-temperature graph, as the athermal section ends once recrystallisation begins, and the hardness decreases more quickly with changing temperature.

Fujii et al. [78, 79, 80, 81, 82, 83, 84] performed important work on developing the growth of Mo single crystals and as a consequence, the recrystallisation properties of Mo. They found recrystallisation behaviour to vary significantly with impurity concentrations (C, N and O) [78]. The grain size of pure molybdenum samples increased markedly from 0.05 to 2 mm at temperatures between 1700 and 2200°C. The grain size of a specimen annealed at 2300°C remained at about 2 mm, which corresponded to the specimen thickness. This type of grain growth was classified as normal grain growth. However, the grain size of the doped molybdenum increased only slightly at temperatures of 2100°C and 2300°C. As the temperature was increased further rapid discontinuous changes in the grain size took place, and this was classified as abnormal grain growth (secondary recrystallization) [79].

The rolling and primary recrystallisation textures in molybdenum are similar to those obtained for other pure BCC metals, i.e. three principal components: $\{001\} < 110 >$, $\{111\} < 112 >$ and $\{112\} < 110 >$. As a BCC metal Mo exhibits a high stacking fault energy and so its recrystallisation behaviour is strongly dominated by concurrent recovery processes, conversely to FCC metals which show a comparably low stacking fault energy. After a high temperature anneal the primary recrystallisation texture (normal grain growth) is retained in pure molybdenum [78].

Lastly, the mode and rate of deformation on cold worked Mo affect its recrystallisation characteristics. For example, after a constant amount of deformation strain, Mo deformed in pure compression recrystallises more slowly and with higher activation energies and coarser grains than that under simple tension, and deformation by rolling produces recrystallisation effects resembling those of compression, while drawing gives similar recrystallisation rates to tension [85].

1.2.4 Elastic Constants of Mo

Bulk elastic properties are necessary for components of the analysis of data in small sections throughout this thesis. Tensor components of these elastic properties (ones that depend on crystal direction) are used in Section 6.2.2 for finite element analysis of single crystal Mo cantilever specimens as directional elastic behaviour improves the accuracy of the model.

As a BCC metal, molybdenum has cubic symmetry. Its elastic constitutive law can be param-

eterised by 3 material constants - C_{11}, C_{12} and C_{44}, as shown in the following equation:

$$\begin{bmatrix} \sigma_{11} \\ \sigma_{22} \\ \sigma_{33} \\ \sigma_{23} \\ \sigma_{12} \\ \sigma_{13} \end{bmatrix} = \begin{bmatrix} C_{11} & C_{12} & C_{12} & 0 & 0 & 0 \\ C_{12} & C_{11} & C_{12} & 0 & 0 & 0 \\ C_{12} & C_{12} & C_{11} & 0 & 0 & 0 \\ 0 & 0 & 0 & C_{44} & 0 & 0 \\ 0 & 0 & 0 & 0 & C_{44} & 0 \\ 0 & 0 & 0 & 0 & 0 & C_{44} \end{bmatrix} \begin{bmatrix} \epsilon_{11} \\ \epsilon_{22} \\ \epsilon_{33} \\ 2\epsilon_{23} \\ 2\epsilon_{12} \\ 2\epsilon_{13} \end{bmatrix}$$

Three major resonance studies have been carried out on the temperature dependence of the elastic constants of molybdenum - Dickinson [86], Featherstone [87] and Koester [88]. A summary of the results are shown in figure 17. Koester only studied polycrystalline Mo, the results of which are used in this project in the polycrystalline experiments. Dickinson and Featherstone both separated the constants into C_{11}, C_{44} and C_{12}. The study by Dickinson is more comprehensive, covering a wider temperature range, and uses samples of a higher purity than those used by Featherstone. Additionally, Featherstone's room temperature values disagree with two other studies that agree with Dickinson [89, 90]. As such, the results from thin rod resonance techniques by Dickinson will be used when crystallographic elastic constants are required.

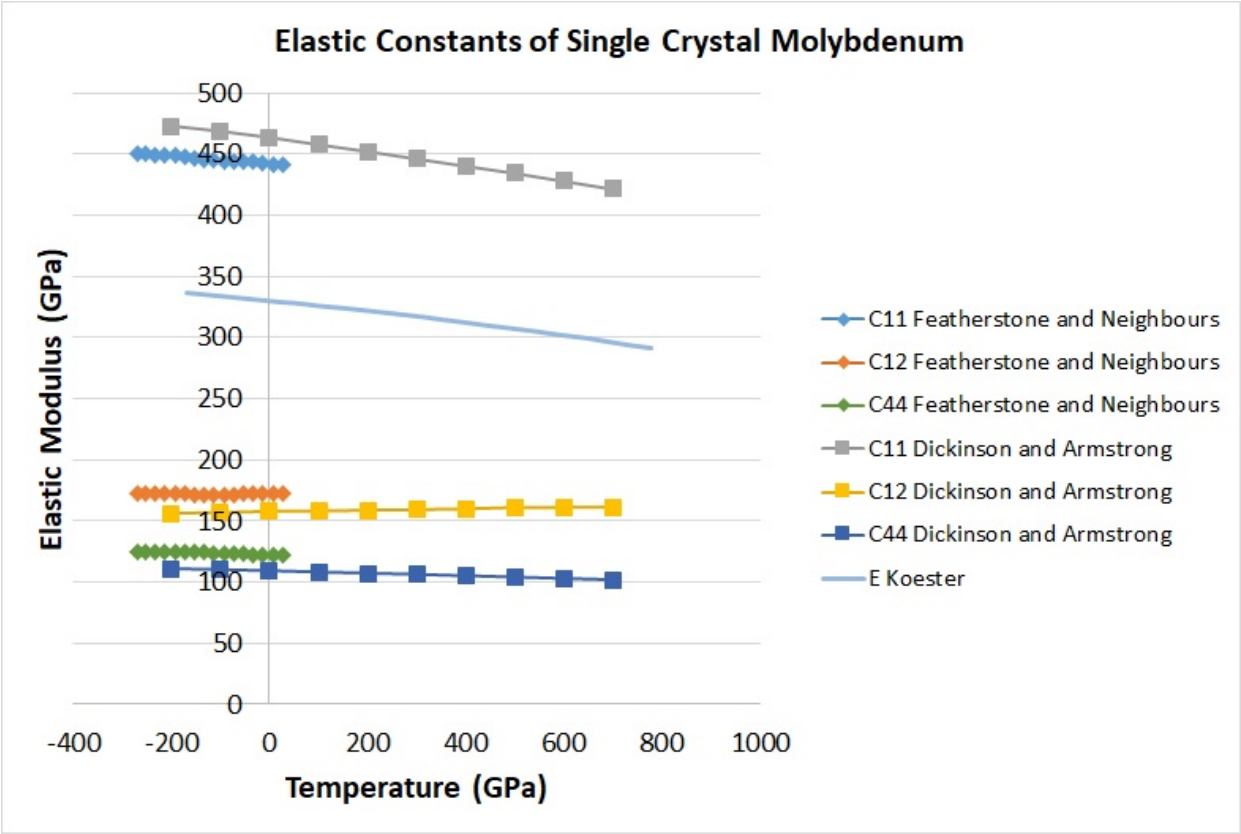


Figure 17: The temperature-dependent elastic constants of Mo taken from three different sources [86, 87, 88].

Figure 18 is a three-dimensional representation of the directional dependence of Young's modulus showing the pronounced anisotropy of Mo with greatest Young's modulus values in the $< 100 >$ directions [91]. This is shown in both the diagram and in the large difference between the C11, C12 and C44 curves in figure 17.

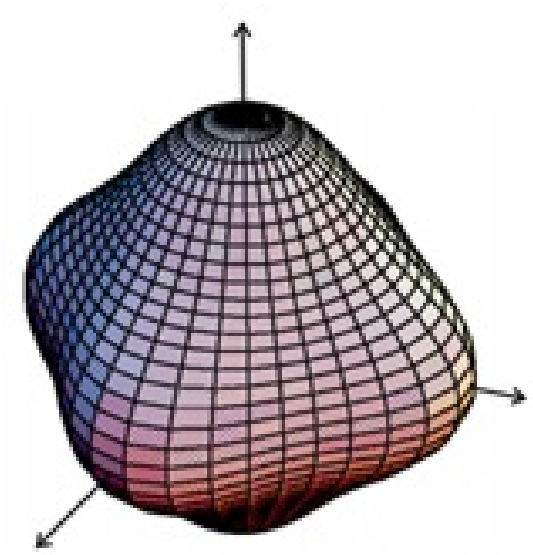


Figure 18: Calculated three-dimensional representation of the directional dependence of Young's modulus showing the pronounced anisotropy of Mo with greatest Young's modulus values in the $< 100 >$ directions [91].

1.3 Investigation of Temperature-Dependent Plasticity in BCC Metals

Plasticity research of BCC metals has been carried out for decades, but the relatively new development of FIB-milled microscale specimens (and temperature controlled nanoindentation systems) has enabled the study of BCC size effect and its dependence on temperature. Additionally, this has enabled the study of irradiated samples, which are typically layers a few microns thick. The majority of plasticity studies have focussed on the ductile-brittle transition, usually on pre-cracked samples.

In the field of DBT research of BCC metals, although the effect of strain rate on T_{DBT} was recognised early on, it was only when Roberts et al. calculated the associated Arrhenius relationship in 1989 [59] that systematic studies of strain rate effects started taking place. Due to their use in new generation energy, the investigation of BCC metals (particularly tungsten) has picked up in recent years, overwhelmingly by the use of matchstick specimen bend tests on the macroscale.

High temperature testing of molybdenum always requires a vacuum chamber due to the high propensity for molybdenum to oxidise.

1.3.1 Macro-testing

Mechanical testing of large (millimetre scale) test specimens was the principal method of plasticity investigation for many years. Single crystal and polycrystalline samples have both been

tested [92]. Arguably the most desirable test method would be the standard tensile test, but this is often difficult and costly, and machine compliance can introduce errors in the measurement of displacement. Compression tests provide difficult interpretation of data and only give compression behaviour [93]. Impact tests have also been widely-used, specifically in the investigation of the ductile-brittle transition; toughness is essentially a measure of energy required to fracture a specimen and the Charpy impact test is based on this principle. During the Charpy V-notch (CVN) impact test, a weighted pendulum impacts a notched specimen and the energy required for fracture is recorded. The CVN test is useful mainly as a guide to the fracture behaviour, giving a good indication of the DBT properties of a material but is not so useful for design purposes. Bend testing with notched specimens gives a value of fracture toughness, as used in linear elastic fracture analysis and so is a much more design-useful parameter. Additionally, the impact energy is measured at a very high strain rate when using CVN and fracture toughness bend testing is normally carried out at a much slower strain rate, possibly more relevant to actual applications.

Bend testing consequently makes up the majority of plasticity research, though with the sacrifice of a more complicated test procedure.

1.3.1.1 Three- and Four-Point-Bend Testing Four-point-bend test investigations of the ductile-brittle transition have been carried out on Mo, W and their alloys by Ellis 1991 [94], Ripley 1981 [31], Giannattasio 2009 [64], Gibson 2011 [95] and Durrans 2013 [96], all in the Oxford Materials Department. Other BCC metal investigations have been carried out, too; namely Gumbsch's work on W [97] and Odette's work on Fe-Si [98]. As aleady explained, T_{DBT} is dependent on strain rate. Most work previous to 1981 (Ripley's study) of W and Mo DBT investigation neglected to test strain rate sensitivity. An exception is Wronski's 1969 study using tensile tests on specimens with no pre-crack [92]; the relationship between transition temperature and strain rate in this case is shown in figure 19.

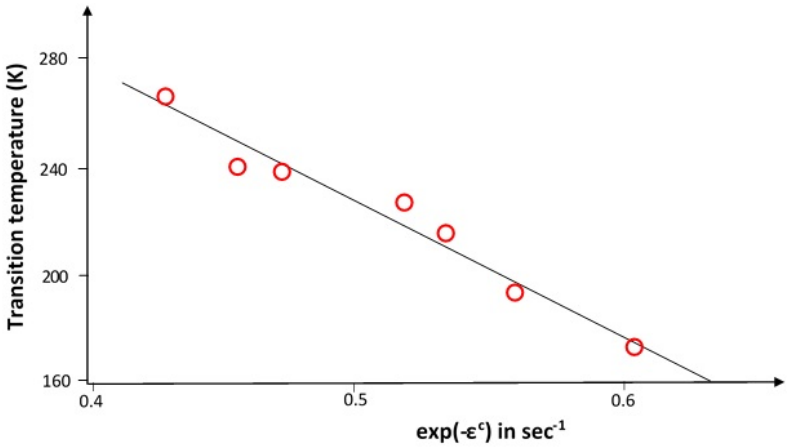


Figure 19: The dependence of the ductile-brittle transition temperature of molybdenum (with mean grain diameter 27 microns) on strain rate, $\dot{\epsilon}$. Redrawn from [92]

In the tests carried out at Oxford, matchstick specimens were cut from single crystal and polycrystalline bars in each case (these were generally 1mm x 1mm x 12mm) and four point bend testing was carried out using an Instron test rig.

A notch (or "pre-crack") can be included in matchstick fracture tests using electro-discharge machining to ensure all specimens have a largest flaw of uniform size and that fracture will occur at the pre-crack. Pre-cracking is not used in the investigation of temperature-dependent plasticity as fracture is not to be encouraged.

Previous work on high purity single crystal Mo had calculated an activation energy for dislocation motion of 0.63eV [99], calculated using an etch-pitting technique to measure dislocation velocities at different strain rates in three-point-bend tests. This value was in close agreement with modelling work [100] based on macrostrain deformation dynamics that gave a value of 0.64eV. Durrans [96] found an average value of 0.51eV for E_{DBT} of polycrystalline Mo.

A study that focussed on the temperature dependence of Mo flow stress using un-notched samples was carried out by [101], shown in figure 20.

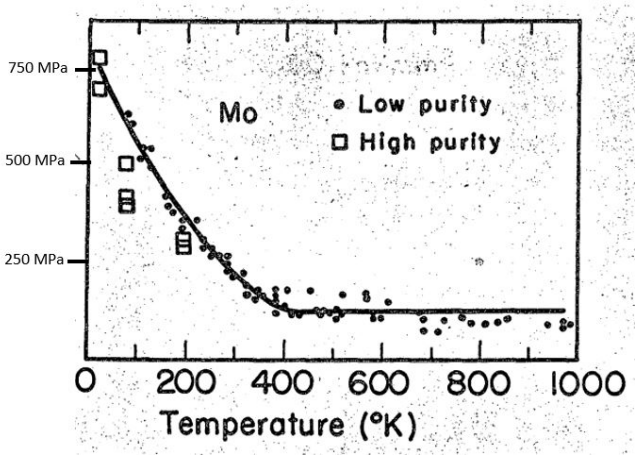


Figure 20: Resolved shear stress vs temperature of Mo. From [101], Y-axis redrawn.

As images of the stress-strain graphs were available from Durrans' work, some information on yield behaviour could be extracted, as shown in figure 21.

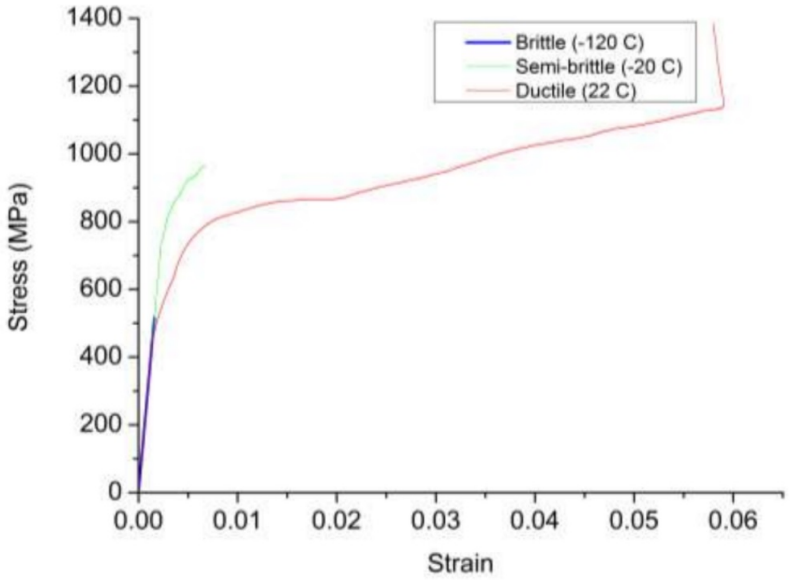


Figure 21: Previous work on the unannealed polycrystalline Mo samples from [96]. Variation of stress with strain at $4.44 \times 10^{-5} s^{-1}$ plotted for three specimens tested at -120, -20 and 22°C.

Approximated using calibration in ImageJ, Durrans found yield stresses at a strain rate of $4.44 \times 10^{-5}\text{s}^{-1}$ to be approximately 510MPa at 22°C and 720MPa at -22°C.

Additionally, Durrans found the ductile-brittle transition in this strain rate range to occur between -40 and 10°C, as shown in figure 22.

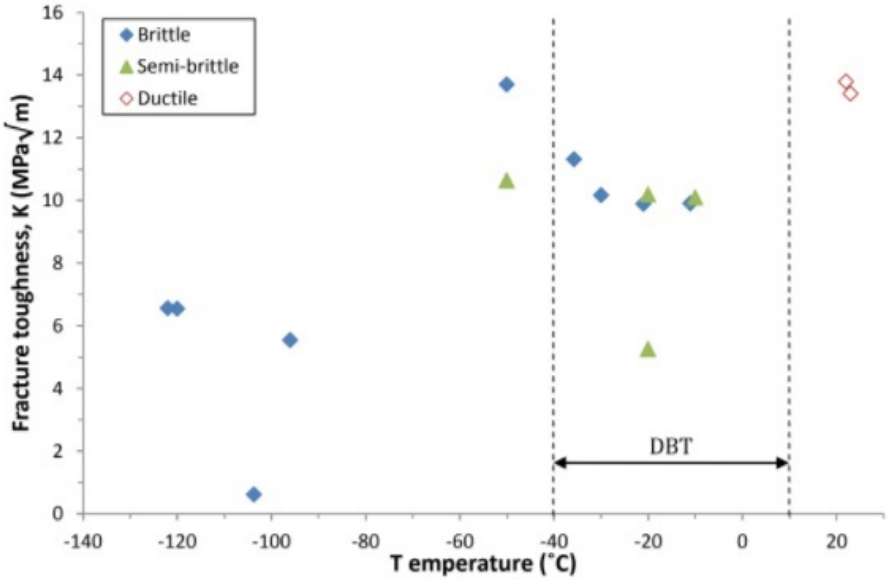


Figure 22: Previous work on the unannealed polycrystalline Mo samples from [96]. Variation of fracture toughness with temperature at $4.44 \times 10^{-5}\text{s}^{-1}$.

1.3.2 Micro- and Nano-Testing

The motivation behind this DPhil project is to further the understanding of the temperature dependence of plasticity in molybdenum, with the wider aim of testing its suitability for use in nuclear fusion. For this reason, it is beneficial to simulate the effect of various components of the fusion reactor on molybdenum. Damage to molybdenum caused by radiation in the fusion reactor such as lattice displacements, hydrogen and helium implantation and transmutation can be simulated using either fission neutron irradiation or heavy ion irradiation. Neutron irradiation is a more representative technique but is time-consuming and produces radioactive specimens [102, 103, 104]. Therefore, ion irradiation is preferable to simulate and understand the effects of radiation damage to inform predictive models. Ion irradiation produces shallow damage layers in materials, of the order of a few microns. This requires specialist testing techniques in order to extract mechanical property data.

Nanoindentation and microcantilever testing are most suitable for this. Nanoindentation allows quick and simple assessment of the change in modulus and hardness of materials after irradiation, which subsequently allows estimates of other properties such as yield stress. Bend tests of microcantilevers are used to fully analyse the mechanical response of an ion-irradiated layer. These cantilevers have been shown to be suitable in determining the elastic, plastic and fracture properties of materials, as will be explained in greater detail in Section 1.3.2.5. However, care must be taken when applying the results of these tests to bulk materials, as micromechanical testing shows a strong size effect, with smaller test pieces generally being stronger and tougher than their bulk counterparts [105].

It is very important to assess the properties of an unirradiated sample as fully as possible before testing thin ion-irradiated layers, as bulk material properties cannot accurately be predicted from microscale properties, or vice versa. As already explained, this is particularly important when bulk irradiated samples are unavailable in large quantities, if at all.

1.3.2.1 Microindentation The most simple technique used for the investigation of flow properties is indentation testing; this is an easy and essentially non-destructive way of measuring hardness and is one of the most important mechanical characterisation techniques in materials science due to its ease of use, speed and wide applicability to various material systems [106].

Micro- and nano-testing enable properties to be tested within very small areas of a sample. Tests can be carried out within single grains of a polycrystalline material, enabling crystallographic information to be found regarding flow properties. To perform these tests on bulk specimens would involve making testpieces from large single crystals, which can be expensive and restrict the orientations possible to test. This property is particularly important when investigating

the varying flow properties of a material with temperature; the yield and flow stresses of BCC metals are extremely sensitive to the crystallographic orientation of the stress axis [31].
The flow stress of a material can be loosely correlated to its hardness, as described by Tabor's hardness rule [107, 108]:

$$H \approx 3\sigma_y \tag{12}$$

and as such, techniques used to measure the hardness of a material can provide useful insight into its flow properties, where H is hardness and σ_y is yield stress.
There have been several studies reported concerned with the development and use of hot hardness testers. Experiments show that, in general, the hardness of materials decreases with increasing temperature, and as hardness and flow stress are closely related, hot indentation experiments can be useful in ductile-brittle transition investigations [109].

Indentation investigations of flow properties of refractory BCC metals have so far been restricted to hardness variation with temperature. Figure 23 shows hot hardness test results from Brenner [110]. In this study, a molybdenum specimen was tested to check the reproducibility of a hot hardness tester, and so the test temperatures are limited to room temperature, 400, 600 and 800°C. However, these points agreed within 4% after four runs were carried out.

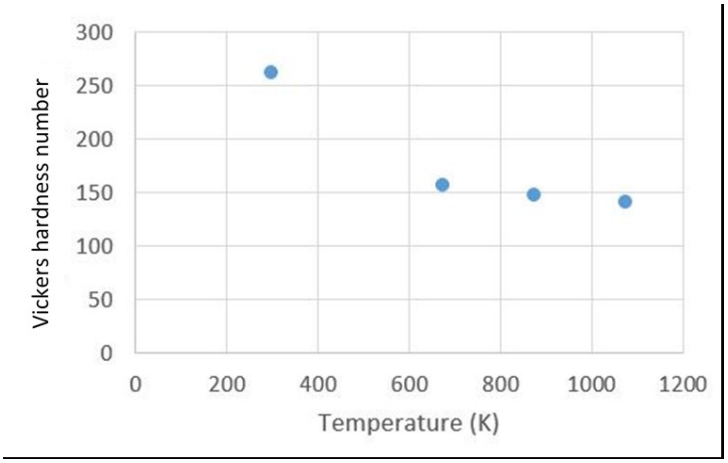


Figure 23: Hot hardness of commercial bulk molybdenum bar. Redrawn from [110]

Pisarenko et al. (1962) [111] performed a study of this kind on Mo and W. A sapphire Vickers indenter was used from 20 to 1750°C, and for higher temperatures (1750°C to 2700°C), the method of flattening one side of a conical specimen was used (apex angle of 120°). Work-hardened and annealed specimens were both tested, with the annealed measurements being taken while cooling from 1700°C. Unfortunately no suggestion of specimen dimensions is made, or of the method or extent of work-hardening.

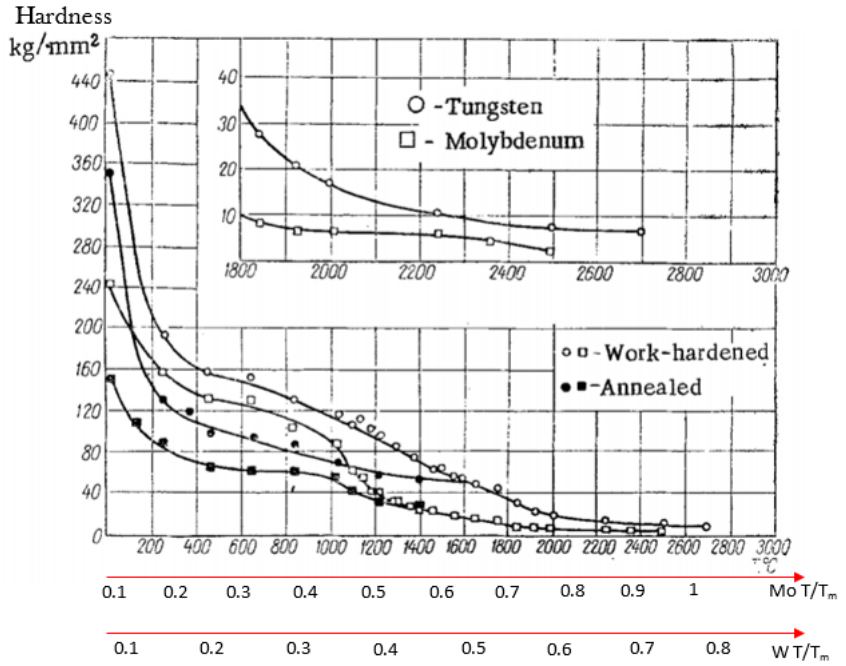


Figure 24: The effect of temperature on hardness of tungsten and molybdenum showing a decrease with temperature that has two 'knees', changing from regions of high thermal dependence to low thermal dependence. The lower temperature knee occurs due to the thermal activation of the kink-pair mechanism; the higher temperature knee occurs after recrystallisation has begun. (Temperature scales normalised by melting temperature have been drawn on for both Mo and W.) [111]

Figure 24 shows Pisarenko's hardness curve for work-hardened specimens of Mo and W (Temperature scales normalised by melting temperature have been drawn on for both Mo and W) containing a drop consistent with figure 9 but followed by two inflexions, which in this paper were found to be 0.14-0.2T_m and 0.4-0.51T_m, and in previous tests on pure metals had values of 0.1-0.15T_m [112] and the second at 0.5-0.55T_m [112, 113, 114].

The position of these discontinuities has been shown previously [113] to depend on the degree of work-hardening; previous plastic deformation lowers the high-temperature discontinuity. It has also been claimed that purity, grain size, rate of deformation, character of the stress state, etc, influence the exact position of both discontinuities.

Pisarenko suggests that the discontinuities are linked with changes in the mechanism of deformation: with increasing homologous temperature, three deformation mechanisms gradually succeed one another in pure metals, and hardness curve discontinuities correspond to one mechanism taking over another. Because the Young's modulus-temperature curve only had a high temperature bend (at 0.5-0.55T_m, similarly to hardness T variation), Pisarenko deduced that the magnitude of the interatomic bond stiffness of metals (modulus of elasticity) plays an important part in the resistance to plastic deformation. It has since been established that thermal activation of the kink-pair mechanism is responsible for the low temperature discontinuity and

the annihilation of cold work dislocations during recrystallisation is responsible for the high temperature discontinuity [25].

A more recent microindentation investigation into the hardness of tungsten is shown in figure 25. A steep initial drop in hardness was seen up to 300°C with an average hardness decrease of 5 MPa/1°C, (a decrease to 45% of the 20°C hardness value over 280°C). Above 300°C the rate of hardness change significantly decreases to 0.7 MPa/ 1°C. These data are in good agreement with high temperature micro-hardness experiments performed by Lee and Flom [115] and Pisarenko [111] who saw a similar rate of change of hardness in the same temperature regimes.

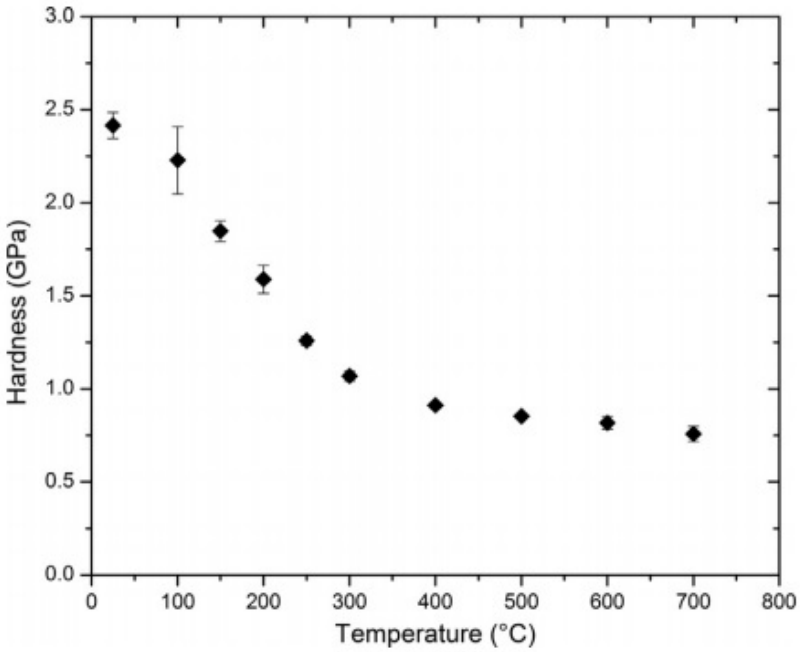


Figure 25: Microindentation hardness of tungsten as a function of temperature. Two distinct regions, above and below approximately 300°C can be seen. Error bars indicate one standard deviation in the measured hardness. [116]

A final observation (the difference between work hardened and annealed curves on figure 24) shows that both W and Mo are subject to strong work-hardening during plastic deformation but after the onset of recrystallisation this difference decreases and the curves fully coincide once recrystallisation has completely obliterated the effect of work-hardening (1600°C for W and 1400°C for Mo).

As yet, the majority of DBT investigation using indentation techniques have involved some form of fracture, although this is not always easy to obtain with an indenter. Studies have been limited to ceramic-like materials such as quartz, olivine [117] and GaAs [118] as they are inherently very brittle and prone to cracking.

Wang et al. [118] succeeded in measuring ductile-to-brittle transition properties of 001-GaAs using two variations of high temperature microhardness testing: “conventional static” and “dy-

namic displacement-sensitive" tests from room temperature to around 500°C, under vacuum. (Dynamic displacement-sensitive testing removes the need to measure indentation diagonals [119].) The temperature dependence of hardness was measured and from the disappearance of indentation cracks, the so-called indentation ductile-to-brittle transition temperature T_{IDBT} was determined. Wang et al. [118] measured the indentation crack length at different temperatures - micrographs are shown in figure 26a and results in figure 26b.

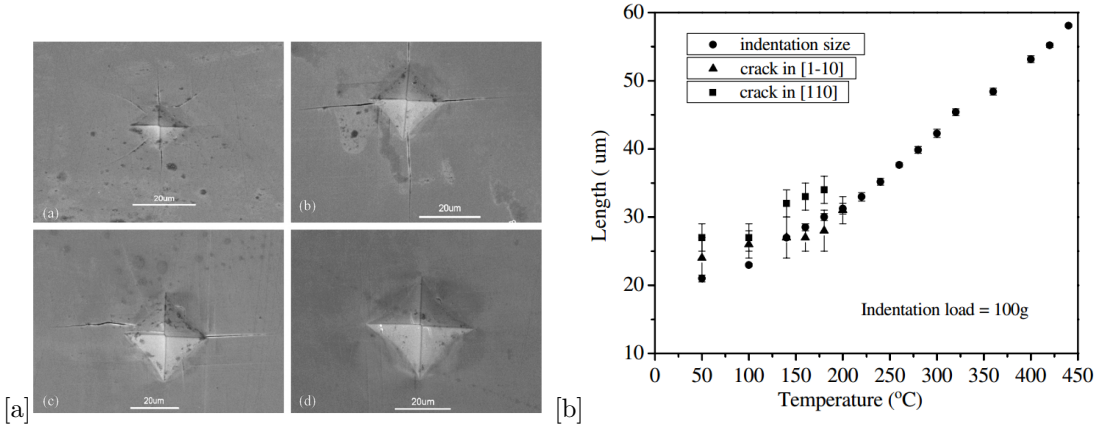


Figure 26: Figure (a) Optical microscopy images of indentations made on the (001) face of GaAs at different temperatures: (a) T = 25°C, (b) T = 90°C, (c) T = 220°C and (d) T = 300°C. Figure (b) Temperature dependence of the indentation size and crack length (half-length from the indentation corner) [118]

These indentation cracks completely disappeared when the temperature approached a critical value of about 200°C, which presumably corresponds to T_{IDBT}. Is notable in figure 26b that the indentation cracks get longer with increasing temperature up to the point when they are no longer observed. This would suggest a decreasing fracture toughness with increasing temperature, which is not to be expected. However, this is not addressed in the text.

This fit well with previous work; indentation-induced crack length in Ge as a function of testing temperature [120] and constant-rate indentation tests of Fujita et al. [69] in GaAs saw crack length decreasing drastically above a certain temperature (approximately 200°), reflecting a sharp increase of the stress intensity factor K_{1C} above T_{IDBT} [69]. A ductile-brittle temperature found by displacement sensitive indentation will be lower than that conventionally found by bend tests due to the superimposed hydrostatic component in an indentation test (Wang's comparison of T_{IDBT} with T_{DBT} found by 4-point bend found a difference of nearly 100°C). Additionally, the indentation method indicates the temperature at which cracks will no longer nucleate (in the indentation plastic zone), whereas four point bend tests indicate the circumstances under which pre-existing cracks will no longer propagate.

Without measuring indentation diagonals (or cracks), load-displacement curves plotted using

the dynamic displacement-sensitive microindenter can be used to determine the elastic/plastic properties of a material, significantly speeding up the measurement process (as the sample does not have to be imaged post-test) and so enabling more repeat measurements. In order to study a material's knee behaviour in this way, load–displacement curves must be obtained at a series of temperatures covering the brittle and ductile regimes of the crystal.

For a typical elastic–plastic crystal [121], the area under the loading curve is proportional to the total energy E_{tot} consumed in producing the impression. The area between the loading and unloading curves is proportional to the plastic energy E_{pl} expended in producing irreversible deformation of the material and the area under the unloading curve (proportional to $E_{tot} - E_{pl}$) is the elastic energy [122]. In a crystalline material, the plastic energy E_{pl} is used in generating and moving dislocations during indentation and for the surface energy of any indentation cracks produced.

Figure 27 shows a series of load–displacement (P–h) curves recorded by Wang [118] (constant maximum load 1.1N at several temperatures up to 350°C in GaAs), with behaviour typical for an elastic-plastic material. At low temperatures, significant elastic recovery is observed during the unloading part of the curve (figure 27a), the loading and unloading curves are not separated too far from each other and the elastic energy is small. As the test temperature increases (from figure 27a–d), so does the maximum indenter penetration depth h; elastic recovery decreases and the crystal tends further towards plastic behaviour. At the highest temperature (figure 27d), the P–h curve is similar to that observed for a nearly fully plastic material [122]) and the unloading curve is nearly a vertical drop. These curves are similar to those obtained for silicon in the high-temperature DSI experiments of Suzuki and Ohmura [123].

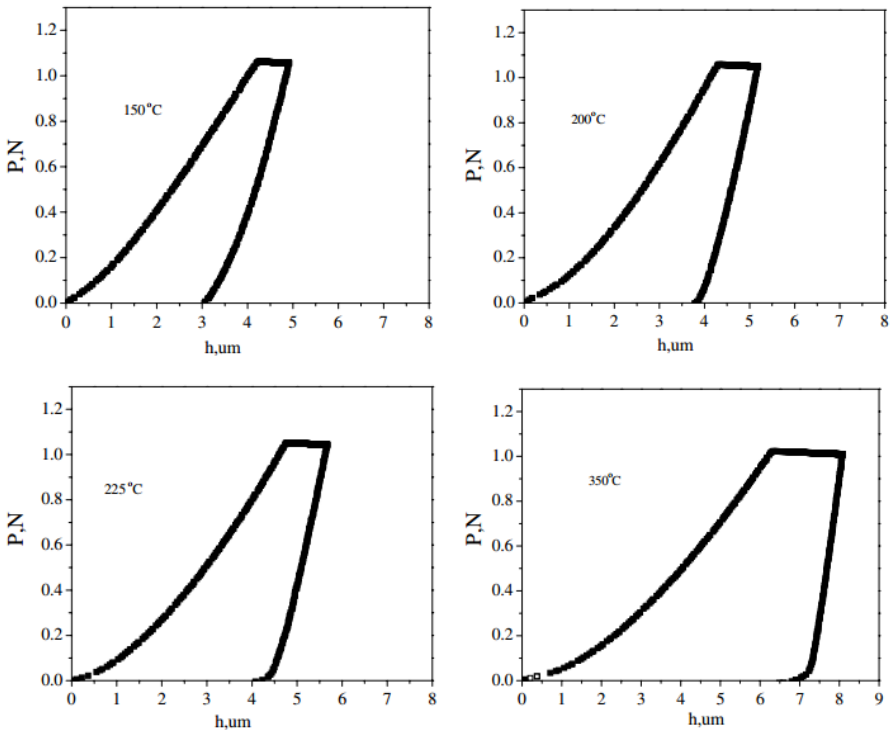


Figure 27: Load–displacement curves for Vickers indentations on the (001) surface of undoped GaAs at different temperatures. The elastic recovery upon changing sample temperature changes from a steep gradient below around 175°C to a shallow gradient above around 225°C [118].

As suggested in the load-displacement curves (figure 27), the elastic recovery upon changing sample temperature changes from a steep gradient below around 175°C to a shallow gradient above around 225°C, as shown in figure 28a. Wang [118] also plotted the change in "Martens Hardness" [124] with temperature, otherwise known as energy density $\frac{E_{tot}}{V_{tot}}$, where V_{tot} is the volume of the residual indentation in the material (figure 28b). At low temperatures, energy density does not vary with temperature and the plot is almost a horizontal straight line. At a certain temperature, there is a sudden change in the plot and energy density starts to decrease rapidly and continuously.

Corresponding changes in the deformation substructure showed cracks emanating from the corners of all the indentations made below the critical temperature, whereas the indentations were crack-free when made above this temperature. Wang's conclusion was that this critical temperature T_c in the energy density plot corresponded to the indentation brittle-to-ductile temperature, T_{IDBT}. This temperature is much lower than DBT tests carried out by other means (for example, the work by Samuels [59] found T_{DBT} values in the range 500 to 650°C across a range of strain rates by bend testing pre-cracked samples.

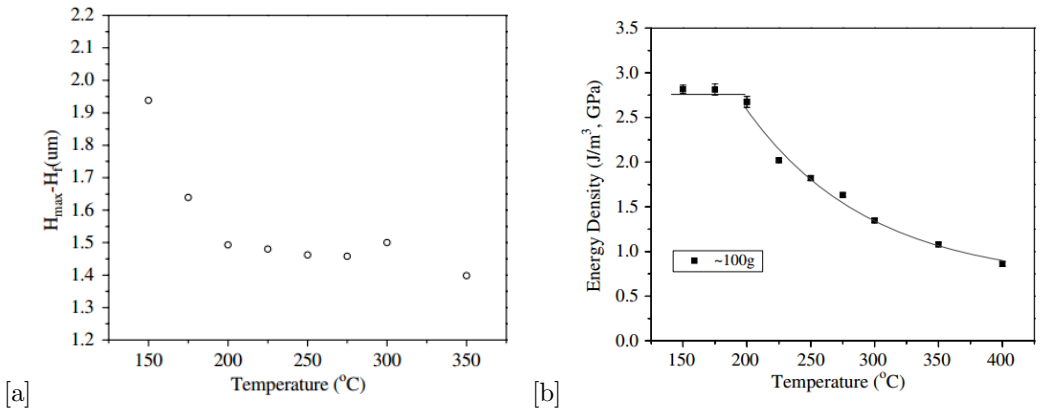


Figure 28: Figure (a) Temperature dependence of elastic recovery of single crystal Si at different temperatures; H_{max} and H_f refer to the maximum indentation depth at the maximum load and the residual indentation depth after unloading. Figure (b) Temperature dependence of the energy density $\frac{E_{tot}}{V}$ [118].

A figure summarising temperature dependent flow stress results of Mo from the literature is shown in figure 29 from [25, 32, 101, 110, 111]. These results were extracted using ImageJ. This has been converted from hardness where necessary using Tabor's relation (equation 12). The results in figure 10 showed only the temperature-dependent component of flow stress, so a temperature-independent flow stress equivalent to that in figure 9 has been added to the data.

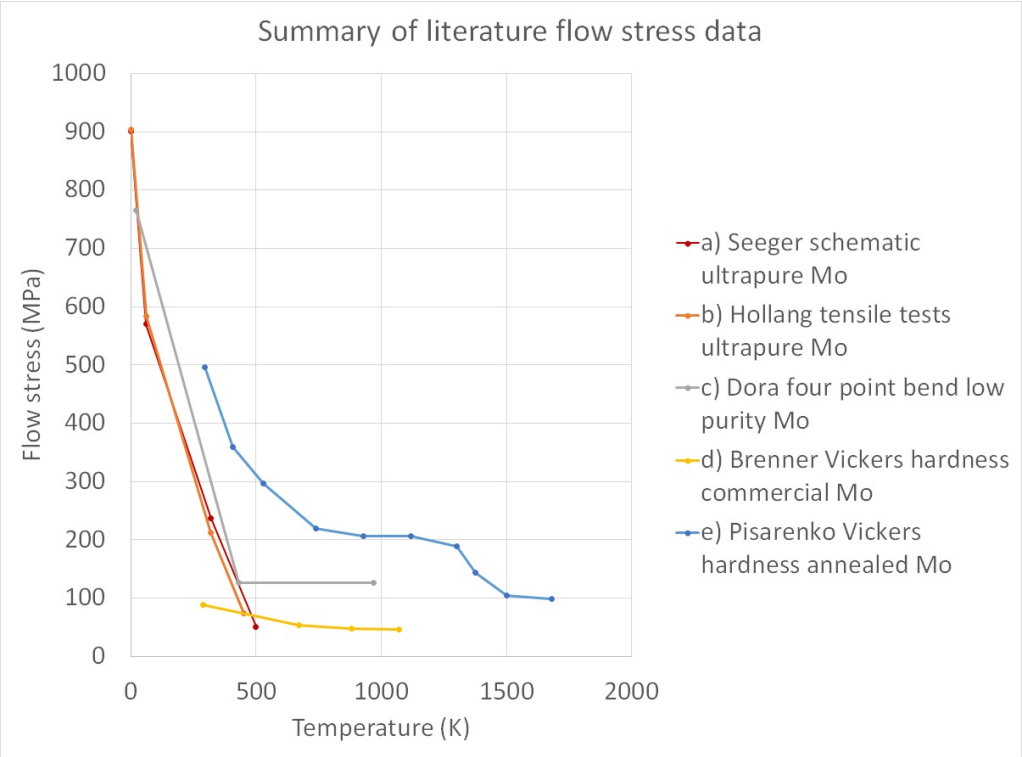


Figure 29: Summary of literature flow stress data (converted from hardness where necessary using Tabor's relation).
a) Schematic of the temperature dependence of the flow stress of ultrapure Mo crystals - Seeger et al. [25], figure 9b
b) Tensile tests on ultrapure Mo single crystals - Hollang et al. [32], figure 10
c) Four point bend resolved shear stress of unnotched low purity Mo samples - Dora et al. [101], figure 20
d) From Vickers hardness of a commercial bulk Mo bar - Brenner et al. [110], figure 23
e) From Vickers hardness of annealed Mo - Pisarenko et al. [111], figure 24

1.3.2.2 Nanoindentation In the past two decades, a revolution has occurred in indentation testing, owing to the development of new sensors and actuators that allow instrumented indentations to be routinely performed on submicron scales. The resulting technique, termed nanoindentation, has now become ubiquitous for mechanical property measurements at surfaces [125]. Nanoindentation is similar to larger scale hardness indentations. A Berkovich pyramidal indenter is pressed into the sample surface and continuous load and displacement measurements are made. Single grains may be indented; force resolution is under 50nN and displacement resolution may be below 0.01nm [126], giving precise measurements of elasto-plastic properties corresponding to individual grains. As with displacement sensitive microindentation, it is not necessary to image indentations as images are not involved in the measurement process, greatly increasing the number of measurements that can be made within a given time period and making nanoindentation especially attractive.

A typical loading graph is shown in figure 30 [127]. Deformation at any point is made up of both an elastic and a plastic component – upon unloading, the elastic component relaxes and

a permanent impression is left.

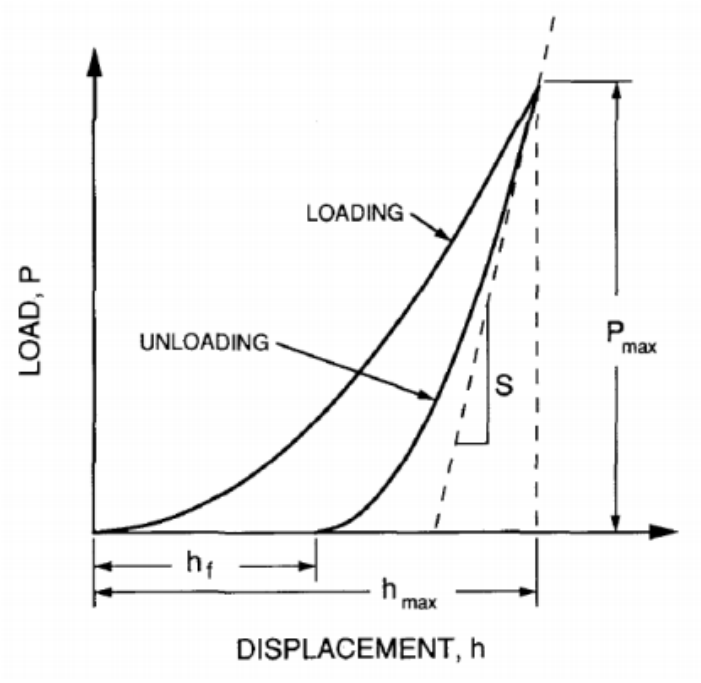


Figure 30: A schematic representation of load versus indenter displacement data for an indentation experiment. The quantities shown are P_{max} (the peak indentation load), h_{max} (the indenter displacement at peak load), h_f (the final depth of the contact impression after unloading) and $S = dP/dh$ (the initial unloading stiffness). From [127]

Several nanoindentation experiments have been performed in scanning electron microscopes under vacuum conditions [128, 129] and in transmission electron microscopes [130, 131], enabling the direct observation of deformation mechanisms during a test.

Despite the simplicity of nanoindentation, its use in the measurement of mechanical properties has its drawbacks. Firstly, the elastic zone surrounding indentations is large and roughly spherically symmetric [132], and so data gathered is dependent on orientation of all grains contained in the zone in polycrystalline samples, and even in single crystal samples, the displacements associated with indentation contact cover all radial orientations within the hemisphere surrounding the contact point, causing the indentation modulus to be an average over many crystallographic directions. This complex stress state under the indenter tip means the exact volume being probed is unclear, especially for measurement of elastic properties. EBSD [133, 134, 135] and TEM [136, 137] analysis of indentations shows that the plastic zone is heterogeneous, with multiple slip systems being activated. The calculation of critical resolved shear stress (CRSS) values is therefore non-trivial [138].

Finally, nanoindentation takes no account of material "piling-up" or "sinking-in" around the indenter tip. This effect can lead to significant overestimates of hardness and modulus as the

contact area increases. It is often observed in elastic-plastic materials [139]. The Oliver-Pharr method also assumes elastic isotropy; most real materials (including BCC metals) are elastically anisotropic, but theoretical models have been developed to predict the indentation moduli of anisotropic materials [140] based on known elastic constants. Additionally, anisotropy often occurs in hardness measurements, but this is not a strong effect in experiments using a triangular indenter and a cubic-symmetry test material such as BCC molybdenum (as will be investigated in this thesis). Further complications arise from the presence of grain boundaries, inclusions or other microstructural features that interact with elastic and plastic stress fields.
These limitations can be resolved by using nanoindention systems to bend, pull and compress test pieces with well-defined geometries and stress states, as described in Section 1.3.2.5. However, these tests are more complicated and time-consuming to carry out.

1.3.2.3 Hot and Cold Nanoindentation Engineering materials are often used in non-ambient conditions in service so the combination of testing in controlled atmospheres at variable temperatures with the benefits of nanoindenter apparatus is extremely useful. Poisl, Oliver and Fabes introduced the idea of elevated temperature nanoindentation in 1995 by placing a commercial nanoindenter in a temperature-controlled room and increasing the room temperature to 32-34°C, testing amorphous selenium [141]. Two years later, Suzuki and Ohmura [123] developed the first prototype of a high temperature indentation instrument, used for fast indentations up to 600°C, but these fast testing rates adversely affected the test sensitivity.
Nanoindentation at elevated temperatures is a less developed procedure than hot microhardness testing (which has been in use for decades), but since Suzuki's fast indenter, many researchers have made improvements to both the instrumentation and the techniques themselves and the technique is now routinely commercially available up to 1000°C [142].
Early high temperature nanoindentation work focussed on hardness and Young's modulus measurements, and inevitably on the establishment of the technique. The majority of later studies focussed on pop-ins, indentation creep, phase transformations and glass transitions of metallic glasses [143]. Figure 31 is graphical summary taken from Trenkle's review [144] of various micro and nanoindentation experiments reported in the literature until 2010, logging the test temperature and characteristic scale of the indentations for each study, with micro- and nanoindentation differentiated by symbol. The points in this graph define a region that reflected the current state of the art in high temperature indentation; all combinations of temperature and depth within the region can be accessed with reasonable experimental resolution. However, if

this region is further divided according to the materials tested, a much smaller region can be identified that is accessible to oxidizing materials such as metals. In the existing experimental literature, studies on these materials either require a sufficiently low test temperature to retard oxide growth [145, 146, 147] or involve flowing inert gas to dilute oxygen content in the atmosphere around the sample [148, 149].

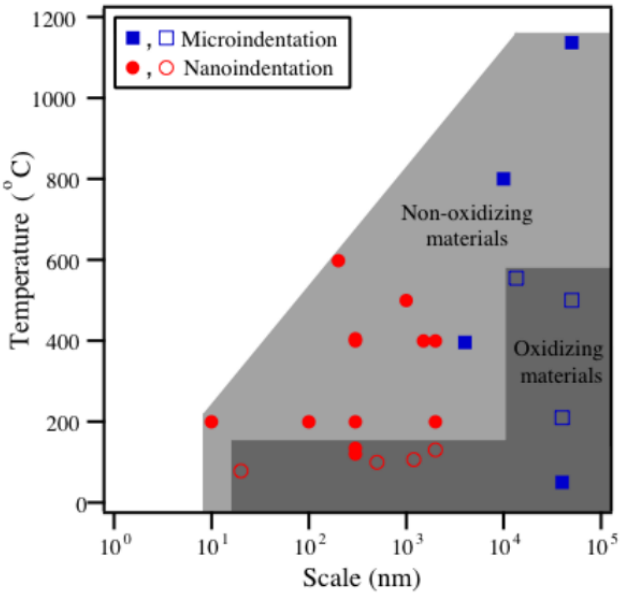


Figure 31: Temperatures and indentation scales reached by previous nanoindentation (circles) and microindentation (squares) experiments. Two regions were identified: one defined by indentation on non-oxidizing materials and a second, much smaller regime defined by metals alone (open symbols). To expand the second regime, minimization of thermal drift and sample oxidation are required. [144] - results taken from 38 sources.

Figure 32 shows the progress made in developing high temperature nanoindentation systems over the last two decades. The symbol points show the rapid increase in the maximum indentation temperature available in nanoindentation systems since 1994. The majority of the highest temperature data points have been made possible by the use of both tip and sample heating, as temperature gradients between the tip and sample can be reduced significantly. The use of a horizontal pendulum has also helped in this regard; it allows convection to vertically remove heat from the sensor region [150].

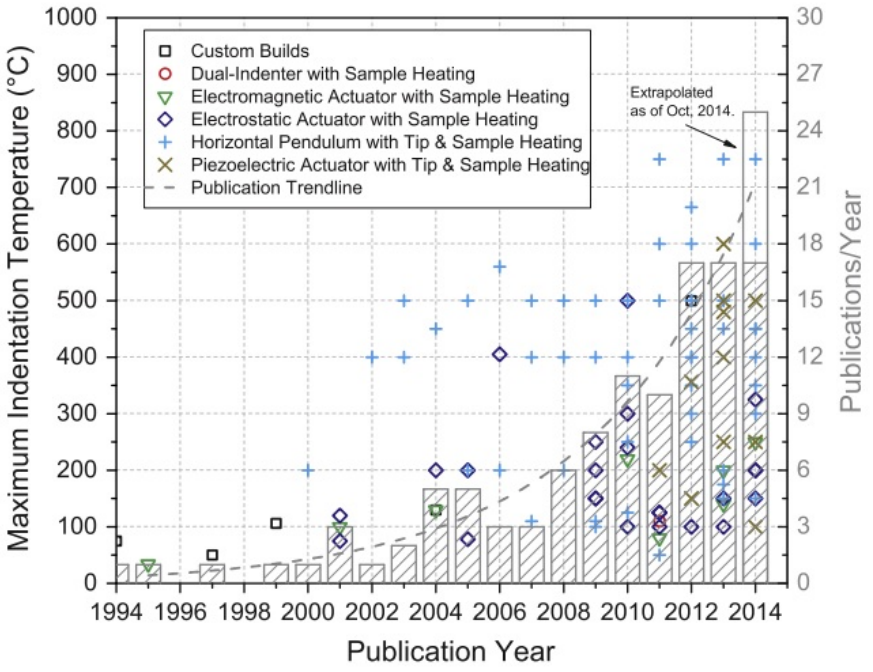


Figure 32: Maximum published indentation temperatures for various system configurations and publications per year in recent years [151, 150].

Universally achieving nano-scale indentations at higher temperatures (and thus expanding the envelopes in figure 31), requires instrumentation advances in two arenas: minimizing or eliminating oxidation and successful management of thermal drift and noise [143].

A controlled atmosphere or vacuum is necessary for tests above approximately 200°C to minimise oxidation in most materials, but this involves large modifications to the nanoindentation system. The avoidance of sample oxidation is critical for the smallest nanoindentation experiments; oxidation causes measured properties to become convoluted with those of the oxide. This concern becomes significant when studying physical phenomena such as dislocation nucleation that are best probed at very shallow indentation depths [144].

Thermal drift, which occurs when any component in the load frame expands or contracts in response to changing thermal gradients, is another major issue in elevated temperature nanoindentation. It results in the measurement of apparent displacement that is not a true reflection of a material's force-displacement response; it is assumed to be constant in room temperature tests as it is generally low. This allows drift to be straightforwardly subtracted from the material response. When a heat source is present it encourages larger thermal gradients and load fluctuations. This in turn leads to higher drift rates, increased variation in drift rate from one nanoindentation to the next, and even a progression of drift rate over the duration of a single test [144]. Schuh et al. [125] controlled thermal drift during testing in air up to 400°C but

concerns were raised about the feasability of high quality testing at higher temperatures when the trend of increasing thermal drift rate with temperature was observed.

Unfortunately, although oxidation is most effectively minimised by testing either in a vacuum or a controlled atmosphere, the introduction of a vacuum or inert gas inevitably changes thermal transport in the system, and thus can impact thermal drift and noise during testing as well. In addition, thermal drift rates increase at higher testing temperatures [125, 152].

Successful high temperature studies have been performed despite these difficulties; Schuh et al. achieved good temperature equilibration and thermal drift control up to 405°C in their study on T-dependence of hardness and Young's modulus in fused silica, as well as results in good agreement with literature data for these properties [125]. Nickel superalloys have been tested up to 600°C in an environmental chamber purged with high purity Ar, with $<0.01\%O_2$ [153]. However, the indenter tip and sample surfaces oxidised at the highest temperatures, so the diamond tip used below 500°C had to be replaced with a sapphire tip at higher temperatures; diamond has the potential to degrade to graphite above 500°C [154].

Trenkle et al. have experimented on a high temperature nanoindenter ($\leq$ 500°C) contained within inert atmospheres including partial vacuum and gas near atmospheric pressures [144].

There have been very few hot nanoindentation studies of BCC metals. Britton, Armstrong et al. [155] made measurements of elastic, plastic and fracture properties of W and Si up to 770°C under vacuum (1×10^{-5} mbar). Both the tip and sample were heated, giving a well-characterised indentation temperature. Britton's work was performed on new equipment (manufactured by Micromaterials Ltd.), and as yet is unpublished. The equipment is also able to test under inert gas (N_2, Ar) or reducing (He, H) atmospheres, with all components vacuum compatible. Load is variable from $10\mu N$ to $500mN$ and displacement from $10nm$ to $20\mu m$, and as well as operating as a nanoindenter, the inclusion of a piezoelectric nanopositioning stage for nanometre resolution surface profilometery allows use in AFM mode, so that small test elements such as microcantilevers can be located, imaged and tested [156].

Rajulapati et al. studied the temperature dependence of plastic flow behaviour in (001) Ta using nanoindentation [152] in the temperature range 25-200°C. Most notably it was found that the shape of the load-displacement curves changes with increasing temperature. This is shown in figure 33, which includes curves measured at 23°C, 100°C and 200°C

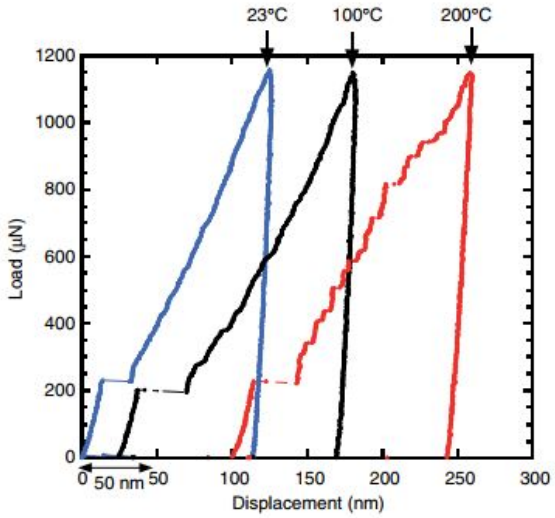


Figure 33: Representative load–displacement curves at a loading rate of 1000 mN/s at temperatures of 23°C, 100°C and 200°C. Curves are offset for viewing purposes [152].

Analysis of the load-displacement indicated that the lattice resistance decreases with increasing temperature; the elastic-plastic part of the curves was fit to the Taylor dislocation model developed by Nix and Gao [107], Qiu et al. [157], and Durst et al. [158]. This model approximates the nanoindentation load to be proportional to the sum of internal friction stress and Taylor stress during loading. Following this method, the friction stress was found to decrease with increasing temperature, from 130 MPa at 23°C to 10 MPa at 200°C as shown in figure 34 consistent with the mobilisation of screw dislocations at the knee temperature T_K by thermal activation.

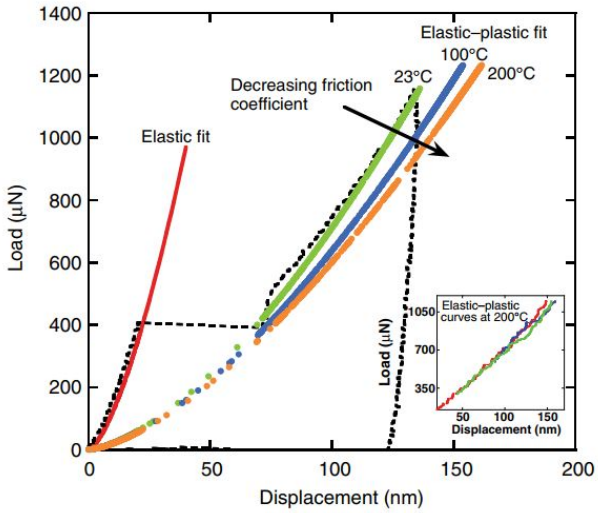


Figure 34: Elastic–plastic and elastic fit at 23°C, 100°C and 200°C; dashed curve is at 23°C. The decreasing friction coefficient as a function of temperature is shown by the decreasing gradients. Inset shows three representative elastic–plastic curves at 200°C used for friction coefficient calculations [152].

Although there are macroscale sub-ambient temperature commercial mechanical testers

[159], up until 2010 there were no reports of low temperature nanoindentation capability [160]. In 2010, a newly-developed sub-ambient temperature nanoindenter was used by Chen et al. [160] to investigate the mechanical properties and creep behaviour of polypropylene around its glass-rubber transition temperature. As with hot nanoindentation, design changes had to be made to the standard nanoindentation system. These included environmental control and cooling on the sample and indenter sides, which were cooled separately using thermoelectric coolers (Peltier elements). The system used by Chen successfully cooled both sample and diamond indenter to -30°C without vapour condensation (prevented by purging with Ar gas) and thermal drift problems. Fused silica was used as a reference sample to validate the equipment. The hardness and elastic modulus of atactic-polyprolythene increased as the testing temperature decreased through the glass transition range and the polymer changed from rubbery to glassy. A temperature reduction of -55°C from room temperature led to a change of about 100% and 150% increments for hardness and elastic modulus, respectively.

The investigation of the ductile-brittle transition in many materials (Mo included) by nanoindentation would be impossible without cold temperature nanoindentation, although this area of research has been limited. At the time of writing, a cryogenic stage is being installed on the MicroMaterials system located in the Oxford University materials department (used by Britton et al. [155] which will enable both sample and indenter to reach -150°C.

1.3.2.4 Indentation Size Effect There have been many reports in the literature on the size effect in metals. It has been reported that the Vickers microhardness of different materials is independent of load [161], increases with load [162], decreases with load [163] or shows complex variation with changes in load [164]. At low loads, the effect of any surface layers with different material properties is more pronounced. As the depth of indentation increases, the effect of bulk becomes more dominant until there is no longer a change in the value of hardness with increasing load [165].

FCC and BCC metals show a rapid increase of strength with smaller indentations. The strain gradient plasticity theory by Nix and Gao [107] attributed this size effect to the presence of geometrically necessary dislocations (GNDs). In smaller indentations, these dislocations exert larger strain fields on the dislocations required for slip. This causes enhanced hardening. For example, an early study on copper is shown in figure 35.

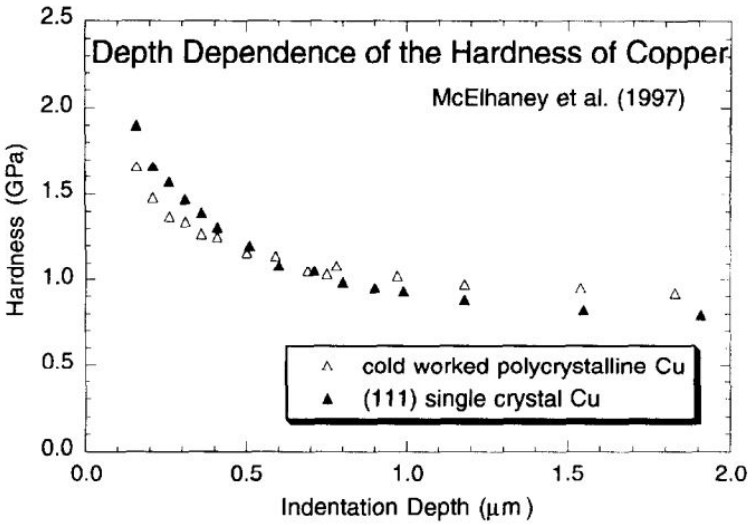


Figure 35: Depth dependence of the hardness of (111) single crystal copper and cold worked polycrystalline copper, taken from the work of McElhaney et al. [166]. Experiments were conducted with a Berkovich diamond indenter.

Few indentation size effect studies have been carried out on BCC metals. However, Durst et al. investigated the depth dependence of the hardness of (100) single crystal tungsten [158]. The results of this study are shown in figure 36. The data were found to agree with Durst's model describing the hardness as a function of indentation depth given by the linear superposition of the GND and SSD density, shown in grey in figure 36.

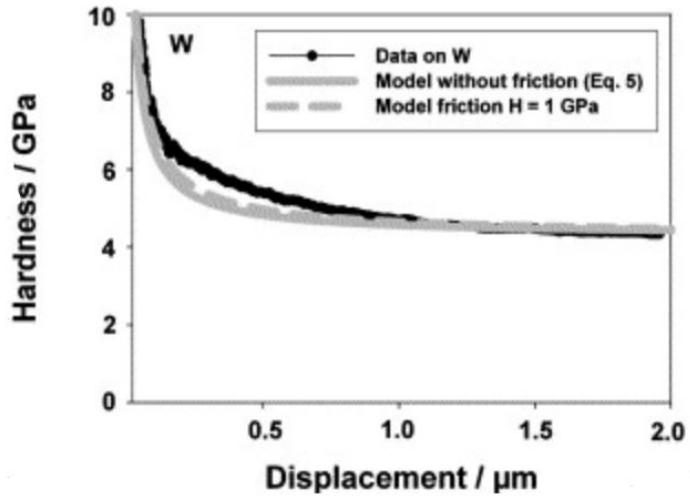


Figure 36: Depth dependence of the hardness of (100) single crystal tungsten from [158].

In a study on different BCC materials (iron, molybdenum, tungsten, and tantalum) by Voyiadjis et al. [167], the indentation size effect was investigated for a large range of indentations, from nanometers to millimeters. The continuous stiffness measurement (CSM) method was used. The results generally showed three distinctive regions for the hardness measurement versus indentation depth for the material. Hardness was noticed to decrease with increasing

indentation depth in two regions; at very low and at very high indentations. On the other hand, hardness increases with indentation depth in a region that lies between the two aforementioned regions. These three regions are shown in figure 37.

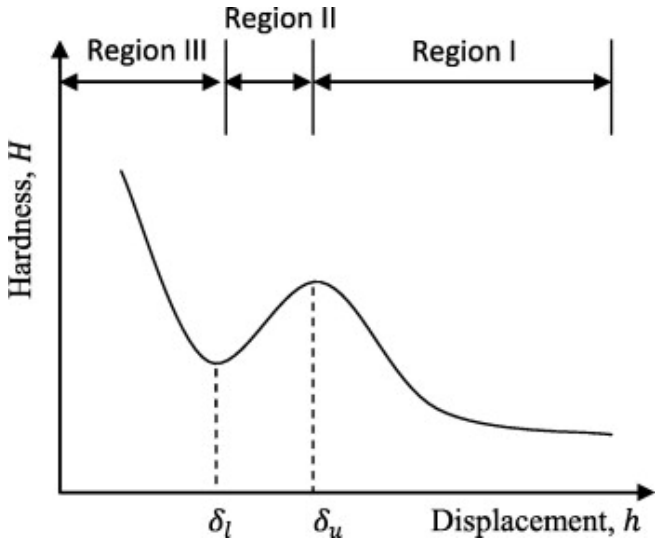


Figure 37: Typical hardness-displacement curve showing the three recognised regions. From [167]

This behaviour was successfully simulated through a power law model, which included the effect of grain boundaries as well as the strain gradient mechanism. [167] The results for molybdenum are shown in figure 38, which do not include behaviour from region III.

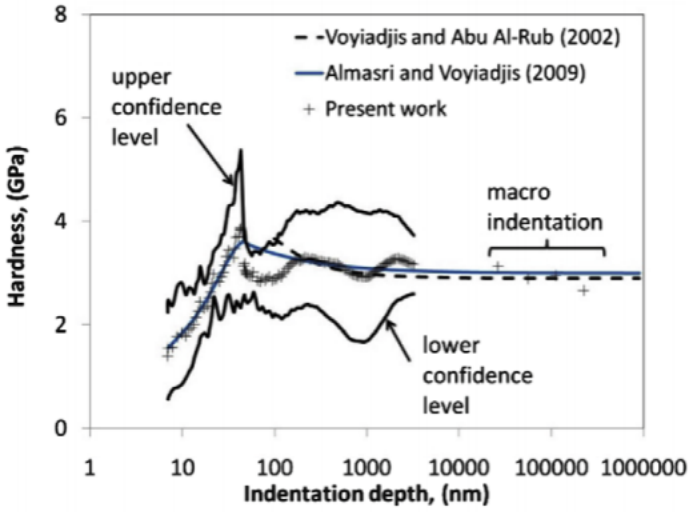


Figure 38: Softening in smaller indentations in Mo - hardness vs. indentation depth from [167] with data from [168] and [165]. 99.95% pure polycrystalline Mo with a hardness peak at 43nm. An upper and lower 5% confidence level is included.

Franke et al. investigated the influence of temperature on the indentation size effect [169]. Copper was indented on a custom-built high-temperature nanoindenter, at temperatures between ambient and 200°C, in an inert atmosphere to prevent oxidation. Over this range of

temperatures, the size effect was reduced considerably. This suggested that thermal activation plays a major role in determining the length scale for plasticity.
This was presumed to be due to a decrease in the intrinsic plasticity length scale, which in turn may be due to either an increase in the characteristic volume into which geometrically necessary dislocations are deposited during indentation, or to an increase in the density of statistically stored dislocations beneath the indentation, or both [169]. However, the model used (the Nix-Gao strain gradient plasticity model [107]) does not account for changes in factors such as the work hardening exponent with temperature, so other physical explanations were considered a possibility.

1.3.2.5 Micromechanical Testing With the increasing use of FIB systems in the fabrication of micro-test specimens, the field of small scale mechanical testing has grown rapidly, enabling microscale test pieces with differing geometries to be produced for testing in compression [170, 171], bending [172, 173, 174], and tension [175]. These specimens are generally deflected using a nanoindentation system, which with its high sensitivity can test mechanical properties on similar length scales to important deformation mechanisms such as dislocations.

Initial work on small scale pillars was published by Uchic et al. in 2004. Focussed ion beam-milled Ni and Ni-alloy micropillars were tested in compression [171] [176]. Pillar compression is usually confined to the measurement of plastic properties but even so it is difficult to measure mechanical properties accurately, because in addition to the nanoindenter measuring pillar compliance, it also measures compliance resulting from the pillar acting like a flat punch pushing into the substrate. Furthermore, geometric factors such as aspect ratio and side taper can have a large effect on measured quantities. Nonetheless, the majority of size effect and temperature-dependent mechanical property studies on BCC metals have been carried out using micropillar compression. However, micropillar testing does have the advantage of being easily automated for the generation of a large number of test specimens [177].

Di Maio et al. [178] first developed focussed ion beam (FIB) milled microcantilever beams, originally used to measure the fracture toughness of thin layer coatings, which were effectively an adaptation of traditional bend tests loaded with a nanoindenter probe that could be performed on the microscale. These, along with conventional nanoindentation, have been developed to measure various elastic and plastic properties of materials, BCC metals included. Using a FIB, microcantilevers are constructed by first milling rectangular trenches at 5nA (figure 39a), cutting a third trench to form the end of the beam at 5nA(figure 39b), straightening the sides at 1nA (figure 39c - the sloping is caused by stray “beam tails” at higher beam currents) and

finally undercutting at 45° on either side at 1nA (figure 39d).

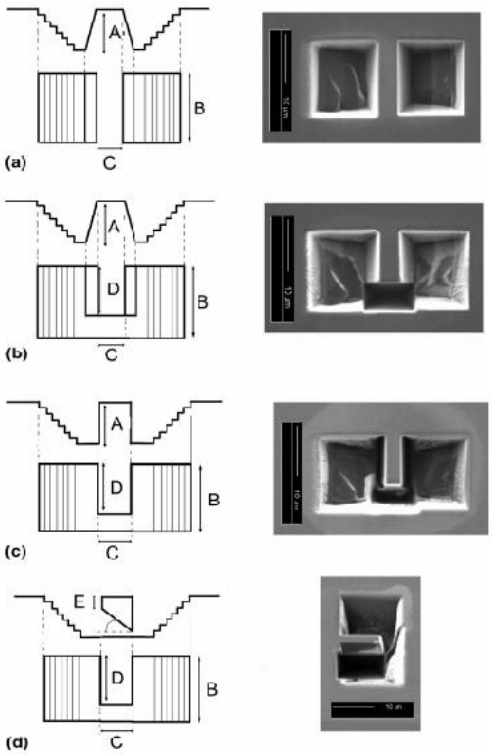


Figure 39: Microcantilever sample preparation process in a silicon sample. (1) trench cutting using a stepped technique to save time, (2) cutting the end free, (3) refining the edges to remove the taper and make them vertical and (4) undercutting to leave a free cantilever beam [178].

The microcantilever is then deflected using a nanoindenter; load-displacement data are recorded, and coupled with simple beam theory or finite element analysis and precise measurement of dimensions to produce stress-strain data. Microcantilevers are typically 10 to 40μm long and 1 to 5μm wide and undercut triangular or pentagonal cross-sectioned beams are preferable for most applications as they can be placed anywhere on the sample surface. These cantilever loading tests have similar loading geometry to macro bend tests, and as such act as a good comparison. However, there are strong effects of specimen size on measured quantities such as flow stress, as shown by the large increase in flow stress as the cantilever width decreases (figure 40) [172].

Several fundamental mechanisms for this size-dependent material behaviour have been reported in the literature including dislocation pile-up (Hall–Petch behaviour) [179, 180] dislocation starvation [181] and microstructural heterogeneity [182]. In addition, strain-gradient-dependent strengthening was observed among small scale metal samples during nanoindentation [107] bending [183] and torsion [184] tests [181].

Studies into the measurement of plasticity size effect using microcantilevers are not as well populated as micropillar studies but it is not unusual for the plasticity of small-scale samples in general to be increased compared to bulk-scale specimens.

Explanations for this size effect have been suggested. Firstly, dislocation starvation may occur in thinner specimens due to the high surface area to volume ratio [185].

Secondly, the number of dislocation sources in a given specimen reduces with smaller size, leading to more frequent pile-ups and a resultant rise in the flow stress due to work hardening (these dislocations are present to support plastic strain gradients in a sample and are known as geometrically necessary dislocations); this particular effect has been confirmed by dislocation dynamics modelling [186]. Motz et al. found flow stress values of single crystal copper measured in this way to be 10 to 50 MPa larger than values commonly reported for the same material [187]. It is necessary to account for these size effects when analysing microcantilevers in order to calculate bulk properties.

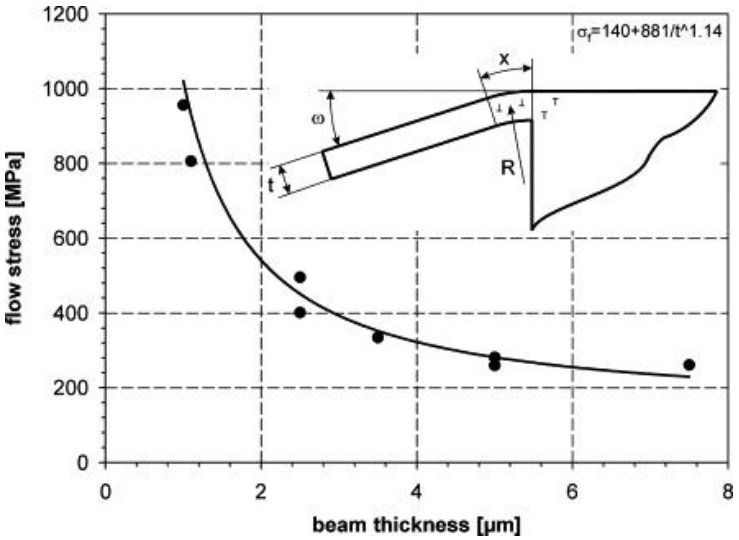


Figure 40: Dependence of the flow stress on the copper micro-beam thickness from [172]. The fit of the data points (solid line) shows a $\approx t^{-1}$ dependence of the flow stress. According to the equation relating flow stress to beam thickness $\sigma_f = 140 + 881t^{-1.14}$(top right corner), the flow stress will approach an asymptote of 140MPa.

Additionally, the elastic properties of microcantilevers can depend on their geometry. This is not a size effect caused by dislocation properties (as with plastic size effects) because even a macroscale beam will show this effect if milled in the same configuration. However, this is an important consideration for microcantilever bend tests that will be performed in this thesis and highlights the importance of Finite Element Analysis in finding microcantilever yield stress values. The flexure of the cantilever's fixed end has an influence on measuring Young's modulus below a critical aspect ratio; for example, Armstrong found a critical aspect ratio (loaded length:beam width) for single crystal copper [188]. A similar experiment was carried out by Gong on titanium samples [174].

In Armstrong's study, each cantilever was indented multiple times at a decreasing distance

away from the fixed end and the variation of the beam's behaviour with loading position identified this ratio to be 6, above which simple beam approximations could be used to calculate Young's modulus [188].

Figure 41 shows a plot of log(compliance) versus log(L) for a typical cantilever. As L is increased, the effect of slope at the fixed end of the beam becomes increasingly less important compared to the beam bending (and below this value flexing of the fixed end leads to underestimation of Young's modulus).

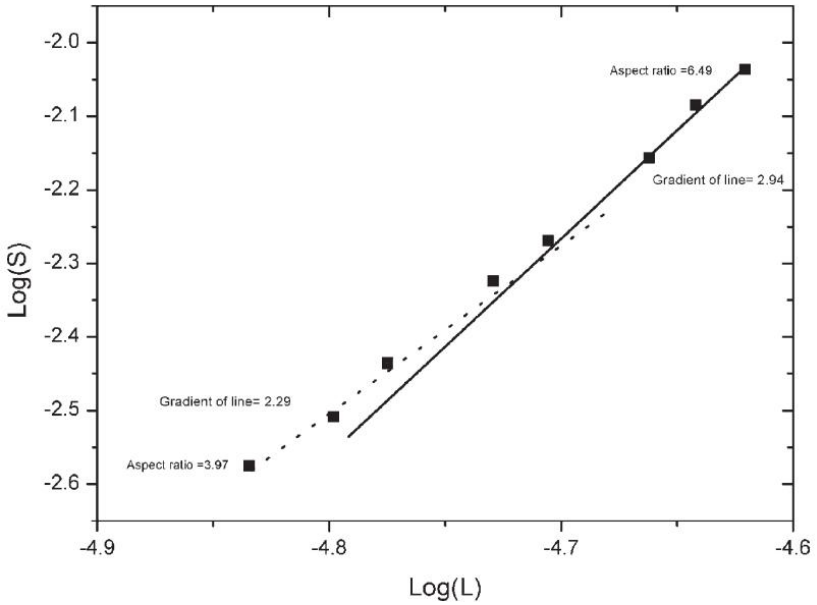


Figure 41: Log(compliance) versus log(test length) for a copper microcantilever, showing a size effect up to an aspect ratio of 6. As L decreases, the gradient decreases from close to 3 for loading points furthest from the fixed end, to closer to 2 for loading points closest to the fixed end [188].

1.3.2.6 Hot and Cold Micromechanics Using the method developed by Armstrong, Gong et al. [126, 174] to accurately measure Young's modulus at room temperature by bending FIB-machined pentagonal cross-sectioned cantilevers, Britton et al. [155] tested silicon and tungsten microcantilevers from 20°C to 770°C. Changes in the fracture behaviour of Si with temperature were studied, as well as brittle fracture behaviour of W-5wt%Ta. In Si, brittle behaviour was observed up to a transition temperature of 530°C with a reduction in yield stress at higher temperatures. These results were comparable with those found previously using macroscopic tests [189]. W-5wt%Ta remained brittle even at 600°C with fracture following a single grain boundary.

Many micropillar studies show the presence of 'strain bursts', the size and nature of which depend on orientation [190], temperature [190], crystal structure [191], microstructural inclusions [191], specimen size [192] and irradiation [193, 194].

In a temperature and orientation study of Fe micropillars, Hagen et al. [190] only tested two temperatures (25 and -75°C) but found that temperature influenced the shape of stress-strain curves, shown in Figure 42. Small strain bursts initially occurred at room temperature arising from the propagation of dislocation avalanches within the sample from dislocation sources [195]. Following the small bursts, extended plastic regimes occurred without strain hardening. These large strain bursts are suggested to be associated with dislocation elimination at the pillar surface [196, 197] when local shearing occurs [198, 199].

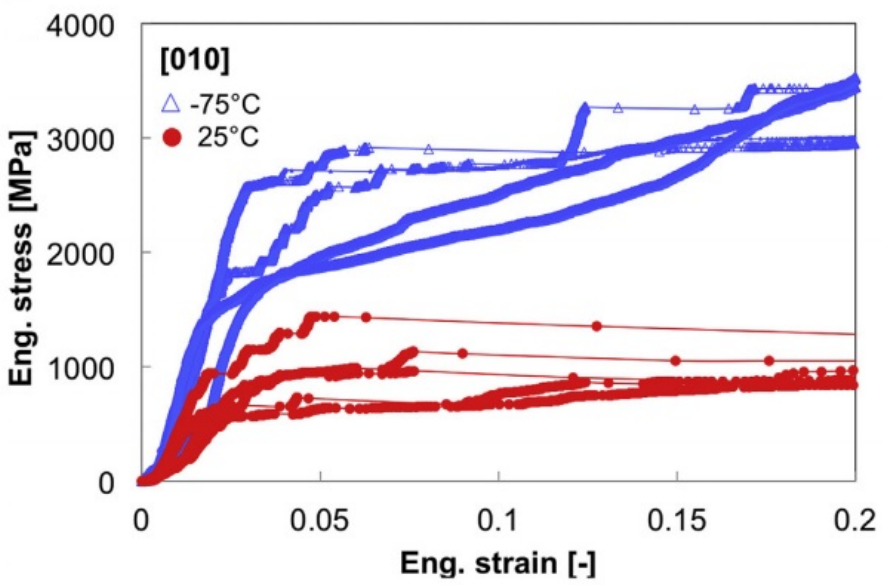


Figure 42: Engineering stress-strain curves for [010] Fe pillars at 25°C and -75°C. Low temperature stress-strain curves reveal multiple strain bursts separated by elastic loading sequences and show a stronger hardening than that observed in the room temperature curves, which consist of larger extended plastic regimes with small amount of hardening [190].

The generation of small strain bursts was more pronounced at the low temperature (figure 42), possibly explained by the larger disparity in dislocation mobility of pure edge and pure screw segments at lower temperatures, affecting the dislocation behavior. As the edge dislocations move quicker away from the dislocation source, a long screw segment remains close to the source, leading to a pile-up with continuing deformation. The screw dislocation pile-ups produce back stresses on the source, reducing its ability to continue to operate [200]. Back stresses or dislocation exhaustion that further suppress plastic deformation are suggested to be reflected in stress strain curves by means smaller strain bursts with limited amount of strain [198, 199].

Strain bursts are also observed in microcantilever studies, but to a lesser extent. An example is shown in figure 43 [191]. As with micropillar compression [190], these are often accompanied by slip traces when the specimen is imaged after testing.

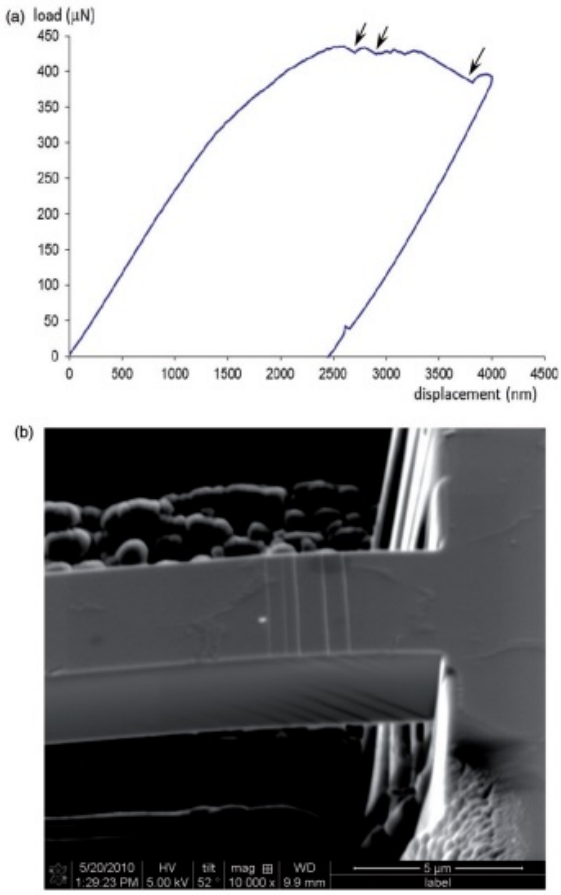


Figure 43: (a) A typical load–displacement curve for a Ti–6Al–4 V 4 mm deflection cantilever indicating strain bursts (arrowed). (b) An SEM image of a cantilever deflected by 4 mm showing more slip traces on the top and side surfaces than on those of the 3 mm deflection cantilever. Five clear slip traces were observed near the top surface. From [191]

1.3.2.7 Micromechanical Size Effect The size effect is not limited to indentation testing. Small scale mechanical testing also shows this phenomenon. As with indentations, the mechanical properties of submicron and micron-sized structures differ from those of bulk material. When the dimensions of a sample are similar to or smaller than the microstructural length scales, interfaces and free surfaces become important. In particular, such 'size effects' have been observed for metals, where the strength usually increases with decreasing sample size [201].

The majority of size-dependence studies on metals have focussed on FCC metals, such as platinum [202], nickel [171], copper [173] and gold [170] [203]. The size dependence was similar across all these studies, with with power law exponents between 0.6 and 1.0. Additionally, compensating for the Burgers vector and shear modulus of each material brings the 'characteristic' value of the exponent towards -0.7 [203, 204, 205, 206, 207].

A large amount of the investigation on BCC metals in this area has been focussed on micropillar compression testing. The BCC size effect is smaller and more variable than that for FCC [208, 209]. This variability can be explained by considering the contribution of the lattice

resistance, which scales with the ratio of test temperature to knee temperature [203]. (This temperature ratio is a measure of how much the yield stress is governed by the lattice resistance [201].) The lower effect can be attributed to the lower mobility of BCC screw dislocations [209]. High temperature micromechanical testing of molybdenum [210], tantalum and tungsten [201] has helped to verify this explanation, as has high temperature nanoindentation of tungsten and chromium [211].

In a room temperature study on Mo micropillars, Kim et al. [208] investigated the size-dependent deformation behaviour of Mo nanopillars in uniaxial compression. To assess the impact of the initial dislocation density, nanopillars with high initial dislocation density were micromachined in the severely deformed plastic zone of residual nanoindentation marks. The size dependence of these pillars in shown in figure 44. HIDD refers to 'high initial dislocation density'. The slope of yield strength vs pillar diameter on log-log scale was 0.44 (the 'power law exponent'). In another micropillar study, Kim et al. found a power law exponent of 1.07 in compression (using a flat punch) and 0.48 in tension (using a custom-built in situ mechanical tester) [212].

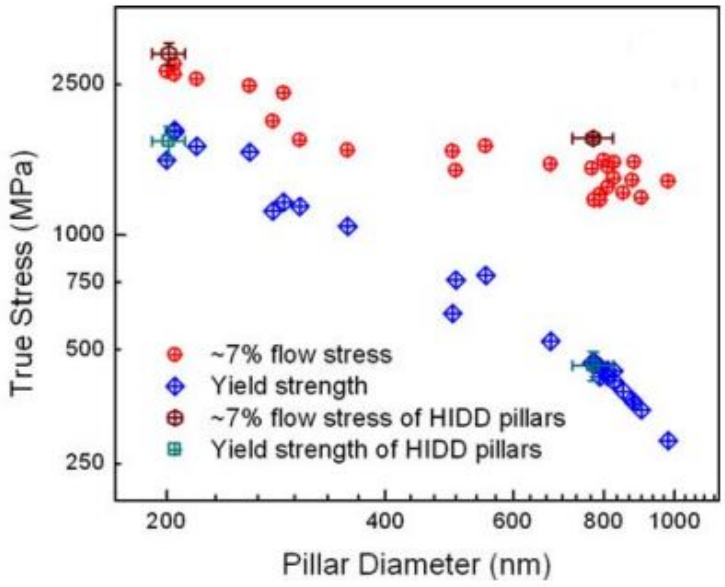


Figure 44: Size-dependent deformation behaviour of Mo nanopillars in uniaxial compression - flow stress at 7% true strain and yield strength vs pillar diameter, showing strong size effects. HIDD refers to 'high initial dislocation density'.

Several studies have investigated the dependence of this effect with temperature. Schneider et al. studied the BCC size effect by performing high-temperature compression tests on FIB-milled Mo [209] and W and Nb single crystal pillars [192]. Figure 45 shows the slope of the line of best fit (exponent) for the size dependence of W and Nb from [192] and Mo from [209] as a function of T_{test}/T_K. These exponents were calculated from the gradient of log-log plots of

yield stress against pillar diameter. Also shown are the power law exponents obtained for the flow stress measured at 5% strain for the same materials. The critical temperatures for W, Mo and Nb are 800 K, 400 K and 350 K, respectively. This figure shows an increasing size effect for all three materials as the temperature is increased.

The difference in the power law exponents shown in figure 45 for different orientations of Mo, W and Nb highlights the need for keeping sample orientation constant when investigating the size effect.

Figure 46 shows a later study by the same research group that indicates the size effect behaviour of BCC metals approaches that of FCC metals towards the transition temperature T_K. Again, the graph shows the slope of the line of best fit (exponent) for the size dependence of W, Mo, Ta and Nb vs normalised test temperature T_{test}/T_K. For a T_{test}/T_K of 1, the Mo pillars show the same size dependence as FCC pillars. [210]

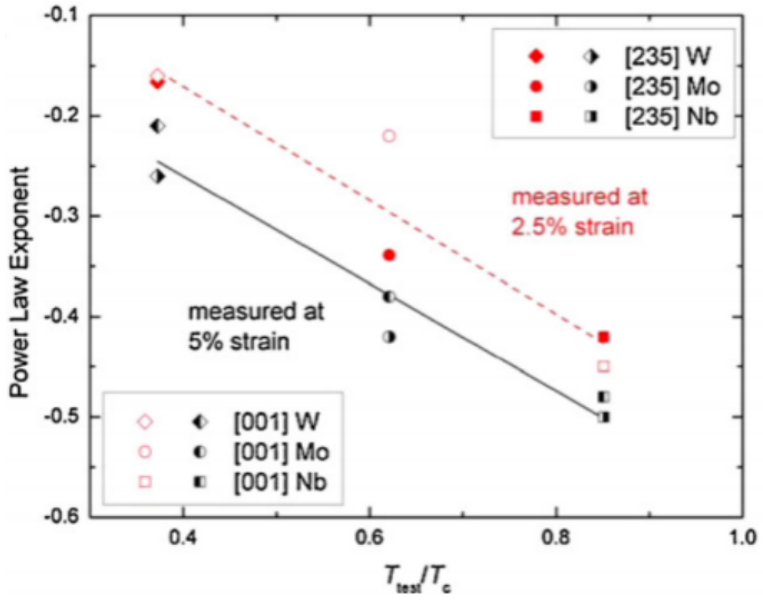


Figure 45: Slope of the line of best fit (exponent) for the size dependence of W and Nb from [192] and Mo from [209] as a function of T_{test}/T_K. Also shown are the power law exponents obtained for the flow stress measured at 5% strain for the same materials. The critical temperatures for W, Mo and Nb are 800 K, 400 K and 350 K, respectively [192].

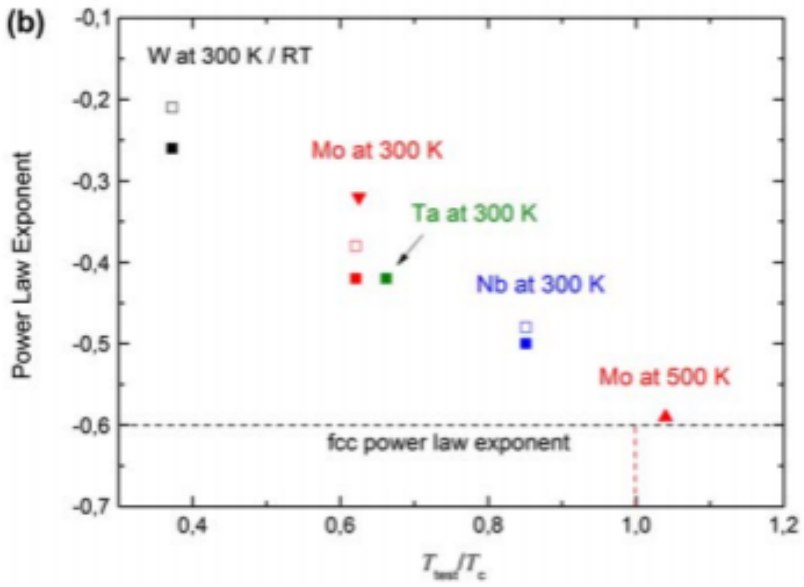


Figure 46: Slope of the line of best fit (exponent) for the size dependence of W, Mo, Ta and Nb vs normalised test temperature T_{test}/T_K. (Filled squares = [001]-oriented pillars taken from [209], open squares = [235]-oriented pillars taken from [213] and open triangles = [110]-oriented Mo pillars from [210].) For a T_{test}/T_K of 1, the Mo pillars show the same size dependence as FCC pillars. [210]

Abad et al. [201] also studied the BCC size effect by performing high-temperature compression tests on FIB-milled Ta and W single crystal pillars ranging in diameter from 500 nm to 5 μm at temperatures up to 400°C. Similarly to W, Mo and Ta in the studies by Schneider [213, 213, 192, 210], both Ta and W showed larger size effects at higher temperatures, reaching values that are in the range of FCC metals at temperatures near T_K. The size effect was shown in terms of the power law exponents calculated from log-log plots of yield stress against pillar diameter, such as the one shown for Ta in figure 47.

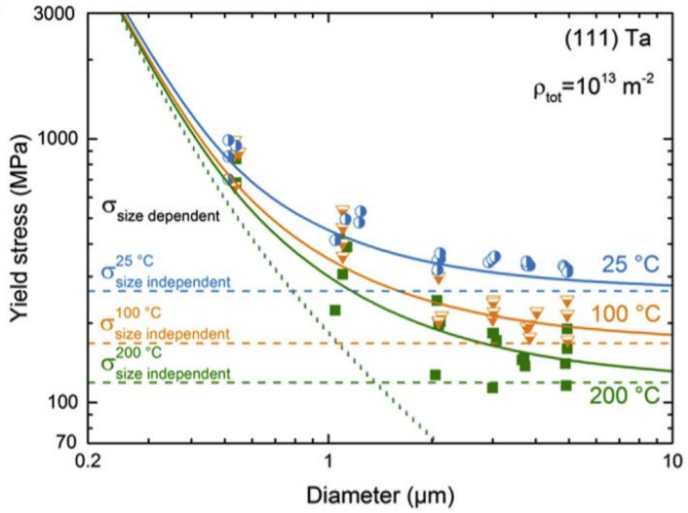


Figure 47: Comparison between experimental yield stresses determined at 2.5% total strain and calculated ones using a model by Parthasarathy et al. [214]. The lines correspond to Ta micropillars compressed at 25, 100 and 200°C. The solid lines represent the predicted yield stresses as a function of pillar diameter, assuming a dislocation density of $10^{13}m^2$. The dashed and dotted lines correspond to the size independent and size dependent contributions to the yield stresses, respectively. From [201]

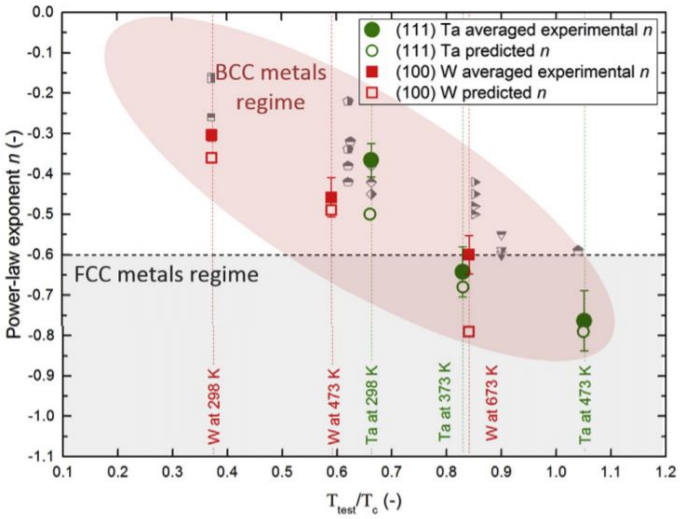


Figure 48: Power-law exponent n as a function of the relative test temperature T_{test}/T_K. The solid symbols represent the experimental results of Abad et al. [201] while the open symbols depict the theoretical prediction of n calculated according to the model by Parthasarathy et al. [214]. Included for comparison are different size effects of BCC micropillars determined in other studies [210, 209, 215, 216].

Furthermore, for tungsten, a change from uniform wavy deformation to localised deformation was observed with increasing temperature and pillar size. This indicated that the temperature ratio T_{test}/T_K strongly influences the relative motion of screw and edge dislocations [201].
In conclusion, when tested at a small ratio of T_{test}/T_K, BCC metals show a weak size dependence, but this dependence increases with increasing temperature. Since the ratio of T_{test}/T_K is a measure of screw dislocation mobility, the screw dislocation mobility is an important pa-

rameter influencing the small-scale deformation of BCC metals.

1.3.2.8 In-Situ Measurements SEM and TEM instruments have successfully been adapted for in-situ high temperature testing of micromechanical specimens. Ultrahigh resolution electron microscopy observation allows quantitative, in situ testing of micro/nanomaterials by providing a direct structure-property relationship [217, 171, 218, 175]. However, in-situ thermomechanical characterisation of micro and nanoscale samples involves several challenges including fabrication, handling, and gripping of small samples, limited available space in analytical chambers and in-situ heating of a sample with quantitative temperature measurement. In addition, large variations in temperature impose unavoidable challenges in loading the sample. For example, the thermal expansion coefficients of stage and sample may be different, causing undesired loading/unloading of a sample with a varying temperature [181].
Custom-made microelectromechanical systems (MEMS) may be used to overcome these problems; Kang et al. developed a novel SiC-based stage for thermomechanical testing small enough for SEM and TEM testing. This allows independent testing of the specimen with concurrent control of sample size and temperature [219, 220].

1.3.2.9 Effects of FIB Milling FIB-milling has been established as a reliable and precise process in the production of microcantilever and micropillar specimens. There are, however, notable disadvantages such as sample surface amorphisation [221] and ion implantation [222] in the interaction area with the ion beam. These both cause defects in mechanical test specimens. Ion beam sources are most commonly liquid-metal ion sources (LMIS) containing gallium; Ga concentrations may reach 40 at.% close beneath the surface and Ga ions may reach depths of 400nm, depending on gallium dose (these figures were measured using secondary-ion mass spectroscopy in Si [223]). This number has been disputed by Lehrer [224], who found concentrations up to 20 at.% in Si [224] but both publications agree in that the gallium concentration saturates at a Ga^+ fluence of about $7 \times 10^{16} cm^{-2}$. Regardless, an atomic concentration of even 20% of a substitutional element is considerable and low gallium fluences must be used where possible to reduce this number when testing micromechanical specimens.
To reduce damage caused by physical sputtering, a lower ion beam energy can be employed but this lowers sputtering resolution [225]. A 5 keV ion beam reduces the amorphization depth in silicon by more than 50% [226].
To investigate the effects of FIB damage on mechanical behaviour of molybdenum, Shim et al. [227] tested Mo-alloy micropillars that were FIB-milled following directional solidification, and compared their compressive response to pillars that were not FIB-milled. They also FIB-milled

at glancing incidence a Mo-alloy single crystal surface and compared its nanoindentation response to an electropolished surface of the same crystal. As expected, FIB-milling was found to have a significant effect on small-scale mechanical properties; the most striking results are shown in figure 49. This graph shows a large decrease in yield stress (9.21 to 0.85 GPa), ultimate tensile strength and ductility of the FIB-milled Mo pillars compared to those directionally-solidified. Additionally, when FIB-milled samples were tested by nanoindentation (instead of directionally-solidified), hardness increased from 3.2 to 6.1GPa and Young's modulus decreased from 328 to 323 GPa.

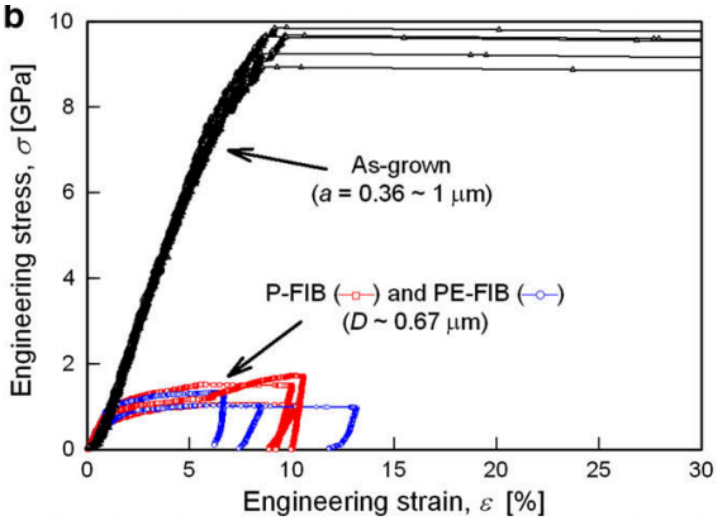


Figure 49: Stress–strain curves for as-grown (directionally solidified) and FIB-milled pillars: P-FIB (polished before FIB) and PE-FIB (polished and etched before FIB). a is the edge length of square cross-section as-grown pillars and D is the diameter of circular cross-section FIB-milled pillars [227].

1.4 Summary

Molybdenum is under consideration for use in a future fusion reactor as a plasma-facing material. Design requirements of fusion reactors require knowledge of the plastic behaviour of molybdenum at different temperatures, particularly as the change from easy to restricted dislocation glide (and from ductile to brittle behaviour) occurs over a short temperature range. As this temperature range generally occurs around room temperature in molybdenum, this will affect the behaviour of components as the in-service temperature changes quickly once the reactor is active.

Fundamentally in BCC metals the transition between brittle and ductile behaviour is caused by the thermal activation of dislocation mechanisms. Due to the polarisation of screw dislocation cores, thermal activation is required to increase their mobility to a similar value to edge dislocations, thereby making the material ductile. The dominant slip mechanism of screw dislocations in BCC metals is the kink-pair mechanism as its energy barrier for dislocation

movement is much lower than for the movement of a whole dislocation line. The mechanism is thermally-activated and initiated by the thermal fluctuation of small groups of atoms.

1.5 Research Goals

This background theory of the temperature-dependent behaviour of molybdenum is very important in understanding the research techniques being used in this DPhil project. The project aim is to investigate the temperature-dependent plastic behaviour of molybdenum, with a wider aim of testing irradiated material in the future. For this reason, microscale testing is necessary to test irradiated layers that are at most a few microns thick. Hence, micro- and nano-scale experimental techniques used for testing mechanical properties at varying temperatures have been covered in detail, including four-point-bend testing of bulk scale matchsticks, microindentation, nanoindentation and micromechanical testing. The nanoindentation tests will cover a wide range of depths to investigate the 'indentation size effect' of molybdenum. Up until now, no size-dependent indentation study in molybdenum has involved the variable of temperature. Additionally, this is the first temperature-dependent molybdenum microcantilever study.
The purpose of this study is to expand the knowledge of the indentation and micromechanical size effect in molybdenum and compare with the information and results from micropillar investigations, which have been extensive.

1.6 Chapter Summary

This thesis aims to add to the knowledge of the mechanical properties of molybdenum, with particular emphasis on the temperature and size dependence of plasticity. Microscale mechanical test results are required for irradiation experiments on metals destined for use in fusion reactors, and Mo is not an exception. The experimental findings of this thesis will help to build a picture of the small scale properties of Mo for future studies on irradiated thin layers.
Chapter 3 details microhardness testing of [001] orientated single crystal Mo from -196 to 872°C using three overlapping techniques, subjected to the same load. These indentations are well within the 'bulk' scale (large enough to avoid size dependent hardness). A total of 264 measurements were made across the temperature range, making this study much more detailed than any other published in the literature.
Chapter 4 addresses nanoindentation testing of [001] single crystal Mo under vacuum at temperatures ranging from -31 to 800°C, with independent tip and sample thermal control to allow for thermal equilibrium. Indentation loads ranged from 2 to 300mN, allowing a full analysis of the temperature dependence of the indentation size effect in Mo, which is an important area that has not previously been covered in the literature for BCC metals.

Chapter 5 discusses four point bend tests on single crystal molybdenum from -165 to 328°C on the millimetre (or 'bulk' scale), with sample edges parallel to {001} crystallographic directions. Additionally, polycrystalline samples were annealed until cold work was observed to decrease significantly and tested using the same test setup and experimental method as the single crystal samples. Polycrystalline test temperatures ranged from -40 to 522°C. All bend tests had a uniform strain rate. Yield stress values were compared against those determined from bend tests on unannealed samples of the same type in a previous study.

Chapter 6 discusses microcantilever bend tests carried out on single crystal molybdenum with microcantilever edges parallel to {001}, with independent tip and sample thermal control to allow for thermal equilibrium. Test temperatures ranged from -30 to 571°C.

Chapter 7 is an overall discussion to tie the four major techniques together for analysis of the activation energy and flow stress dependence on temperature, as well as the transition temperature of each technique.

Chapter 8 discusses future work that builds on this thesis.

2 Materials and Sample Preparation

The information and results calculated over the course of this work were obtained using SEM, EBSD, FIB machining, nanoindentation, microindentation, macroscale flexure tests and micromechanics. The four mechanical testing techniques were combined with temperature variation above and below room temperature, the methods for which are discussed at the beginning of each chapter.

Most experiments in this research were carried out on pure single crystal Mo, with selected four point bend experiments also carried out on polycrystalline Mo.

2.1 Single crystal Mo

Single crystal molybdenum was purchased from Goodfellow with a purity of 99.999%, with the [100] lattice vector oriented along the crystal's long axis. The crystal was cut by electro-discharge machining (EDM) into discs of 1mm thickness. Surfaces were then ground from 400 grit to 4000 grit using a series of SiC papers, followed by 72 hours of chemo-mechanical polishing using a colloidal silica suspension (0.05 micron diameter abrasive particles in a pH10 solution). This provided a surface with minimal polish damage with a quality suitable for electron backscattered diffraction (EBSD). EBSD was used to confirm the (001) surface orientation and to determine the location of the other $< 100 >$ type directions within the sample face.

Additionally, a slice was taken from the end of the single crystal to orientate using EBSD before cutting for matchstick purposes (where samples were square cross sections, with dimensions 1.2mm x 1.2mm x 12mm) so matchstick sides were aligned with the $< 100 >$ directions.

Matchsticks were also cut using EDM. The rod was 12mm diameter by 25mm length. Edge roughness was removed during the polishing and grinding stages.

2.2 Polycrystalline Mo

Polycrystalline molybdenum was purchased from Goodfellow with a purity of 99.9%, in a centreless ground condition. The processing history of this sample was unknown but the rod shape and elongated grains shown by optical analysis and EBSD suggest it was extruded - see figures 50 and 59.

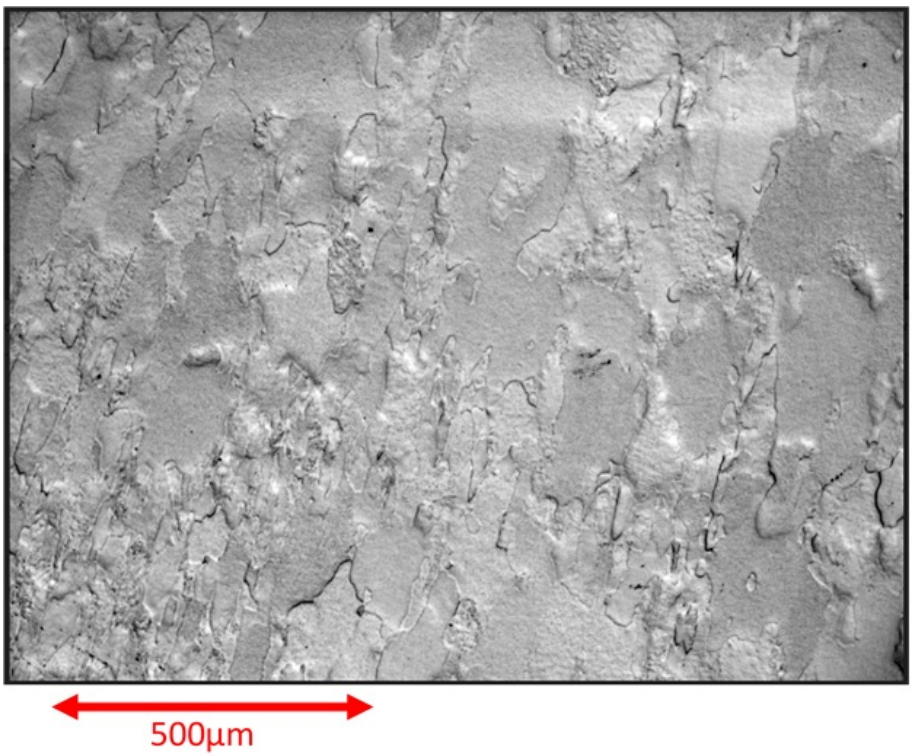


Figure 50: Optical image showing the longitudinal grain structure. The colloidal silica polishing stage was slightly extended to expose the grain structure. The microstructure is slightly elongated in a vertical direction (extrusion axis) but the grain size is varied and clearly bimodal. EBSD scans are required to quantify this observation.

For reference, the transverse microstructure is shown in an optical image in figure 51. The colloidal silica polishing stage was slightly extended to expose the grain structure.

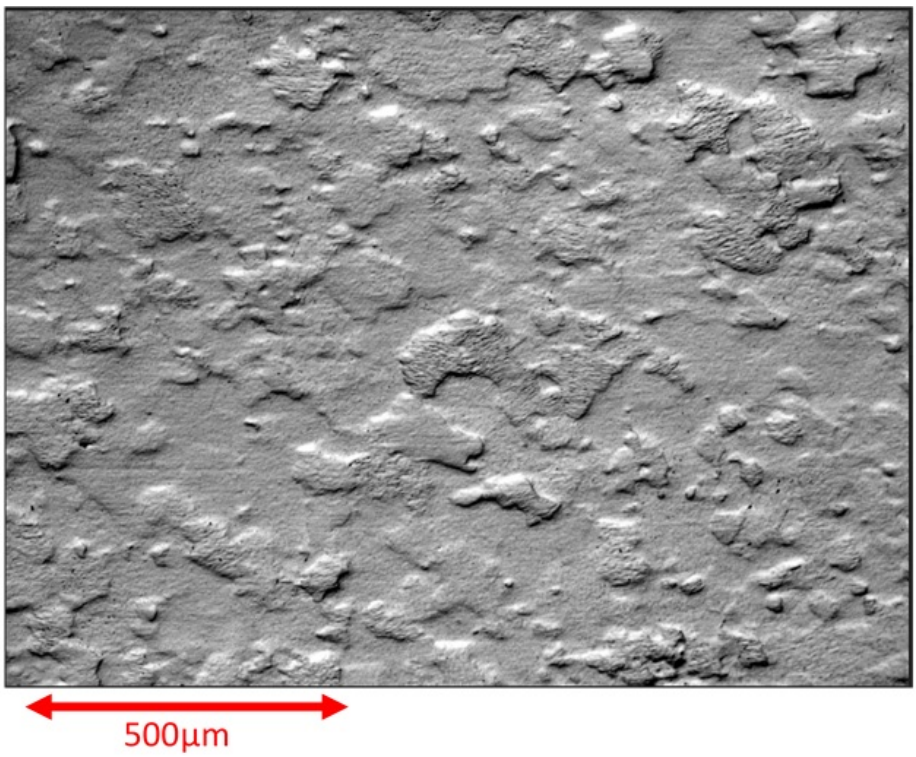


Figure 51: Optical image showing the transverse grain structure. The colloidal silica polishing stage was slightly extended to expose the grain structure.

Matchsticks for microstructural characterisation and discs were both then ground from 600 grit to 4000 grit using a series of SiC papers, followed by polishing for 3 hours each with 9, 6, 3 and 1 micron diamond paste. Due to the large variation of abrasion rate with grain orientation by colloidal silica, the suspension was only used for 20 minutes on polycrystalline samples; large grain relief was otherwise found to result, which is disadvantageous for both mechanical property testing and EBSD analysis.

EBSD analysis showed a large range of grain sizes (10 to 200 micron diameter), including some variation of orientation within grains (very low angle subgrains). EBSD also showed texture, with preferential grain deformation as a result of the likely extrusion forming process.

For the later EBSD scans, a prototype Precision Etching and Coating System (PECS) system by Gatan was used as a final step for excellent surface quality and cleanliness. This was restricted to a 1mm diameter sample area and so this technique is only suitable for microscale test specimens or small regions for analysis. During the PECS process, a beam of Ar ions is fired at the specimen surface at a glancing angle (2° to 10° from the surface plane) and under a specified accelerating voltage for a controlled time interval.

In a similar way to FIB milling, material is removed atom by atom, leaving a well-polished surface. The beam energy and length of time are limited by grain relief (in polycrystalline

samples) as ion-milling rate is dependent on crystallographic orientation. As with chemo-mechanical polishing such as colloidal silica, a large variation in grain surface height makes EBSD ineffective due to shadowing. After the PECS stage, Kikuchi patterns are much better defined (figure 52) and IPF (Inverse Pole Figure) maps are much clearer (figures 53 a and b compared with figure 59). PECS was applied at a voltage of 8keV for 20 minutes, at an angle of 10°.

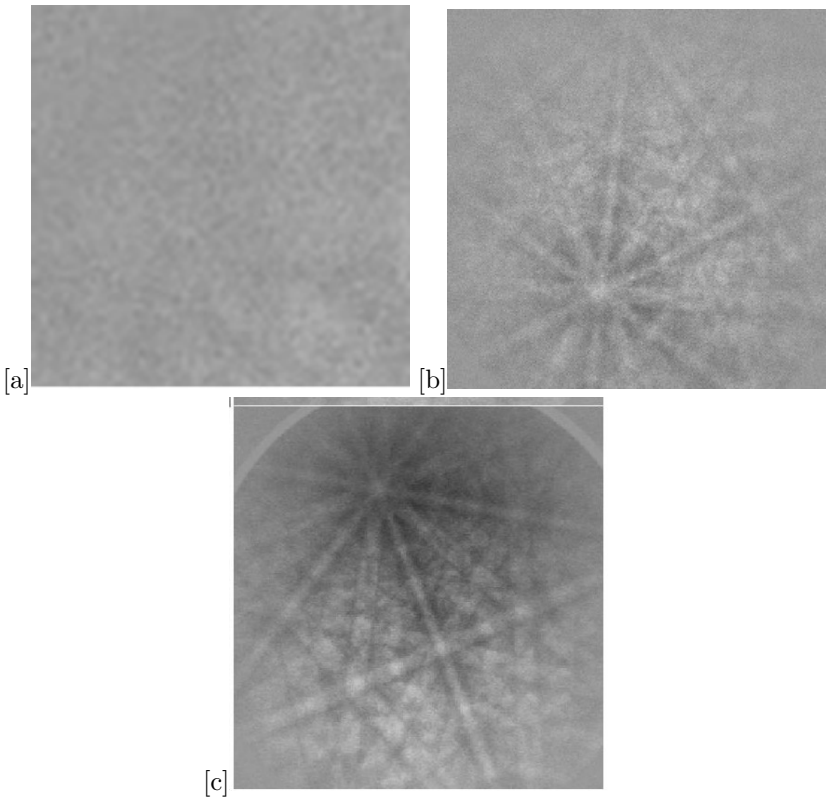
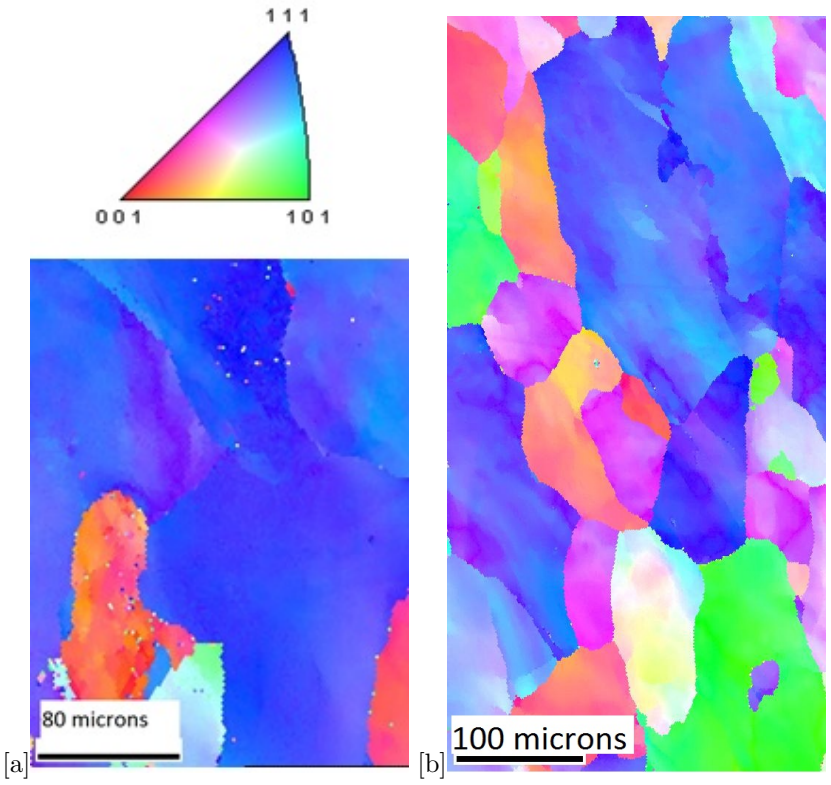


Figure 52: Kikuchi patterns after PECS, 8keV, 10°: a) 0 minutes (only faint bands were found - grain maps only possible with the collection of many small data points), b) 15 minutes (bands becoming clearer) and c) 20 minutes (crisp, easily-indexable bands).



[a] [b]

Figure 53: EBSD patterns after PECS, 8keV, 10°: a) 15 minutes and b) 20 minutes.

EBSD scans for the PECS comparison used the following conditions: probe current 6×10^{-9}A, working distance 17mm and accelerating voltage 20kV on the SEM-840A. Scans used a step size of 1.5μm and a scan area of 300x600μm.

2.2.1 Annealing Polycrystalline Molybdenum

The motivation behind this section was to compare cold worked polycrystalline Mo with annealed polycrystalline Mo (and ultimately single crystal Mo) to see the extent of the behavioural differences caused by grain boundaries vs cold work within grains. The extent of the cold work was not known; the samples were obtained in the 'as-extruded' condition. Previous work was carried out on these samples by Durrans [96] involving four point bend tests on matchstick specimens.

The annealing process was intended to remove the subgrain-like cold work as far as possible without a significant increase in grain size. The recrystallisation temperature of Mo is approximately 1200°C for samples with a 5% degree of deformation, dropping to 1100°C for those with a 25% degree of deformation, and finally 850°C for samples with a 68% degree of deformation, as shown in figure 16.[77]

For the investigation of heat treatment effects on microstructure, matchsticks were annealed to three conditions in a vacuum furnace (6 hours at 900°C, 12 hours at 900°C and 10 hours at

1400°C), with EBSD used to observe the extent of recrystallisation.
For detailed EBSD analysis of annealed polycrystalline matchsticks requiring enhanced surface quality compared to the samples prepared in "Polycrystalline Mo" on page 61, lapping films ranging from 15 micron to 1 micron grit were used. They give excellent surface flatness and remove any bevels introduced by grinding on a flexible paper mat. Diamond paste was not used for EBSD samples - even a short time using diamond destroyed a good surface due to particle agglomeration. The samples were finally polished for a short time using colloidal silica followed by PECS, as described on page 61.

Figures 54, 56, 57 and 58 show the IPF and grain maps for each annealing condition, also listed in table 2. As the PECS polish only affects a small area, the edges of the large scale maps are of a lower quality. The high magnification scans are a slightly misleading representation of grain size due to the low sample population, but they do show in great detail the grains of the highest surface quality at the centre of the PECS-polished region.
IPF maps show the orientation obtained for every pixel (or raster point) that is scanned by the electron beam. The colour displayed is derived from the IPF colour key, an example of which is shown in figure 54a. Grain maps show the grain structure independent of indexing; these are useful for visualising the grain structure separately from the internal work.

Table 2: Annealing conditions for polycrystalline matchstick specimens

.	Annealing conditions	EBSD scan
Annealing condition 3	1400°C, 10 hours	figure 58
Annealing condition 2	900°C, 12 hours	figure 57
Annealing condition 1	900°C, 6 hours	figure 56
No anneal	.	figure 54

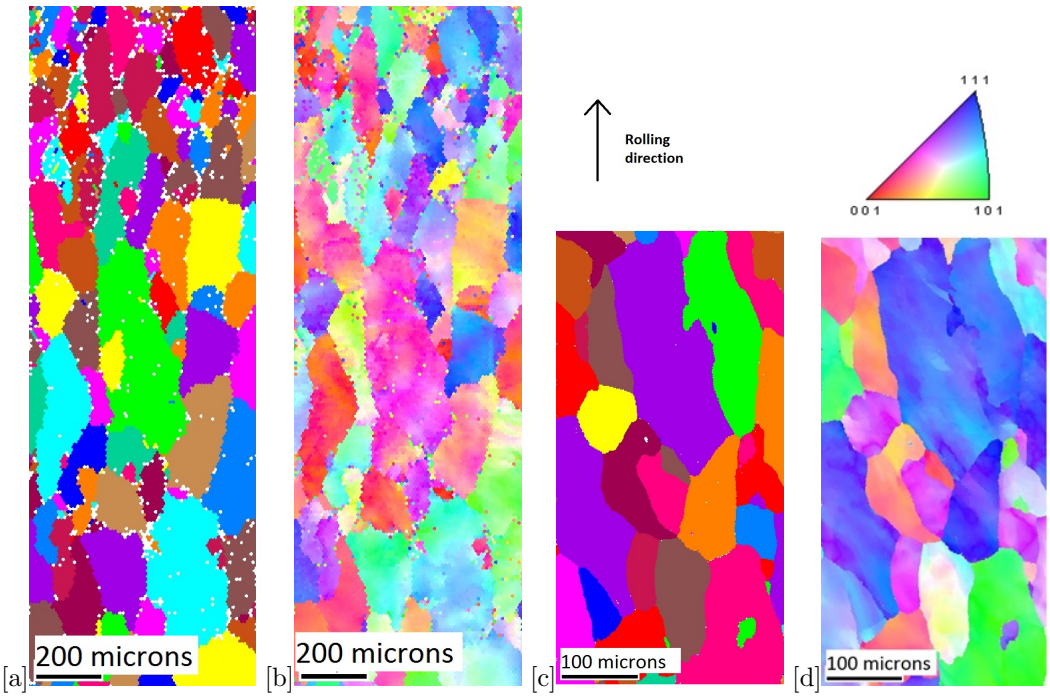


Figure 54: No anneal: grain map low mag, IPF map low mag, grain map high mag, IPF map high mag. The larger grains appear to be elongated vertically up the page in the direction of the length of the rod. These elongated grains suggest the material was extruded. Furthermore, a bimodal structure was also observed in the longitudinal direction on the unannealed sample. Some internal strain is visible in some of the grains (more visible in figure d than b). This is distinguishable from separate grains, as these are shown in the grain maps (in a and c), and there are distinct changes to the orientation within those grains.

In the EBSD map shown in figure 54 (before any annealing), the larger grains appear to be elongated vertically up the page in the direction of the length of the rod. These elongated grains suggest the material was extruded. Furthermore, a bimodal structure was also observed in the longitudinal direction on the unannealed sample. This was also found by Durrans[96] in an EBSD study of the same sample - figure 55. Some internal strain is visible in some of the grains (more visible in figure 54d than 54b). This is distinguishable from separate grains, as these are shown in the grain maps (in figures 54a and 54c), and there are distinct changes to the orientation within those grains.

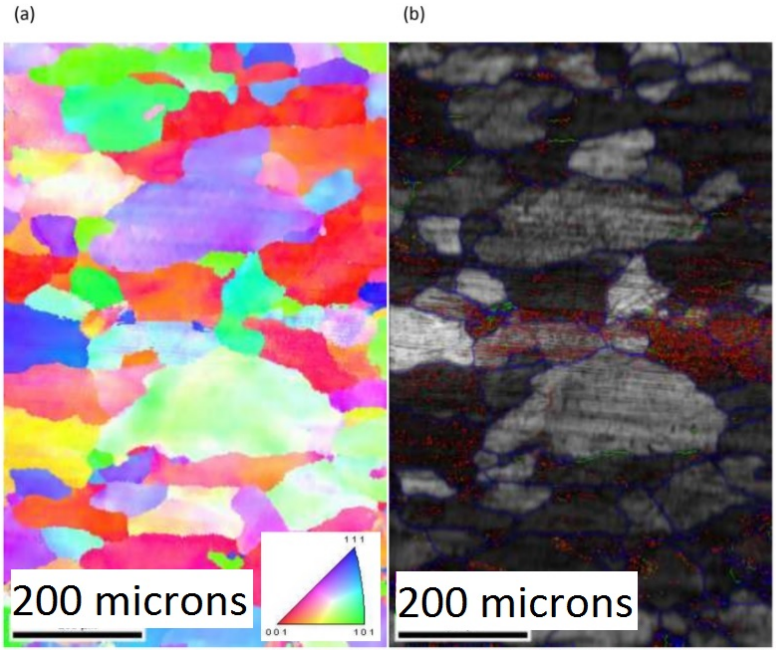


Figure 55: EBSD scans of the same sample by Durrans[96] (a) EBSD inverse pole figure (IPF) of the longitudinal cross-section. The direction of the length of the rod is across the page. The area is much greater than the cross-sectional area of a four- point bend specimen. This is to gain a realistic value for average grain size. (b) Corresponding grain map highlighting types of grain boundaries; blue lines are high angle, > 15, green lines are < 15 and red lines are < 5, both low angle.

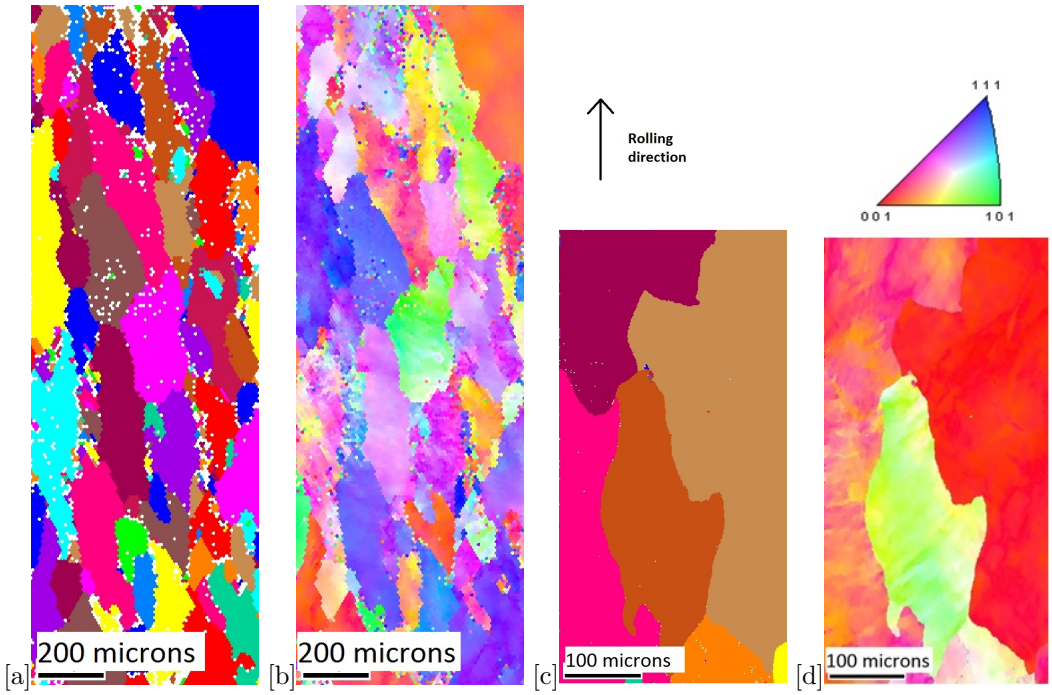


Figure 56: Anneal 1 (900°C for 6 hours): grain map low mag, IPF map low mag, grain map high mag, IPF map high mag. Some cold work is still visible in the IPF maps and the grains are still elongated.

The EBSD maps in figure 56 show the microstructure after annealing condition 1 (900°C for 6 hours). Some cold work is still visible in the IPF maps and the grains are still elongated.

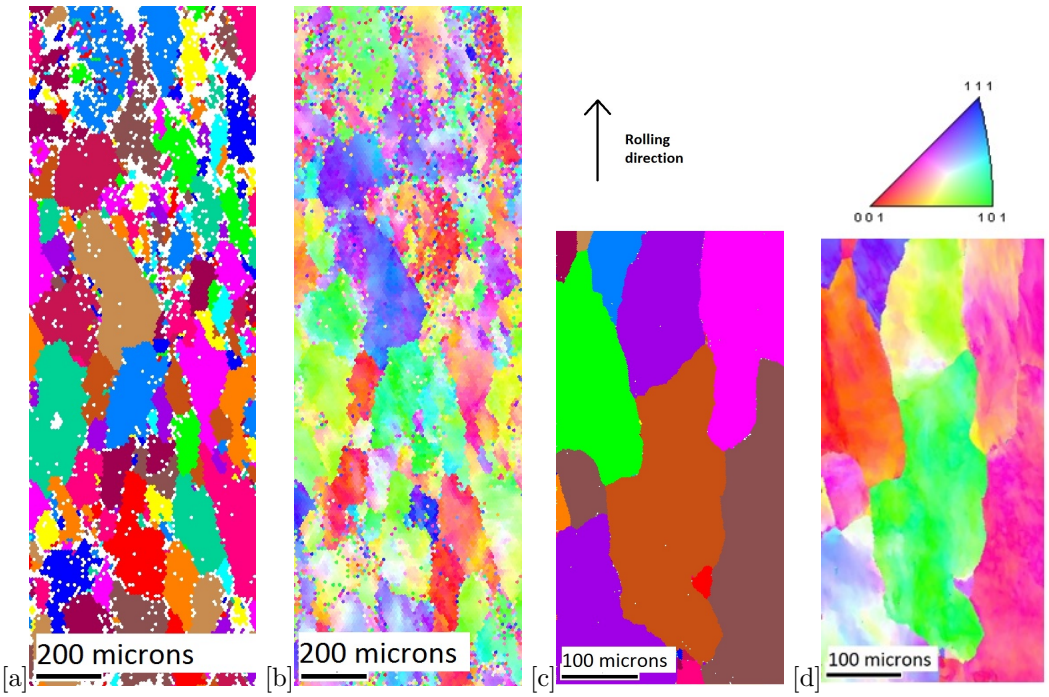
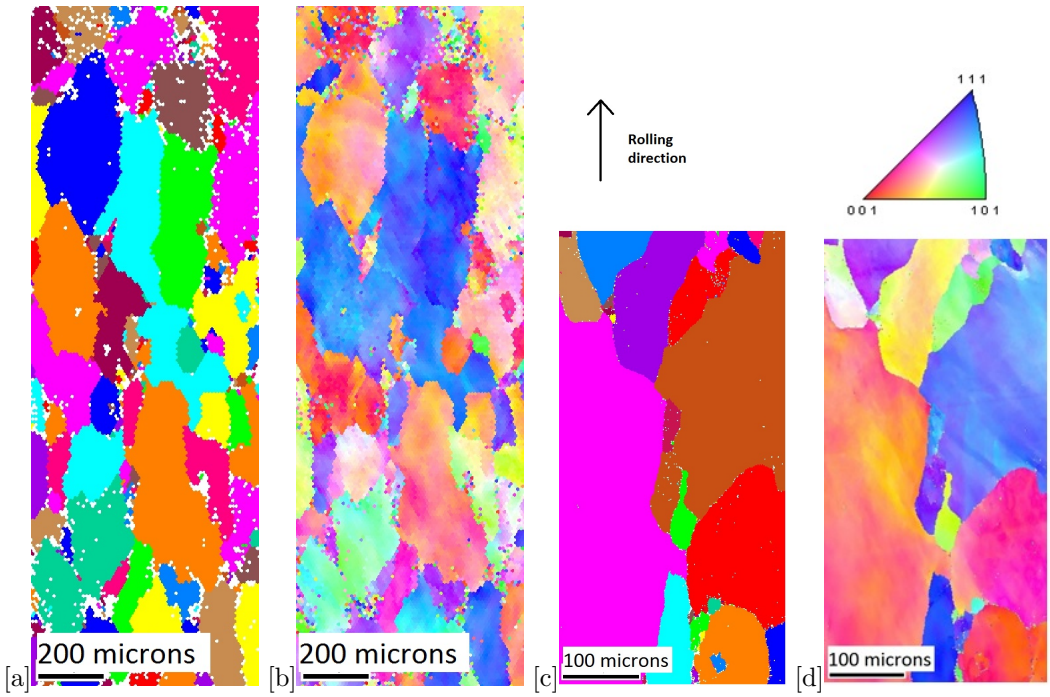


Figure 57: Anneal 2 (900°C for 12 hours): grain map low mag, IPF map low mag, grain map high mag, IPF map high mag. As with figure 56, some cold work is still visible in the IPF maps, but in a less obvious subgrain formation. However, the grains in (a) appear to be more equiaxed than those (a) of figure 56.

The EBSD maps in figure 57 show the microstructure after annealing condition 2 (900°C for 12 hours). As with figure 56, some cold work is still visible in the IPF maps, but in a less obvious subgrain formation. However, the grains in (a) appear to be more rounded than those (a) of figure 56.



[a] [b] [c] [d]

Figure 58: Anneal 3 (1400°C for 10 hours): grain map low mag, IPF map low mag, grain map high mag, IPF map high mag. The grains do not appear to have changed shape significantly since figure 57. Some cold work is still visible.

The EBSD maps in figure 58 show the microstructure after annealing condition 3 (1400°C for 10 hours). The grains do not appear to have changed shape significantly since figure 57. Some cold work is still visible.

The amount of internal strain (characterised by changes in orientation within grains, visible on the IPF maps) only appears to have decreased by a small amount throughout the three annealing conditions. Even after anneal 3 (1400°C for 10 hours), some work is still visible.

Considering the grain maps, no drastic change occurred apart from the rounding that occurred after annealing condition 3 (1400°C for 10 hours), and potentially a small decrease in the internal work. The IPF plot shows no texture developed during any of the annealing conditions. Hence annealing condition 3 was chosen with the hope of the most significant change to the microstructure. It is likely that the as-received samples had a degree of deformation lower than 5%, as defined by Primig [77], as the recrystallisation temperature appears to be above 1400°C.

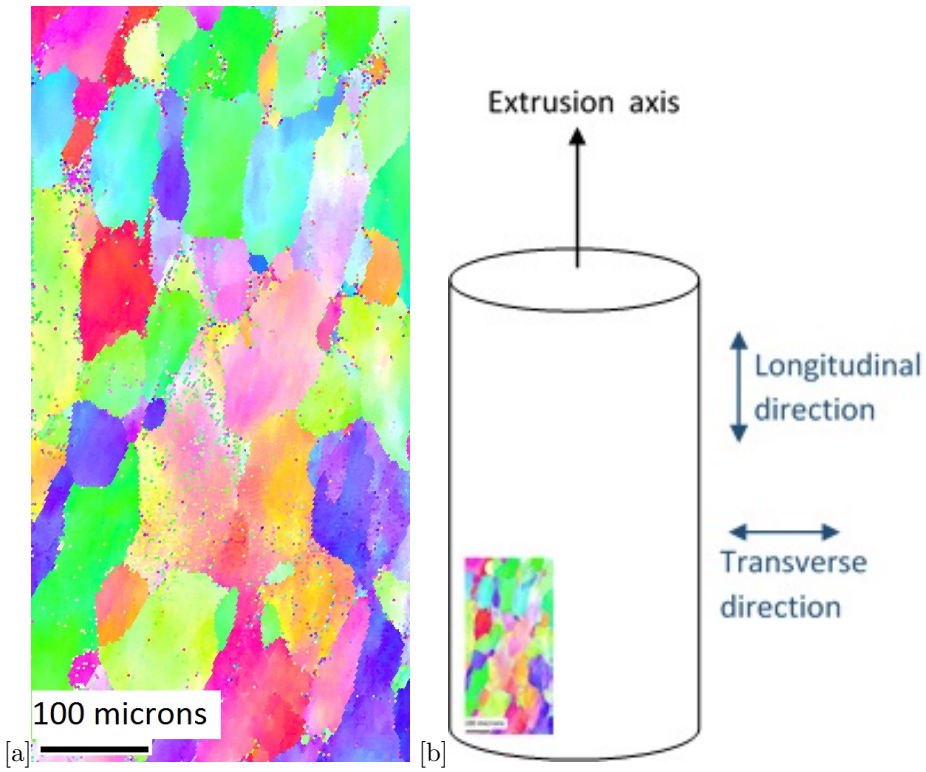


Figure 59: Longitudinal EBSD of a polycrystalline Mo sample. The elongated grains shown by EBSD suggest it was extruded.

The sample was cut into discs for characterisation and preliminary micromechanical testing using an abrasive wheel cutoff machine, and matchsticks for bend testing using CNC grit wire eroder.

The polycrystalline molybdenum rod was cut into 1.2mm x 1.2mm x 12mm matchsticks using an electro-discharge machine (EDM). Material is removed when a voltage is applied to two electrodes and successions of frequent current discharges take place between the electrodes separated by a dielectric liquid. The rod was 12mm diameter by 50mm length.

3 Microhardness Testing

3.1 Microhardness Testing

The microhardness technique in this project was the simple "dead loading" technique, in which a load of known weight is applied to a hard, sharp point, pushing it into the sample surface. The size of the resulting impression gives the hardness of the material. In a standard Vickers hardness test, an indenter made of a hard ceramic such as diamond or sapphire takes the form of a square-based pyramid with an angle of 136° between the opposite faces at the vertex. A schematic of this geometry is shown in figure 60

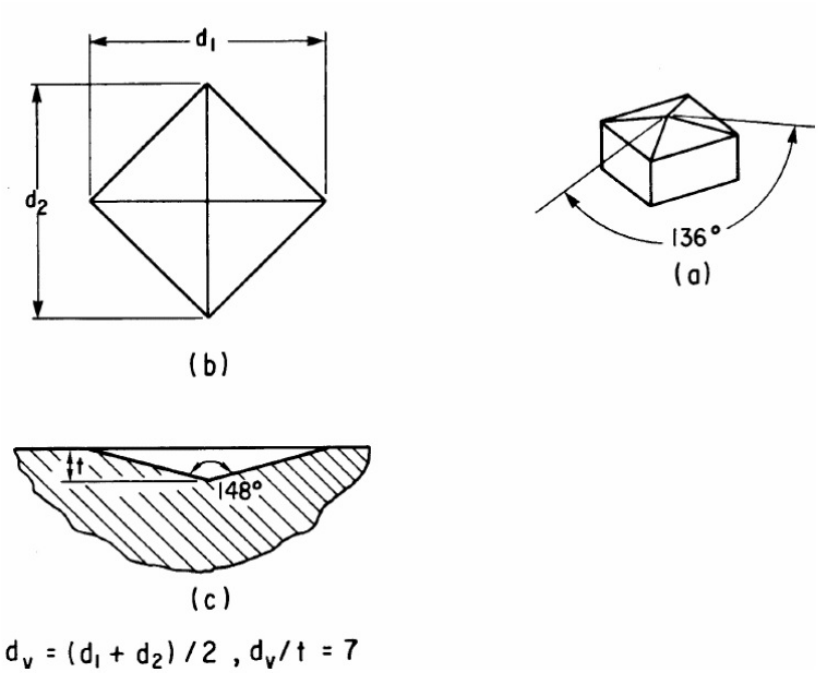


Figure 60: Schematic of Vickers indentation process - (a) indenter shape, (b) measurement of diagonals, (c) indenter profile. From [228].

Once the force is removed, the indenter leaves a square-shaped impression where material has made way for the indenter by plastic deformation. Additionally, a small amount of residual elastic deformation is likely to remain.

Methods 1 to 3 below cover microhardness testing over the temperature range -179 to 880°C. Test parameters were kept the same wherever possible between the three techniques, and the temperature and results overlap verifies the comparison of these methods. Method 1 used a custom-built machine (the 'Oxford University High Temperature Indentation Tester' [229]) shown in figure 61 - this was commissioned by the Department of Metallurgy and Science of Materials at Oxford, and made by Stanton Redcroft, Wimbledon, UK. Tests can be made at temperatures up to 1500°C, under vacuum, and it has both an upper furnace (around the indenter) and a lower furnace (around the sample). A thermocontroller is used to maintain

set temperatures, but control of the indentation time is manual. Loading is by a dead weight system. The load is applied via a dashpot-damped, counterbalanced arm [230].

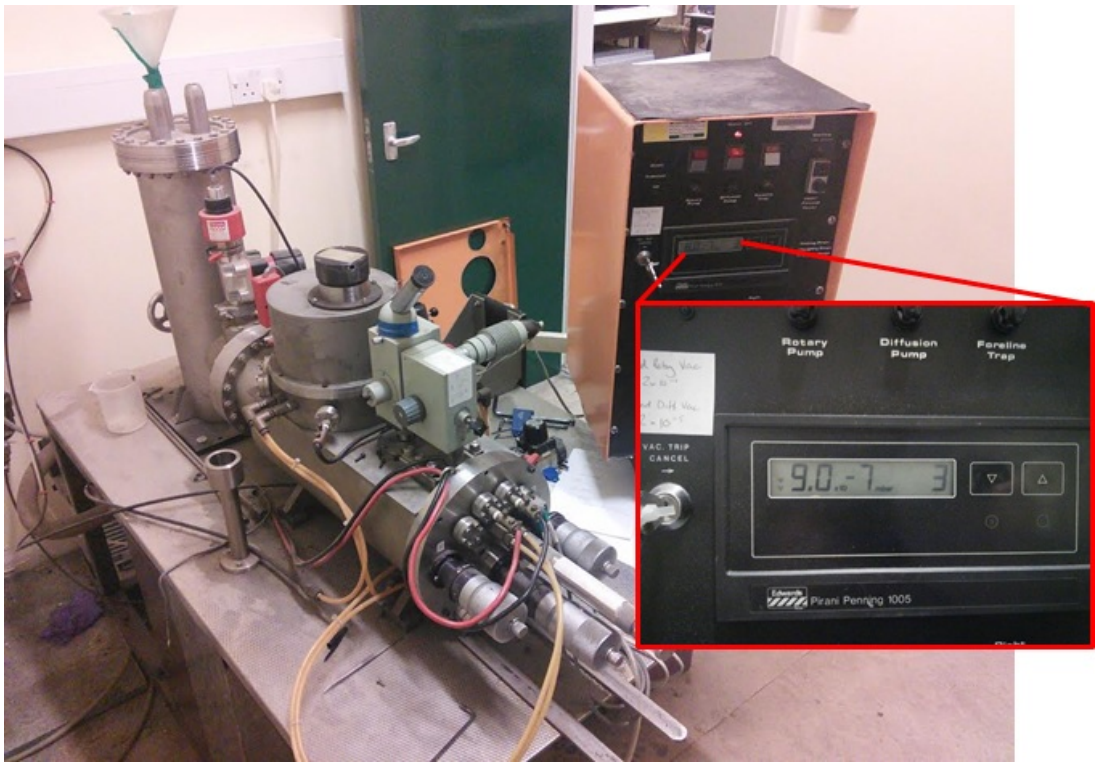


Figure 61: The 'Oxford University High Temperature Indentation Tester' [229] with the vacuum display magnified (units mbar). The sample is loaded by pulling out the front carriage.

Methods 2 and 3 used a Matsuzawa Seiki microhardness tester, with temperature control described in the following sections.

3.1.1 Method 1: Temperature range 20 to 880°C, under vacuum

Hardness testing was performed under vacuum from 20 to 800°C. The applied load was 502g, calibrated using indentations in the surface of polished single crystal copper (which has well-known hardness properties). A sapphire Vickers tip was used - diamond reacts readily with molybdenum at high temperature. Loads were held for 15 seconds at every temperature.
Once both the sample and indenter temperature had stabilised by adjusting the power applied each component from their respective heaters and observing the time at which the temperature fluctuations settled, five tests were performed at each temperature, with indentations set $50\mu m$ apart. The vacuum pressure was recorded during each indentation and varied from 5×10^{-5} to 2×10^{-7} mbar.

3.1.2 Method 2: Temperature range 20 to 350°C, hot air gun

The Mo sample was adhered to a large aluminium block using silver conductive paint. A hot air gun capable of heating to 650°C was mounted adjacent to the microhardness tester, with the air stream blown over the sample surface and indenter. This had the advantage of heating both the sample and indenter at the same time. A diamond Vickers indenter was held under a load of 496g for 15 seconds. Indentations were $50\mu m$ apart. The temperature range during each indentation was recorded using a T-type thermocouple attached to the sample surface.
An array of 12 indentations into a standard hardness block with hardness 729.4 HV10 was used to calculate the exact load as 496g.

3.1.3 Method 3: Temperature range −179 to 20°C, liquid nitrogen submersion

A polystyrene vessel with an aluminium base was constructed to house a single crystal Mo sample. This setup is shown in figures 62 and 63. Liquid nitrogen was poured into the sealed vessel until the sample temperature (read by a PTFE insulated, low T thermocouple) and surroundings were stable enough such that the temperature rose more slowly than $0.2°Cs^{-1}$. A 496g weight was applied for 15s and the temperature range again measured during each test. A thin layer of frost was present on the sample surface below 0°C but this was unavoidable using liquid nitrogen submersion, where a vacuum cannot be applied.
An array of 12 indentations into a standard hardness block with hardness 729.4 HV10 was used to calculate the exact load as 496g.

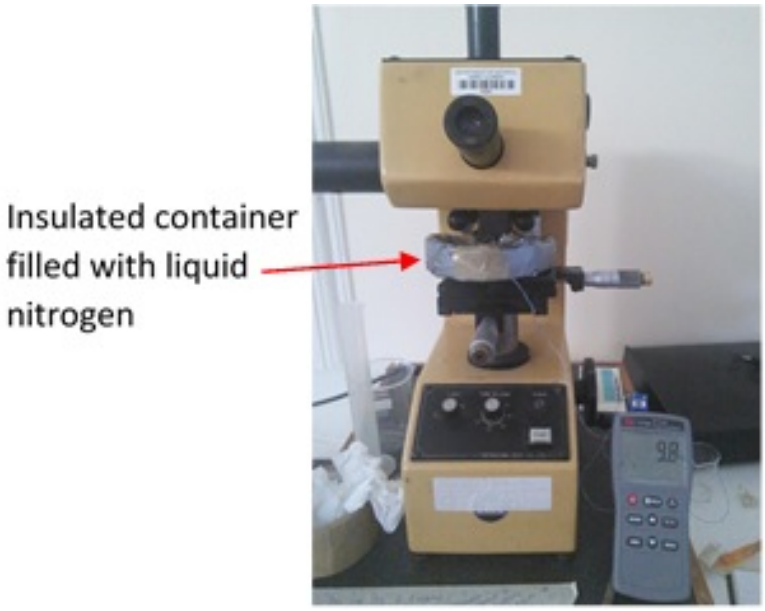


Figure 62: The Matsuzawa Seiki microhardness tester assembled with an insulated container filled with liquid nitrogen.

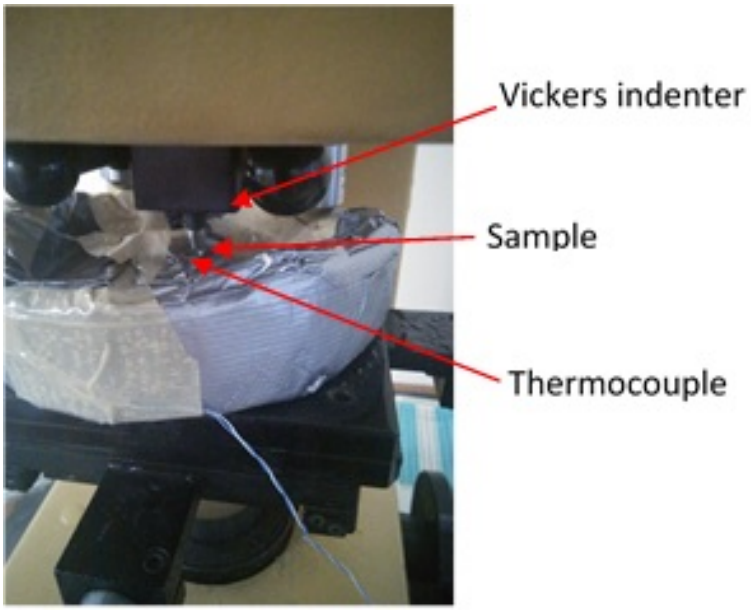


Figure 63: The Matsuzawa Seiki microhardness tester assembled with an insulated container filled with liquid nitrogen. The sample thermocouple, indenter and sample are all labelled.

All experiments in this section were carried out on the (100) slices of single crystal Mo described in the previous section. Indentation long axes were aligned with $< 100 >$ directions. The load-drop method and temperature control were outlined in Section 3.1.

3.2 Indentation Area Measurement

For ease of analysis when a fast hardness result is desirable from an indentation test, microhardness measurements are usually analysed using the "Vickers Equation" [228], describing the pressure on the actual contact area of a hardness impression:

$$H_v = 2F\frac{sin\frac{136^\circ}{2}}{d^2} = 1.854\frac{F}{d^2} \tag{13}$$

where the mean diagonal is $d = (d_1 + d_2)/2$ as shown in figure 60 and its units are mm. The unit of load F is kgf. The units of Vickers microhardness are frequently reported as kgf/mm^2 but these units make comparison with other hardness techniques (such as nanoindentation) or measurements of yield stress difficult. This mean diagonal calculation is not ideal, especially if the indentation is not close to a square shape.
Vickers measurements will be given in SI units in this thesis, where

$$1MPa = 9.807kgf/mm^2 \tag{14}$$

However, certain hardness tests will leave an impression that is not a perfect square, particularly if there is a large amount of elastic recovery.

Additionally, non-perfect surface flatness or an indenter or sample that "rocks" may be the cause (as was the case in figure 64) and this cannot always be avoided, particularly when using older machines. An indentation made using a better supported sample is shown in figure 65.

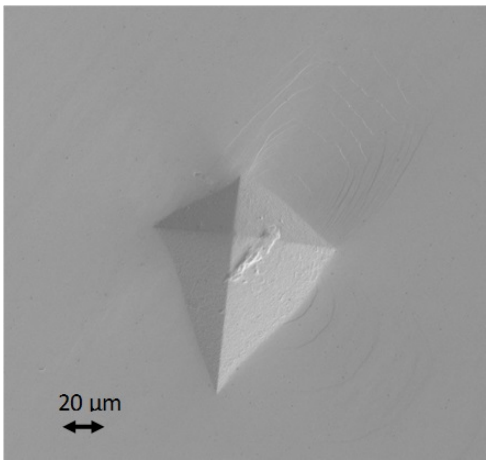


Figure 64: Vickers indentation on (001) single crystal Mo at 800°C, on a sample that "rocked" as the indenter penetrated the surface. SEM micrograph.

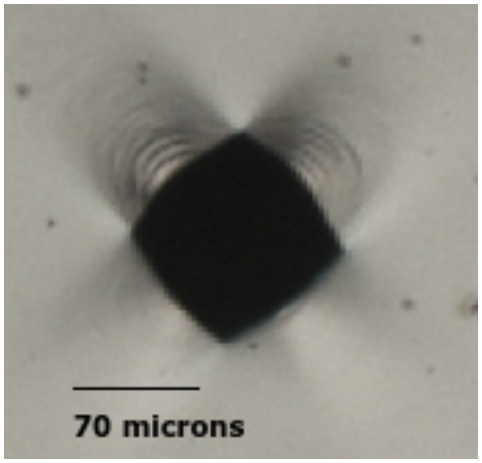


Figure 65: Square Vickers indentation on (001) single crystal Mo at 150°C. Optical micrograph.

As will be discussed in Section 3.2.1, Meyer hardness is also calculated, and for this an accurate measurement of projected indenter contact area is required. Hence, rather than using the measurement of indentation diagonals, microscope software (NIS Elements 5) was used along with optical microscopy to measure the exact indented area of each indent.

The NIS Elements auto measurement function measures the area of objects which are extracted from images by the creation of a binary layer through thresholding using RGB/HIS or intensity values; ie. the image is converted to black and white to find distinct boundaries. It reads the image's greyscale values and applies a threshold, whereby pixels in the local area above a particular greyscale value are included in the selected (and measured) area [231].

The large difference in contrast between a polished sample surface and the material in the centre

of an impression made this technique particularly useful. The optical microscope in question was calibrated using a graticule before any area or length measurements.
This measurement of the whole indentation area avoided error where the impression deviated from a perfect square, rather than using the standard diagonal Vickers measurement method. All areas were measured directly from above (with no tilt). Additionally, the optical microscope was calibrated each time it was used using the same ferrule.

3.2.1 Meyer Hardness

The Meyer hardness number (H_M) is based on the same indentation test data as for Vickers hardness. However, the Meyer hardness number is the mean contact pressure, expressed as the indentation load divided by the *projected* area of the indentation. Therefore,

$$Meyer\ Hardness\ (MPa) = \frac{force}{area} = 10^{-6}\frac{load\ (N)}{projected\ indentation\ area\ (\mu m^2)} \tag{15}$$

The Meyer hardness is said to be a true representation of the hardness of the material [228]. The use of the actual contact area of impression in Vickers hardness is not a satisfactory physical concept, as H_v does not yield the mean pressure over the surface of the indentation impression due to the compensation of the horizontal component of indentation load by the axial symmetry of the indenter used. The Meyer hardness is literally the resistance to penetration and has been related to the plastic flow stress σ_y (yield stress) and Youngs Modulus E. H_m has been expressed as $C\sigma_y$ using the constraint factor C, implying a relation to the "plasticity" of materials [228]. This constraint factor C for ideally plastic materials is approximately 3 in theory, although this value significantly depends on the geometry of indenter and the ratio of $\sigma_y : E$ [228].
For most types of pyramidal indentation, there is a significant elastic recovery of the indentation impression when the indenter is removed although the main recovery in dimensions occurs in the depth rather than in the in-surface projected area of impression. This is important for non-instrumented indentation testing, as the indentation areas are measured after the load has been released (when there is no load-depth data).

3.2.1.1 Converting Meyer Hardness to Vickers Hardness

In a Vickers measurement, the diagonal length used is an average of two separate diagonals, so the calculation effectively considers a square of side $d_v/\sqrt{2}$ as shown in figure 66.

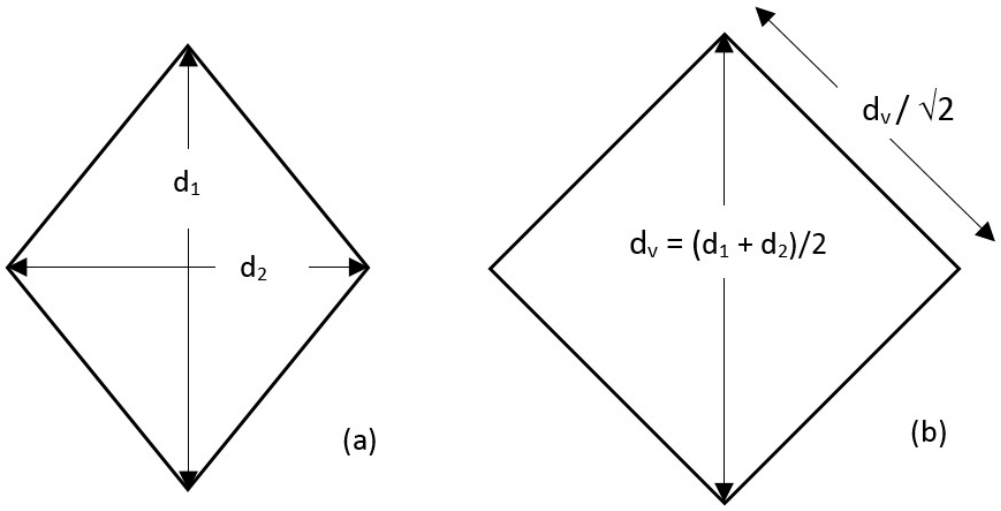


Figure 66: Schematic of Vickers indentation diagonals - (a) diagonals 1 and 2, (b) average of diagonals equates to a square

Therefore, the projected area measured using optical microscopy A_{pr} can be approximated as

$$A_{pr} = \frac{d^2}{2} \tag{16}$$

and from equations 13 and 16, to convert from Meyer to Vickers:

$$H_v = \frac{1.854F}{2A_{pr}} \tag{17}$$

so

$$H_M = 1.0787H_v \tag{18}$$

3.2.2 Thermal Expansion Correction

The projected indentation area measurements of indentations formed when at high temperature are made after cooling the specimen to room temperature. This naturally introduces an error into the hardness, since in the cooling from the experimental temperature the dimensions of the indentations diminish and therefore the value of hardness apparently changes. This is especially important as hardness values will later be compared with those taken during instrumented indentation, which allows the collection of data at the temperature in question. For investigations concerned with the accurate determination of hardness at high temperatures, corrections must be introduced in the measurement of projected indentation areas. The same applies to low temperature indentation, but instead the specimen will expand when warming to room temperature [232].

3.2.2.1 Thermal Expansion of Molybdenum Molybdenum has the lowest thermal expansion coefficient of all the refractory metals, and as such the effect of thermal expansion on microhardness will be small. However, for accuracy of results, the correction to hardness data will be applied here. In their compilation of the thermal and structural properties of fusion materials, Karditsas et al. [233] used the data from three sources [234, 235, 236] and fit a polynomial curve to describe the thermal expansion coefficient α of Mo and its variation with temperature:

$$\alpha = 4.9904 + 1.1837 \times 10^{-4}T + 3.5877 \times 10^{-7}T^2 \tag{19}$$

This equation describes the *linear* expansion of Mo; Meyer hardness measurements deal with the expansion of an area. The two are easily interchanged.

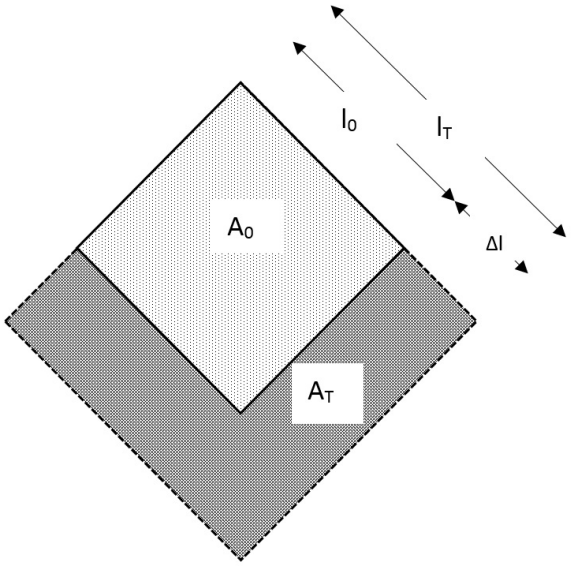


Figure 67: Schematic to show the change in length and area of a shape during thermal expansion. L_0 and A_0 are original length and area, L_T and A_T are length and area at reference temperature T and Δl is the change in length.

As shown in figure 67, the strain of a material upon a temperature change from T_0 to T is given by:

$$\frac{\Delta L}{L_0} = \frac{L_T - L_0}{L_0} = \alpha \Delta T \tag{20}$$

and so

$$L_T = L_0(1 + \alpha \Delta T) \tag{21}$$

The original area of this shape is:

$$A_0 = L_0^2 \tag{22}$$

Area at temperature T is given by

$$A_T = L_T^2 = L_0^2(1 + 2\alpha\Delta T + \alpha^2\Delta T^2) \tag{23}$$

Therefore, dismissing the α^2 term as negligible,

$$A = A_0 + 2A_0\alpha\Delta T \tag{24}$$

This function of temperature will be used with equation 19 to calculate the area of an indentation at a temperature T, using the reference area A_0 as measured at 300K under the optical microscope.

For example, with a coefficient of linear expansion of the material equal to $5.596 \times 10^{-6}K^{-1}$ per degree of cooling from 872°C, an indentation made at 872°C that has an area of $9422\mu m^2$ at room temperature will have a corrected area of $9511\mu m^2$ - the actual projected area made by the indenter at 872°C. The reduction in area equals $89\mu m^2$ and this area variation gives an error of 0.94%.

3.3 Elastic Recovery

Once an indenter has been fully loaded, the load is removed and a permanent impression is left behind. If the indenter has an internal angle between faces θ, the impression will most likely be a shallower version of the indenter, with internal angle $> \theta$. The dimensions of microindentations across the tested range of temperatures were measured using the Auriga SEM, from which the internal angle was calculated using trigonometry. An example measurement is shown in figure 68.

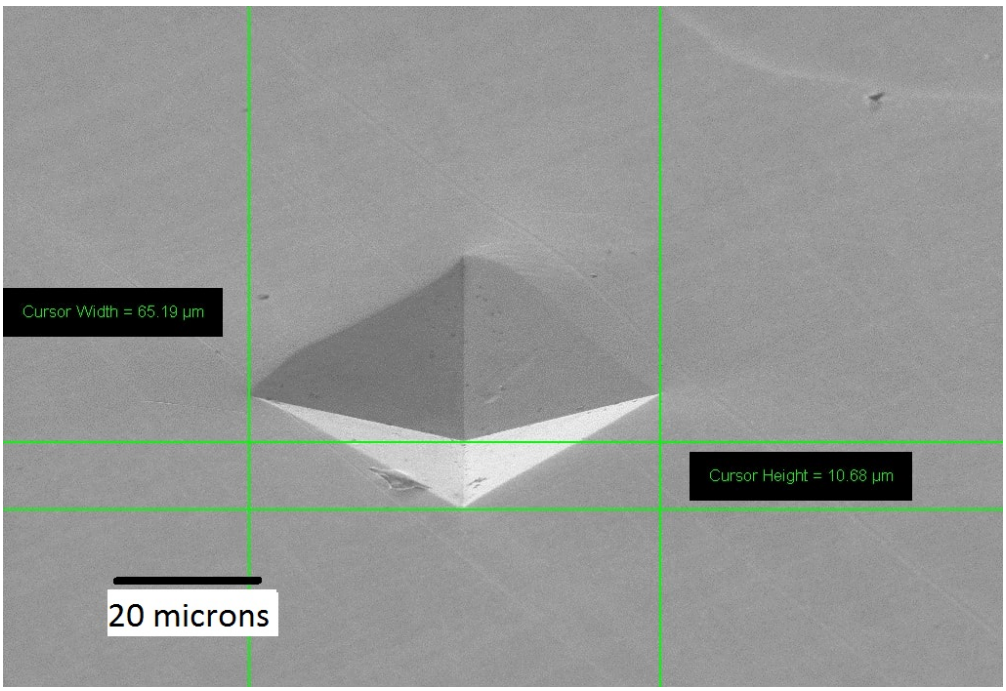


Figure 68: Internal angle measurement of an unloaded indentation made at -22°C using the Auriga-SEM at a tilt angle of 54°

As shown in figure 69, the residual indentation height is expected to be smaller than the fully loaded height. As above, SEM images and trigonometry were used to calculate residual height. There were generally very small pile-ups so the indentations were assumed to be perfectly flat.

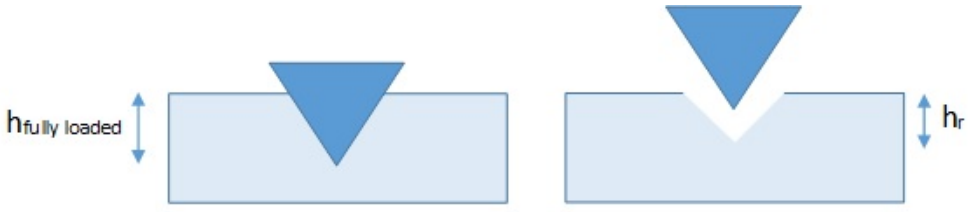


Figure 69: Representation of the residual height measurement - loaded indentation (left) and unloaded indentation (right).

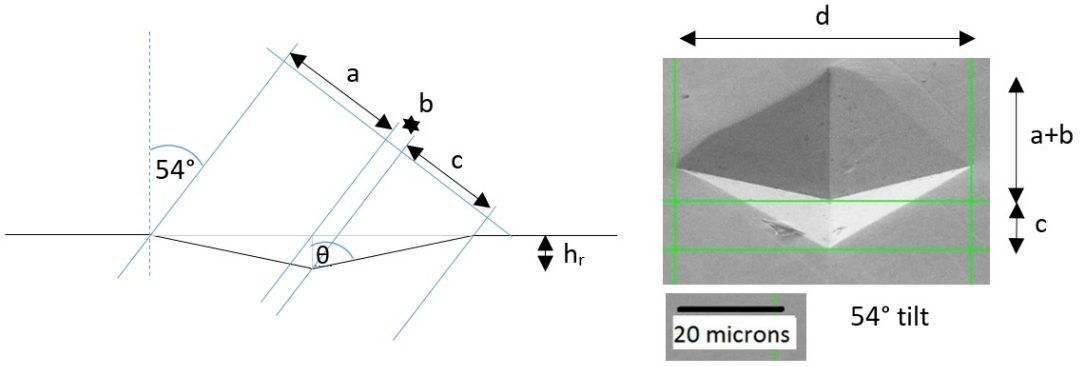


Figure 70: Residual height measurement - geometry and measured dimensions at 54° tilt (left) and the same dimensions on an imaged indentation (right).

Figure 70 shows the geometry and measured dimensions of a 54° tilted indentation in the SEM. These measurements are used in the trigonometric calculation of the residual depth, h_r. The equation used to calculate the residual indentation depth is described below. An important assumption was made that the indentation diagonals did not recover (change in length) after unloading. The Vickers diagonal measurement was taken to be length d in figure 70, and this was checked against the component of the vertical diagonal (a+b+c) resolved 54°. Length b is the residual depth of the indentation projected onto the plane perpendicular to the viewing angle. It is measured on the micrograph as the distance between the bottom of the indentation and a line joining the side corners.

The residual height was calculated from length b:

$$h_r = \frac{b}{sin54°} \tag{25}$$

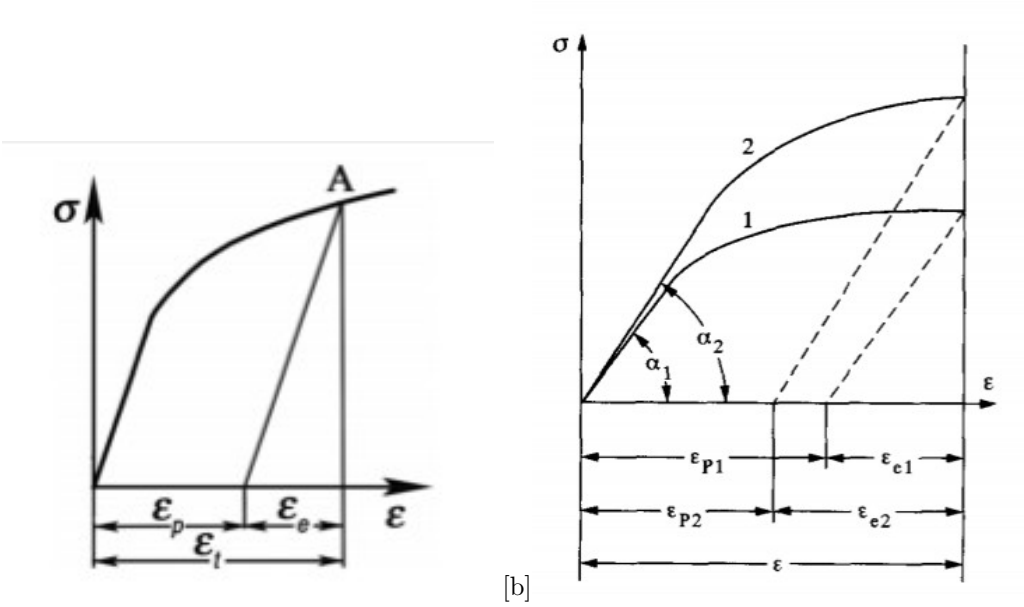
The fully loaded depth was calculated from the indentation diagonals, assuming a depth to diagonal ratio of 1:7, which is standard for a Vickers indenter.

3.4 Milman Plasticity Parameter

The Milman plasticity parameter δ_{Mil} is a dimensionless parameter characterised by the proportion of the plastic deformation in the total elastoplastic deformation of a mechanical test:

$$\delta_{Mil} = \frac{\epsilon_{pl}}{\epsilon_{tot}} = 1 - \frac{\epsilon_{el}}{\epsilon_{tot}} \tag{26}$$

where ϵ_{pl} is plastic strain, ϵ_{el} is elastic strain and ϵ_{tot} is total strain up to a predetermined strain (point A in figure 71a).



[a] [b]

Figure 71: Milman plasticity parameter - the proportion of the plastic deformation in the total elastoplastic deformation of a mechanical test. ϵ_{pl} is plastic strain, ϵ_{el} is elastic strain and ϵ_{tot} is total strain up to a predetermined strain (point A in figure a). Figure b shows the comparison of two materials, 1 and 2. Material 1 has a larger plasticity parameter as can be seen from the large ratio of ϵ_{p1} to the total strain ϵ.

Figure 71b shows the comparison of two materials, 1 and 2. Material 1 has a larger plasticity parameter as can be seen from the large ratio of ϵ_{p1} to the total strain ϵ.

Using Milman's analysis for calculating the plasticity parameter for microindentation [237], the elastic indentation strain must be substituted into equation 26. The average elastic strain on the indenter–specimen contact area in the direction of the load applied to the indenter is of the form [238]:

$$\varepsilon_e = -\frac{HM}{E}(1 - \nu - 2\nu^2) \tag{27}$$

where HM is the Meyer hardness, E is Young's modulus and ν is Poisson's ratio. All elastic constants used in this study will be those of the correct temperature described in Section 1.2.4. Milman determined the total strain under pyramidal indenters to be:

$$\varepsilon_t = -ln(sin\gamma) \tag{28}$$

where γ is the angle between a face and the axis of the pyramid. Then according to equation 26, for a pyramidal indenter, the plasticity characteristic determined in indentation is as follows:

$$\delta_H = 1 - \frac{HM}{E.\varepsilon_t}(1 - \nu - 2\nu^2) \tag{29}$$

And for a Vickers indenter, $\gamma = 68°$.

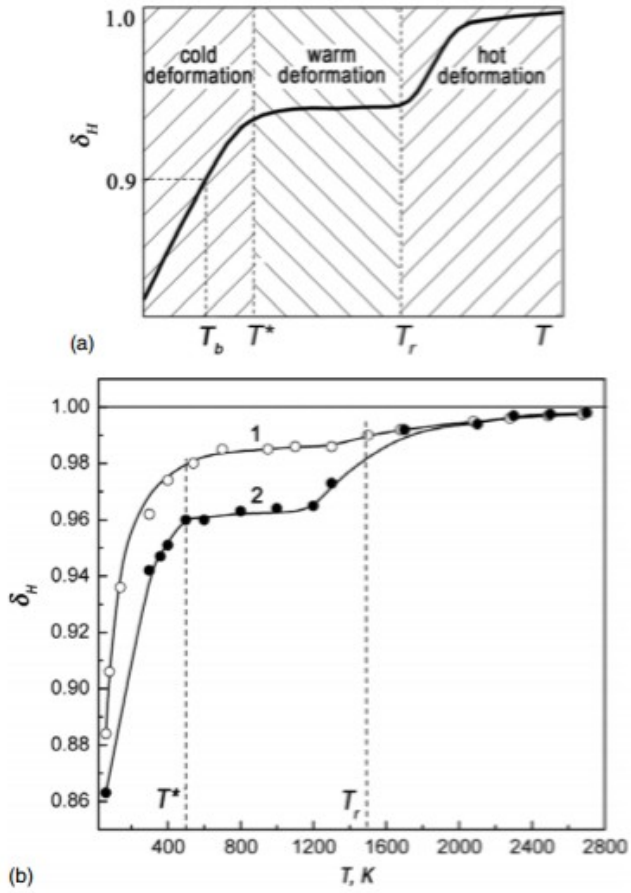


Figure 72: The temperature dependence of the plasticity characteristic for BCC metals. Part (a) shows a scheme of change of the plasticity characteristic in temperature ranges of cold, warm and hot deformation and part (b) shows the temperature dependence of the plasticity characteristic for polycrystalline molybdenum: 1—as annealed and 2—as deformed. From [237]

Figure 72 shows the temperature dependence of the plasticity characteristic for BCC metals (or crystalline materials in which the resistance to dislocation motion is determined by the Peierls-Nabarro stress and phase transformations are absent). Part (a) shows a scheme of change of the plasticity characteristic in temperature ranges of cold, warm and hot deformation and part (b) shows the temperature dependence of the plasticity characteristic for polycrystalline molybdenum: 1—as annealed and 2—as deformed [237].

3.5 Results

3.5.1 Indentation Area

Figure 73 shows the variation of projected indentation area with temperature. Area increases with increasing temperature in a non-linear fashion with a major point of inflexion at approximately 50°C.

This figure shows the continuity and overlap of the three microhardness methods used. Horizontal error bars were calculated from the maximum and minimum temperature recorded during each indentation and vertical error bars were calculated using the percentage change during thermal expansion.

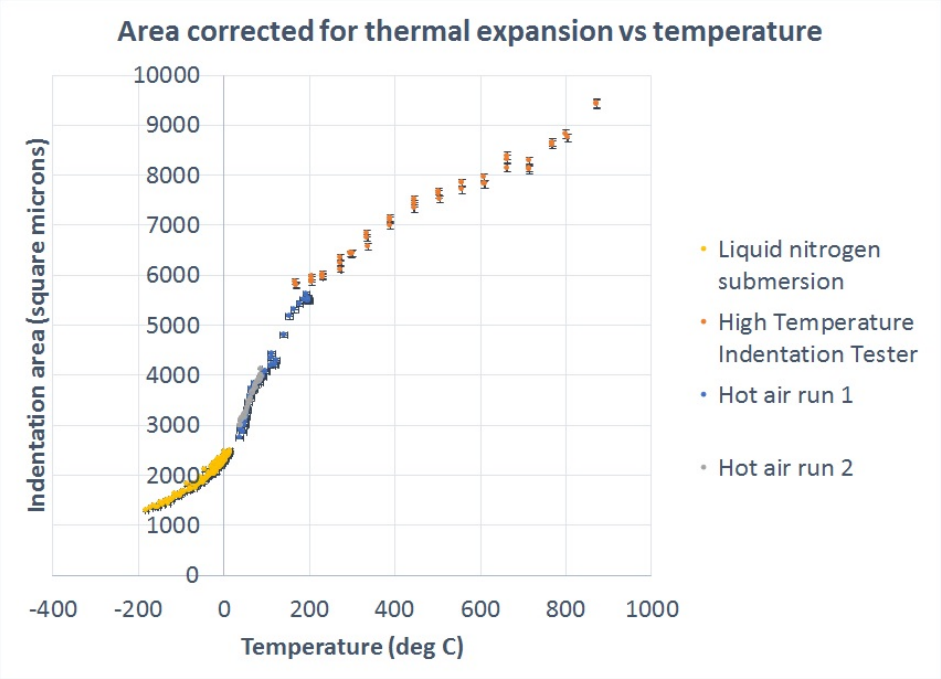


Figure 73: Projected indentation area measured by automatic capture (NIS Elements software). This shows data from all three temperature control techniques. Two runs using hot air temperature were carried out (labelled).

3.5.2 Meyer Hardness

Figure 74 shows the variation of Meyer hardness with temperature. These hardness values have been corrected for thermal expansion. The data from the three test types have been brought together into a common cross-calibrated data set. Error bars are equivalent to those in figure 73.

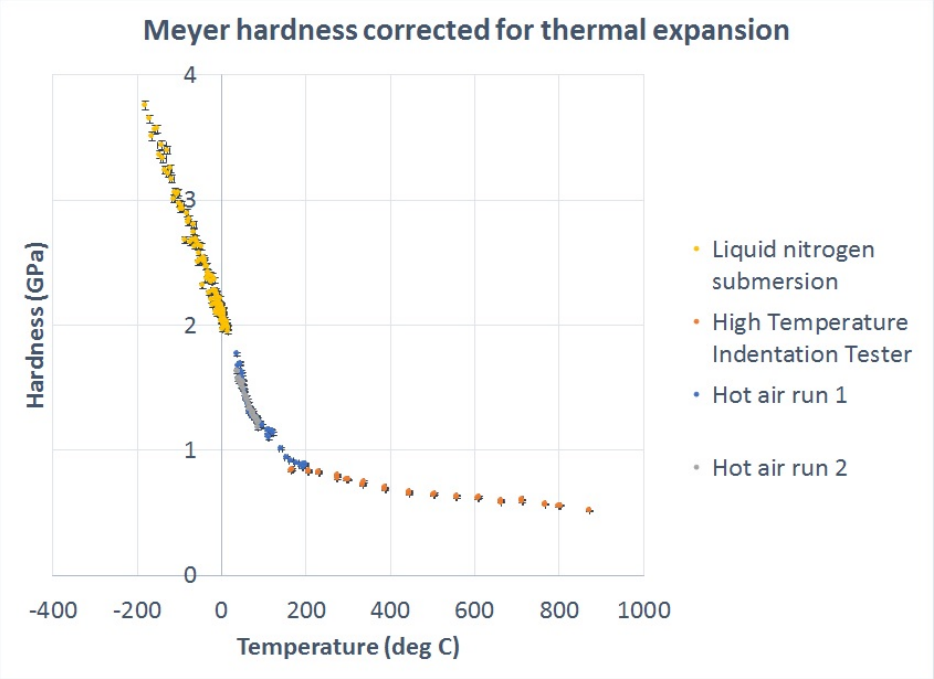


Figure 74: Hot microhardness testing of single crystal Mo. The hardness decreases with temperature, but shows two distinct behavioural regimes. Hardness was observed to decrease linearly from 3.75GPa at -180°C to 1.5GPa at 53°C followed by a change in gradient at approximately 100 to 150°C, and then another linear decrease from 0.77GPa at 274°C to 0.52GPa at 872°C.

The hardness decreases with temperature, but shows two distinct behavioural regimes. Hardness was observed to decrease linearly from 3.75GPa at -180°C to 1.5GPa at 53°C followed by a change in gradient (or 'knee') at approximately 125 ± 85°C, and then another linear decrease from 0.77GPa at 274°C to 0.52GPa at 872°C.

The data from figure 74 has been added to the summary of literature flow stress data in figure 29. This is shown in figure 75.

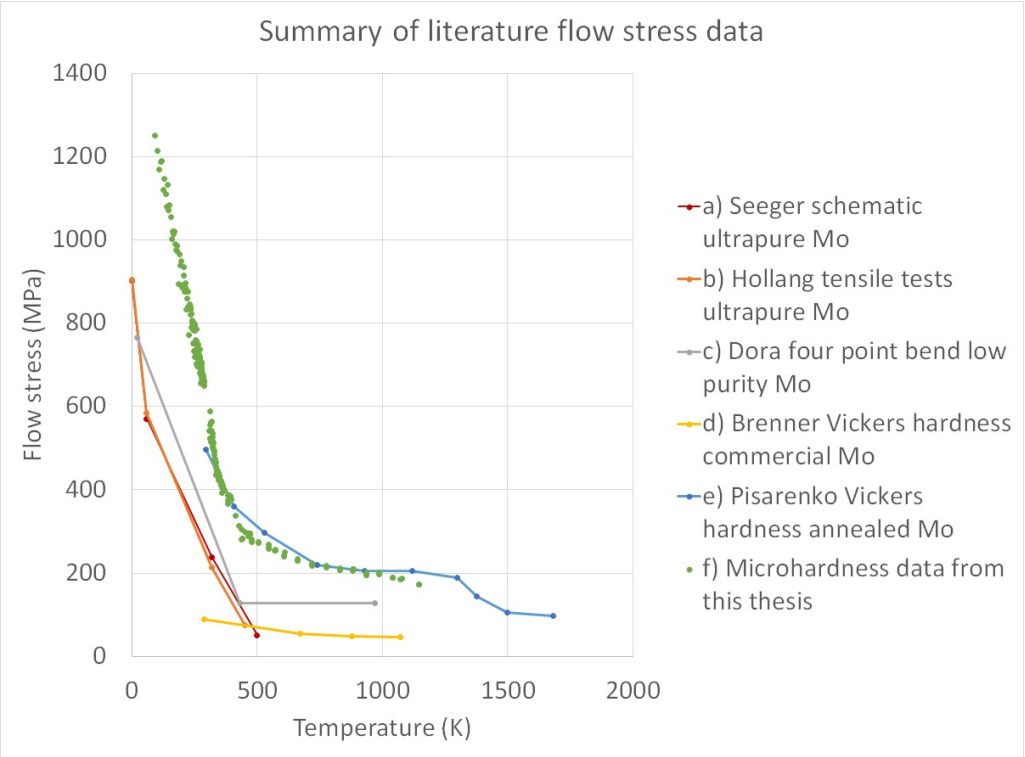


Figure 75: Summary of literature flow stress data (converted from hardness where necessary using Tabor's relation).
a) Schematic of the temperature dependence of the flow stress of ultrapure Mo crystals - Seeger et al. [25], figure 9b
b) Tensile tests on ultrapure Mo single crystals - Hollang et al. [32], figure 10
c) Four point bend resolved shear stress of unnotched low purity Mo samples - Dora et al. [101], figure 20
d) From Vickers hardness of a commercial bulk Mo bar - Brenner et al. [110], figure 23
e) From Vickers hardness of annealed Mo - Pisarenko et al. [111], figure 24
f) Microhardness data from this thesis.

3.5.3 Indentation Micrographs

The following figures show indentations made at six different temperatures and the resultant plastic deformation. All images were taken at 30° tilt in the Auriga-SEM. All images had tilt correction applied.

(a) Well below the transition temperature there is very little evidence of plasticity apart from the indentation itself - there are no pile-ups or buckling. The surface around the indentation is flat and there are no slip steps in the corners (-196°C, figure 76).

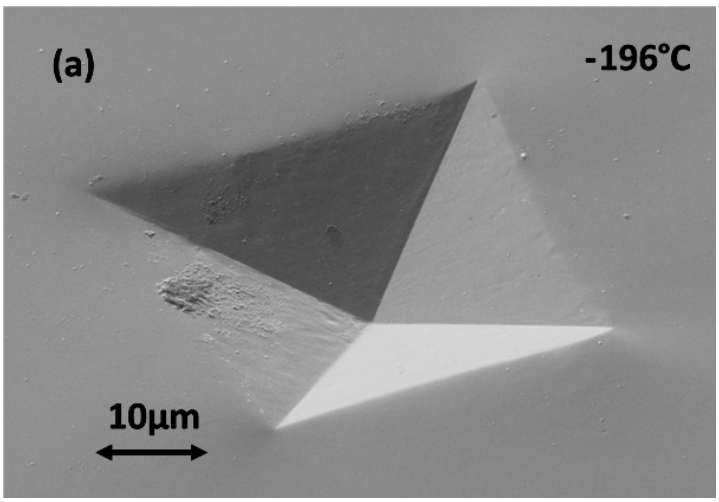


Figure 76: Vickers indentation in single crystal Mo, collected at -196°C

(b) Above approximately 0°C small slip lines start to appear in the indentation corners. These can be seen in the top left edge (6°C, figure 77). This also corresponds to the start of the transition in hardness behaviour.

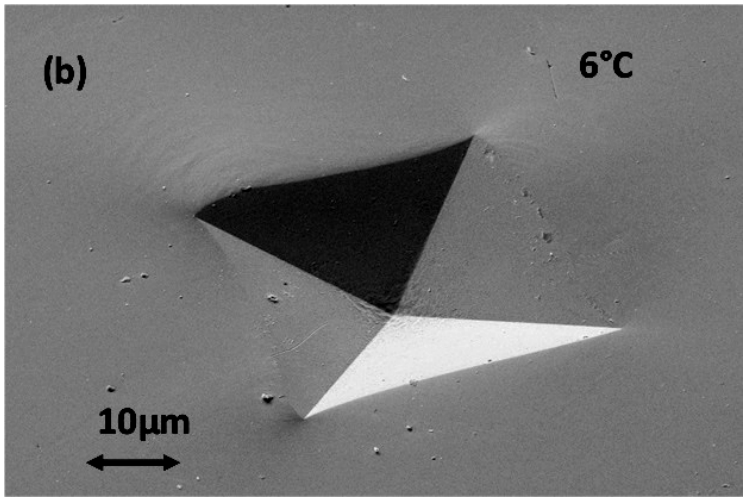


Figure 77: Vickers indentation in single crystal Mo, collected at 6°C

(c) Figure 78 shows and indentation made in the middle of the transition temperature "region", at 38°C. Slip lines are now becoming more distinct.

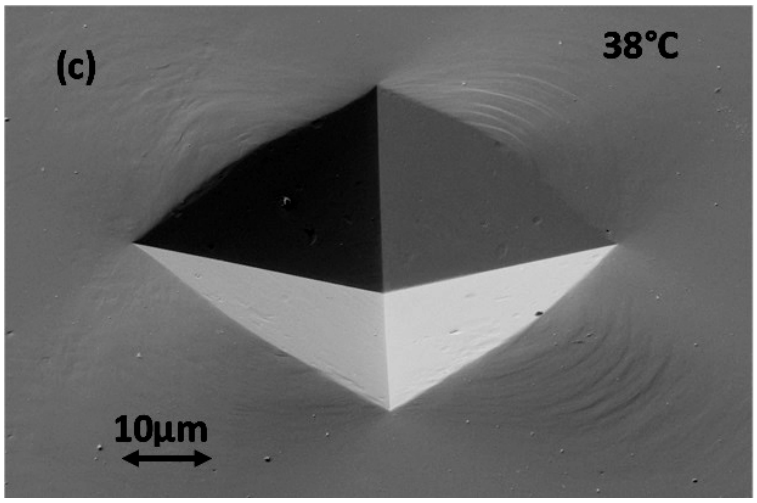


Figure 78: Vickers indentation in single crystal Mo, collected at 38°C

(d) This indentation was made in the higher end of the transition (76°C, figure 79). Slip lines are becoming raised (slip steps) as can be seen in the bottom left of the figure.

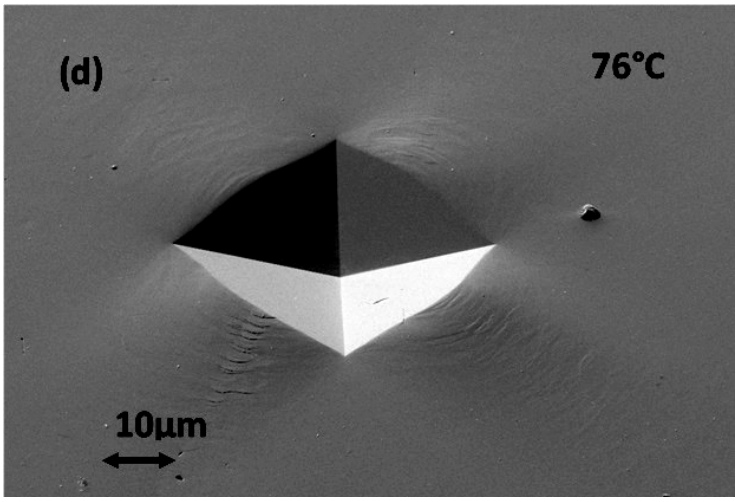


Figure 79: Vickers indentation in single crystal Mo, collected at 76°C

(e) Well above the transition temperature (504°C, figure 80), slip lines are extending.

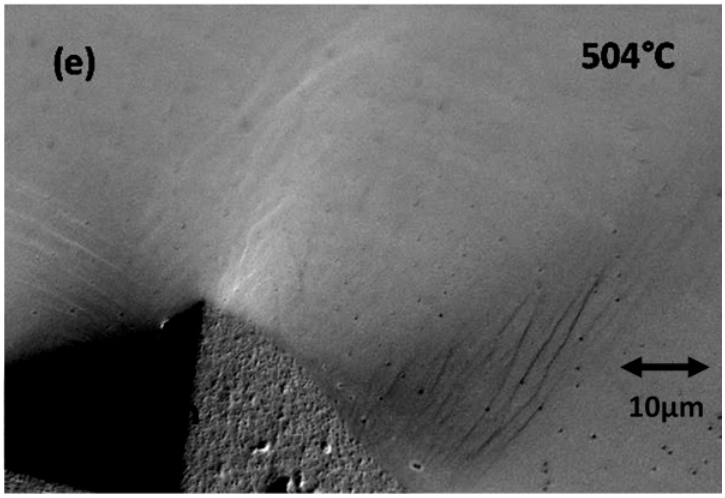


Figure 80: Vickers indentation in single crystal Mo, collected at 504°C

(f) This is one of the highest temperature indentations made in this sample (800°C, figure 81). Slip lines are raised and extended.

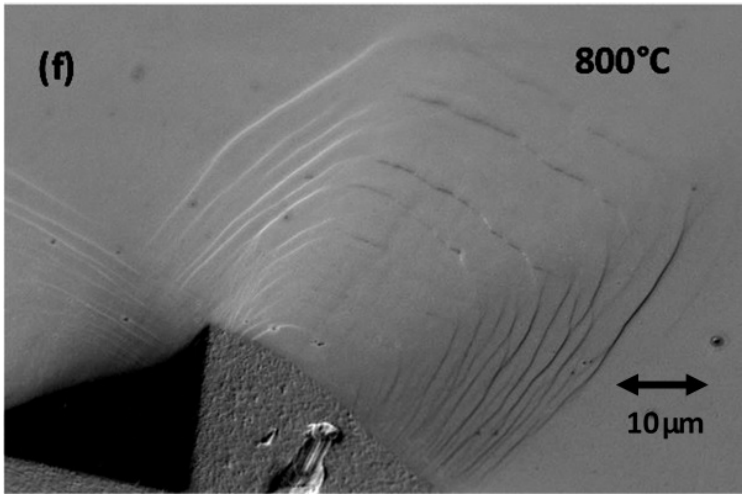


Figure 81: Vickers indentation in single crystal Mo, collected at 800°C

Further information can be drawn from indentations of known geometry (in this case the axes are aligned with the [001] crystal directions, and the indentation is within a (001) plane). The planes on which slip is taking place can be calculated from the angles between traces. An example is shown in figure 82, from an indentation made at 800°C. The approximate direction of the [100] vector is shown using a dotted line.

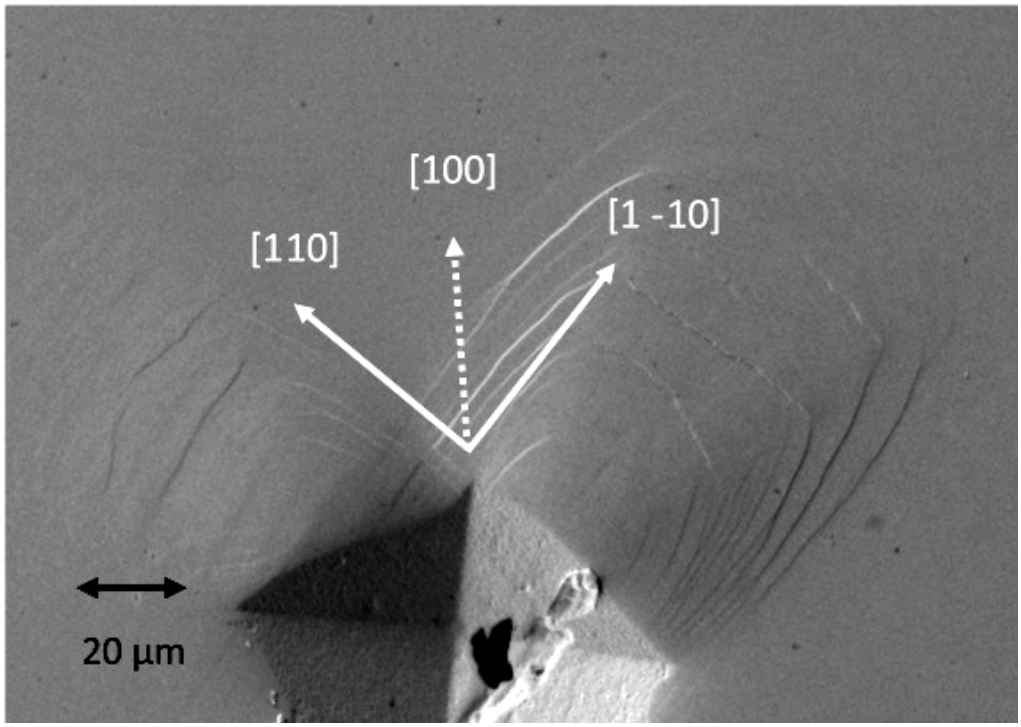


Figure 82: Slip trace analysis - Vickers indentation on a (001) face of single crystal Mo, 800°C. The approximate direction of the [100] vector is shown using a dotted line.

This indentation made well above the transition temperature shows $\{011\} < 111 >$ type slip. At high temperature in BCC metals, $\{123\} < 111 >$ and $\{112\} < 111 >$ are also expected to be activated. This was not directly observed in these SEM images, although the $\{011\} < 111 >$ slip is likely to have been composed of elementary slip steps on the other slip systems. This was explained on page 14.

3.5.4 Elastic Recovery

Figure 83 shows the ratio of residual depth to fully loaded depth, h_r:h_f, and its dependence on temperature.

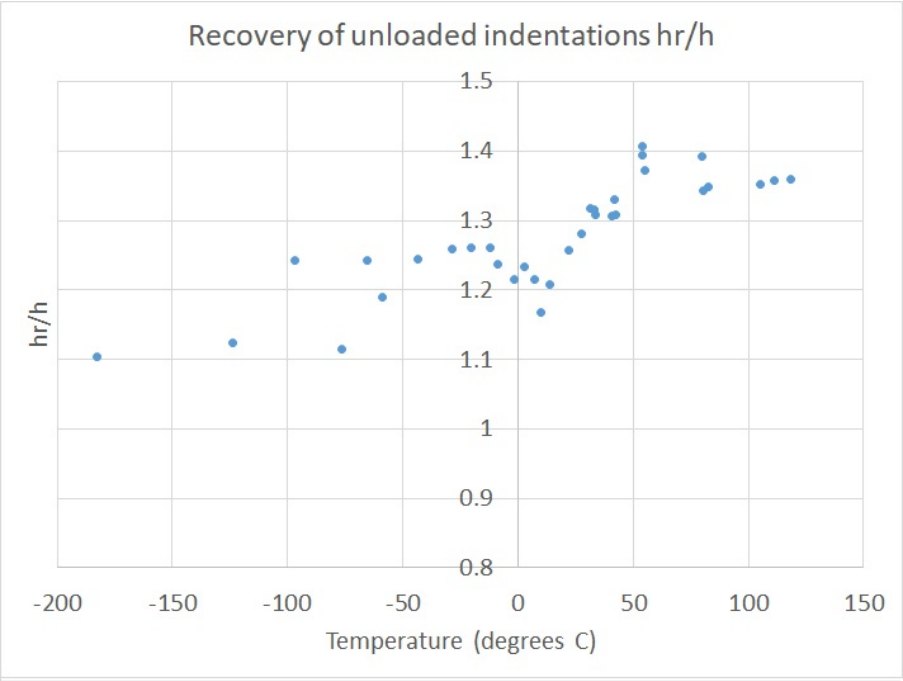


Figure 83: The ratio of residual depth to fully loaded depth, h_r:h_f, and its dependence on temperature. There is a marked change in gradient at around room temperature.

The most striking feature of the graph in figure 83 is the fact that the ratios of residual to fully loaded depth are all greater than 1. This was not expected, as the depth was expected to decrease as elastic recovery takes place. However, there may be some error associated with the assumption that the indentation diagonals do not deform in any way after unloading.

In an STM study of microindentations on tungsten, Stelmashenko et al. [239] found that all indentations that were investigated had an increase in diagonal length after unloading by a factor of 5 to 17% (which is a conservative estimate). A possible explanation of this effect might be that the material adjacent to the area of contact of the corners of the indenter with the surface is plastically deformed and it contributes to the apparent length of the diagonal. It is usually assumed that the material not in immediate contact with the indenter is deformed elastically and recovers completely after unloading [240]. Another assumption is that the amount of plastic deformation in the area adjacent to contact is smaller in comparison with the material under the indenter so that it will give rise to an angle different from that on a diagonal cross section in the contact area [241] [239].

However, Stelmashenko observed almost linear diagonal profiles for indentations on tungsten single crystals in almost all cases. The possible deviation of the shape of the indenter from an ideal pyramid might contribute to the results by 1-2%, but does not account for an increase in the diagonal length by 17% [239]. Stelmashenko concluded that the plastic deformation during indentation takes place not only in the area of contact with indenter but also in the adjacent area.

The possibility of an increase in diagonal after unloading does not go towards explaining the ratios greater than 1 shown in figure 83, as these would suggest a decrease in diagonal length. The fully loaded height assumed as 1/7 of the post-loading diagonal is smaller than the residual height, which is counterintuitive. Unfortunately, instrumented microhardness indenters were not available with the temperature controls used in this study. One definite conclusion that can be drawn from the measurements in this study is that the diagonals cannot have remained the same length after unloading.

Some error may have occurred during the cooling to room temperature (for high temperature indentations) or heating to room temperature (for low temperature indentations). However, the only factor that would account for this error is warping during this temperature change, although as the coefficients of thermal expansion for molybdenum are equal in the {100} directions, this is not likely.

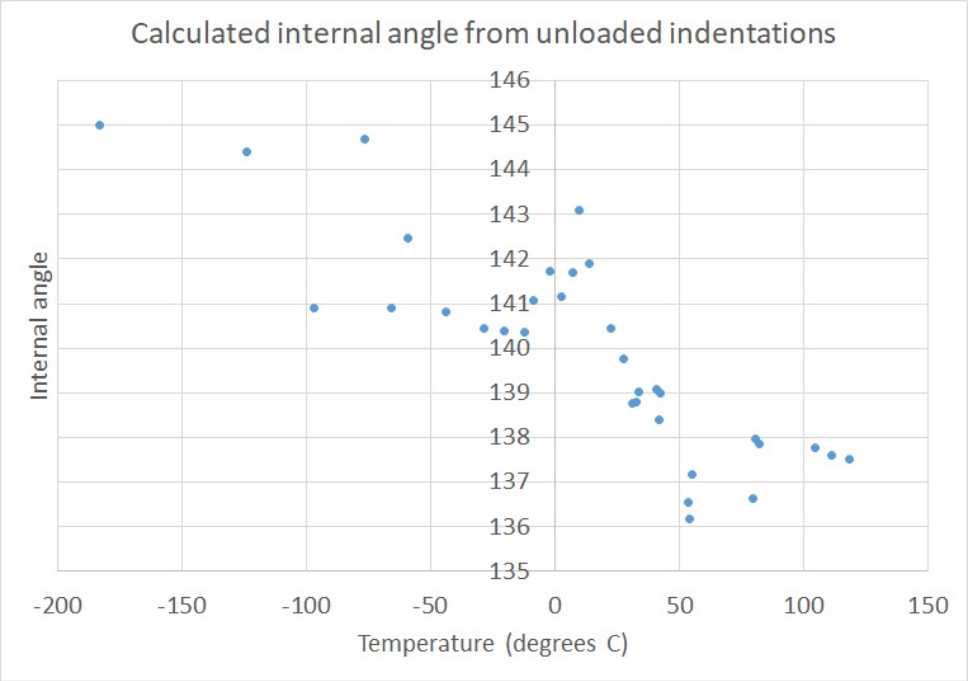


Figure 84: Internal angle of indentations (angle between diagonals) measured using tilted SEM micrographs after unloading. For reference, the internal angle of the indenter is 148°.

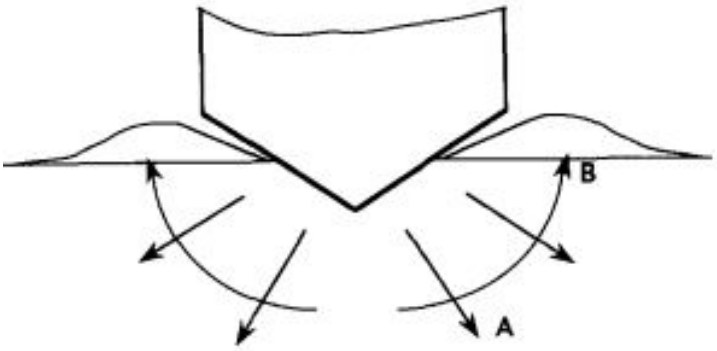


Figure 85: Patterns of flow under an indentation. From [239].

By looking at the angle between diagonals of the unloaded indentations (θ in figure 70), it can be seen that the angle is sharper than that of the indenter internal angle (148°). The calculated values for each indentation temperature are shown in figure 84. This figure shows that after unloading a 148° indenter, every indentation becomes sharper - an effect that increases as the test temperature increases. The trend is a decreasing angle with temperature, with the possibility that the angle decreases more quickly above a temperature of approximately 20°C, which is around the transition temperature T_K for the microindentations, shown by a steeper negative gradient above this temperature.

Referring to the Patterns of flow under an indentation (figure 85, from [239]), this would suggest that more type A flow is occurring during the higher temperature indentations. More importantly, as the indentation temperature increases, the ratio of plastic to elastic behaviour is shown to increase, demonstrated by the lower elastic recovery (and sharper indentation angle).

3.5.5 Milman Plasticity Parameter

Milman's data for as-annealed polycrystalline Mo from this figure has been extracted and is shown in figure 86 along with the Milman plasticity parameter results for the microhardness testing in the current study, calculated using equation 29.

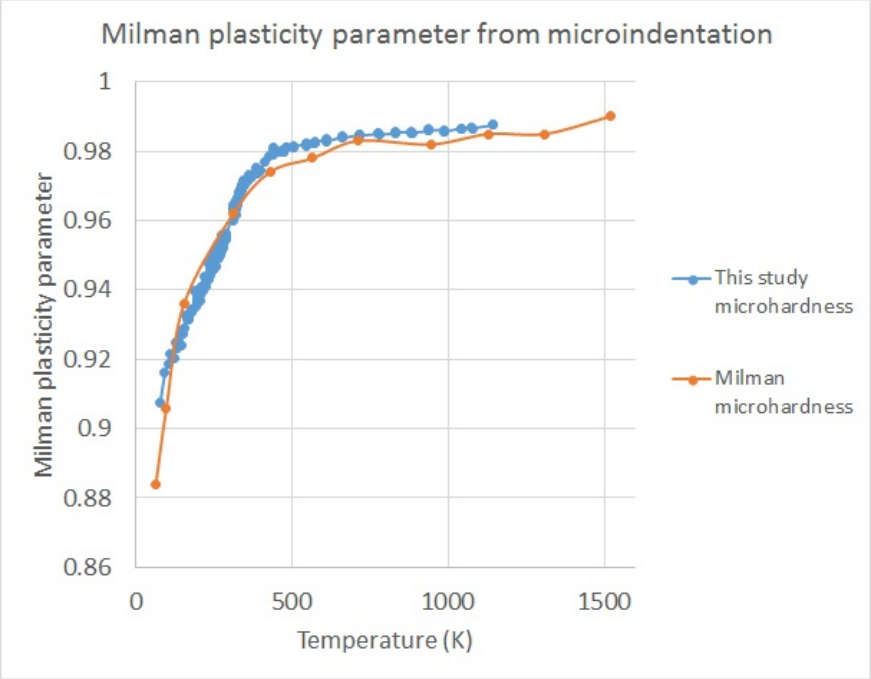


Figure 86: The temperature dependence of the plasticity characteristic for single crystal Mo (this study) and annealed polycrystalline Mo (from figure 72 [237]).

The plasticity characteristic values in both studies shown in figure 86 are very similar across all temperatures. The characteristic knee temperature, T_K, is shown by a change in gradient in these graphs. For single crystal Mo it is approximately 438K; for annealed polycrystalline Mo it is approximately 429K.

The geometry of sharp indentations is the same at all depths, and so indentation strain should be independent of indentation size for the same indenter angle. However, indentations on smaller scales ($< 1\mu$m) show size effects, with increasing hardness as indentation size decreases. This is usually explained in terms of increased geometrically-necessary dislocation densities at small indentation sizes, which causes higher strain gradients. None of the microindentations in this section were small enough to show size dependent hardness, as shown in the following chapter that discusses nanoindentation.

3.6 Discussion

Three temperature adjustment techniques were used to perform Vickers microhardness indentations in the surface of polished [100] molybdenum. The Meyers hardness calculated from area values showed a distinct change in character from low temperature to high temperature. This change in character was reflected in optical micrographs taken of a range of unloaded indentations; somewhere between 6 and 38°C, slip lines suddenly became much more distinct, showing an increase in dislocation activity. Above 38°C these slip lines became stronger and

became more linear at approximately 504°C, again indicating a higher dislocation mobility (for an indentation taking the same length of time, the slip bands were able to travel further). Slip trace analysis of an 800°C indentation showed that the slip lines were aligned approximately with {110} planes. However, wavy slip lines were not observed optically, which was unexpected, as elemental slip steps on {211} planes are the likely deformation mechanism, particularly at such a high temperature.

The measurements on indentation recovery showed a possible change in recovery behaviour above this transition temperature, as indentation angle became progressively sharper after unloading each temperature, and this trend increased above the transition. Pile-ups were observed around many of the indentations at high temperature, which would go some way to explain this unusual behaviour. For example, the bowed edges of figure 65 are typical of an indentation with a large amount of pile-up. If pile-ups are present at the diagonal corners, the fully unloaded indentation depth will appear higher.

The Milman plasticity parameter was shown to increase as temperature increased, shown in figure 72. It is also apparent that the temperature dependence is non-linear; two different deformation mechanisms are clearly distinguished, which show a very similar dependence to Milman's results, also plotted in the same figure. These mechanisms are characterised by the thermal activation of the kink-pair mechanism, allowing for a much larger degree of plastic deformation (as dislocations can now move on two further slip systems), and an increased plasticity parameter. These are the regions of cold and warm deformation discussed by Milman [238], as temperatures were not high enough for recrystallisation to begin. The temperature boundary between cold and warm deformation is the characteristic knee temperature T_K.

This microindentation chapter has provided results that will form the basis of comparison with the newer technique of nanoindentation testing in the following chapter, but has also provided some insight into the temperature dependence of molybdenum in its own right. The data points in the microhardness regime are well into the bulk of molybdenum's depth scale, in which the hardness does not increase with increasing depth - any size effects are not operating at this length scale. The data recorded in this chapter are extremely useful for the investigation of the temperature dependence of size effect in the following chapter.

4 Nanoindentation

The previous chapter discussing high and low temperature microhardness tests showed the importance of thermal activation in the dislocation movement and resultant mechanical behaviour of molybdenum. This is crucial information, bearing in mind molybdenum will not be in service in the fusion reactor at room temperature. As previously explained, future studies on the irradiation behaviour of molybdenum will require the assessment of thin layers (a few microns) of irradiated material. Consequently, the behaviour of molybdenum in nanoindentation is important to assess, particularly its dependence on the size of indentation. Nanoindentation also gives important information on the size effect of hardness.

4.1 High and Low Temperature Nanoindentation

The nanoindenter used for high and low temperature work was a NanoTest Xtreme by Micro-Materials, a system that was first developed for deployment in Oxford. It provides a vacuum environment testing from -50 to 950°C and the option of nitrogen atmosphere testing from -50 to 30°C. The system is also fitted with an optical microscope for accurate positioning.

4.1.1 Load and Displacement Control

During an indentation on this instrument, a Berkovich tip is driven into the sample surface with possible loads ranging from $10\mu N$ to $500mN$. Loading is provided by an electromagnetic force actuator - the coil shown in figure 87, where a permanent magnet generates a force on the current flowing through the foil with the force proportional to current [242]. The displacement of the diamond is measured by means of a parallel plate capacitor, one plate of which is attracted to the diamond holder. When the diamond moves, the capacitance changes and this is measured by means of a capacitance bridge. The instrument is also fitted with a 10^{-5} mbar vacuum. The limit stop defines the maximum outward movement of the diamond, and also the operating orientation of the pendulum, when a load is applied. Its position is manually adjusted with a micrometer. The equilibrium position of the pendulum, with zero load current, is adjusted with balance weights.

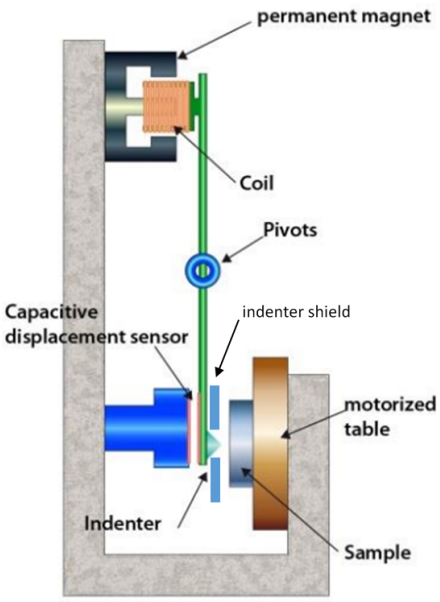


Figure 87: The Micromaterials Nanotest loading and measurement system. The indenter loading system is horizontal with the indenter mounted on a pendulum [242].

In the NanoTest Xtreme, the indenter loading system is horizontal (unlike vertical mounting in conventional nanoindenters) with the indenter mounted on a pendulum. This is because the system was originally designed to operate in an atmosphere rather than vacuum, and this arrangement minimised difficulties that arose from convection currents around a vertical setup. The shield setup restricts conductive heat flow into the loading head and depth measurement sensors, which are positioned to the left of the probe. There is negligible vertical motion of the indenter tip as the pendulum moves through a very small arc during an indentation (of typical depth $2\mu m$) [243]. Gibson [244] found the room temperature data to be identical to those collected on the Agilent Nanoindenter G200 and MTS Nanoindenter XP - two conventional systems with vertical loading. Tip displacement is measured using a pair of capacitive plates. One disadvantage of the NanoTest is the inability to perform CSM (continuous stiffness measurement) indentation. This is a technique used to find information on hardness with depth [245]. The load signal is constantly varied by superimposing a small sinusoidal signal onto the normal load signal, which partially unloads the indenter at each load increment [109]. Instead, all hardness-depth data had to be obtained by a series of indentations with increasing load.

4.1.2 Imaging

The microscope is fitted with a high resolution optical microscope (NanoTest Vantage). An in-situ 3D profiler (a piezo-driven stage behind the sample) is also available allowing 3D topographical maps to be created in-situ. A piezo-driven stage behind the sample rasters the sample across the probe, held at a constant load, typically $0.5\mu N$, building up a 3D image in a similar

way to an AFM - the tip displacement at constant load is recorded along with its x-y position. This also doubles as a nanopositioning stage giving a sample repositioning accuracy of 3nm and a maximum scan size of $200\mu m$ by $200\mu m$. The nanopositioning system is particularly useful for the testing of microcantilever beams, which are discussed in chapter 6. Testpiece dimensional accuracy is very important for working out stress and strain in microcantilevers (by using FEA or simple beam theory) and this nanopositioning system is the only way to find out the tested length as it is not possible to do it post-test (the indenter leaves no mark on the beam and the beam is curved). The 3D profiler is compatible with the hot and cold stages.

4.1.3 Sample Mounting

High temperature mounting: samples were adhered to a stage with a built-in furnace using high temperature cement, water-based Forta Fix Autostic FC6 (Hartlepool, UK). A thermocouple touching the specimen surface was also adhered using this cement, allowing the control of the specimen temperature to a high degree of accuracy ($\pm 0.1°C$).
Low temperature mounting: the sample and adjoining thermocouple were adhered to a Peltier-cooled stage using superglue.

4.1.4 Cold Stage

The NanoTest cold stage uses three-stage Peltier cooling stages on both the indenter and the sample, ensuring isothermal contact during testing (figure 88).

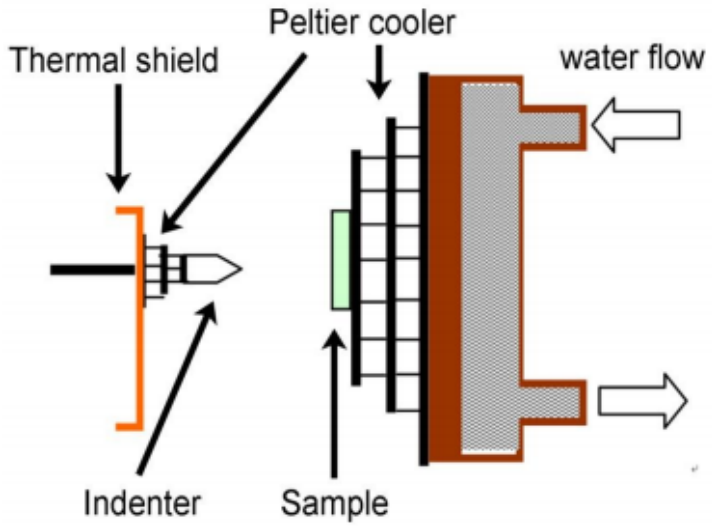


Figure 88: Micromaterials peltier stage showing the triple stacked stage below the sample, water flow coolant system and the tip thermal shield [246].

Peltier coolers exploit the heating or cooling at the junction of two dissimilar metals in the

presence of an electrical current. Depending on the direction of current flow, heat is either removed from a junction to lower the temperature, or by reversing the current, heat can be generated. The heat absorbed or created at the junction is proportional to the electrical current [247]. The Peltier effect corresponds to the heat transfer from one end of a conductor to the other caused by the passage of an electrical current. When a voltage is applied across a semiconductor thermocouple, electrons in the n-type material move towards the positive terminal. Similarly, holes in the p-type material migrate towards the negative terminal. The charge movement is accelerated by the electric field (yellow arrows) created by applying a voltage between the terminals of the device , so heat is dissipated through a heat sink. The schematic diagram in figure 89 illustrates the Peltier effect.

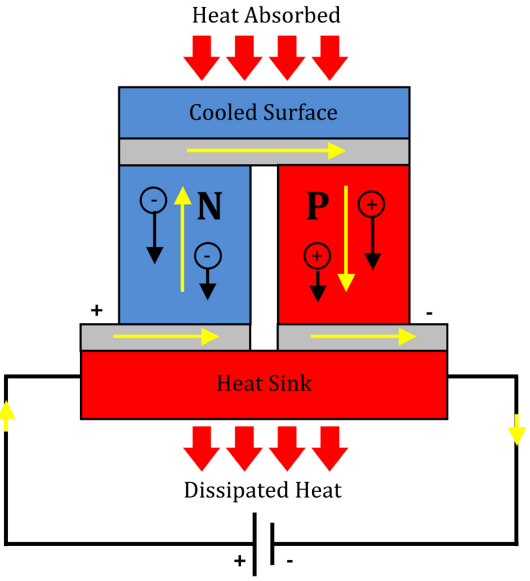


Figure 89: The Peltier effect - heat transfer from one end of a conductor to the other caused by the passage of an electrical current. When a voltage is applied across a semiconductor thermocouple, electrons in the N-type material migrate towards the positive terminal. Similarly holes in the P-type material migrate towards the negative terminal. The charge movement is accelerated thanks to an electric field (yellow arrows) created by applying a voltage between the terminals of the device and this result into heat being dissipated through a heat sink [248].

As with high temperature testing, there are new difficulties that have to be overcome when cooling a nanoidnentation system below room temperature. Between 0°C and room temperature, the sample acts as a cold finger and so will gather condensation. Below 0°C, this condensation freezes and becomes frost. Any indentations performed below 0°C simply test the mechanical properties of the ice layer, unless all moisture is successfully removed from the environment. The equipment used in this research avoids this problem with the use of a vacuum system.

4.1.5 Hot stage

There are two main challenges associated with mechanical testing of materials at high temperatures that must be overcome - oxidation and thermal drift.

4.1.5.1 Oxidation Testing under vacuum conditions negates one limitation of nanoindentation in air - oxidation at temperatures above 500°C in Mo. As seen in figure 90, a $30\mu m$ oxide film grew on the surface of polished single crystal Mo held at 500°C for 72 hours in air. The images were taken using an SEM and the trench was milled using a focussed ion beam. Taking into account that this is a typical length of time for a run of nanoindentation tests, a $30\mu m$ oxide would be disastrous for nanoindentation (with a typical indentation depth of $2\mu m$) and so a good vacuum is very important. The NanoTest Xtreme vacuum system is capable of a vacuum of 10^{-5}mbar, which is successful in preventing oxidation during a two week run at high temperature [116].

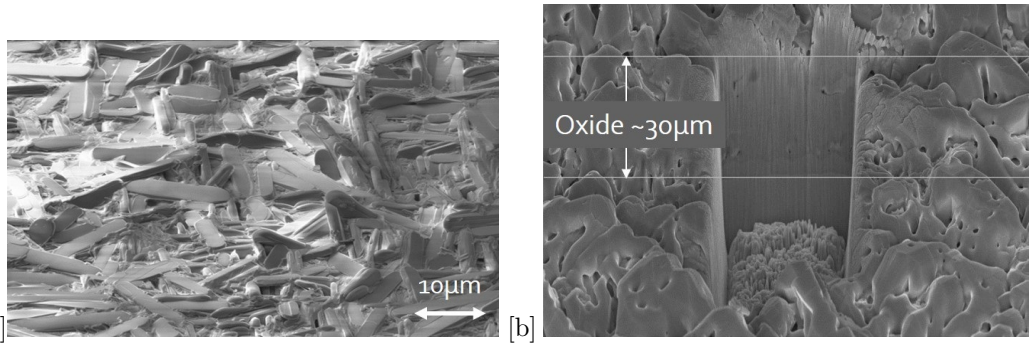


Figure 90: A vacuum system is necessary: Mo single crystal at 500°C for 72 hours. The images were taken using an SEM and the trench was milled using a focussed ion beam.

4.1.5.2 Tip Material Diamond is the usual choice of nanoindenter tip material, but due to high reactivity with BCC metals at high temperature this was deemed unsuitable. Available alternatives were sapphire, silicon carbide and cubic boron nitride (CBN). The mechanical properties of sapphire were not ideal for the indentation of Mo; with a modulus of around 400GPa at room temperature it is too close to the Young's modulus of Mo (323GPa at room temperature). Gibson [244] found the SiC tip to blunt more rapidly at elevated temperature. As a result, CBN was chosen (with a polycrystalline Young's modulus of 630 to 770 GPa [249] and single crystal elastic constants of 798.4 GPa for C_{11}, 469.0 for C_{44} and 172.4 GPa for C_{12}) [250].

4.1.5.3 Thermal Drift The importance of isothermal contact is magnified in vacuum conditions - the absence of an atmosphere removes all paths of heat flow between the tip and sample apart from conduction at their mutual contact point and radiative heating, which is a weaker effect.

The sample and tip temperatures are independently controlled by their individual thermocouples (the sample thermocouple as in "Sample Mounting" on page 99; the indenter thermocouple is held in the indenter shaft). This enables isothermal contact with approximately 0.1°C of accuracy. If the sample and indenter temperatures are not closely matched, thermal drift can occur. This is an alteration of the indenter displacement, caused by thermal contraction or expansion of the indenter once it hits the sample. A thermalisation time, typically 120s, was used before each indentation. During this time the tip is held close to the sample immediately before contact to allow for thermal stabilisation. Drift is measured by a hold period at a constant load, 90% of unloading (i.e. 10% of the peak load). The subsequent displacement is subtracted from the measured load-displacement curve. It is not a simple subtraction, as drift is time-dependent, so the correction uses a function of distance per time.

The following method was used for isothermal contact on the NanoTest Xtreme. The tip was positioned 500 μm from the sample surface, to prevent thermal expansion of the sample damaging the tip. Both the tip and sample were heated to the desired sample temperature followed by a delay of 6 hours for the sample temperature to stabilise. The tip was positioned $25\mu m$ from the sample surface, at which point the tip temperature increased due to radiative heating from the sample. The tip temperature was then set to the current sample surface temperature. A series of trial indentations was performed to determine the drift behaviour and the variation of tip temperature with depth. The tip temperature was adjusted as necessary based on drift rate. Finally, once the drift rate was low enough (typically 0.2 nm/s, comparable to room temperature drift rates), the array of indentations was performed.

As hardness and modulus calculations depend on indentation depth, an accurate value of measured displacement is crucial. Thermal drift when present can lead to inaccuracies in displacement measurements. Consequently, the level of drift is recorded before and at the maximum load of each indentation, at a 60 second hold each time. The data is in the form of a drift rate $\frac{dx}{dt}$ at each of these two hold periods and an average is taken. This is then subtracted from the load-displacement data to give a true displacement from which mechanical properties can be calculated.

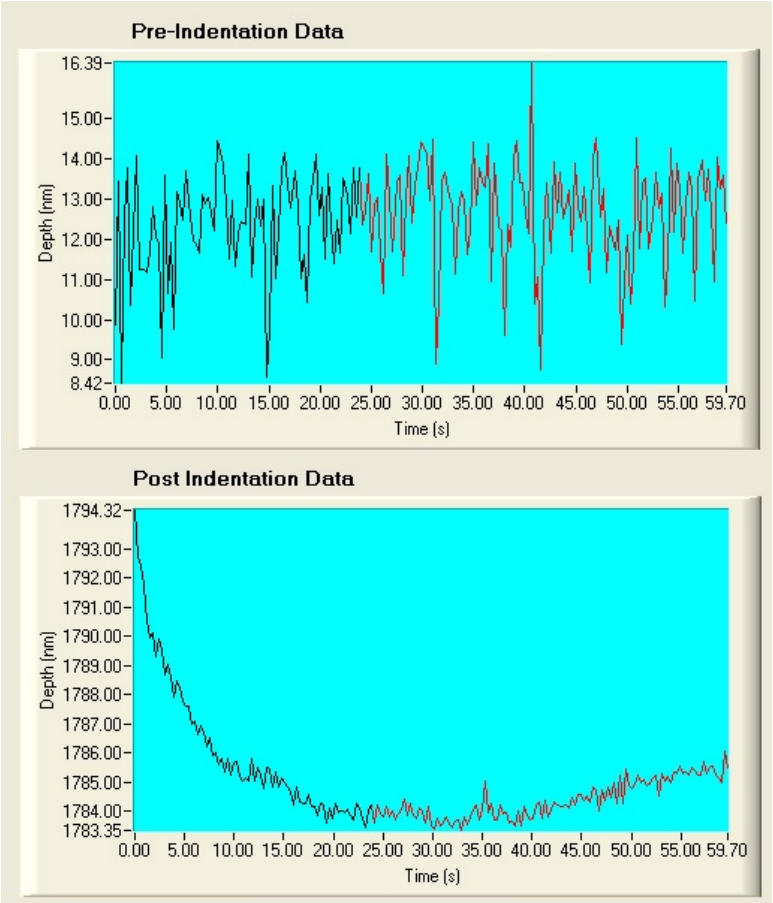


Figure 91: Drift before and after an indentation at 100°C. Pre-indentation drift = -0.01nm/s. Post indentation drift = 0.05nm/s. Calculated mean drift 0.02nm/s. Thermal drift was calculated over the final 60% of data shown in the two graphs.

Figure 91 shows a pair of typical drift data graphs. Pre-indentation drift = -0.01nm/s. Post indentation drift = 0.05nm/s. Calculated mean drift 0.02nm/s. Thermal drift was calculated over the final 60% of data shown in the two graphs.

Considering a typical room temperature indentation to 200mN, a loading rate of 5mN/s will take 40s to load. A typical drift rate was 0.1nm/s, which corresponds to 4nm of drift over the loading time. An indentation of this nature has a maximum depth of approximately 1500nm, which gives an error of 0.3%. Drift tends to be increased in indentations made at higher temperatures as isothermal contact is harder to achieve. Test indentations were used at each temperature to help obtain isothermal contact by examining their drift. The temperature balance between the tip and sample was adjusted if the drift was bigger than 0.2nm/s.

The depth signal (measured as a voltage) of the indenter tip swinging on its pendulum was useful for reducing the system drift each time the stage was moved or the temperature adjusted. This was monitored before all indentation tests. The depth signal was constantly fluctuating by a small amount . The system is considered “stable” once the standard deviation of fluctuation has dropped below 0.1V.

4.2 Experimental Method

Nanoindentation was performed under vacuum from -30°C to 850°C using the NanoTest Xtreme by MicroMaterials. The NanoTest Xtreme setup is shown in figure 92 - the vacuum chamber (left) contains the indentation setup. The motor and vacuum control system are on the right. A close-up of the NanoTest Xtreme while at 800°C and under vacuum is shown in figure 93.

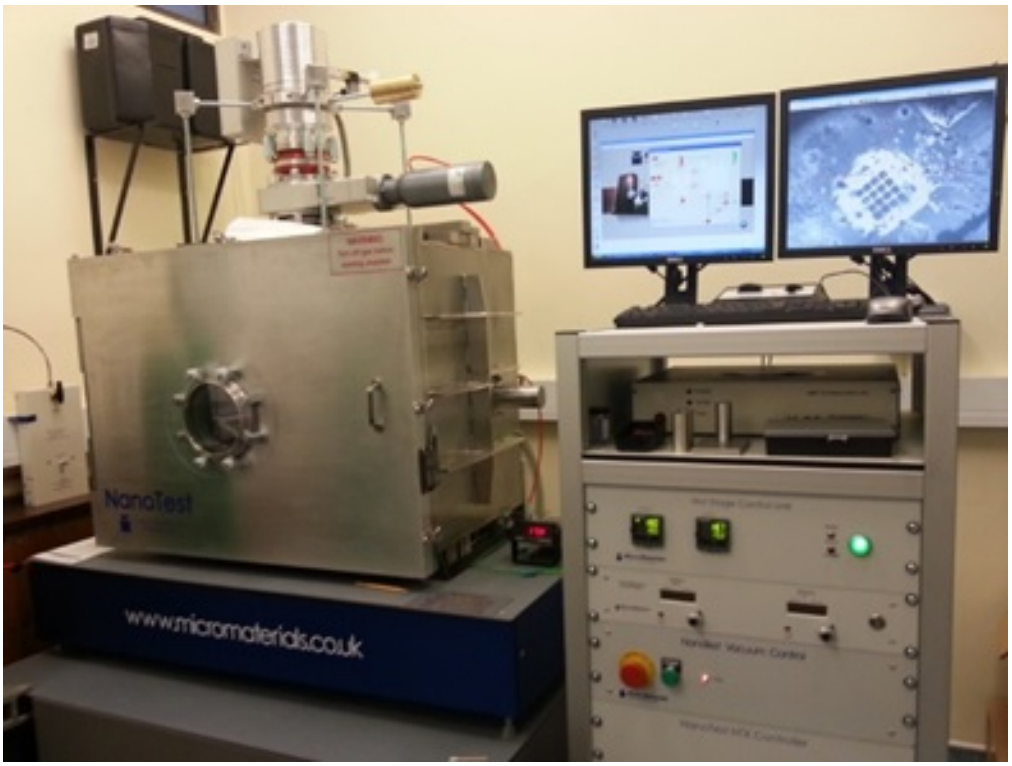


Figure 92: NanoTest Xtreme setup; vacuum chamber (left) containing the indentation setup and the temperature, motor and vacuum control system (right).

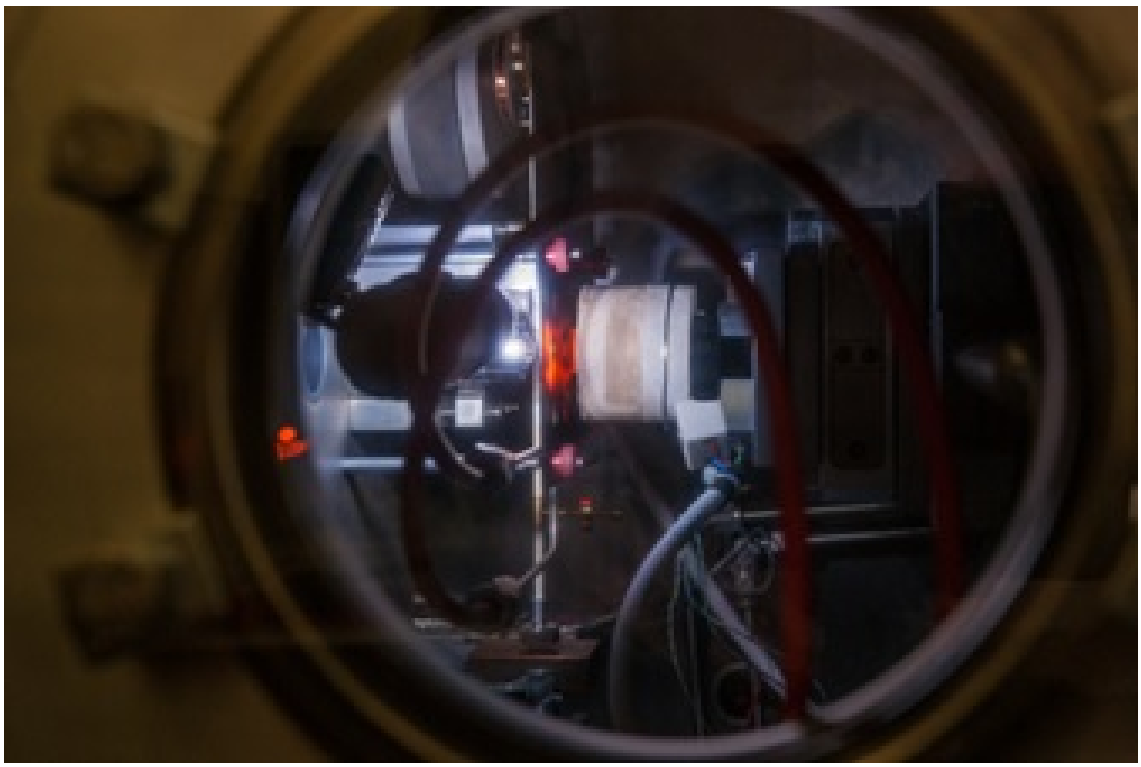


Figure 93: Close-up of the NanoTest Xtreme while at 800°C and under vacuum.

Thermal drift correction was carried out with 60s data collection time, with the correction calculated using post-indentation drift calibration data. A hot (or cold) stage thermalisation time of 240s was used at a distance of 0nm.

Load and displacement were recorded up to a maximum load of 200mN in an initial run. In a second run investigating size dependent hardness, load controlled indentations were carried out at a minimum load of 2mN, with 8 indentations at increasing intervals up to a maximum load of 300mN.

An initial load of 0.1mN was used. The same loading and unloading rate (5mN/s) was used in all indentations. A dwell of 60 seconds at maximum load was used. All indentations were spaced 90μm apart; a large polished area enabled this.

There is a size effect associated with mechanical testing (as outlined in the literature review on page 48) which causes smaller tests to result in larger hardness values. As a result, nanoindentation and microindentation will see difference in hardness values. Hence, nanoindentation across a wide range of loads (2 to 300mN) was performed in order to tie the two techniques together. Rather than load-increasing load cycles on the same indentation as is often used in this type of work, separate indentations were used of differing maximum loads. This made analysis more simple and there was ample sample area for space not to be a problem.

The hardness of a metal undergoing indentation depends on the depth of the indentation as well

as its temperature and strain rate. The strain rate was kept as constant as possible across the various techniques; the area to depth ratio of Vickers (microhardness) and Berkovich (nanoindentation) are the same, and the speed of indentation on the nanoindenter was kept as close as possible to the uncontrollable indentation speeds of the two microhardness testers.

As such high temperatures are being investigated, there is a slight linear change in compliance of the hot nanoindenter itself. This change is described by the following function, supplied by the manufacturer (with units of nm/mN). This is shown in figure 94.

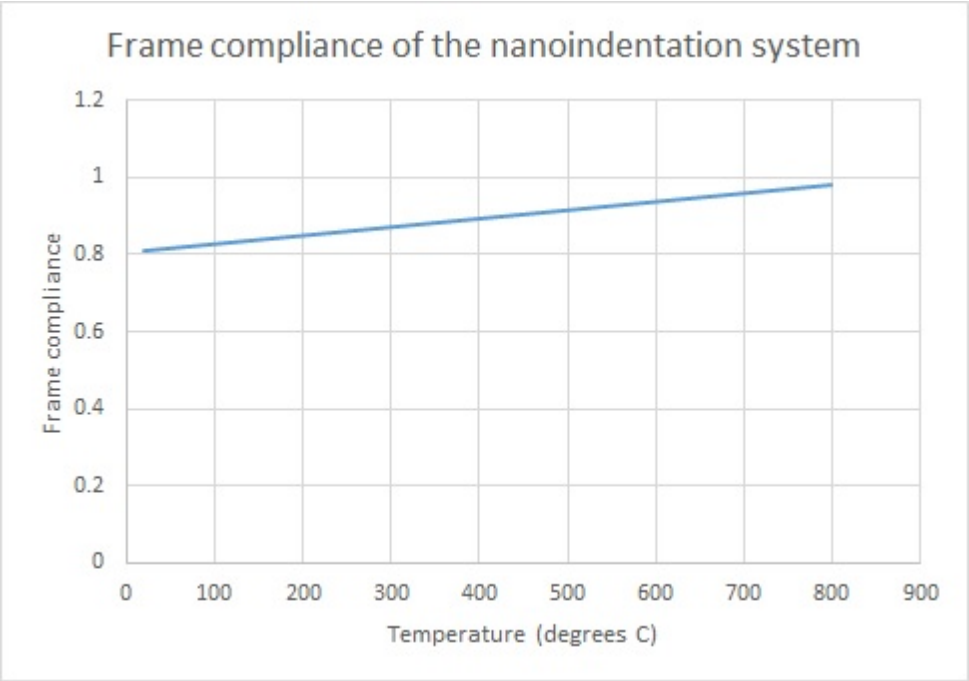


Figure 94: Nanotest Xtreme frame compliance function (provided by the manufacturer - units of nm/mN).

4.2.1 Nanoindentation Data Analysis

As the load-dependent displacement is recorded during nanoindentation testing, properties such as hardness and elastic modulus can be found using information on the tip's geometry and the load-displacement graph, a typical example of which is shown figure 30. The load-displacement data is converted into hardness and elastic modulus by using the Oliver-Pharr method. This was introduced on page 37. Instrument compliances and any thermal drift present are removed from data automatically before export.

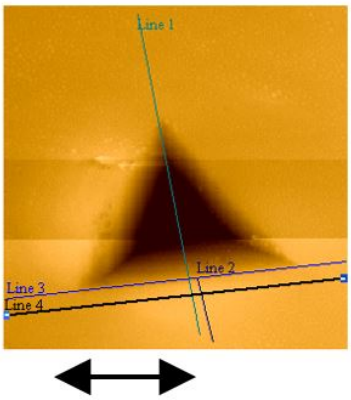
4.2.1.1 Area of a Nanoindentation As with microindentation, hardness is essentially a pressure measurement and so depends on the reciprocal of residual indented area - a larger

area corresponds to a softer and more easily deformable material. Hence, an accurate area measurement is crucial for reliable hardness data.

The load placed on the indenter tip is increased as the tip penetrates further into the specimen until it reaches the user-defined value. The indentations are much smaller than microindentations - in this thesis, typically 10 microns across compared to tens of microns across. Measuring the area using an optical microscope is therefore too inaccurate, and using an SEM is time consuming (not to mention the edges are difficult to resolve in the SEM). Instead, the contact area is calculated by determining an area function for the indenter tip, $A_p(h_c)$, which typically describes the projected area of an indentation as a 2nd-order polynomial function of the indenter depth h_c. This function is measured by performing an array of test indentations at differing depths in a reference material. Fused silica was used in this case, the mechanical properties of which are well-catalogued. These indentations are used to build up a map of the indenter's shape.

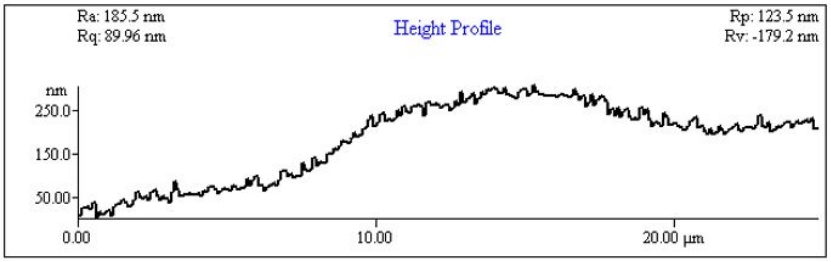
The method of using an area function to find an area value gives a Meyer's hardness value, which was also the method of hardness calculation in the microindentation chapter, so cross-comparison is possible.

Some AFM over nanoindentations was attempted using an external AFM. However, difficulties arose during AFM scanning due to large steps in the scans. These were AFM artefacts and not real features. However, the example images shown in part [a] of figures 95 to 97 show scans of Berkovich nanoindentations (indentation temperatures 100, 250 and 443°C). The pile-up heights calculated from the height profiles in part [b] of the figures were approximately 200nm for the 100°C indentation, 220nm for the 250°C indentation and 250nm for the 443°C indentation (on indentations approximately 15 to 20μm across). These heights were approximated as the difference between the top of the pile-up peak and the height of the bulk material.



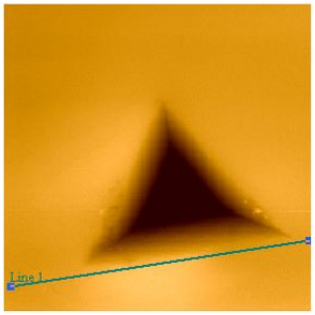
15µm

[a]



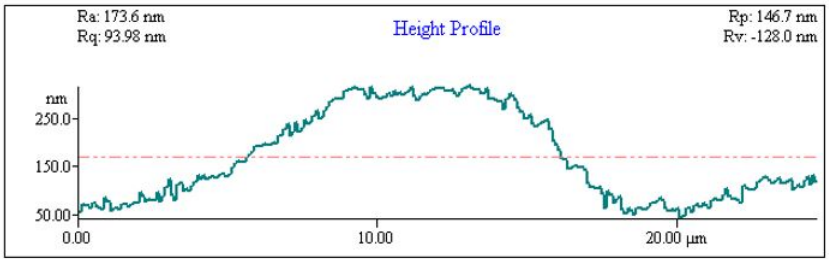
[b]

Figure 95: (a) AFM scan and (b) AFM pile-up profile of a Berkovich nanoindentation (indentation temperature 100°C). Approximate depth from top of pile-up to bulk level of 200nm.



15µm

[a]



[b]

Figure 96: (a) AFM scan and (b) AFM pile-up profile of a Berkovich nanoindentation (indentation temperature 250°C). Approximate depth from top of pile-up to bulk level of 220nm.

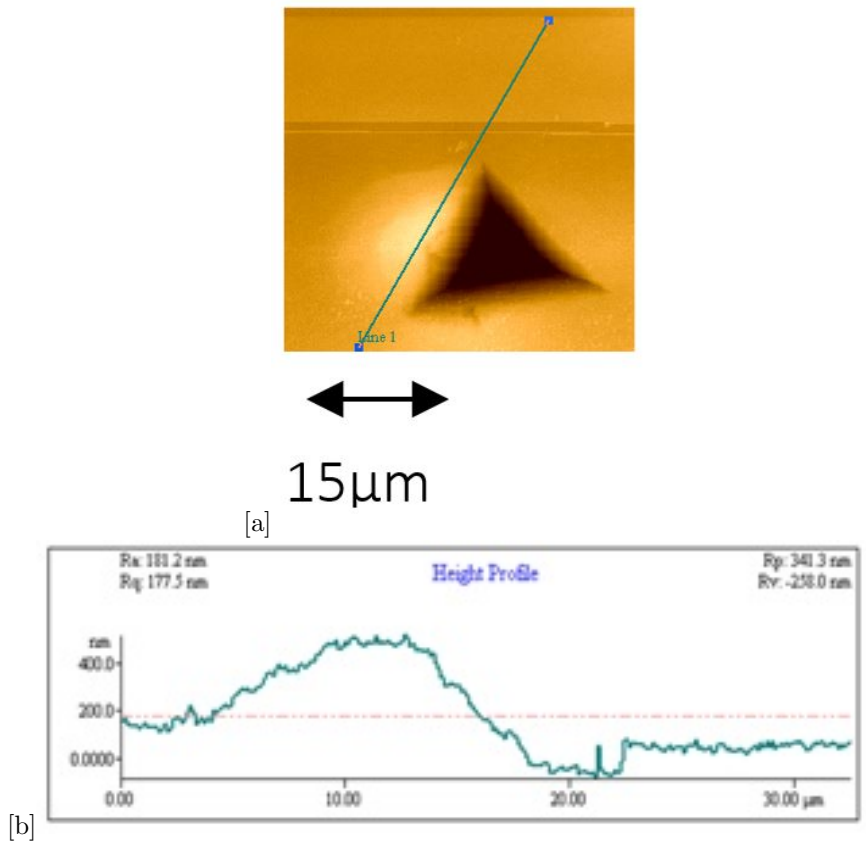


Figure 97: (a) AFM scan and (b) AFM pile-up profile of a Berkovich nanoindentation (indentation temperature 443°C). Approximate depth from top of pile-up to bulk level of 250nm.

4.2.2 Area Function Calibration

Quantitative evaluation of the elastic modulus and contact hardness of a nanoindentation depends strongly on knowledge of the indenter-sample contact area. The accuracy of this area measurement depends on careful calibration, which needs to be checked frequently as the area changes with tip blunting. Near the tip of the Berkovich indenter, some rounding inevitably occurs during the grinding process and after series of indentation arrays, particularly at high temperature and in a hard metal such as molybdenum.

Tip area calibration is relatively simple - indentation tests are performed on a material with well known mechanical properties, and the contact area calculated indirectly, finding the area function required to obtain the expected mechanical properties on the well-known material.

The form of the contact area function, which relates the contact depth of the tip in the material to the projected contact area, is of the form:

$$A(h_c) = C_0 h_c^2 + C_1 h_c + C_2 h_c^{1/2} + ... \tag{30}$$

The first two terms are dominant and are usually sufficient. The use of Oliver-Pharr analysis in finding the tip area function is simple and straightforward, although it is prone to errors

from both the curve fitting and the enforced numerical value of the elastic modulus taken from the literature. Fine-tuning of the area function is usually required. The area coefficients are adjusted and the contact area re-calculated until the elastic modulus for one or more materials is constant with depth (but not necessarily of a "forced", known numerical value from the literature).

The reduced modulus accounts for elastic displacements in both the specimen and indenter. It is evaluated from

$$E_r = \frac{1}{\beta}\frac{\sqrt{\pi}}{2}\frac{S}{\sqrt{A_c}} \tag{31}$$

β is a constant equal to 1.034 for a Berkovich indenter. S is the same contact stiffness of unload described above. A_c is contact area calculated from the area function and known contact depth. Identification of the area coefficients along with identification of the frame compliance complete the overall calibration.

The Oliver-Pharr analysis takes into account the non-perfect indenter geometry, which is a problem worsened by performing large indentation arrays in a hard material at high temperature (such as performed here) [139]. This method was developed to measure the hardness and elastic modulus of a sample from a load-displacement graph of one indentation load-unload cycle.

4.2.2.1 Elastic Modulus A schematic diagram of a typical load-displacement graph for a Berkovich indentation of an elastoplastic material is shown in figure 30. The unloading portion of load-displacement curves is usually used to measure elastic properties as there is a minimal plastic component on unloading. Due to the non-linearity of this section of the curve [127], unloading data are described by the power law relation:

$$P = \alpha(h - h_f)^m \tag{32}$$

P is indenter load, $(h - h_f)$ is elastic displacement of indenter and α and m are material constants determined by a least squares fitting procedure.
The unloading slope of the load-displacement curve, $\frac{dP}{dh}$, represents the stiffness of the contact. The elastic modulus is extracted in the form of a "reduced modulus". The effect of a non-rigid indenter on load-displacement behaviour can be effectively accounted for by defining a reduced modulus, E_r, through the equation:[127]

$$E_r = \left[\frac{1-\nu_s^2}{E_m} + \frac{1-\nu_i^2}{E_i} \right]^{-1} \tag{33}$$

where E_r is reduced modulus, ν_s and ν_i are sample and indenter Poisson's ratio and E_m and E_i are measured and indenter Young's modulus. The Poisson's ratio of the sample, pure molybdenum, was taken from Köster [88]. The reduced modulus accounts for elastic displacements in both the specimen and indenter (in the form of tip compliance).

The instrument and specimen can be modelled as two springs in series. The machine compliance, C_f, and the specimen compliance, C_u, are related through the equation:

$$C_{total} = C_f + C_u \tag{34}$$

And so the specimen stiffness, S, can be calculated from:

$$\frac{1}{S} = C_u = \frac{\sqrt{\pi}}{2\beta E_{eff}} \frac{1}{\sqrt{A}} \tag{35}$$

Following from this, the elastic modulus is related to the contact area and the measured unloading stiffness through:

$$S = \beta \frac{2}{\sqrt{\pi}} E_{eff} \sqrt{A} \tag{36}$$

This equation is not limited to a specific sample geometry and applies to both elastic and elastic-plastic contact. It is also unaffected by pile-up and sink-in. E_{eff} is the effective modulus, defined in equation 33. The term β is a correction factor, deemed necessary from both experiments and finite element analysis. At present, there appears to be no consensus as to why the factor arises and what value it should take. A large range of experiments [251, 252, 253] suggest the factor should be larger than the commonly used estimate 1.034 [254], but as no exact value has been ascertained, the value of 1.05 suggested by Oliver and Pharr [139] will be used here. [255]

The unloading stiffness at maximum load is calculated from the differential:

$$S = \frac{dP}{dh}|_{h_{max}} = \alpha m (h - h_f)^{m-1} \tag{37}$$

4.2.2.2 Hardness With the contact area established using the area function, hardness measurement is simply an extension of the Oliver-Pharr method, using the standard definition:

$$H = \frac{P_{max}}{A} \tag{38}$$

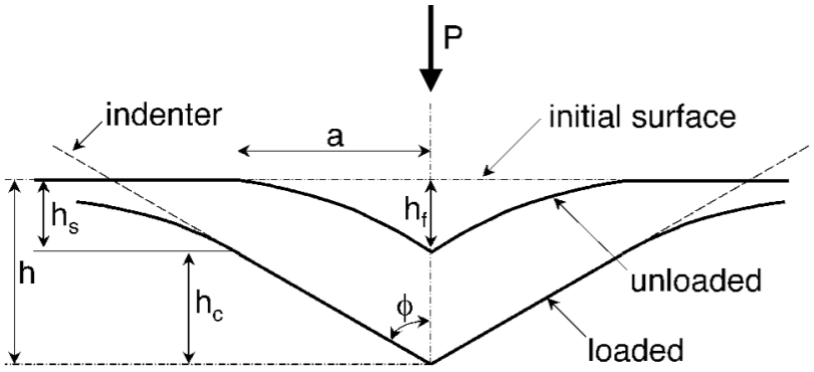


Figure 98: Schematic indentation unload diagram showing the parameters that characterise contact geometry. From [139].

Figure 98 shows the geometry of a fully loaded and an unloaded indentation, and the measurements of H and E are based on the unloading process shown in this figure. This models the Berkovich indenter as a conical indenter with an included half angle of 70.3° that gives the same relationship between depth and area as a Berkovich indenter. This method does not take into account the material that piles up around the indenter.

With the assumption that the pile-ups are negligible (which becomes less valid at higher temperatures), Oliver and Pharr's elastic model shows that the amount of sink-in, h_s, is given by:

$$h_s = \epsilon \frac{P_{max}}{S} \tag{39}$$

where ϵ is a constant that depends on the geometry of the indenter, and:

$$\epsilon = \frac{\pi(\pi - 2)}{\pi} \tag{40}$$

This term evaluates to 0.72 for a Berkovich tip but it is common practice to use a value of 0.75 since this has been shown to account for non-uniformities in the material response as the load is withdrawn [255]. This value was recommended by Oliver and Pharr and has since become the standard value used for analysis.

The following equation is used to approximate the vertical displacement of the contact edges, following from the geometry of figure 98 that the depth through which specimen-indenter contact is made is:

$$h_c = h_{max} - h_s \tag{41}$$

$$h_c = h_{max} - \epsilon \frac{P_{max}}{S} \tag{42}$$

It is this contact depth, h_c, that is used in the area function:

$$A = A(h_c) \tag{43}$$

As outlined in the previous chapter, the use of projected area rather than contact area is the best measure of hardness. The area function taken from nanoindentation experiments is already in this form, and so nanoindentation hardness could also be called "Meyer hardness".

4.3 Results

4.3.1 Load-Displacement Data

Both the hot and cold stages output data to the Micromaterials software. The data contains a load (mN), displacement (nm) and time (s) value for each data point. These data were corrected for thermal drift in the software then exported to Microsoft Excel for further analysis. All drift rates were kept below 0.2nm/s as ascertained in the thermal equalisation method outlined in Section 4.1.5.

4.3.2 Hardness-Temperature Behaviour at One Load

The first graph shows results from the first nanoindentation run carried out on the (001) planar surface of single crystal Mo. These hardness values were calculated from the nanoindentation data by the method outlined above with an average of 25 indentations taken. The temperature ranged from 20 to 900°C to a maximum load of 200mN, and on first inspection the hardness shows a sharp change in temperature dependence between 100 and 200°C. The indentation modulus was found to be fairly stable with temperature up to 600°C, at which point the values drop off from the literature values for the Young's modulus of single crystal Mo.

Figure 99 shows nine separate nanoindentations at 22°C to successively higher loads, demonstrating the stability between indentations. It is important to note here that although figure 30 and the following analysis describe the process for an idealised load displacement curve that goes up to a point at maximum load, in reality there is usually a significant additional depth at the maximum load. During analysis, the load and depth used in the necessary equations use the point at which the maximum load is first reached, and not the depth after a hold period.

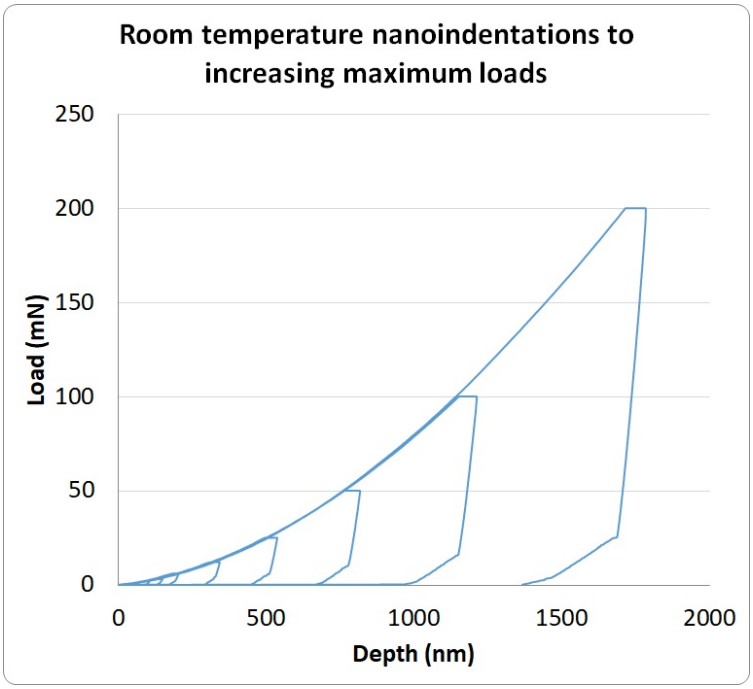


Figure 99: 9 nanoindentations at 22°C to successively higher loads.

The initial high temperature tests had some problems associated with creep - the hold period was not long enough to thoroughly establish the elevated creep behaviour [256], but this was not observed until after testing. The elevated temperature hardness values drop off as a result, as shown in figure 100. The modulus calculations imply that these hardness data are unaffected up to 600°C, but are affected at 700 and 800°C. This was adjusted in later runs.

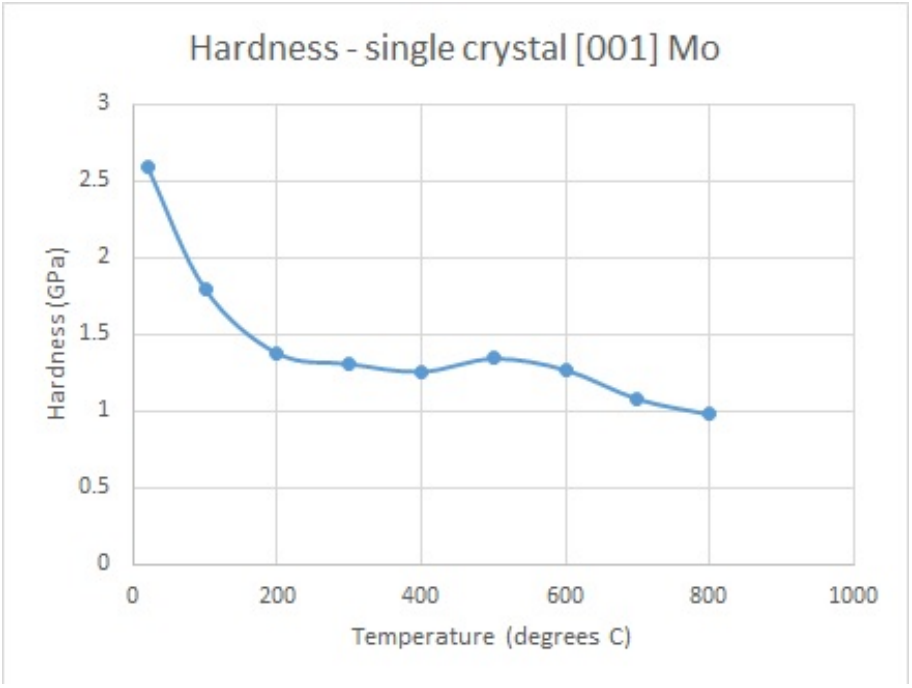


Figure 100: Hardness of a [001] single crystal Mo surface found by nanoindentation to a constant load of 200mN.

The reduced modulus results are shown in figure 101 and indentation modulus in figure 102.

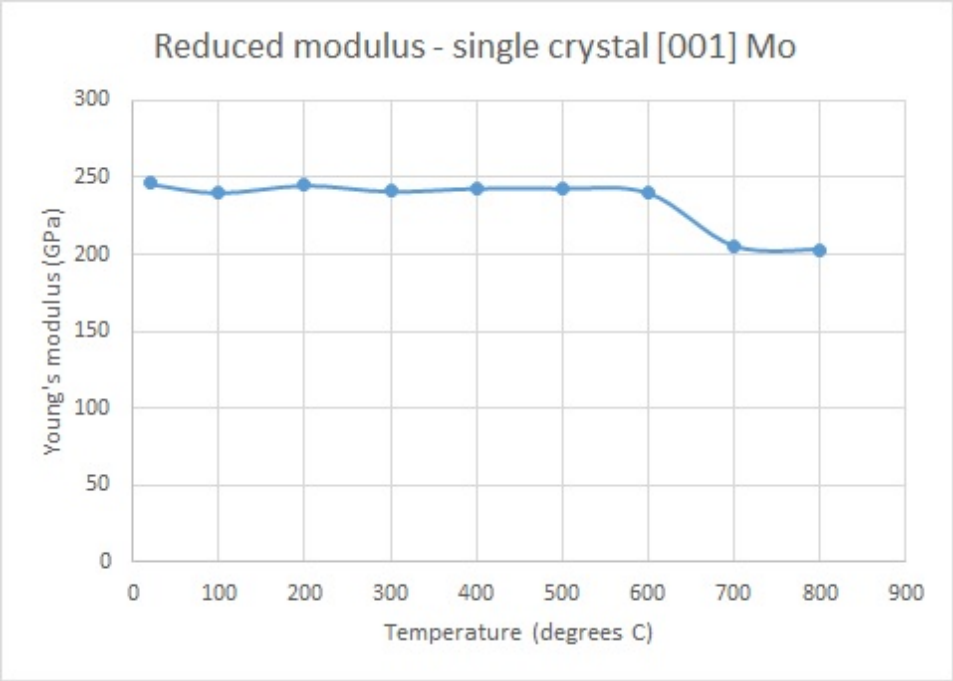


Figure 101: Reduced modulus of single crystal Mo found by nanoindentation. The drop in modulus at around 700°C confirmed the need for hold period adjustment.

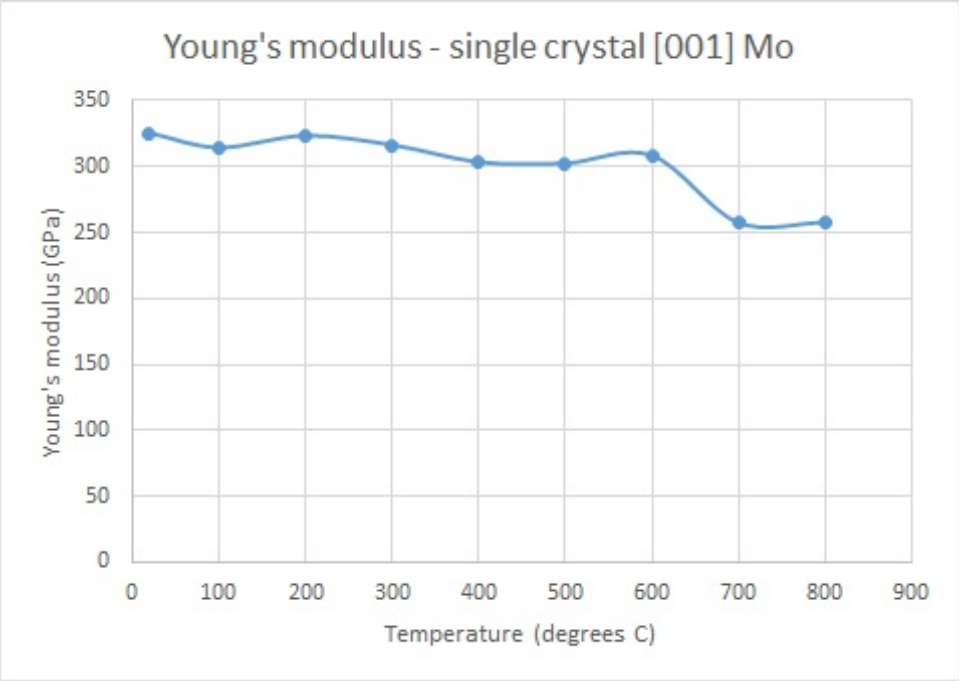


Figure 102: Indentation modulus of single crystal Mo found by nanoindentation. The drop in modulus at around 700°C confirms the need for hold period adjustment.

A second run of nanoindentations was carried out, as outlined in the next section, across a similar temperature range but also with varying loads (with either one or two indentations carried out at each load and temperature).

4.3.3 The Effect of Temperature on the Size Effect

In order to investigate the "size effect" related to indentation and its dependence on temperature in BCC molybdenum, indentations of varying load (2mN to 300mN) were made in the single crystal samples over a range of temperatures (-30 to 800°C). This led to a variety of maximum depths tested with the objective of comparing these results with the larger Vickers microindentations, which are well into the bulk depth range.

As a way of validating these results, this set of tests can be compared with the previous temperature vs hardness data in which 25 indentations were made at each temperature. The hardness values from the target load closest to the load used on page 114 (300mN as opposed to 200mN) is now plotted along with the above hardness points. The analysis was carried out in the same way. The samples were cut from the same single crystal and also had (100) plane faces, but were prepared at a different date.

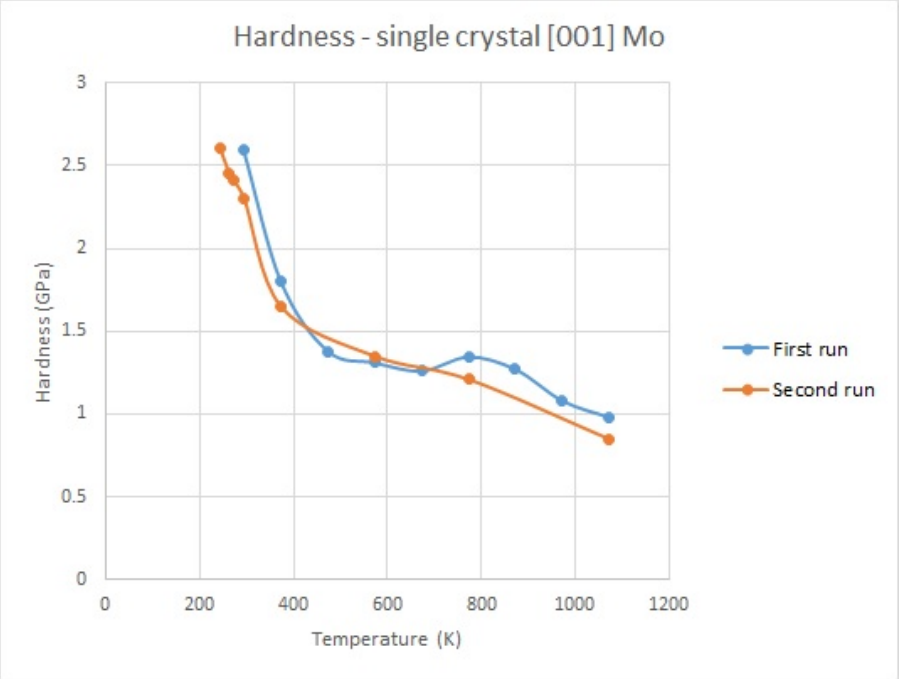


Figure 103: Hardness of single crystal Mo found by nanoindentation. Two sets of indentations carried out at different dates on separate single crystal Mo [100] plane faces. The first run was loaded to 200mN and the second run to 300mN.

The points lie very close to each other as shown in figure 103. The first run (to a 200mN target) shows points that are in general slightly higher, which may be explained by the lower load and associated lower depth. However, the closeness of these data series and the similarity of the maximum force used suggests good repeatability of this method. It should be noted here that as the sub zero work was carried out on the Peltier stage, different values for the area function and frame compliance were required (with the frame compliance again provided by

the manufacturer).

The hardness of single crystal Mo found by nanoindentation across the whole range of test temperatures and under different loads (corresponding to varied maximum depths) is shown in figure 104.

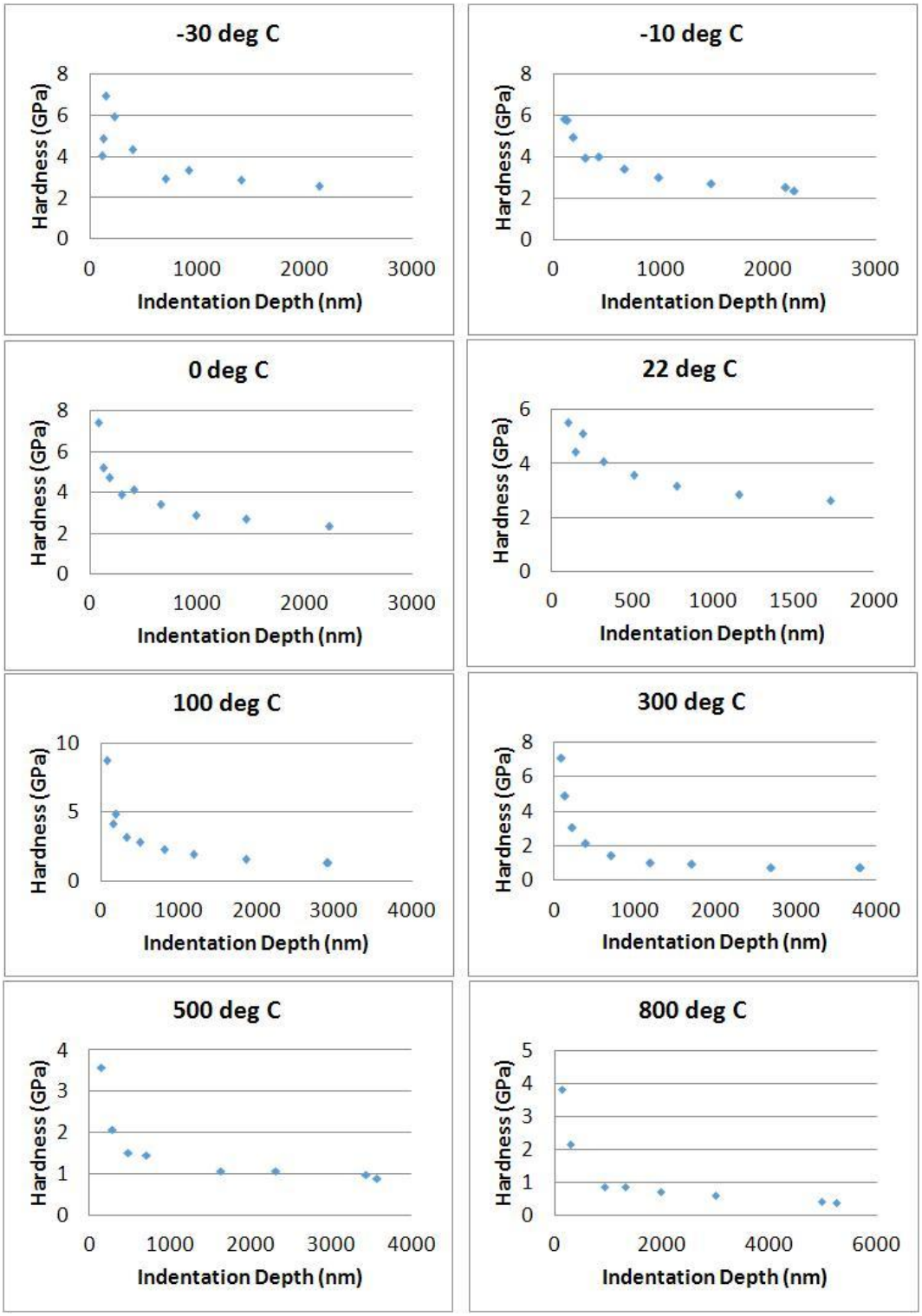


Figure 104: Hardness depth graphs collected at all temperatures. Hardness of single crystal Mo found by nanoindentation at different temperatures and under different loads (corresponding to different maximum depths). Note the low depth softening in the data points taken at -30°C.

It can be seen that there is a distinct dependence of hardness on the maximum depth of indentation, with the material harder at low loads.

4.3.4 Low Depth Softening

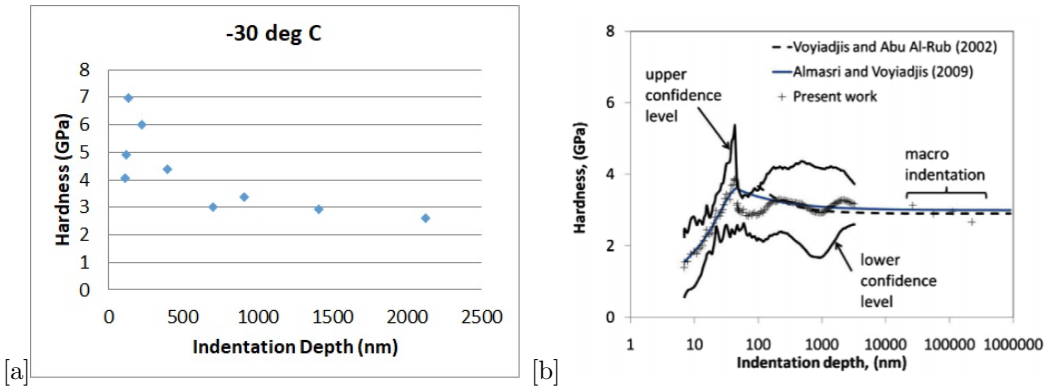


Figure 105: Softening in smaller indentations in Mo - hardness vs. indentation depth. [a] shows the results from this study at -30°C on single crystal Mo with a hardness peak at 136nm. [b] shows results from [167] with data from [168] and [165]. 99.95% pure polycrystalline Mo with a hardness peak at 43nm. An upper and lower 5% confidence level is included. All at room temperature.

The lowest temperature depth graph showed a hardness hump at 136nm (figure 105a), below which the hardness decreased. Although the other temperature graphs showed a small amount of scatter, none showed this low depth softening behaviour. Previous literature references have only demonstrated this effect in polycrystalline samples, due to dislocation-grain boundary interaction at characteristic length scales. The data for Brinell hardness indentation for Mo from three sources is shown in figure 105b - an average of multiple indentation trials - the upper and lower confidence levels give an indication of the scatter of experimental results from [168], [165] and [167].

There is a close correspondence between the graph form of the single crystal Berkovich data in this study and the polycrystalline Brinell data in the previous three studies. It is worth noting that the current data was collected at -30°C (whereas the literature values were all measured at room temperature), hence the higher hardness values at all depths.

Voyiadjis [167] attributed the increase in hardness from 10nm to approximately 43nm to the Hall-Petch effect - indentations much smaller than the grain size in polycrystalline Mo are effectively only indenting single crystal, but the hardness is expected to increase while the indenter begins compressing the grain near its boundary. No information was given on the grain size distribution.

This does not apply to the softening effect in low temperature single crystal Mo. In a study

on single crystal copper [257], a similar hardening effect was interpreted as jogs created during the indentation process, which can be removed by applying more load at higher indentation depths. Although a similar explanation may apply to Mo, further experimental work would be required to investigate this effect as no previous small-scale low temperature indentation has been carried out on Mo. Additionally, further testing may show that this is an anomaly.

4.3.5 Strain Gradient Plasticity Model

The geometry of sharp indentations is the same at all depths, and so indentation strain should be independent of indentation size for the same indenter angle. However, indentations on smaller scales show size effects (below approximately 1 micron [184]), with increasing hardness as indentation size decreases. This is usually explained in terms of increased geometrically necessary dislocation (GND) densities at small indentation sizes, which causes higher strains. The density of GNDs is related to the curvature of the crystal.

Nix and Gao [107] found that the indentation size effect for crystalline metals can be accurately modelled using the concept of GNDs, also taking into account the density of statistically stored dislocations (SSDs), which are created by homogeneous strain and do not vary with indentation depth. SSDs and GNDs both contribute to the flow stress.

In Nix and Gao's model, the assumption is made that indentations are accommodated by circular loops of GNDs with a Burgers vector b normal to the surface of a specimen, as shown in figure 106. Two further assumptions are also made - that the total dislocation density is equal to the sum of GNDs and SSDs, and that that the GNDs are constrained to reside within a hemispherical volume, where the radius of the volume is equal to the radius of contact of the indenter in the surface [258].

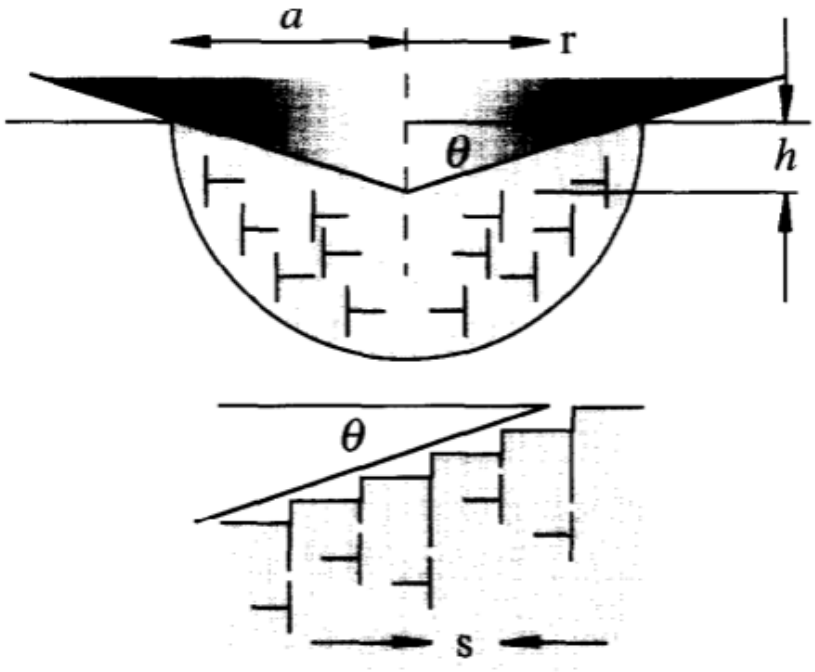


Figure 106: Geometrically necessary dislocations created by a rigid conical indentation. The dislocation structure is idealised as circular dislocation loops with Burgers vectors normal to the plane of the surface. As the indenter is forced into the surface of a single crystal, geometrically necessary dislocations are required to account for the permanent shape change at the surface. From [107].

Taking into account both GNDs and SSDs, the following expression was obtained:

$$\frac{H}{H_0} = \sqrt{1 + \frac{\rho_{SSD}}{\rho_{GND}}} \tag{44}$$

leading to

$$\frac{H}{H_0} = \sqrt{1 + \frac{h^*}{h}} \tag{45}$$

where H is the hardness of an indentation of depth h, H_0 is the hardness of a bulk indentation (measured using microindentation) that would arise from the SSDs alone, in the absence of GNDs, and h^* is a characteristic length scale that also depends on H_0. This is the characteristic length at which the hardness starts to increase, typically of the order of 1 micron [258].

This calculation requires the incorporation of 'bulk' microhardness tests. Figures 107 and 108 show the continuity between Berkovich nanoindentation data and Vickers microhardness data, with microhardness shown in black.

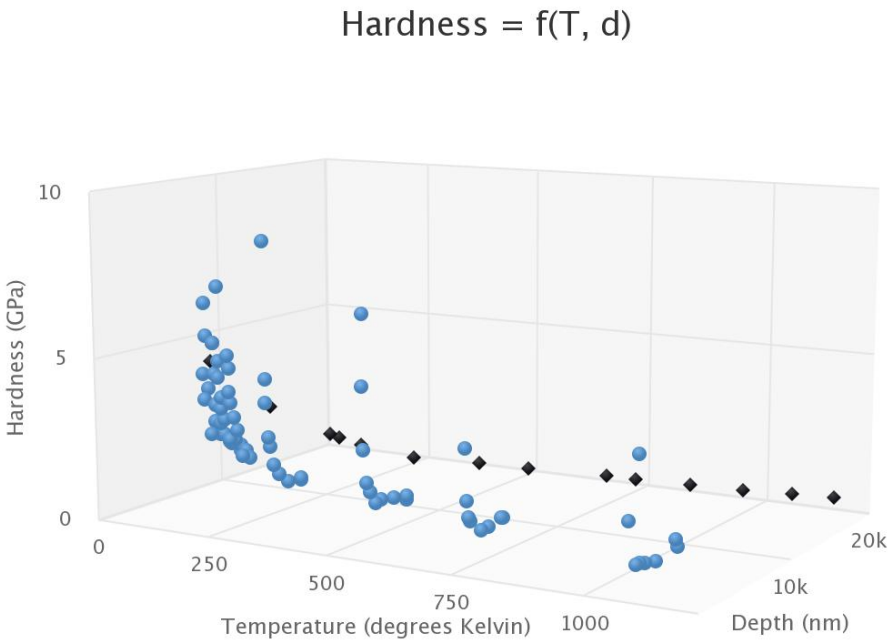


Figure 107: 3d scatter plot - Berkovich nanoindentation data and Vickers microhardness data, with nanoindentation shown in blue and microhardness shown in black.

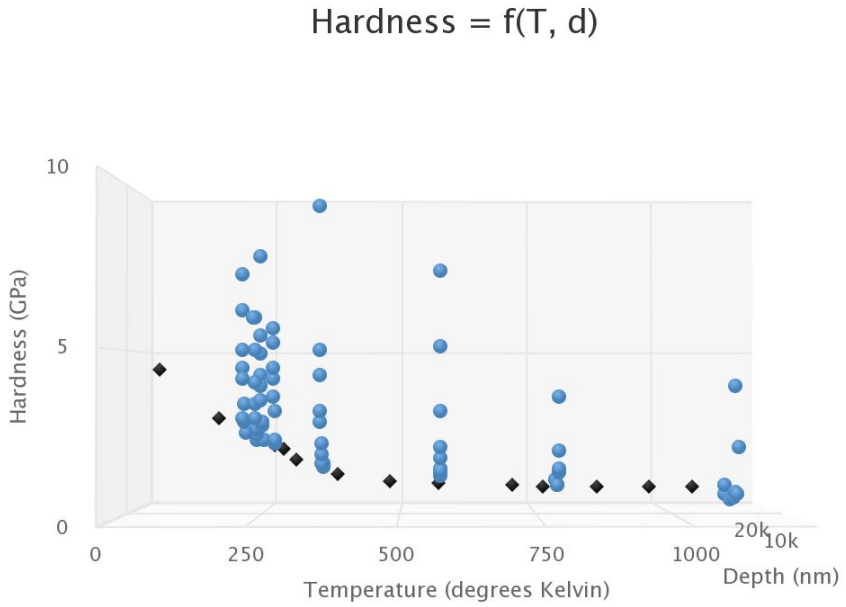


Figure 108: 3d scatter plot orientated with hardness as the vertical axis against temperature as the horizontal - Berkovich nanoindentation data and Vickers microhardness data, with nanoindentation shown in blue and microhardness shown in black.

This characteristic form for the depth dependence of the hardness shown in equation 45 suggests that the square of (hardness/bulk hardness) should be plotted against the reciprocal of the depth of indentation. When the data are plotted in this way a straight line is found, the intercept of which is 1 and the slope of which is h*.

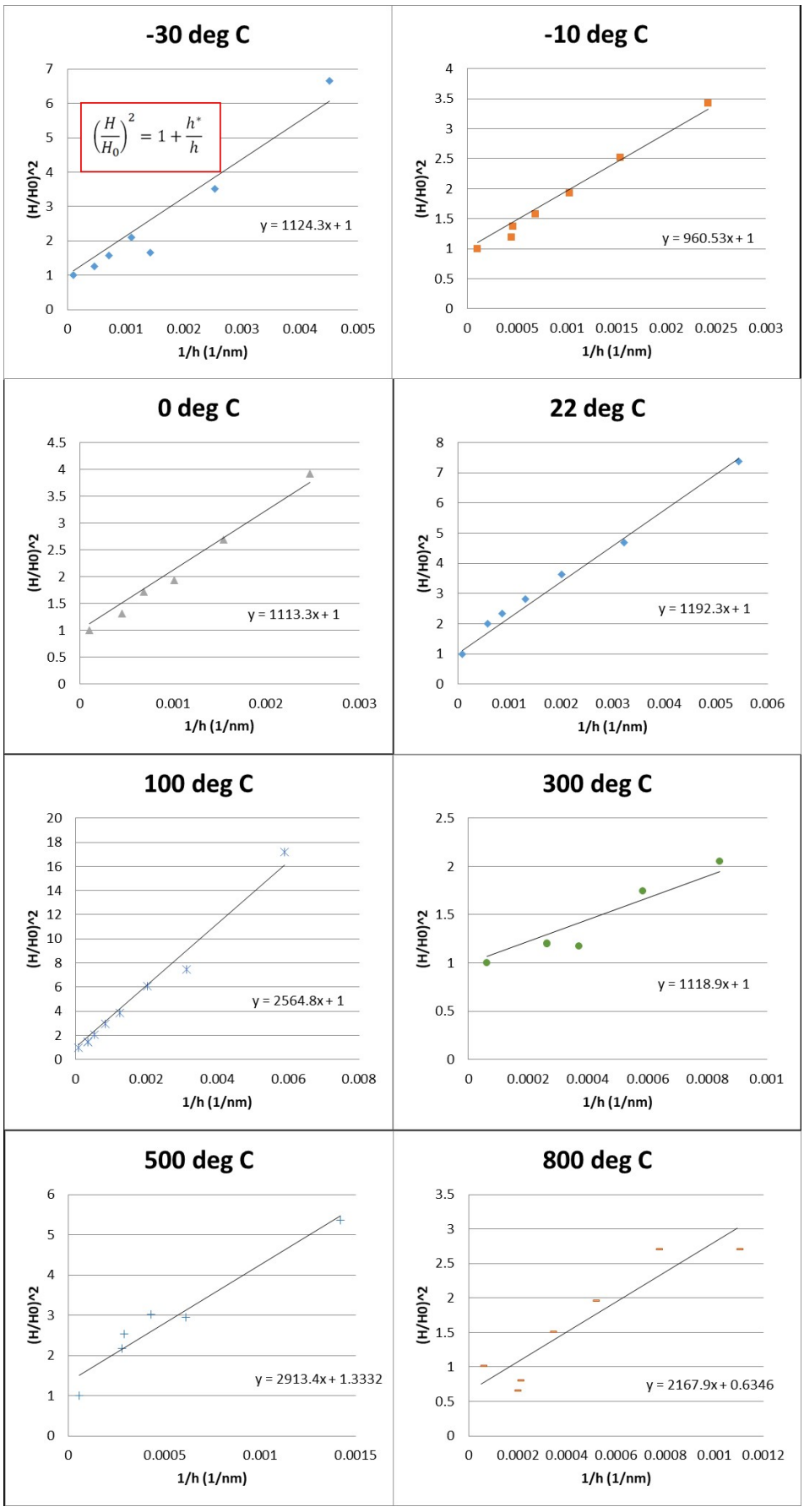


Figure 109: Graphs of $(H/H_0)^2$ against 1/h with the data measured at each temperature. The intercept is set to 1, giving a gradient equal to h*.

Figure 109 shows graphs of $(H/H_0)^2$ against 1/h with the data measured at each temperature. The intercept is set to 1, giving a gradient equal to h*. The bulk hardness value at each temperature was also included, measured using a Vickers tip. These results were taken from the previous chapter on microhardness testing (with a load of 4.9N), using the values for the corresponding temperature. The values are shown in table 3. When no test was made at the exact temperature required, an average of the two closest values was taken. The area-to-depth ratio of Vickers and Berkovich are nominally the same, so Vickers should not require a different model.

Table 3: Bulk Vickers hardness values reported in the previous chapter on microhardness testing. Load of 4.9N.

T (°C)	Bulk hardness (GPa)
-30	2.33
-10	2.17
0	2.11
22	1.88
100	1.18
300	0.76
500	0.64
800	0.55

Indentations of depth less than approximately 100nm do not lie on this trend (for all temperatures), presumably because the shape of the indenter was not self-similar at smaller depths due to blunting of the Berkovich tip (and self-similar geometry is assumed in the Nix-Gao model). They were consequently discarded.

The quantities H_0 and h^* are not independent. They are related through:

$$h^* = \frac{81}{2} b\alpha^2 tan^2\theta \left(\frac{\mu}{H_0}\right)^2 \tag{46}$$

α is a constant to be taken as 0.5 at all temperatures [107]. μ is shear modulus, the literature values for which were used as described in Section 1.2.4. b is the Burgers vector, which is 0.273nm for Mo. θ is the internal indenter angle.

A check of self-consistency can be made by computing the expected value of h^* from the measured values of H_0 using the model and the known shape of the indenter.

The geometry of figure 106 gives:

$$tan\theta = \frac{h}{a} \tag{47}$$

and for a Berkovich indenter:

$$A_c = 24.5h^2 = \pi a^2 \tag{48}$$

Combining these equations gives:

$$tan\theta = \frac{h}{a} = \sqrt{\frac{\pi}{24.5}} = 0.358 \tag{49}$$

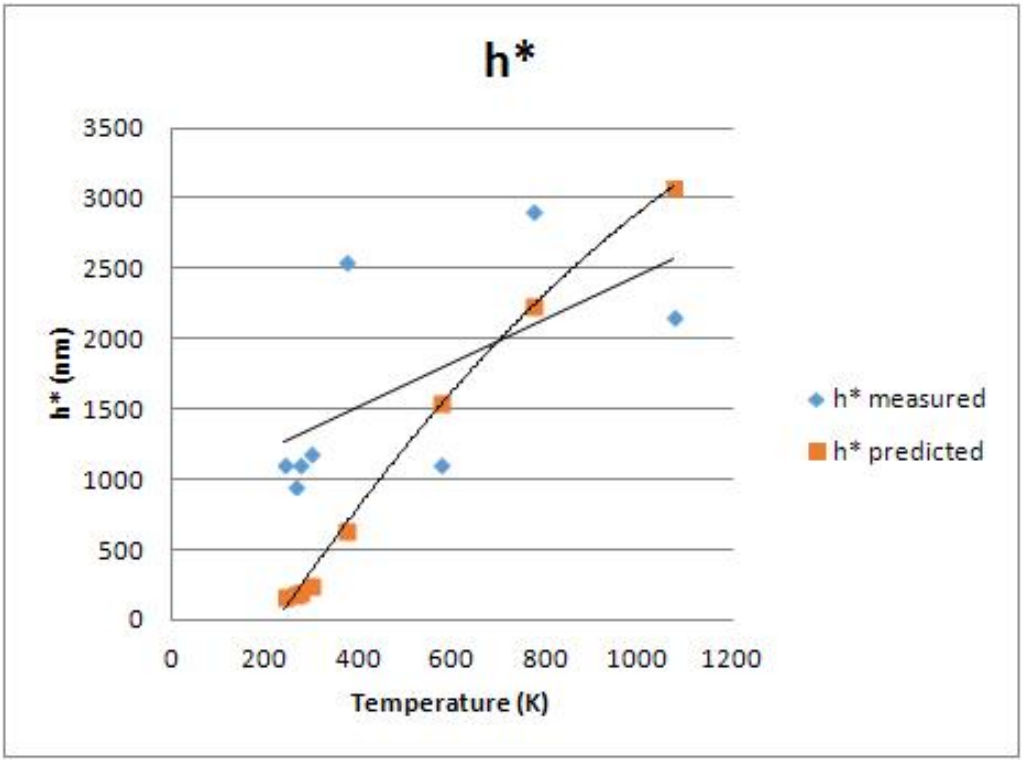


Figure 110: The predicted values of h* for the indentation data taken at all temperatures using equation 46

Figure 110 shows the predicted values of h* for the indentation data taken at all temperatures using equation 46. This shows that the depth below which the size effect becomes apparent (the length scale) increases with increasing temperature. The measured length scale increased from approximately 1 micron at room temperature up to approximately 2.5 microns at 1100K. Figure 111 shows the data from figure 109 plotted with the values of $(\frac{H}{H_0})^2$ calculated from the predicted values of h^*. There is clear divergence between the two lines at all temperatures below 300°C. Figure 112 shows the predicted hardness-depth relationship that results from this, along with the measured values of hardness at each depth.

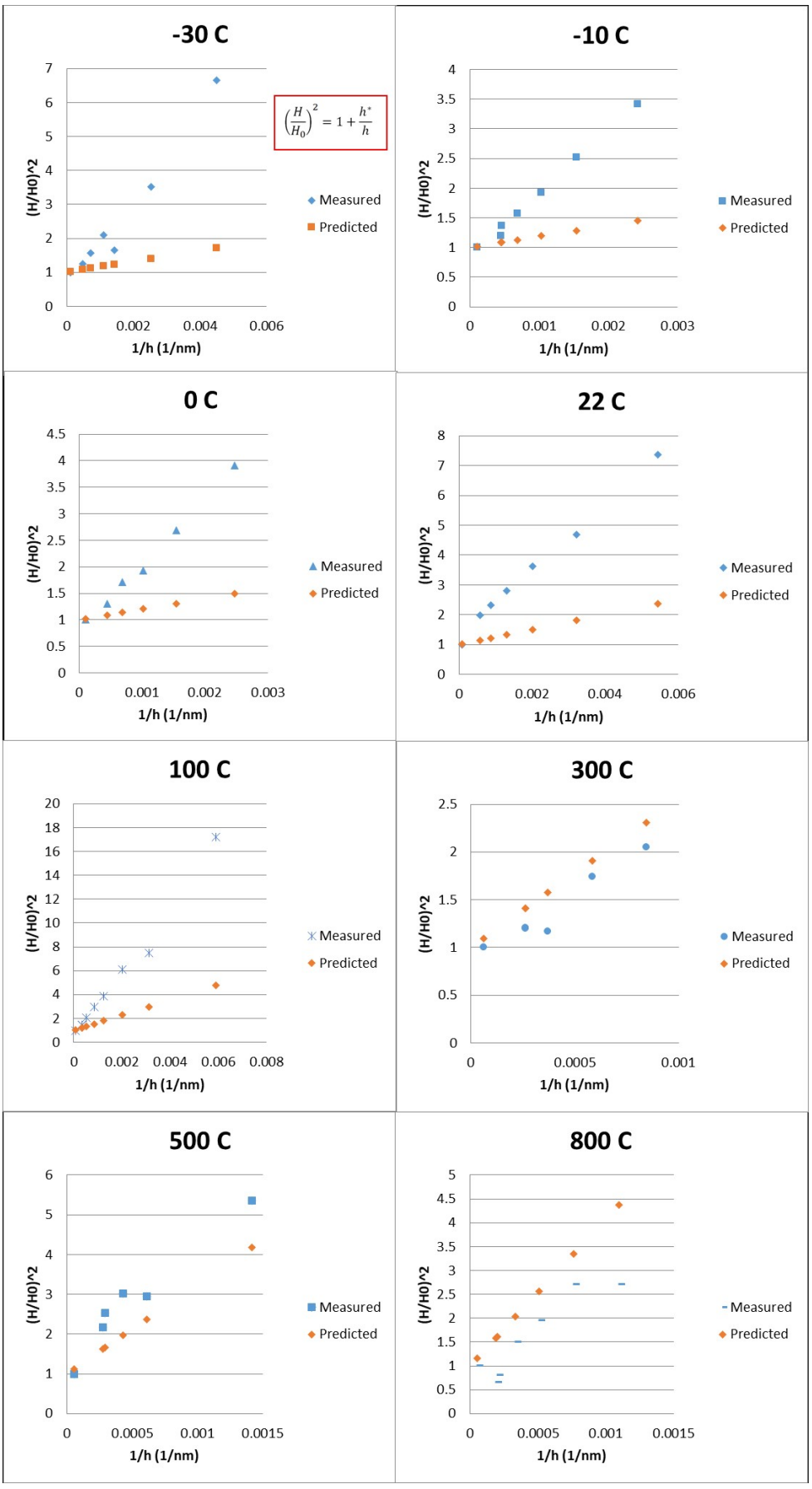


Figure 111: The data from figure 109 plotted with the values of $(\frac{H}{H_0})^2$ calculated from the predicted values of h^*

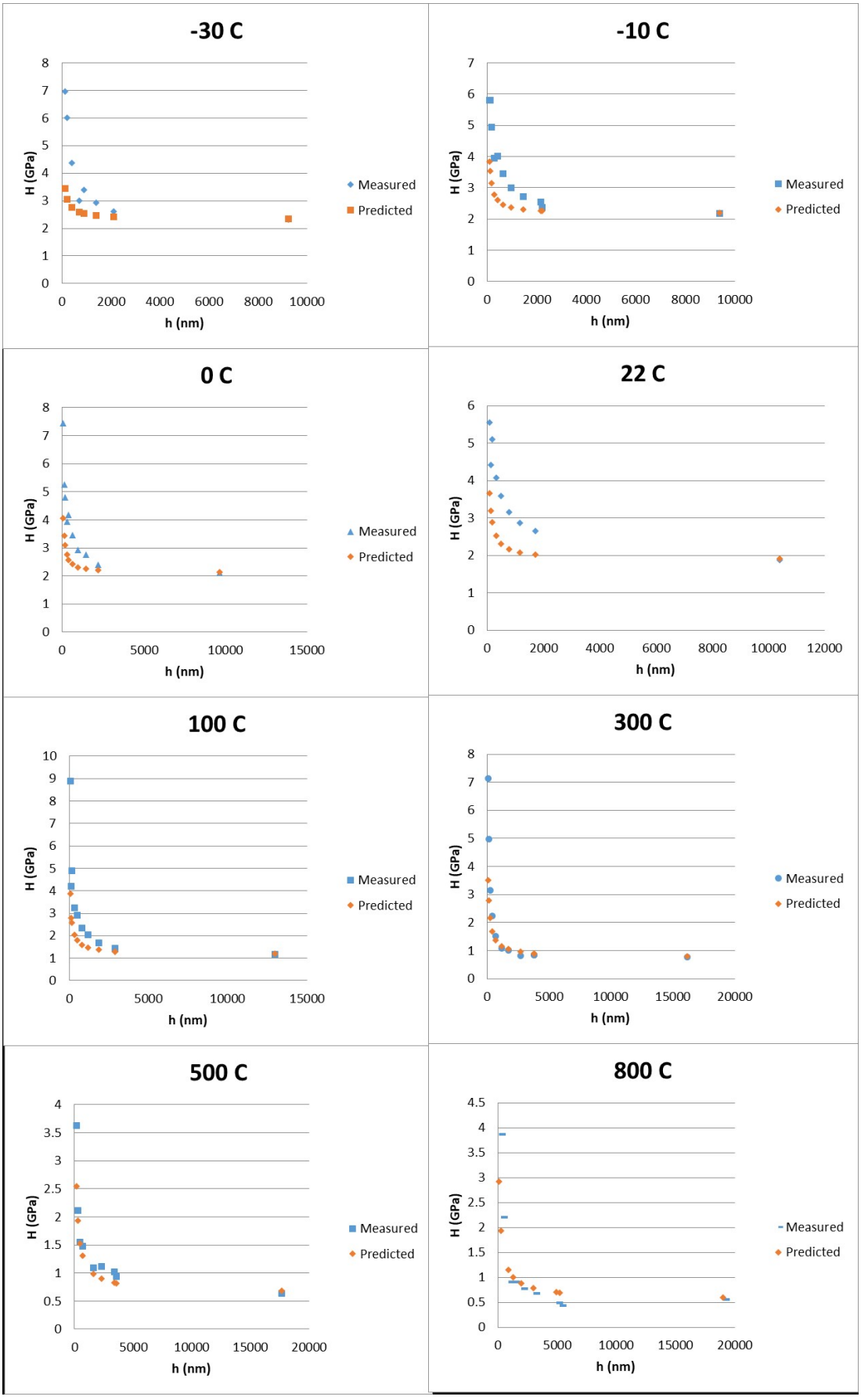


Figure 112: The predicted hardness-depth relationship that results from the prediction of h^*, along with the measured values of hardness at each depth.

The trendline fitted to the predicted values of h^* in figure 110 are in reasonably good agreement with the measured values above a temperature of 600K but deviate below. There is some scatter in the points, but the two data sets are of similar values above 600K, diverging below. This suggests the model in this form is potentially unsuitable for the low temperature indentation and associated change in mechanical properties of molybdenum. The model was originally applied to the results of FCC tests [259], which show no such change in mechanical properties.

4.3.6 Power Law Model

As well as the above model of the dependence of hardness on depth (equation 45), the power law dependence of hardness on indentation depth is often used in the literature for the characterisation of the indentation size effect [260, 261, 262]. This model is based on curve fitting rather than a physical interpretation for its key parameters (which is the case with the Nix and Gao model), but it may help to explain the less satisfactory fit of the Nix and Gao model to tests at lower temepratures, as will be covered in this section. The following equation is the basis of the power law model:

$$H = k(\frac{h}{h_0})^n \tag{50}$$

where H is hardness, h is indentation depth, h_0 is a length scale parameter and k and n are constants. The dependence of hardness on depth in logarithmic coordinates for the Mo nanoindentation tests at all temperatures is shown in figure 113.

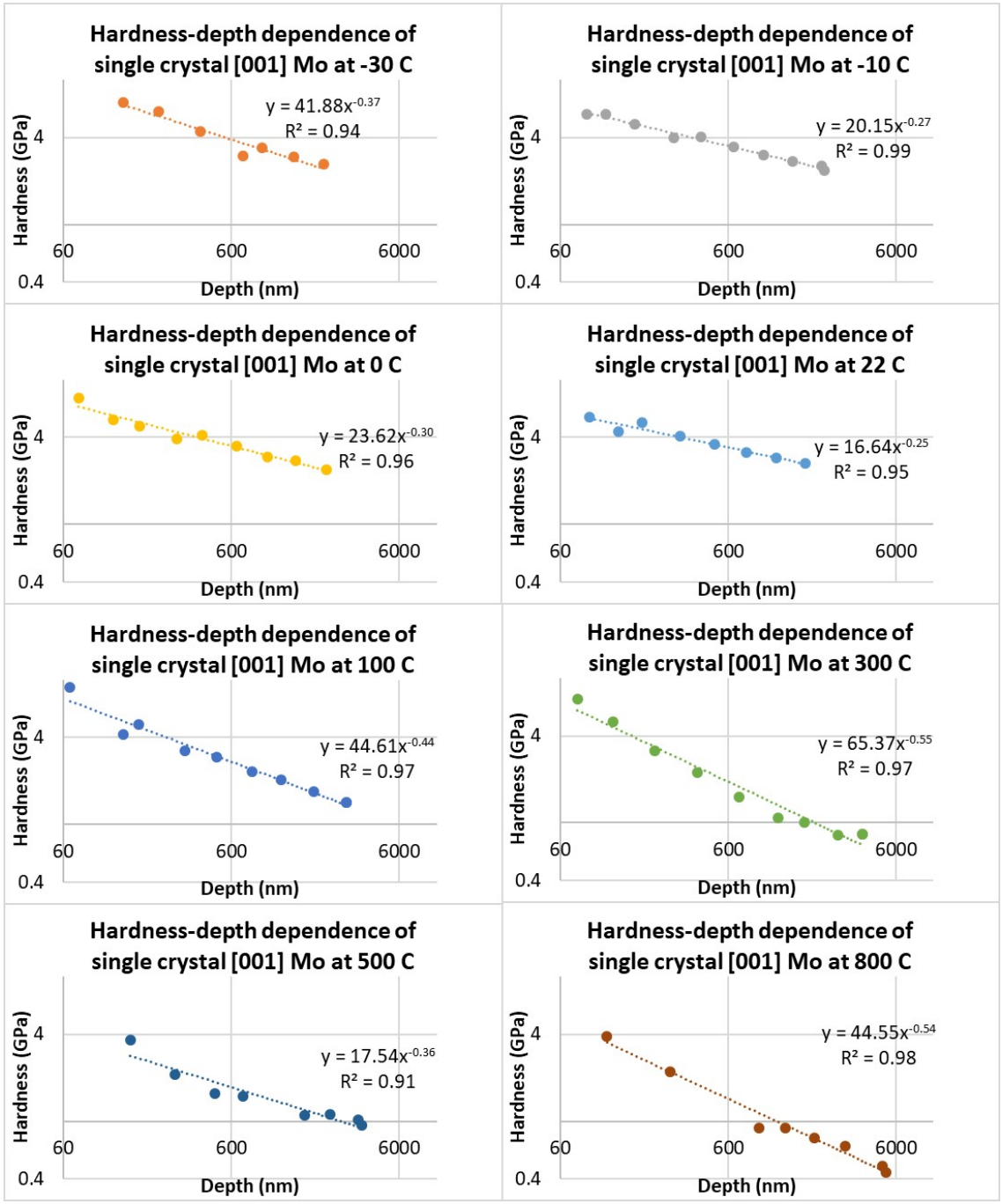


Figure 113: Hardness depth graphs showing all temperatures. The lowest two depths for -30°C were not included.

It is apparent from the high R^2 values ($R^2 > 0.91$) in this figure that equation 50 is satisfied, and the values of the exponent n are shown in figure 114. This graph of exponent vs temperature shows a more negative exponent with increasing temperature. The error bars are taken as a percentage deviation from the R-squared value of the best line fit. The line of best fit was plotted using Excel's linear trendline function.

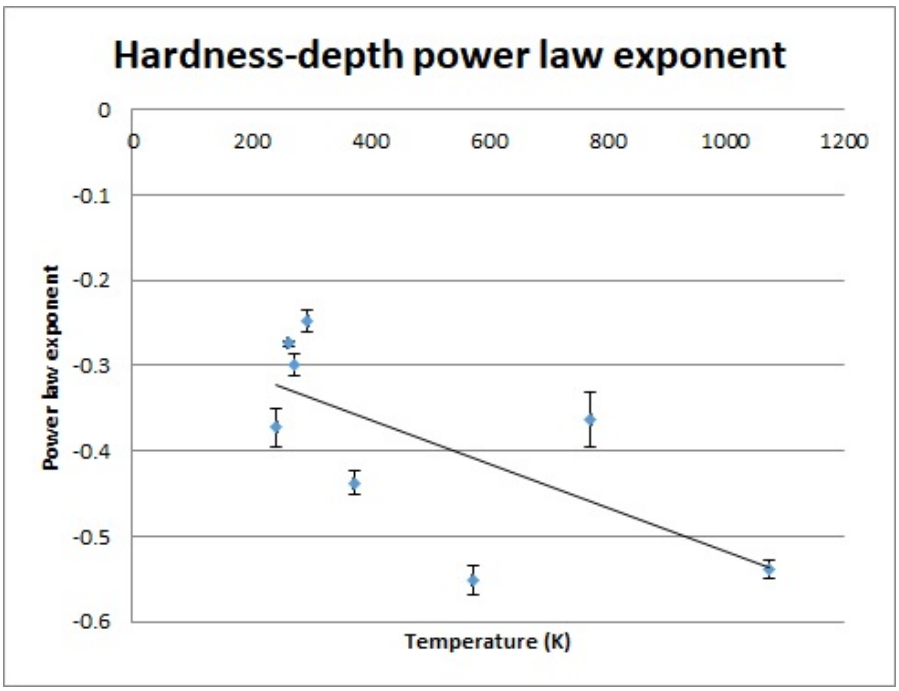


Figure 114: The slope of the line of best fit (exponent) for the size dependence of the nanoindentation data shown in figure 113 as a function of temperature.

As a simple check of the reliability of these results, Milman's indentation study on single crystal Mo gave a power law exponent of -0.29 at room temperature [260], and a room temperature exponent of -0.25 was found in this study.

Figure 45 shows the slope of the line of best fit (exponent) for the size dependence of W and Nb from [192] and Mo from [209] as a function of T_{test}/T_K. Also shown are the power law exponents obtained for the flow stress measured at 5% strain for the same materials. The critical temperatures for W, Mo and Nb are 800 K, 400 K and 350 K, respectively.

Figure 46 shows a later study by the same research group that indicates the size effect behaviour of BCC metals approaches that of FCC metals towards the transition temperature. The graph shows the slope of the line of best fit (exponent) for the size dependence of W, Mo, Ta and Nb vs normalised test temperature T_{test}/T_K. (Filled squares = [001]-oriented pillars taken from [209], open squares = [235]-oriented pillars taken from [213] and open triangles = [110]-oriented Mo pillars from [210].) For a T_{test}/T_K of 1, the Mo pillars show the same size dependence as FCC pillars. [210]

Once the exponent is plotted against the test temperature normalised by the knee temperature, the points show close adherence to the pattern published by Schneider et al. [210] for the [001] micropillar compression of BCC metals, decreasing to a value of -0.54 when $T=T_K$, the knee temperature (with Schneider's values approaching -0.6 at this point). This is demonstrated in figure 115 with Schneider's data shown by the red line. The point at 500°C appears to be an anomaly.

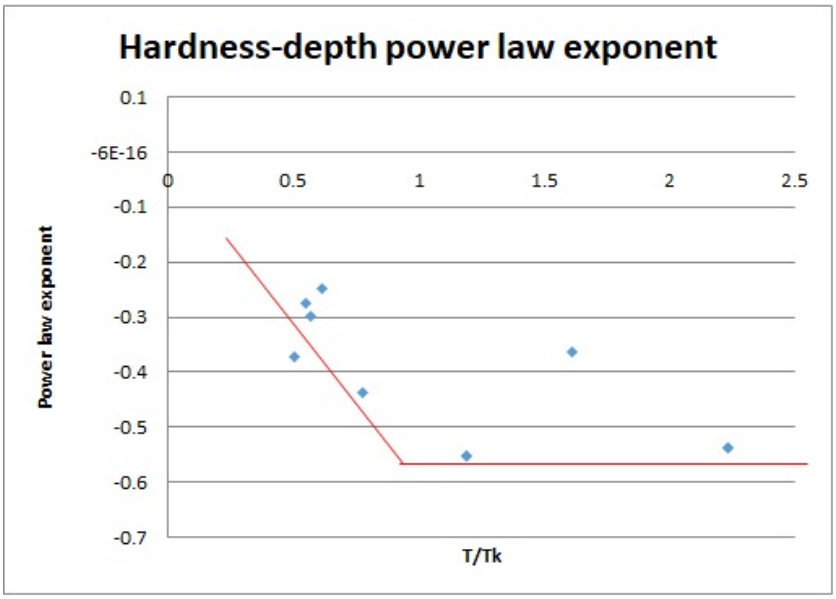


Figure 115: The slope of the line of best fit (exponent) for the size dependence of the nanoindentation data shown in figure 113 as a function of temperature normalised by the knee temperature. The power law exponent appears to decrease to the FCC value of approximately -0.58 stated by Schneider as the temperature increases to the knee temperature of 480K. Schneider's data is shown by the red line [210].

4.3.7 Elastic Recovery

As the test temperature increases, so does the maximum indenter penetration depth; elastic recovery decreases and the crystal tends further towards plastic behaviour. The elastic recovery calculated in this section is the same parameter as discussed in Section 3.5.4. The measurement technique has to be altered as nanoindentations are too small to measure accurately in the SEM, even with tilt and high contrast. However, as the indentation is instrumented, the relevant depths can be read from the load-displacement graph.

The loaded depth was taken as that after the hold period, and the unloaded depth as the value where the unloading line would cross the displacement axis if the line was extrapolated (as the indenter used gave a small kink at the end of each unloading period as it came out of contact with the sample surface), shown in figure 116.

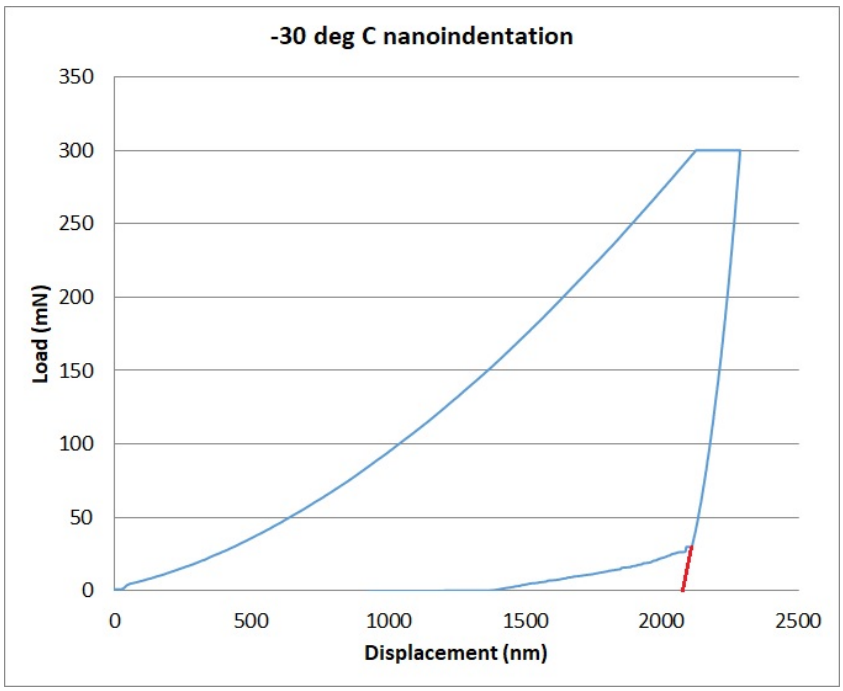


Figure 116: Unloading curve extrapolated to the x-axis to cut off the 'knee' left by this particular indenter.

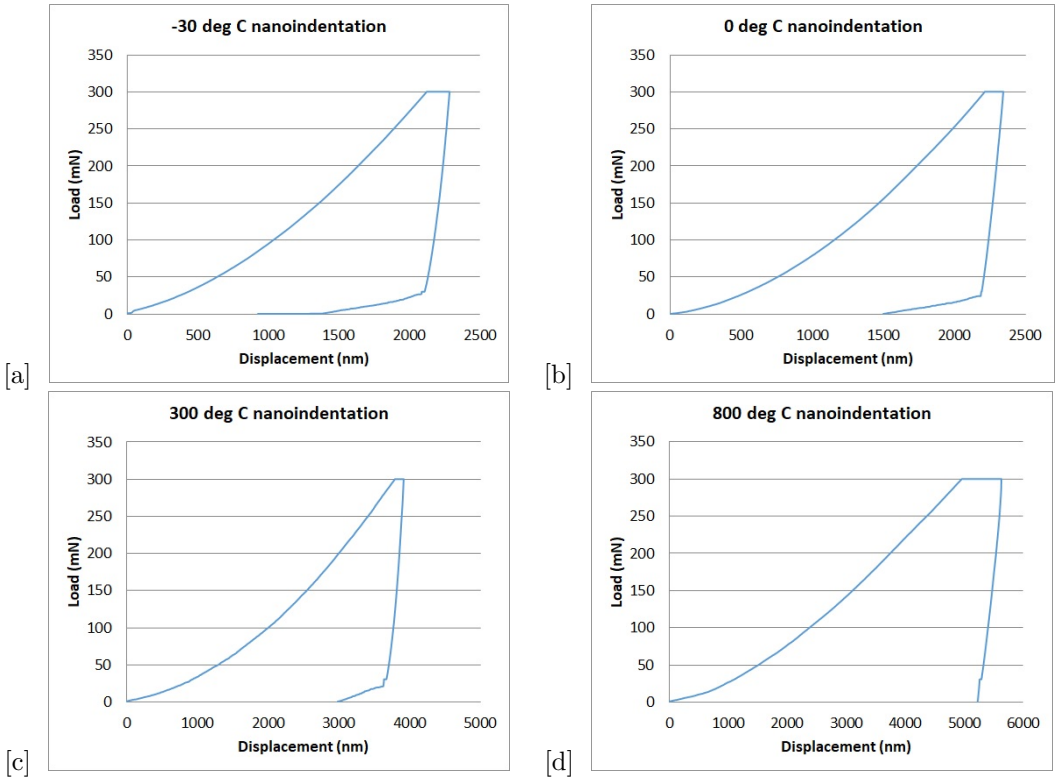


Figure 117: Single crystal Mo nanoindentations at -31, 0, 300 and 800°C.

The series of load-displacement curves (maximum load 300mN) in figure 117 suggest a change in the elastic recovery upon changing sample temperature as the unloading section becomes slightly more vertical. A perfectly elastic material would follow the loading curve

when unloaded; a perfectly plastic material would have a completely vertical unload. Similar curves by Wang [118] on GaAs are shown in figure 27.

More significant elastic recovery is observed during the unloading curves at lower temperatures - this can be confirmed by measuring the ratio of fully loaded to recovered indentation height. Values of this ratio (as a measure of elastic recovery) over the range of test temperatures are shown in figure 118. The depth ratio on this graph decreases with temperature, with the gradient becoming shallower at approximately 450K. Equivalently, the 'plasticity characteristic' is shown to increase after approximately 450K, which is close to the knee temperature T_K.

The curves for Mo are not as extreme as those for GaAs in figure 27 below T_K, as even a brittle BCC metal shows a higher plasticity characteristic than a brittle ceramic.

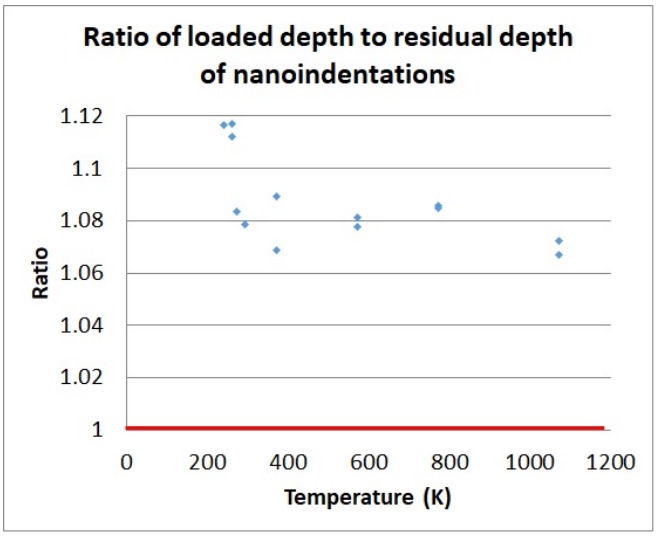


Figure 118: Elastic recovery across all temperatures - $\frac{loadeddepth}{unloadeddepth}$. Increased plasticity characteristic after T_K shown by the drop in elastic recovery.

4.4 Discussion

The strain gradient plasticity model developed by Nix and Gao suggests that the hardness of a material should not depend strongly on the depth of indentation if the material is intrinsically hard. Specifically, large values of H_0 would cause h^* to be very small (equation 46) and this would cause the hardness to depend less strongly on depth at a given depth of indentation [107]. This observation alone would suggest that the dramatically increased hardness at low temperature below the knee in Mo would lead to a decreased size effect.

Strain gradient plasticity models apply to any testing geometry (such as bending of small beams or torsion of fine wires) in which a plastic strain gradient is produced - not only to indentation testing [258]. This would be helpful for understanding the size effect of microcantilever bend tests outlined in Section 6 if a range of cantilever sizes were to be manufactured in a future study.

Finding the power law fit of each hardness-depth graph was more successful in showing the change in size effect with temperature for Mo. As previously explained, the ratio of test temperature to knee temperature is a measure of the thermal activation of screw dislocations - the higher the ratio, the higher the thermal activation and so the more mobile the dislocations. At the knee temperature, screw and edge dislocations have equal mobility in BCC metals. Previous studies on FCC metals, which also have equal screw and edge mobilities, found they had a power law exponent of around -0.6 [192]. As also found by Schneider et al., this study has found the depth dependence approaches FCC behaviour towards the knee [192, 210].

The hardness-depth power law exponent in figure 115 becomes more pronounced with increasing temperature up to a ratio of test temperature to critical temperature of approximately 0.75 - 1.1, indicating the depth dependence increases with temperature. In contrast, above this point, the exponent values for 300 and 800 °C are almost equal (-0.55 and -0.54). These results show a very similar trend to those collected by micropillar compression by Schneider (figures 45 and 46). This suggests that the temperature dependence of the size effect in both cases is controlled by a similar mechanism. This graph is particularly useful for calculating the dependence of size effect on temperature by looking at the power law exponent of the hardness-depth graph at each test temperature, allowing a comparison with the micropillar compression tests by Schneider.

The thermal activation of the kink-pair mechanism appears to play a role in the temperature-dependence of the indentation size effect in molybdenum. Below the critical (or 'knee') temperature T_K, the power law exponent smaller than that for FCC metals suggests that the screw dislocation mobility has an influence on BCC size dependence. As with Schneider's micropillar testing, the indentation hardness can be assumed to comprise of a lattice resistance component and a component subject to obstacle controlled flow, which undergoes the same size effect as FCC metals.

As screw dislocations overcome the lattice resistance assisted by thermal activation, the lattice resistance component has a strong temperature dependence (as seen by testing a sample at one load - 300mN - over a range of temperatures). Above T_K, the lattice resistance component is negligible (this is the same athermal region seen in all bulk BCC hardness data above T_K), and so the hardness is only controlled by obstacle controlled flow. The size effect now approaches that of FCC metals. Below T_K, the lattice resistance is more significant as temperature decreases, and increasingly begins to reduce the impact of the size effect [210].

The similarity between the indentation size effect in this study and that found by Schneider using micropillar compression (taken from power law fitting to the hardness-size graphs at each temperature) suggests that the size effect in both indentation and micromechanical deformation in molybdenum is controlled by similar mechanisms. The increase of the size effect to the FCC

level as the knee temperature is approached strongly suggests that the size effect in molybdenum is controlled by the activation of the kink-pair mechanism. Thermal activation increases kink-pair mobility, but the higher strain gradients under successively smaller indentations may also play a role in kink-pair mobility.

The strain gradient plasticity model by Nix and Gao does not take account of the knee in lattice resistance in BCC metals, hence the model becomes less suitable at lower temperatures (demonstrated by the difference in predicted and measured hardness values). Without knowing the physical basis behind the 'characteristic length scale' in the strain gradient plasticity model, no adjustments can be made to the fit below the knee temperature, where the predicted and measured hardness values diverge.

The physical basis and the size of this length scale are crucial for accounting for size effects in the plastic behaviour of all metals at small scales. Considering the data in this chapter, the physical interpretation of the length scale may have some bearing on why the "predicted" and "measured" values diverge from each other in the low temperature regime, below the knee temperature T_K. However, the underlying physics of the length scale is ambiguous [263].

It has been observed [107, 264] that the length scale h^* is proportional to the dislocation mean free path, suggesting that the length scale is not a fixed material parameter but changes with the deformation of the microstructure. This is due to the variation of the mean free path with dislocation nucleation, temperature and strain rate effects [165]. However, for most metals (including BCC metals), the yield stress increases with the strain rate and decreases with increasing temperature. This causes the length scale to decrease with increasing strain rate and decreasing temperature.

The length scale, governing flow against the resistance of the lattice, is likely to be an intrinsic property in an indentation test. It is controlled by the sample's microstructure, as there is no limit to the sample size that is seen in a micromechanical test. This length scale may be related to the length scale of a stable kink segment above the knee temperature; the critical span between two kinks decreases with increasing stress. The length scale might have a different physical basis below the knee temperature, based on the spacing of obstacles to edge dislocation movement (such as locks or jogs). This might suggest that two different forms of the Nix-Gao model may be necessary above and below the knee temperature.

The increased plasticity characteristic shown by the decrease in elastic recovery in figure 118 is caused by the thermal activation of the kink-pair mechanism, resulting in a decreased lattice resistance and a tendency towards greater dislocation movement.

Although the indentation work was carried out on many different instruments (furnace-controlled microhardness tester, hot air temperature control, liquid nitrogen, a hot stage nanoindenter and a cold stage nanoindenter), the microhardness data did fit the depth trend well, as shown by the smooth curve in figures 108 and 112. Most variables were kept as constant as possible (BCC deformation is very dependent on rate and although the rate of microhardness indentation could not be controlled, the rate of nanoindentation could be and was matched as closely to the microhardness from a timed microhardness indentation). The tip geometries used, Vickers and Berkovich, should provide similar total strains in the material when testing. Both tips exhibit the same projected contact area with respect to the penetration depth into the sample.

5 Four Point Bend Testing

Mechanical testing of a sample by bending is a commonly used and simple testing technique as it leads to the fast acquisition of load and displacement data for a given sample. During bend testing a specimen of known geometry is bent about three or four fixed points. Load and displacement data are recorded. Four point bend testing has the advantage over three points due to the region of constant stress between the inner rollers - a larger length of the specimen is in a pure bending state as opposed to a peak stress point, making analysis easier and generally more accurate.

Static four-point bend tests were carried out using an "Instron" loading rig, model 3366, in which a loading ram compresses a molybdenum jig, putting a matchstick specimen in a four point bending configuration. Figure 119 shows the experimental setup: a loading ram (i) compressing a molybdenum jig (ii) which contains the molybdenum matchstick (iv) sitting on four molybdenum rollers (iii).

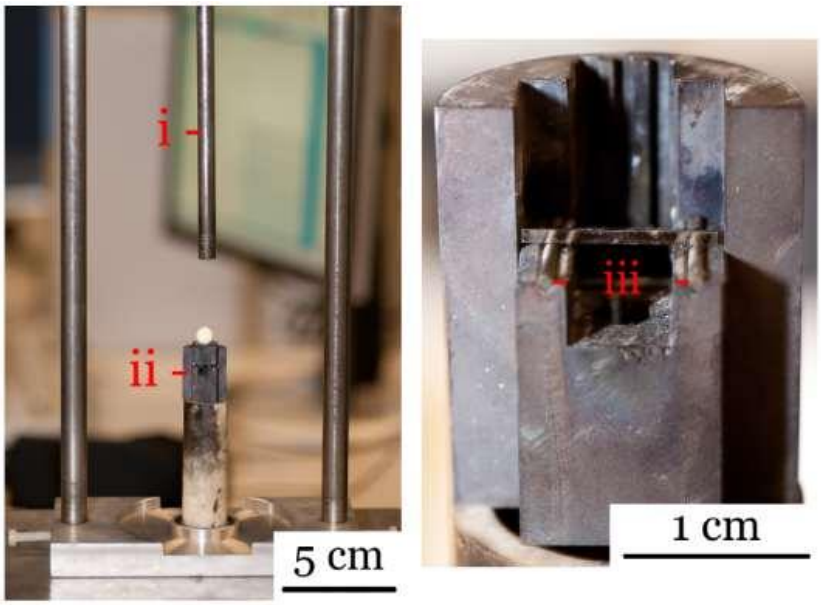


Figure 119: Instron four point bend rig - loading arm (i), Mo rig (ii) and support rollers (iii) magnified from (ii). From [95].

This is the same rig as previously used in studies on molybdenum [94, 96] and tungsten [39, 95]. The geometry of the specimen and rollers is shown in figure 120. The bottom surface is in tension and there is a constant bending moment across the inner span, L_2, with no transverse shear stresses. The top surface is in compression.

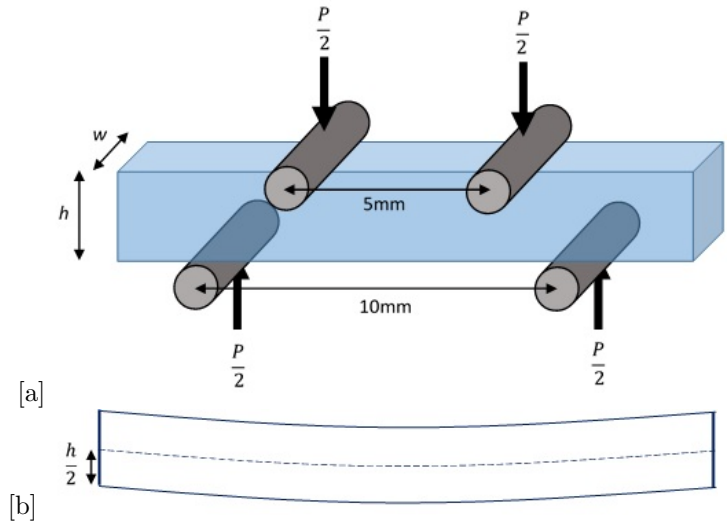


Figure 120: (a) Diagram of the geometry of the matchstick specimens used in four-point bend testing. P is load, w is width and h is depth. (b) The load cell is applied in the y-axis downwards and causes the beam to bend inducing a strain in the x-y plane proportional to the beam curvature, from [265]

At the specimen surfaces, the strain, ϵ is proportional to the measured deflection. All four point bend testing was performed at a constant cross-head velocity of 0.1mm/minute. The beam dimensions were close to uniform due to the sample preparation method (the polycrystalline samples ranging from 0.92 to 0.99mm and the single crystal samples 1.09 to 1.23mm thick; they were polished in two batches). The raw load-displacement data were then converted into stress-strain data with frame compliance caused by machine deformation subtracted. This analysis will be outlined in Section 5.2.

Two specially designed rigs were used for two different temperature regions. A 'cold rig' was used for tests between -180 and 25°C and a 'hot rig' for tests between 25 and 500°C (see figure 121). In the cold rig, cold nitrogen gas from a liquid nitrogen dewar is pumped through the molybdenum jig and a valve on the liquid nitrogen tank is used to adjust the temperature, measured using a thermocouple just below the sample. The hot rig uses an electric furnace to heat the specimen and water-cooled collars on the upper and lower parts of the jig ensure the rest of the apparatus does not overheat.

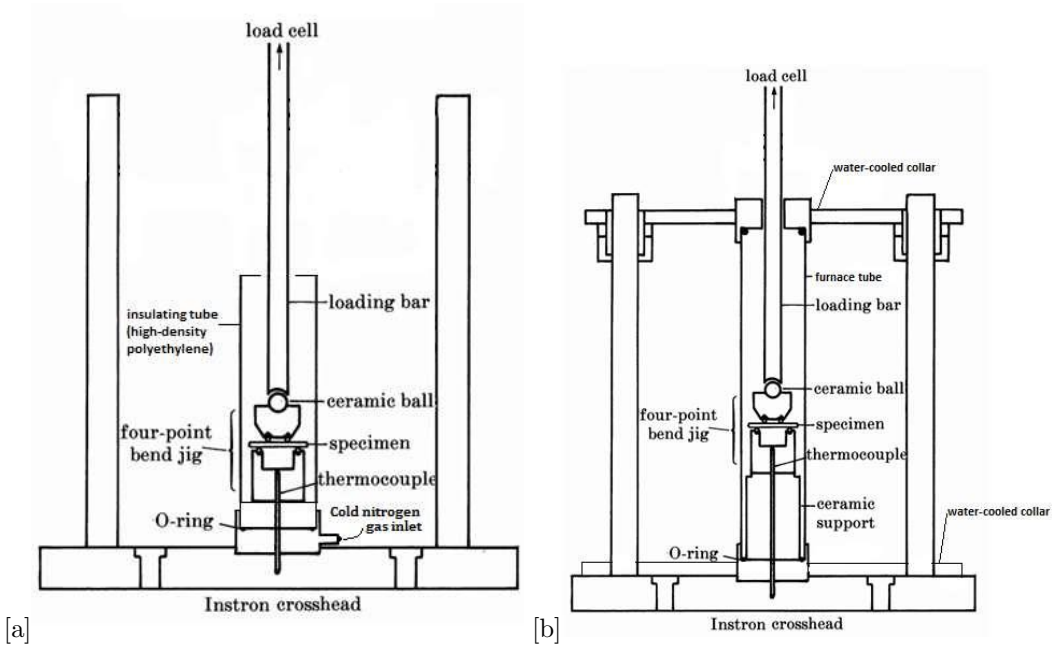


Figure 121: Different temperature control systems built around the Instron rig. From [59]. [a] - 'cold rig' for tests between -180 and 25°C. Cold nitrogen gas from a liquid nitrogen dewar is pumped through the molybdenum jig and a valve on the liquid nitrogen tank is used to adjust the temperature, measured using a thermocouple just below the sample [b] - 'hot rig' for tests between 25 and 500°C, using an electric furnace to heat the specimen and water-cooled collars on the upper and lower parts of the jig to prevent the rest of the rig overheating.

5.1 Samples

A previous study by Durrans [96] used bend tests to investigate the temperature and strain rate dependence of the brittle-ductile transition temperature (and associated activation energy) of unannealed polycrystalline molybdenum. This experiment was carried out on sections of the same polycrystalline bar to assess the dependence of the DBT in molybdenum on the presence of grain boundaries. As described in the following section, an annealing condition after which grain boundary movement was observed was selected for the repeat experiment.

In addition to the work on polycrystalline samples, all tests were carried out on a section of the same single crystal used in the other experiments in this thesis. This enabled fair comparison of results from the other mechanical testing techniques used. The samples used in this work were outlined in Section 2. For consistency and ease of comparison with indentation work, all tests were carried out on single crystal Mo, with flat surfaces and long axes aligned with [001] plane normals as shown in figure 122.



Figure 122: Approximate dimensions of a single crystal molybdenum matchstick - accurate measurements are taken of each sample before testing. Crystallographic orientations are also shown.

Durrans [96] studied four different strain rates; a displacement rate from the middle of the range used in that study was chosen (0.1 mm/min) and tests carried out on identical samples, but annealed to 1400°C for 10 hours, as outlined section 2. This enabled the investigation of the influence of residual work within grains and grain boundary nature on the brittle ductile transition. The test parameters were kept the same with the exception of notching; notching was not used in this work to discourage the propagation of cracks as the object of investigation was solely the change in nature of plasticity at lower temperatures.

5.2 Data Analysis

Data from the Instron is recorded in the form of applied load and crosshead displacement. To extract useful information such as yield stress and elastic modulus, the data must be converted into stress and strain.

The four point bend rig used for these bend tests was originally intended for use as a tensile testing rig. As a result, it has a higher compliance than would normally be found in a compression rig. There is a difficulty associated with machine compliance in four point bend testing - the recorded displacements are an overestimation due to the comparatively high rigidity of the molybdenum sample in comparison to the bend rig. The two bend simultaneously but the movement of the compliant rig will increase any displacement measurements. Previous work has found most of the compliance to come from the loading rod in this particular instrument [266].

A possible solution to this problem is the use of a strain gauge on the specimen but the system used lacked the ability to have one fitted. DIC (digital image correlation) is a good

alternative, but can be complicated and time-consuming to implement. The frame compliance may be measured manually by performing a bend test on a very rigid sample to find the worst case scenario and subtracting the relevant machine displacement from measured displacement values using simple beam theory. However, this can still lead to large errors as the large amount of movement in the rig at low strain can lead to 'set-in', giving variations in frame compliance for each test. Bend testing is inherently a low strain technique and so a compliant tensile rig is not ideal in this way.

As a consequence, each graph was scaled so the gradient of the elastic region was equal to the literature value of Young's modulus at the sample's test temperature, as outlined in Section 1.2.4.

After applying this correction for strain, the constant cross-head velocity of 0.1mm/minute resulted in outer fibre strain rates of $1.86 \times 10^{-5} \pm 1.03 \times 10^{-5} \mathrm{s}^{-1}$ in the polycrystalline samples and $2.30 \times 10^{-5} \pm 1.09 \times 10^{-5} \mathrm{s}^{-1}$ in the single crystal samples.

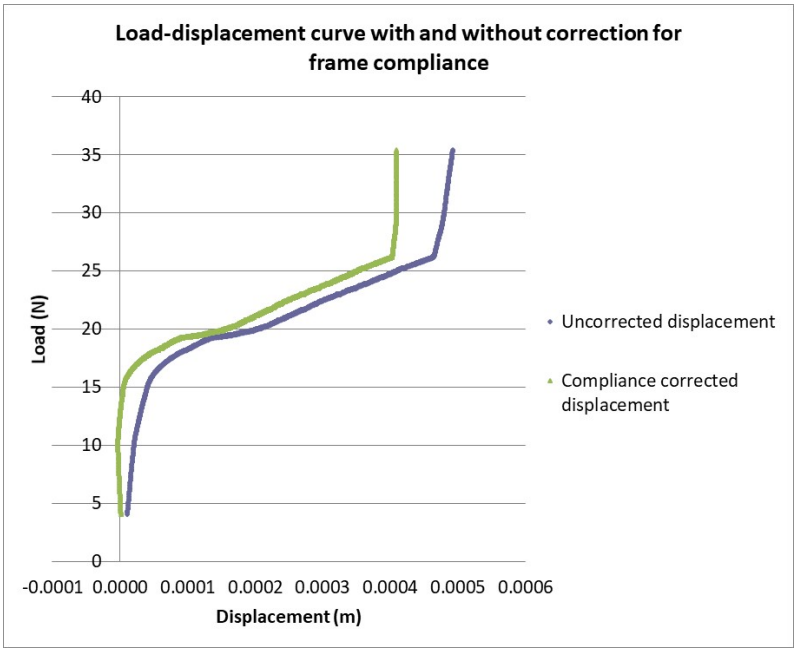


Figure 123: Load-displacement graph of a polycrystalline Mo matchstick (at 522°C before and after frame compliance removal by scaling to a known value of Young's modulus. Note the final section on the corrected curve where the rig is being compressed against itself that is now near-vertical.

Using data without correction does not affect stress values, but displacement values will always be over-exaggerated if the assumption of a perfectly stiff testing rig is made. This would result in underestimated Youngs modulus values as the rig will elastically deform during tests and the crosshead displacement would not be equal to the actual loading point displacement at each stage during the test. For example, in figure 123, the initial slope increases after removal. The yield stress will not be affected, however, as this adjustment is solely a transformation in x.

5.2.0.1 Defining the yield point The yield point is the load at which elastic deformation ends and plastic deformation begins. To define the yield point in a consistent way which removes user error or bias, the LINEST function in Microsoft Excel can be used. This uses the least squares method to calculate the gradient of a straight line - in the elastic region. The point at which the slope drops by 2% or more from the measured elastic gradient, the sample is considered to have yielded. A 2% drop was chosen to ensure the gradient drop was not a local noise minimum, but instead a definite change in the graph's gradient. This corresponded to an outer fibre yield strain in the range 0.0003 to 0.0013.

5.2.1 Simple Beam Theory

Finite Element Analysis was not employed to analyse four point bend specimens as the experimental setup is close to the assumptions underpinning simple beam theory during elastic deformation. Location of the yield point does not require information on the strain hardening behaviour, so yield stress values will not be affected by the use of simple beam theory.
The elastic region is suitable for simple beam theory calculation and the application of Hooke's law for a uniaxial stress [267]. Stress and strain of the matchstick specimen may be calculated from the displacement of the loading points, which for a 'hard' testing rig is equal to the cross-head displacement, by the following series of equations (referring to figure 120). Table 4 gives a summary of the quantities used along with their corresponding symbol.

Table 4: Parameters used in stress-strain calculations.

Parameter	Symbol
Load	P
Outer roller span	L_1
Inner roller span	L_2
Moment	M
Young's modulus	E
Stress	σ
Radius of curvature	R
Second moment of area	I
Distance from neutral axis	y
Beam width	w
Beam thickness	h

5.2.1.1 Stress Taking moments about the beam LHS,

$$M = \left(\frac{P}{2} \times \frac{L_1}{2}\right) - \left(\frac{P}{2} \times \frac{L_2}{2}\right) = \frac{1}{4}P(L_1 - L_2) \tag{51}$$

From simple beam theory:

$$\frac{M}{I} = \frac{E}{R} = \frac{\sigma}{y} \tag{52}$$

Second moment of area for a rectangular beam:

$$I = \frac{wh^3}{12} \tag{53}$$

Taking a point between the inner rollers at the free surface of the beam on the side in tension, y will have a value of $\frac{h}{2}$

Substituting equations 51 and 53 into equation 52, and taking $y = \frac{h}{2}$,

$$M = \frac{\sigma I}{y} \tag{54}$$

$$\frac{1}{4}P(L_1 - L_2) = \frac{\sigma}{\frac{h}{2}} \times \frac{wh^3}{12} \tag{55}$$

$$\sigma = \frac{3P(L_1 - L_2)}{2wh^3} \tag{56}$$

As this is the stress at the sample surface, it is the maximum stress at any point in the beam.

5.2.1.2 Strain As the displacement at the rollers is unknown, the following method is used to calculate strain.

The linear equation for Young's modulus ($E = \frac{\sigma}{\epsilon}$) is substituted into the expression for stress, equation 56, to give an equation describing strain:

$$\epsilon = \frac{3P(L_1 - L_2)}{2wh^3}\frac{1}{E} \tag{57}$$

This is the maximum surface strain in the region between the rollers.

5.3 Results

Four point bend testing produced load-displacement data over a temperature range of -40 to 530°C in the polycrystalline samples and -198 to 340°C in the single crystal samples. This has been converted to stress-strain data using the beam theory described in the previous section.

5.3.1 Polycrystalline Samples

Figure 124 shows the results for polycrystalline Mo yield stress from the LINEST calculation.

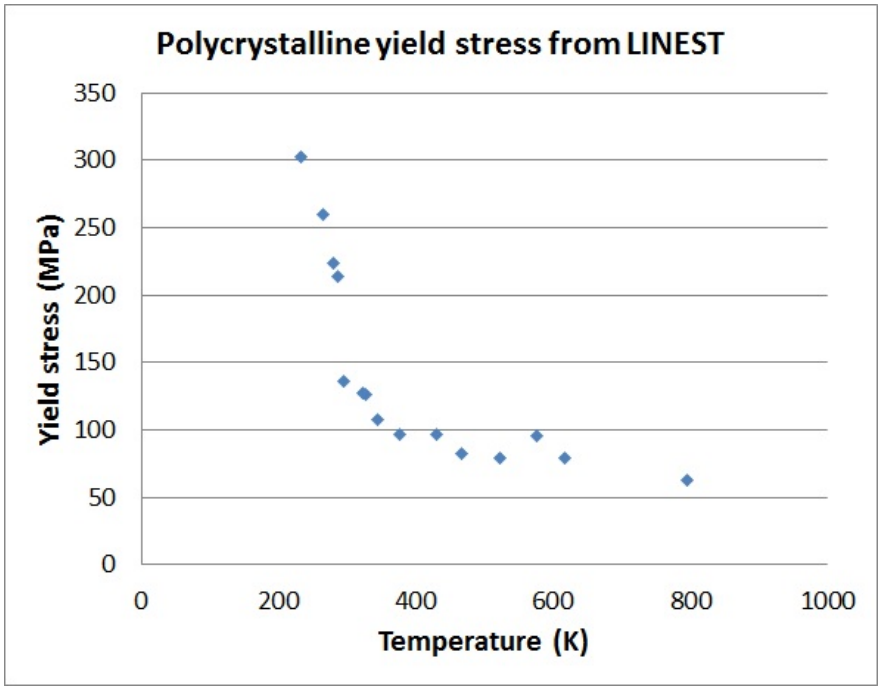


Figure 124: Polycrystalline Mo yield stress calculated using a 2 per cent drop in gradient compared with the Young's modulus value. Two distinct thermal dependencies are seen, separated by a knee.

5.3.2 Single Crystal Samples

Figure 125 shows the section preceding yield of three typical single crystal stress-strain graphs once data have been converted from load-displacement to stress-strain, at -19, 88 and 328°C before frame compliance correction and the removal of 'set-in', where there was a small amount of rig friction before the bend specimen was contacted.

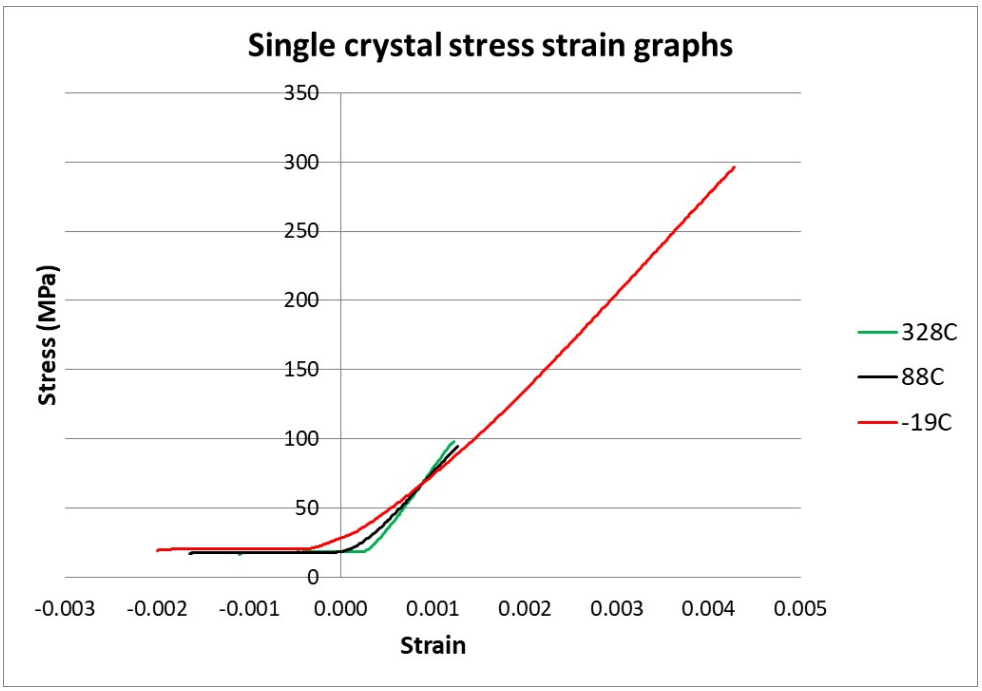


Figure 125: Stress-strain graphs (showing the section preceding yield) for single crystal four point bend tests at -19, 88 and 328°C before frame compliance correction and the removal of set-in.

Some of the single crystal bend tests had greater difficulties with set-in, where the test did not begin with a perfect straight line corresponding to elastic deformation of the sample, and instead had a slightly curved line of lower gradient. This was most likely due to initial friction between the rig and thermocouple, which was initially rigid. It was replaced with a flexible insulated thermocouple that was suitable for use within the range of temperatures required of this experiment. The set-in problem was solved in this way, but due to a limited number of samples the tests could not be repeated. It did not appear to affect the yield stress values (as these were located using a gradient drop rather than relying on absolute gradient values). Figure 126 shows an example.

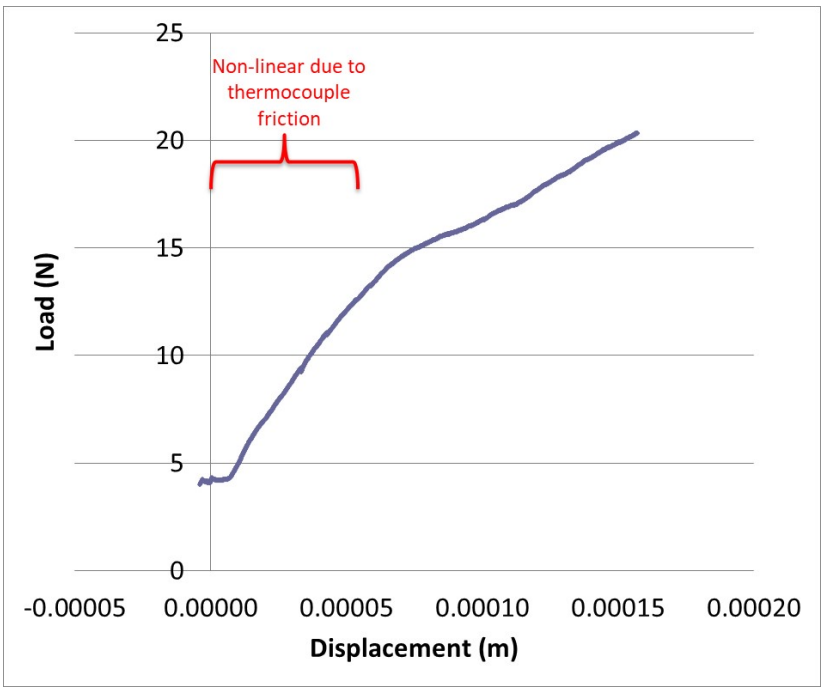


Figure 126: Initial non-linear region due to friction from a rigid thermocouple.

Figure 127 shows single crystal Mo yield stress values located using the LINEST function.

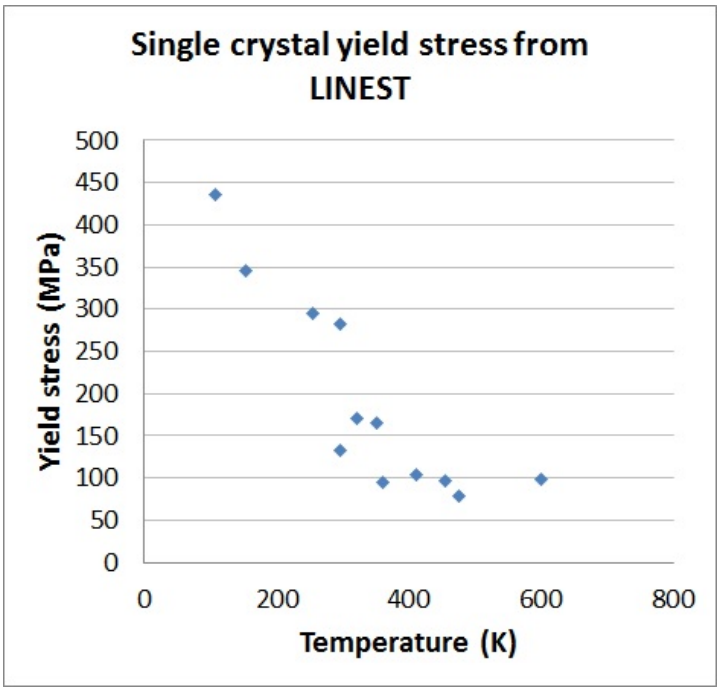


Figure 127: Single crystal Mo yield stress calculated using a 2 per cent drop in gradient compared with the Young's modulus value. There is more scatter in this graph compared to the polycrystalline results in figure 124, but two thermal dependencies are still observable, separated by a knee.

5.3.3 Comparison of Single Crystal and Polycrystalline Results

Figure 128 shows a comparison of yield stress vs temperature for poly and single crystal molybdenum. The values are much more similar than might be expected for polycrystalline and single crystal samples of the same material. As explained on page 28, Durrans found yield stresses at a strain rate of $4.44 \times 10^{-5}s^{-1}$ to be approximately 510MPa at 22°C and 720MPa at -22°C. These are also plotted on this graph.

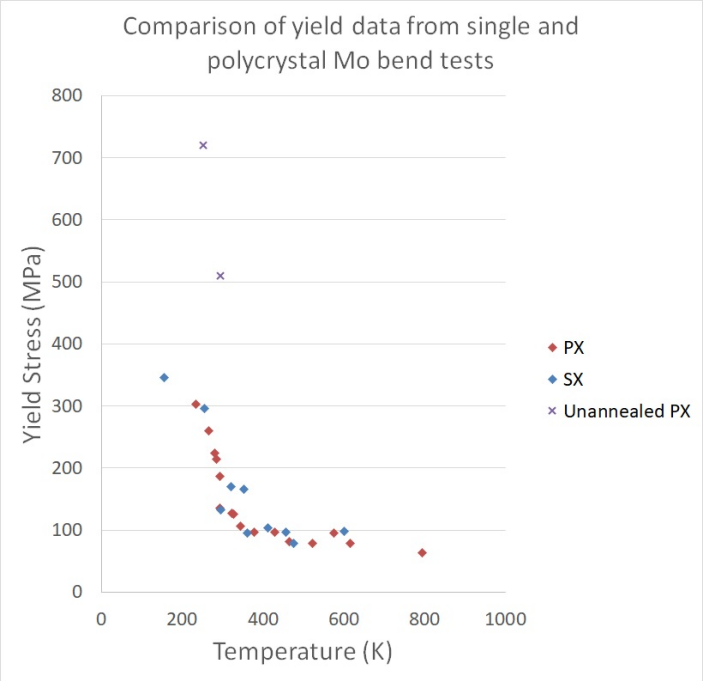


Figure 128: Comparison of single crystal and poly crystal Mo yield stress values. The values are much more similar than might be expected for polycrystalline and single crystal samples of the same material.

5.3.4 Graph Characteristics

One of the polycrystalline tests (figure 129) resulted in a graph with an upper and lower yield point. This is most likely due to the Cottrell atmosphere provided by interstitial impurities, and it is likely that the temperatures at which they occurred for this strain rate range, the dislocation movement and impurity diffusion happen on a similar timescale. The sample used only had a purity of 99.9%, which is not a very high purity when considering lightweight interstitial impurities. It is somewhat surprising then that this upper yield point was only observed in one test, rather than all the tests within the appropriate temperature range, especially as Portevin le Chatelier effects were observed at higher temperatures (figure 130).

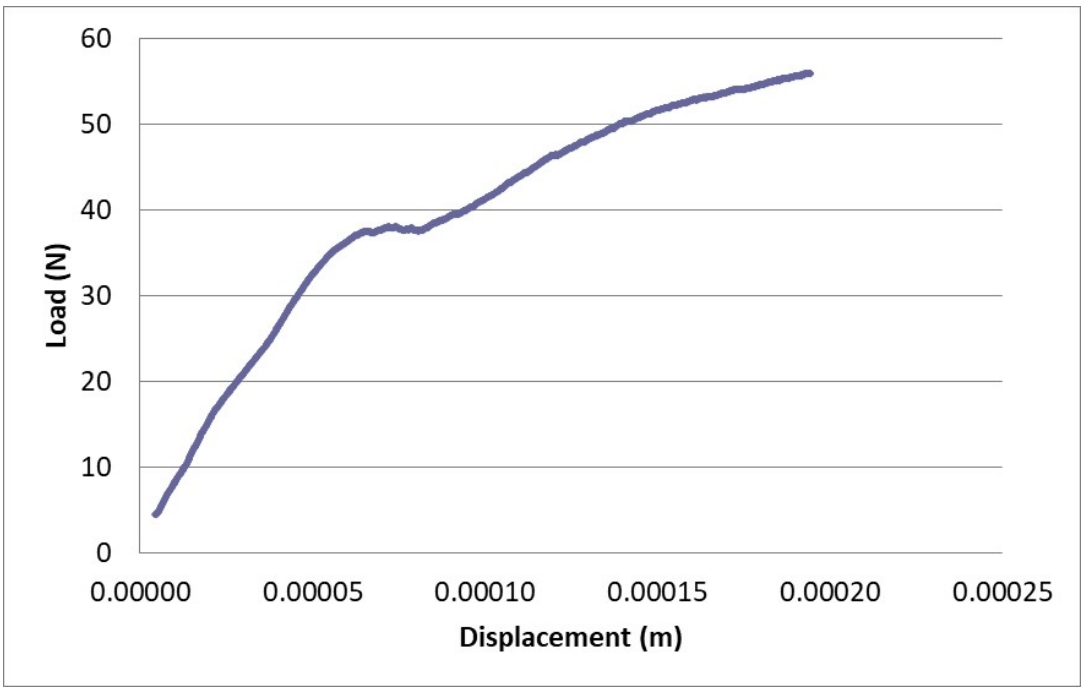


Figure 129: Load-displacement graph for a polycrystalline four point bend test at -8°C showing an upper yield point.

Secondly, serrations were observed on the 328°C single crystal graph (figure 130) and on the 344°C polycrystalline graph (figure 131). These are most likely due to dynamic strain ageing (specifically, the Portevin le Chatelier effect), which produces uneven flow as diffusing solutes repeatedly pin moving dislocations, which repeatedly break free. The size and form of serrations depend on factors such as specimen surface quality and inclusions as well as strain rate and temperature.

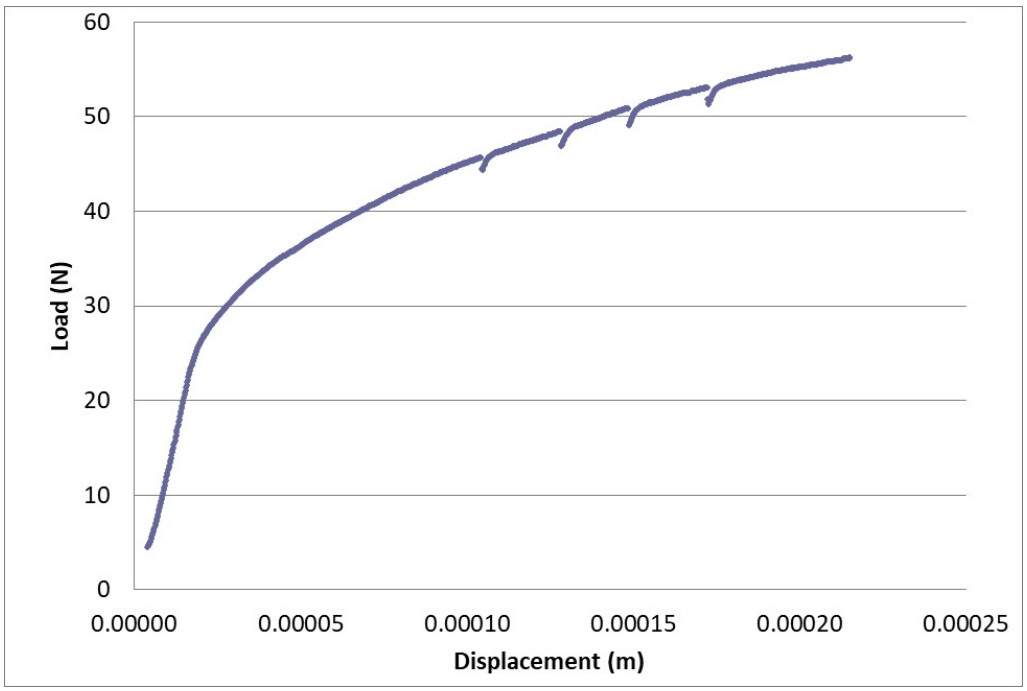


Figure 130: Load-displacement graph for a single crystal four point bend test at 328°C showing serrations likely to result from the Portevin le Chatelier effect.

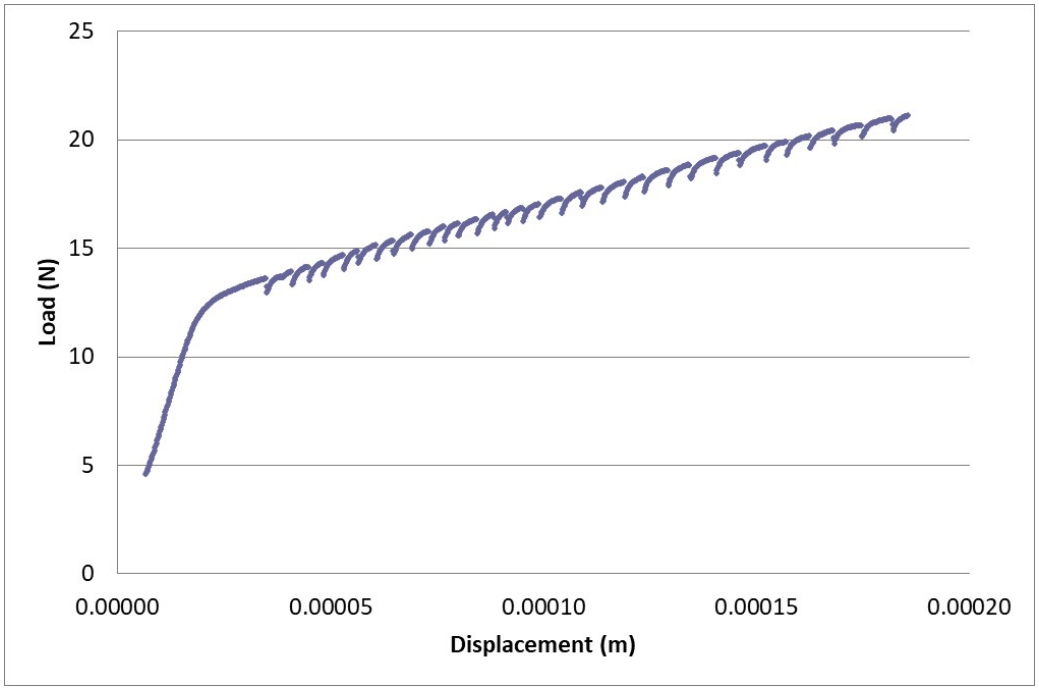


Figure 131: Load-displacement graph for a polycrystalline four point bend test at 344°C showing serrations likely to result from the Portevin le Chatelier effect.

In the majority of cases, the onset of plasticity, found using a 2% drop in gradient, was unambiguous allowing for precise yield strength determination.

Due to the linear increase of stress with distance from the neutral axis in bending, dislocations under the highest stress will be those at the top and bottom surfaces of the match-

stick. However, due to the tension-compression asymmetry of molybdenum discussed in Section 1.2.1.4, those located close to the compressive surface will have an elevated flow stress. Consequently, the dislocations that are most likely to slip first can be said to have an applied [100] tensile axis due to the crystallographic alignment of each bending specimen (all edges parallel to {100} directions.)

By applying Diehl's rule to the stereogram shown in figure 132, the two $\{110\} < 111 >$ type slip systems with the highest Schmid factor are $(110)[1\bar{1}1]$ and $(1\bar{1}0)[111]$. Both have an equal Schmid factor of $\frac{1}{\sqrt{6}} = 0.41$.

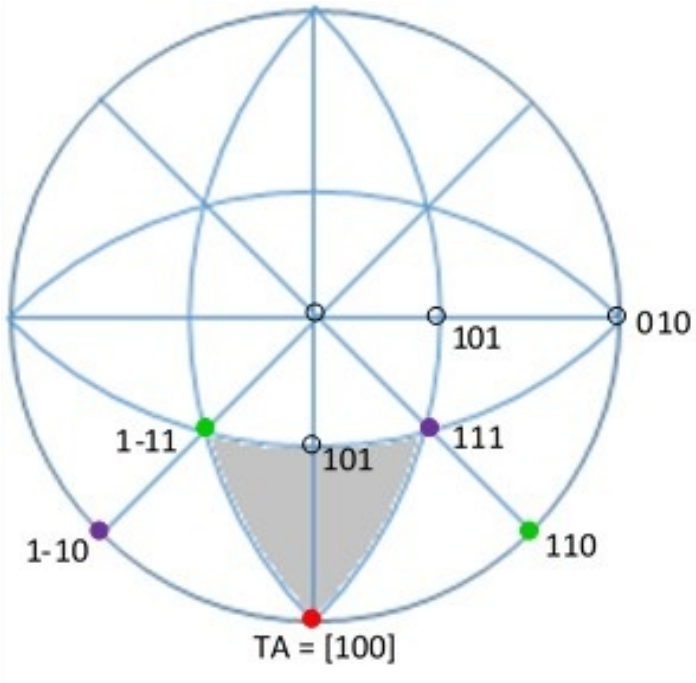


Figure 132: [001]-orientated stereographic projection of the BCC unit cell. Tensile axis TA=[100] - two active slip systems by Diehl's rule - $(110)[1\bar{1}1]$, $(1\bar{1}0)[111]$. Both with equal Schmid factor of $\frac{1}{\sqrt{6}} = 0.41$

However, as discussed on page 14, although Schmid's law suggests slip should take place on the densest packed, {110}, planes (which is true at temperatures below the lower bend shown in figure 9 [25]), upon heating the operating slip planes are not exclusively those with the densest packing. Possible slip planes are {110}, {112} and {123}, with all slip systems intersecting the $< 111 >$ axis. The common $< 111 >$ direction is identical to the Burgers vector, so that screw dislocations lie along this common axis. Since τ_0 cannot be expected to be the same for all slip planes, Schmid's law becomes difficult to apply.

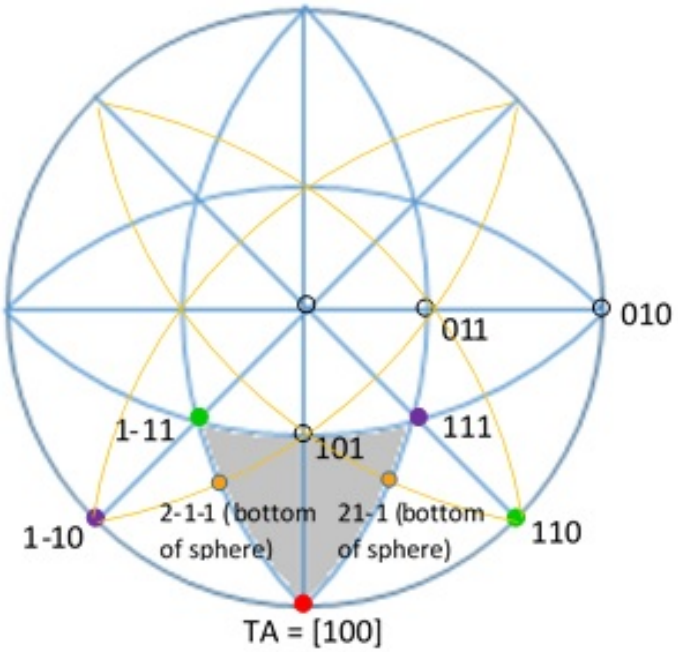


Figure 133: [001]-orientated stereographic projection of the BCC unit cell. Tensile axis TA=[100]. $(110)[1\bar{1}1]$ and $(1\bar{1}0)[111]$ both have an equal Schmid factor of 0.47

As fist discussed on page 14, the first active slip plane is likely to be one of type {112}. In BCC crystals, the $< 111 >$ {211} slip system with the largest Schmid factor is not the same inside the entire stereographic triangle [43, 32]. Diehl's rule cannot be applied, but the {211} slip planes are identified by locating the {110} plane normals (shown in figure 132) and finding the {211} slip planes on either side, by following the {111} zone.

Referring to the stereographic projection in figure 133, for the slip direction [111], the {211} slip plane with the largest Schmid factor is $(2\bar{1}\bar{1})$ and for the direction $[1\bar{1}1]$ it is $(21\bar{1})$.

The two slip systems of this type subjected to a [100] tensile axis will be $(21\bar{1})[1\bar{1}1]$ and $(2\bar{1}\bar{1})[111]$, both with Schmid factors of 0.47. This Schmid factor of 0.47 was used in the calculation of the flow stresses shown in figures 134 and 135. These values of flow stress will be used in a final discussion chapter comparing the mechanical test techniques.

The difference in the {110} and {112} Schmid factors (0.41 and 0.47) is not large, especially as other factors come into action, such as tension-compression asymmetry, that remove the strict application of Schmid's law. So whether a maximally stressed {110} or a maximally stressed {112} slip system operates first is more likely to be related to which of them has the lowest critical resolved shear stress. There are, therefore, many slip systems in the single crystal tests with very similar if not identical Schmid factors, so stage II work hardening will almost always be reached straight away.

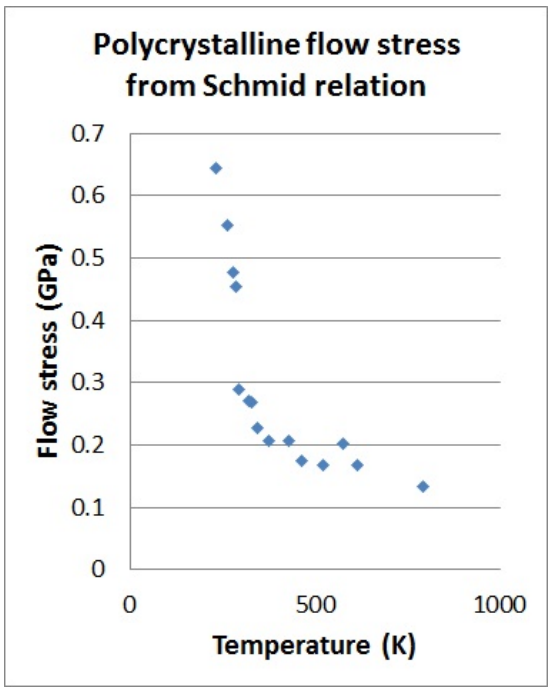


Figure 134: Flow stress values calculated as the ratio between yield stress and a Schmid factor of 0.47 for the polycrystalline samples.

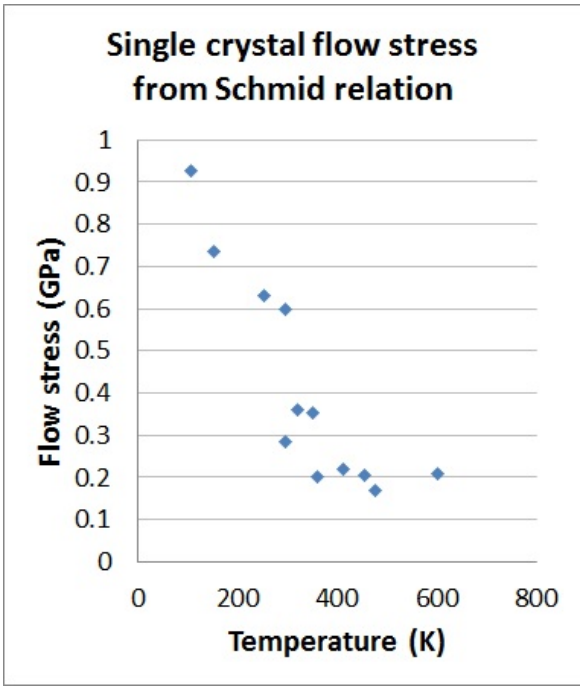


Figure 135: Flow stress values calculated as the ratio between yield stress and a Schmid factor of 0.47 for the single crystal samples.

5.4 Discussion

As stated above, both polycrystalline and single crystal matchsticks were investigated, with the single crystal specimens [100] aligned and the polycrystalline with a small amount of texture in the direction of the long axis.

The yield stress values for single crystal and annealed polycrystalline samples were much more similar than expected (figure 128). The yield stress of a polycrystalline metal is typically elevated compared to its single crystal form due to the Hall-Petch effect, but this was not seen here. However, bend tests on unannealed samples of the same material by Durrans [96] showed a much elevated yield stress, also shown in figure 128.
The EBSD-assessed sample had grains of diameters approaching 200μm. Considering the polycrystalline matchsticks had widths ranging from 0.92 to 0.99mm, a 200μm grain would cover a significant fraction of the cross-section of a matchstick of this size.

These observations suggest that the polycrystalline bend tests in this project may have lower yield stresses than expected due to the structure of the specimen. It appears from figure 21 that Durrans applied a correction for frame compliance to these results for two reasons - the Youngs modulus values are self-similar and of a correct order of magnitude, and the ductile curve shows the stress value goes beyond vertical once the rig is compressing itself.
Additionally, a large amount of work had been annealed away inside the grains (apparent in the EBSD scans of annealed samples), and the fact that the unnannealed samples had much higher yield stresses suggests that the removal of cold work had a strong influence on this low polycrystalline yield stress.
It is likely that the yield stresses were so much higher in the study by Durrans due to the combination of cold work within the grains causing the initiation of dislocation movement to be restricted, and by the Hall-Petch effect, as the grains are likely to have a higher average diameter after the annealing treatment.
Another potential reason for the unexpected relationship between the single crystal and polycrystalline samples is the impurity level of the samples. There is quite a difference between the impurity levels, and mechanical properties can be strongly influenced by very small quantities of interstitial impurities in BCC metals, so the difference between 10 ppm impurities in the single-crystal samples and 1000 ppm in the polycrystalline samples may be significant. The higher impurity level of the single crystal samples would act to elevate their hardness.

6 Micromechanical Testing

6.1 Micromechanical Bend Testing

Microcantilevers were manufactured using the Di Maio method described on page 47. The first run of tests was carried out in triangular cantilevers milled in polycrystalline Mo for a trial of the milling conditions and mechanical test technique; the results are not reported here. Both the polycrystalline sample and faster triangular cross-section were suitable for preliminary testing. For ease of analysis and consistency with other testing techniques in this thesis, microcantilevers were then milled in single crystal Mo.

Pentagonal cross-sectioned specimens were originally made for intended fracture work. It was later decided that only plasticity would be investigated. However, although they take longer to mill, pentagonal cantilevers are equally valid. They have a different geometry (and so a different second moment of area) which is taken account of during the analysis.

6.1.1 Focussed Ion Beam

The FIB microscopes used for milling work were a Zeiss Auriga FIB-SEM dual beam system and an FEI FIB200 single beam system. Gallium-based liquid metal ion sources were operated at a primary acceleration voltage of 30kV with an emission of approximately 2μA. In both systems the ion beam current was then reduced by passing through a selected aperture producing a collimated beam from 1pA to 20nA, with the capability of imaging to 2.5nm resolution, or milling with a spot size of approximately 2.5nm. The focussed ion beam is rastered over a specified area for both imaging and milling, using scanning coils. The Auriga is also equipped with the "Nanopatterning Engine" which enables the direct writing of complex patterns and objects using the ion beam.

The dual beam system in the Auriga with both SEM and FIB columns enables imaging the sample without the use of the ion beam. This is very useful for preventing damage while imaging, and also for monitoring the progress of microcantilever manufacture.

6.1.2 Microcantilever Preparation

In single crystal samples where cantilever orientation was of high importance, the single crystal surface with plane normal [100] was examined using EBSD, in order to locate the orientation of the [010] and [001] directions. This enabled microcantilevers to be aligned along a $< 100 >$ direction. To perform this procedure, an arrow was FIB-milled, then the sample scanned using EBSD. The angle between the unit cell axes and this arrow was measured 10 times (using automatic orientation in the EBSD software) and an average taken. The sample was then

placed back in the FIB and a long straight line drawn at this angle to the line. The EBSD alignment is shown in figure 136; a slight deviation from a (001) plane normal is shown in (a), with the pole not perfectly situated on the [001] pole. The FIB-milled line used as a point of reference for microcantilever orientation is shown in (b). This is also shown schematically in (c).

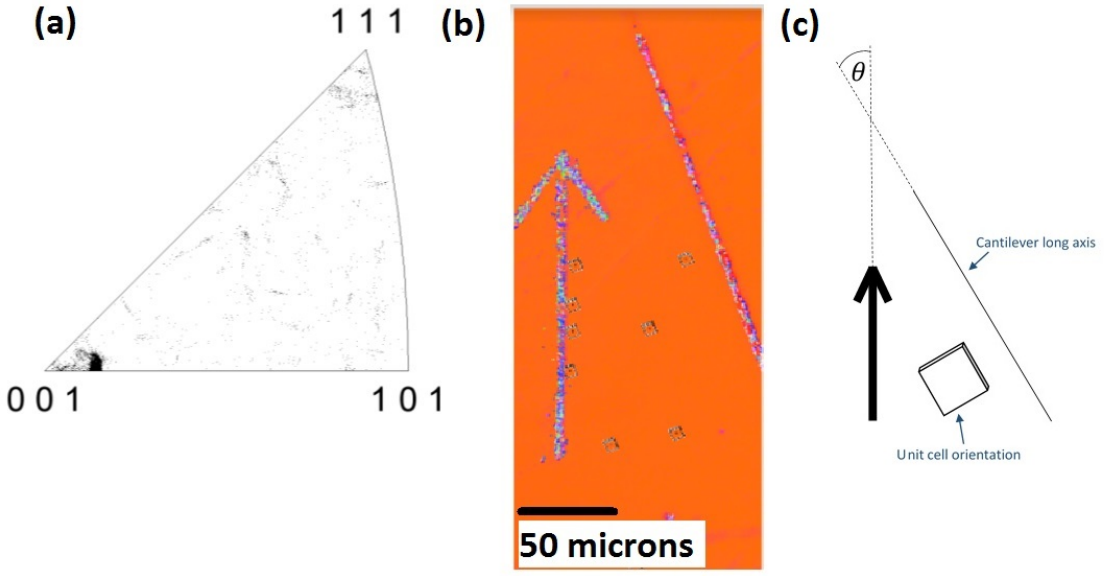
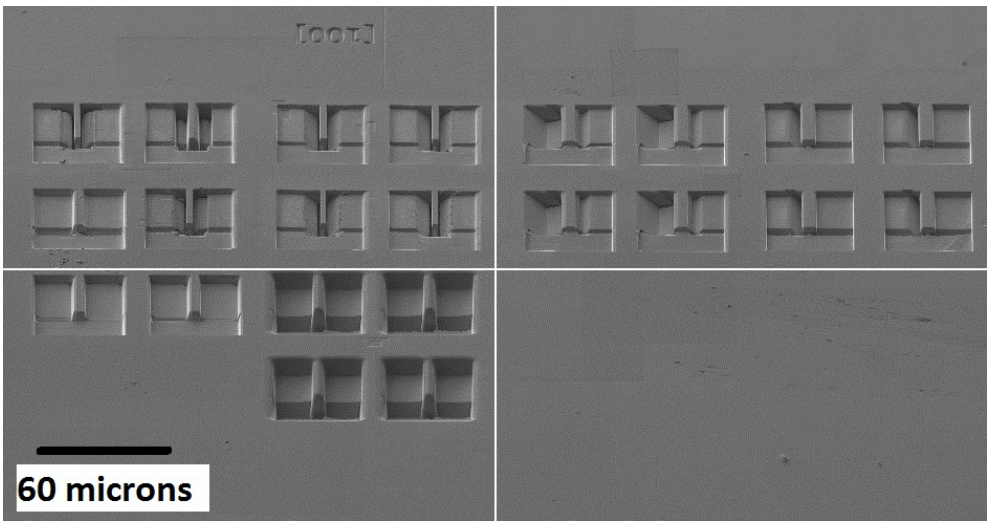


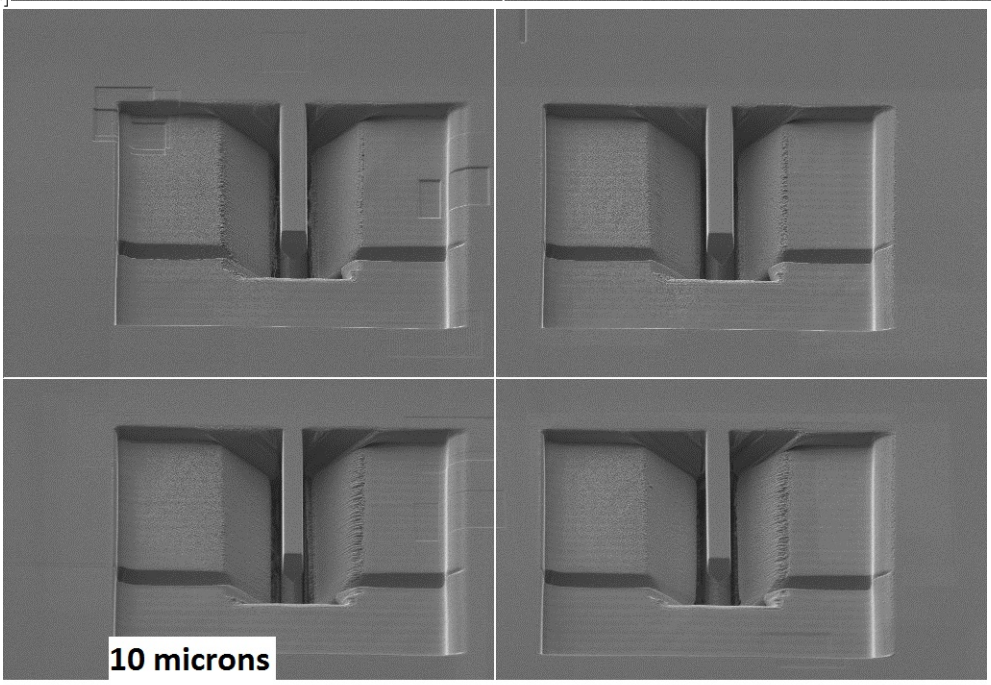
Figure 136: EBSD alignment; a slight deviation from a (001) plane normal is shown in (a), with the pole not perfectly situated on the [001] pole. The FIB-milled arrow used as a point of reference for microcantilever orientation is shown in (b). This is also shown schematically in (c).

Microcantilevers were manufactured with a pentagonal cross section using a FIB, following the technique first described by Di Maio et al. [178]. A rough U-shaped trench was milled normal to the sample surface using a beam current of 16nA, followed by a neater trench using 1nA. The sample was then tilted to 45 degrees and undercut using a beam current of 1nA. The sides and undercut of the cantilever were finished with a final polish using a beam current of 600pA, in order to make a cantilever with the straightest possible sides to reduce experimental error due to uncertainties in cantilever geometry.

Figure 137 shows the single crystal pentagonal microcantilever array during manufacture. [a] also shows the [100] direction vector used for alignment (top centre). [b] shows four complete cantilever beams.



[a]



[b]

Figure 137: Pentagonal microcantilever array during manufacture. [a] also shows the [100] direction vector used for alignment (top centre). [b] shows four complete cantilever beams.

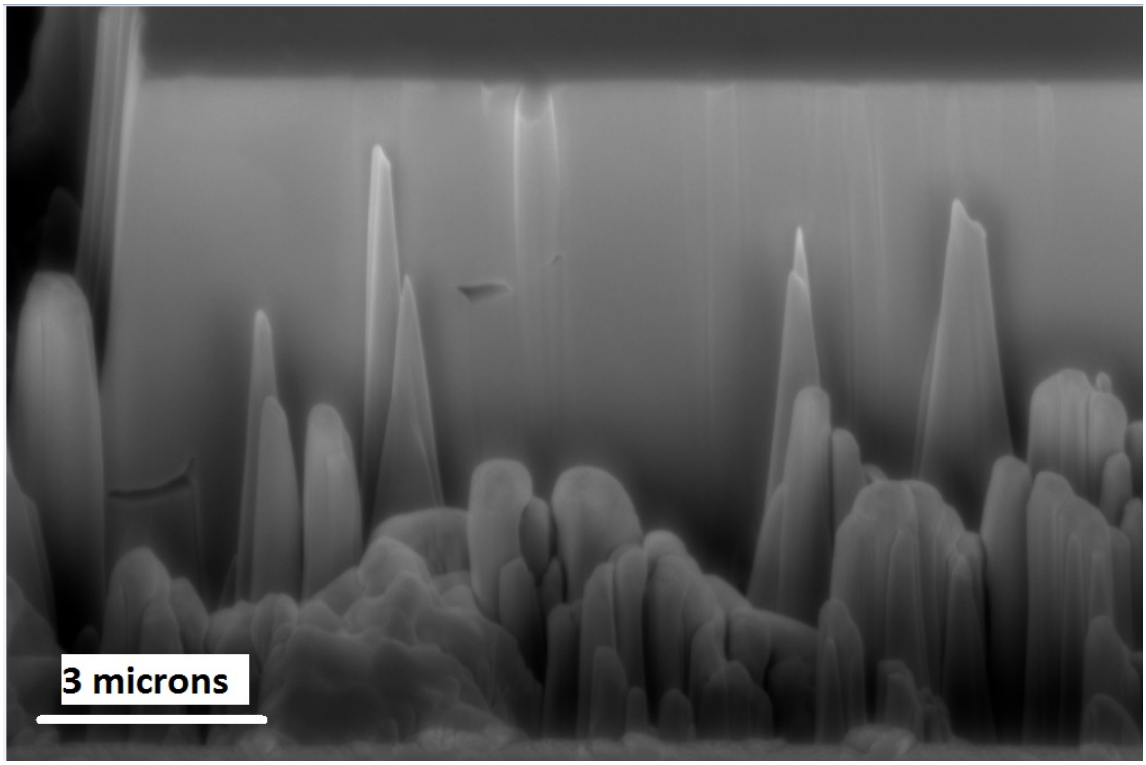
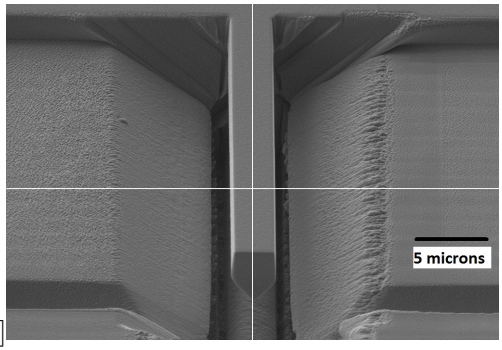


Figure 138: This image shows the erratic sputtering that FIB-milling a single crystal molybdenum surface with a high beam current can produce, making sample manufacture more time-consuming.

Figure 138 demonstrates the erratic sputtering that FIB-milling a single crystal molybdenum surface with a high beam current can produce. For this reason, after the initial rough cut with the high beam current, a lot of time must be taken to cut the cantilever sides down with a low beam current so they are neat, planar and perpendicular to the surface.

Figure 139 shows an example FIB-milled microcantilever beam before and after bend testing.

[a] 

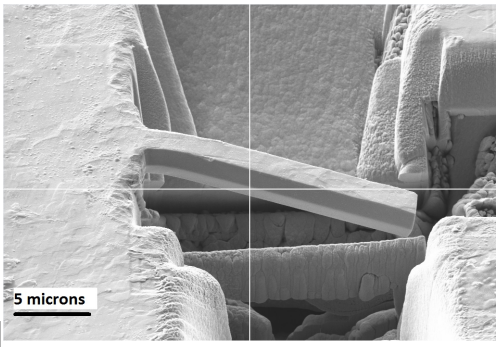
[b] 

Figure 139: FIB-milled microcantilever beam pre- and post-bend test.

All cantilever dimensions were measured in the same Auriga-SEM after manufacture. The length of the cantilevers was measured at 0° tilt for reference later on when they were being tested (the measured length was not important, as an AFM technique was used to locate the fixed end and test point of the cantilever). The width of the cantilevers was also measured at 0°

tilt, but five measurements were made along the length of each cantilever, and an average taken. The vertical dimensions were measured at 30° tilt at three magnifications, and an average taken. The cantilevers had the following dimensions:

Table 5: Cantilever dimensions (microns)

Width	3.31±0.49
Height	4.32±0.56
Test length	27.7±3.5
Aspect ratio - length/width	7.98±1.5

6.1.3 Experimental Method

The sample was loaded in the NanoTest Xtreme on either the hot or cold stage as necessary, with thermocouples adhered in place using high temperature cement. Each microcantilever to be tested was located using the optical microscope and positioned under the spatially-calibrated indenter tip. In scanning mode, the indenter was then used to form a topographical map of the cantilever in an array of 50 by 50 data points, which in turn was used to position a higher resolution array of 400 by 400 data points (with a step size of $0.25\mu m$) over the microcantilever. An example high resolution scan is shown in figure 140a. The free and fixed ends of the microcantilever were identified on the map. Then the indenter was placed over the test site (near the free end), recording precisely the distance from the fixed end to the test position, as shown in figure 140b.

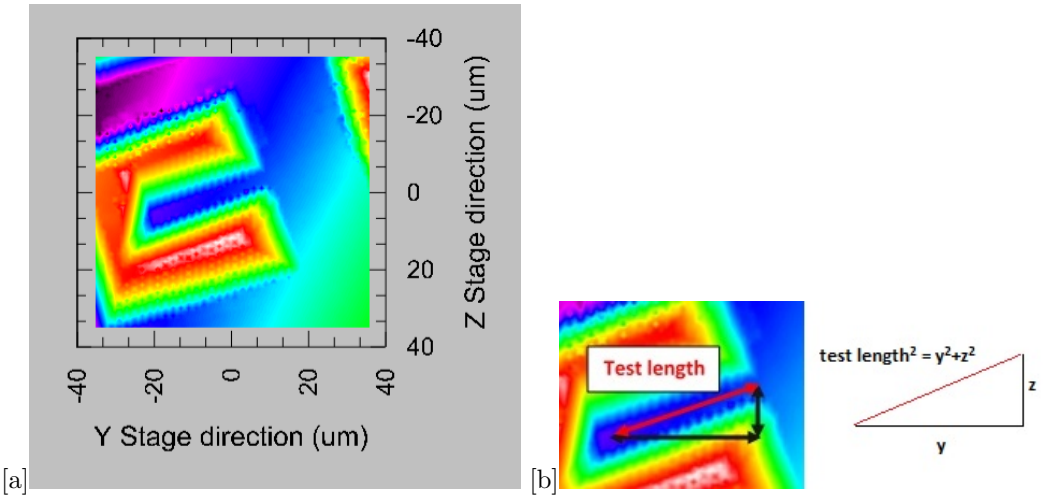


Figure 140: AFM scan of cantilever (a) with test length calculation shown in (b), taken as the length between the centre of the fixed end and the test location.

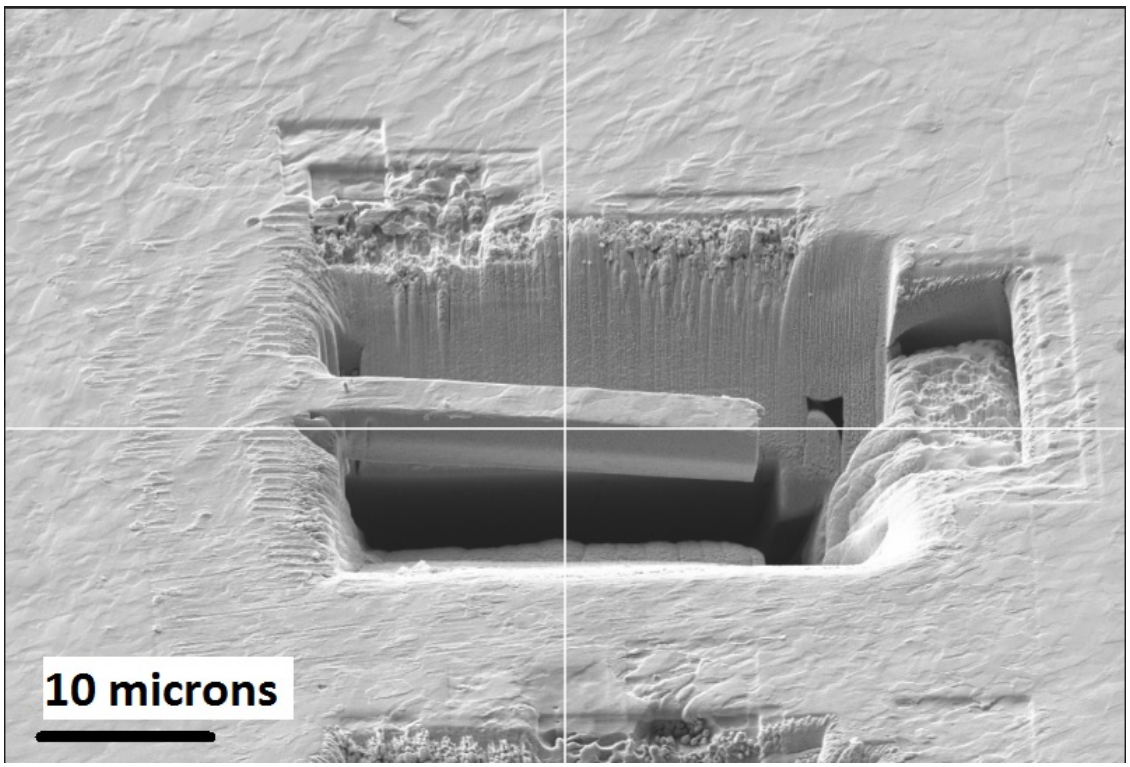


Figure 141: SEM micrograph of a polycrystalline Mo microcantilever (from a preliminary microcantilever trial) after scanning and bend testing at 500°C, when the material is significantly softened. Faint scan lines on the left hand side, showing little surface disruption.

Figure 141 shows an SEM micrograph of a polycrystalline Mo microcantilever (from a preliminary microcantilever trial) after scanning and bend testing at 500°C, when the material is significantly softened. The scan lines on the left hand side of the image are very faint, showing little surface disruption. This is due to the low scanning load used. No post-test images of single crystal cantilevers are available due to the failure of the vacuum system during the latter stages of testing, and the subsequent oxidation of the surface.

Once located, the test was performed similarly to an ordinary indentation, by applying a load and recording load vs. displacement data. A loading rate of 0.1mNsec^{-1} was used to a target displacement of $1\mu m$, corresponding to outer fibre strain rates of $2.82 \times 10^{-4} \pm 1.33 \times 10^{-4}\text{s}^{-1}$ up to the yield point. Load and displacement were continually monitored throught the full load-unload cycle. So as not to disrupt the stress-strain graph, corrections for thermal drift were taken from pre- and post-test thermal data.

6.2 Data Analysis

6.2.1 Simple Beam Theory

In all analysis, the calculation of stresses and strains from load-displacement data used the dimensions measured individually from each cantilever. The major stresses induced due to

bending are normal stresses of tension or compression but the state of stress within the beam also includes shear, transverse and torsional stresses, due to beam geometry (triangular crosssection, joined to deformable bulk material). These other stresses are generally of a smaller order [268]. For simplicity the analytic model only considers major (longitudinal) stresses. As all others are negligible, results for stress and strain should not be inaccurate and it is a useful, simple tool to use as a first approximation.

From Timoshenko [269], the equation used for calculating stress was:

$$\sigma = \frac{PLc}{I} \tag{58}$$

where P is the applied load, L is the length between the fixed end and the indenter, c is the distance between the neutral axis and the outermost fibre and I is the second moment of area. Also from Timoshenko[269]:

$$\delta = \frac{PL^3}{3EI} \tag{59}$$

Rearranging equation 59 for Young's modulus:

$$E = \frac{PL^3}{3I\delta} \tag{60}$$

Dividing equation 60 by equation 59 for strain:

$$\epsilon = \frac{\sigma}{E} \tag{61}$$

$$\epsilon = \frac{3c\delta}{L^2} \tag{62}$$

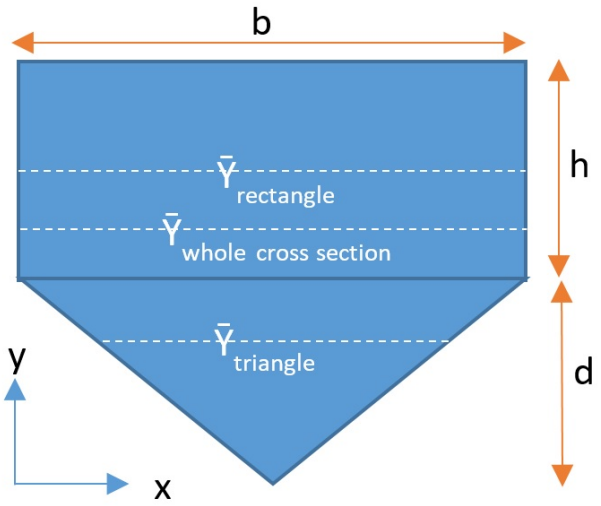


Figure 142: Cross section of a pentagonal cantilever with the relevant dimensions for calculation of the beam centroid - b is the cantilever width, h is the rectangle height and d is the triangle height.

The location of the centre of mass of the pentagonal cross section is calculated by separating the shape into a rectangle and a triangle (shown in figure 142) and applying the following function:

$$\bar{y} = \frac{\bar{y}_{tri}.A_{tri} + \bar{y}_{rec}.A_{rec}}{A_{tri} + A_{rec}} \tag{63}$$

Where $\bar{y}$ is the overall beam centroid, $\bar{y}_{tri}$ is the triangle centroid, $\bar{y}_{rec}$ is the rectangle centroid, A_{tri} is the triangle area and A_{rec} is the rectangle area. Centroids are measured relative to the axes shown in figure 142.

Substituting values for the two shapes,

$$\bar{y} = \frac{\frac{2d}{3}\frac{bd}{2} + (d + \frac{h}{2})bh}{\frac{bd}{2} + bh} \tag{64}$$

which simplifies to

$$\bar{y} = \frac{2d^2 + 6dh + 3h^2}{3d + 6h} \tag{65}$$

with all centroid locations measured from the bottom of the triangle (y=0).

The second moment of area of the pentagon, I, is also calculated by treating the two shapes separately and applying the parallel axis theorem to each shape:

$$I_{centralaxis} = I_{centroid} + A.c^2 \tag{66}$$

where the "central axis" is the centroid of the composite pentagonal shape relative to y=0. For the rectangle,

$$I = \frac{bh^2}{12} + bh.c^2 \tag{67}$$

For the triangle,

$$I = \frac{bh^3}{36} + \frac{bd}{2}c^2 \tag{68}$$

The second moment of area for the composite pentagonal shape is equal to the sum of the two separate second moments of area calculated about the common axis - the composite centroid.

$$I_{pentagon} = I_{triangle} + I_{rectangle} \tag{69}$$

Finite element analysis (FEA) considers more stresses to give a more accurate result but it is a more complicated model and requires more computation time.

6.2.2 Finite Element Analysis

FEA was used to simulate microcantilever deformation, modelling the displacement of the fixed end of the cantilever, helping to determine more accurate yield stress values at the time of yield. FEA discretises a domain (e.g. a microcantilever) into a mesh consisting of elements defined by nodes. As element size decreases, the numerical solution approaches the exact solution and has the advantage of being applicable to problems that cannot be solved analytically. The finite element method allows complex geometries to be modelled and takes into account longitudinal stresses as well as transverse, shear and torsional stresses that the analytic model (Euler-Bernoulli beam theory) neglects. In the case of a loaded cantilever beam made within a single block of one material, this refers to the stresses in the 'fixed end' or material bulk. The movement of the fixed end of the cantilever is not considered in the simple beam theory analysis method. However, there is a small displacement in this material, which has identical properties to the beam itself. This adds a small amount of deflection in addition to the beam's deflection, increasing the measured strain and leads to inaccuracies in the yield stress. By including the fixed end in the finite element model, the strain at this end can be determined and accounted for leading to more accurate measurements of yield stress.

A finite element model was created for each cantilever, containing its specific dimensions (including the actual test length relative to the base at the fixed end) and the temperature-specific Youngs modulus. The model included the whole cantilever beam and a section of the 'bulk' material to which it was attached at the fixed end.

The element type was an 8-node linear brick with reduced integration and hourglass control - element type C3D8R. Only elastic behaviour was considered in the model - elastic constitutive laws were used. The boundary conditions used were to fully fix any surfaces that were attached to the bulk - encastré, with no displacement or rotation permitted. A typical FEA microcantilever beam once it has been meshed is shown in figure 143.

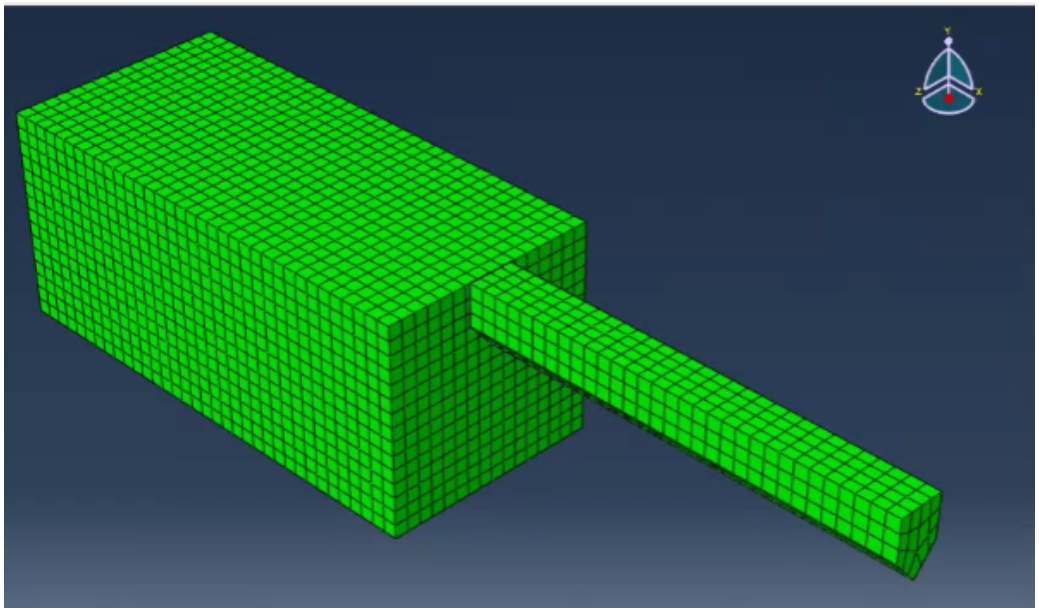


Figure 143: A typical FEA microcantilever beam once it has been meshed.

Figure 144 shows the cantilever deformation in the y-direction and figure 145 shows the Mises stress gradient in the beam, cut in half across the vertical plane.

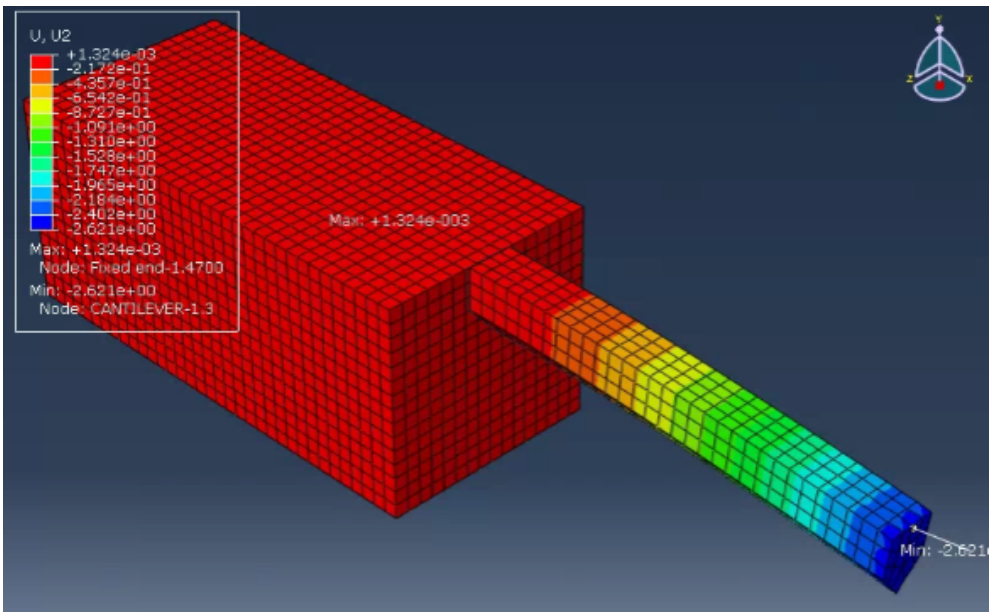


Figure 144: Deformation in the y-direction

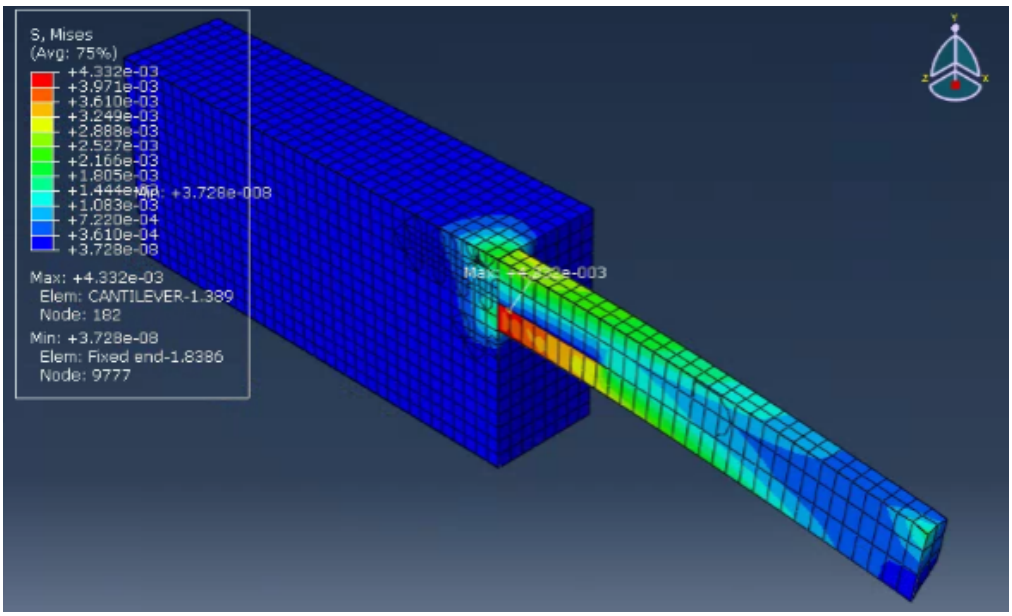
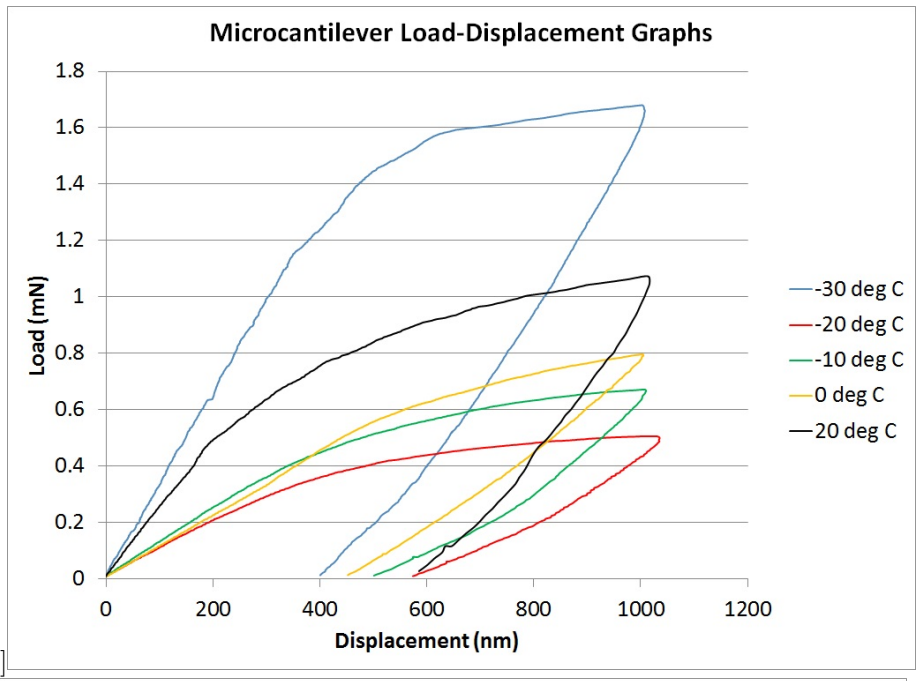


Figure 145: Mises stress gradient in the beam, cut in half across the vertical plane.

6.3 Results

6.3.1 Load-Displacement Graph Characteristics

Cantilever load-displacement curves across all temperatures are shown in figure 146.

[a]


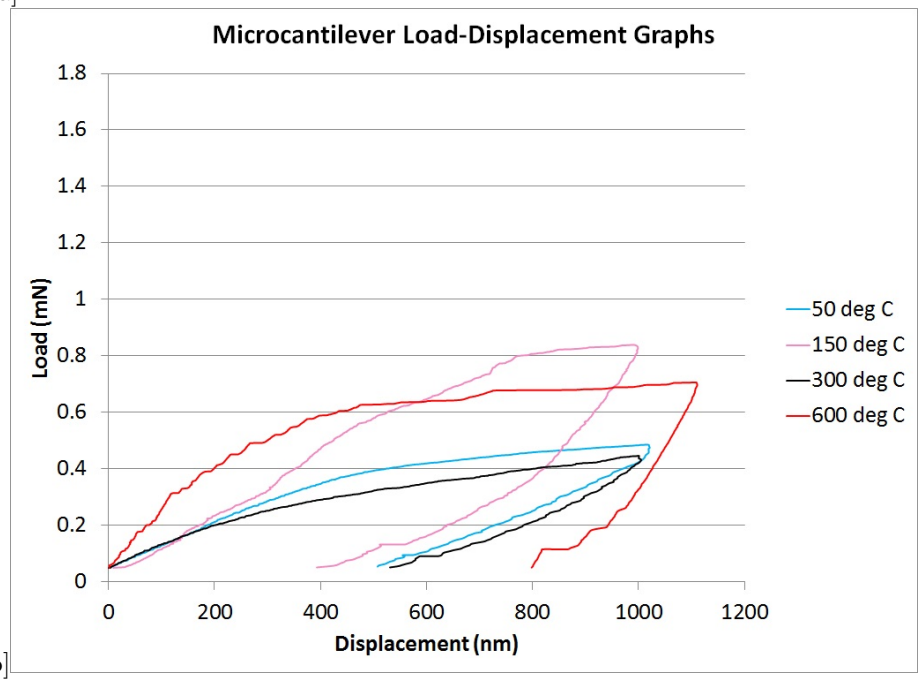
[b]


Figure 146: Microcantilever load-displacement curves across all temperatures before frame compliance correction. (a) -30 to 22°C. (b) 50 to 600°C.

An interesting feature of these curves is that unlike the smooth load-displacement curves of the bulk single crystal four point bend tests, the highest temperature load-displacement relationship did not only undergo stage II/III work hardening but also contained several elastic loading segments followed by discrete displacement bursts. Some very small bursts also take place in the elastic regime. These are shown in figure 147.

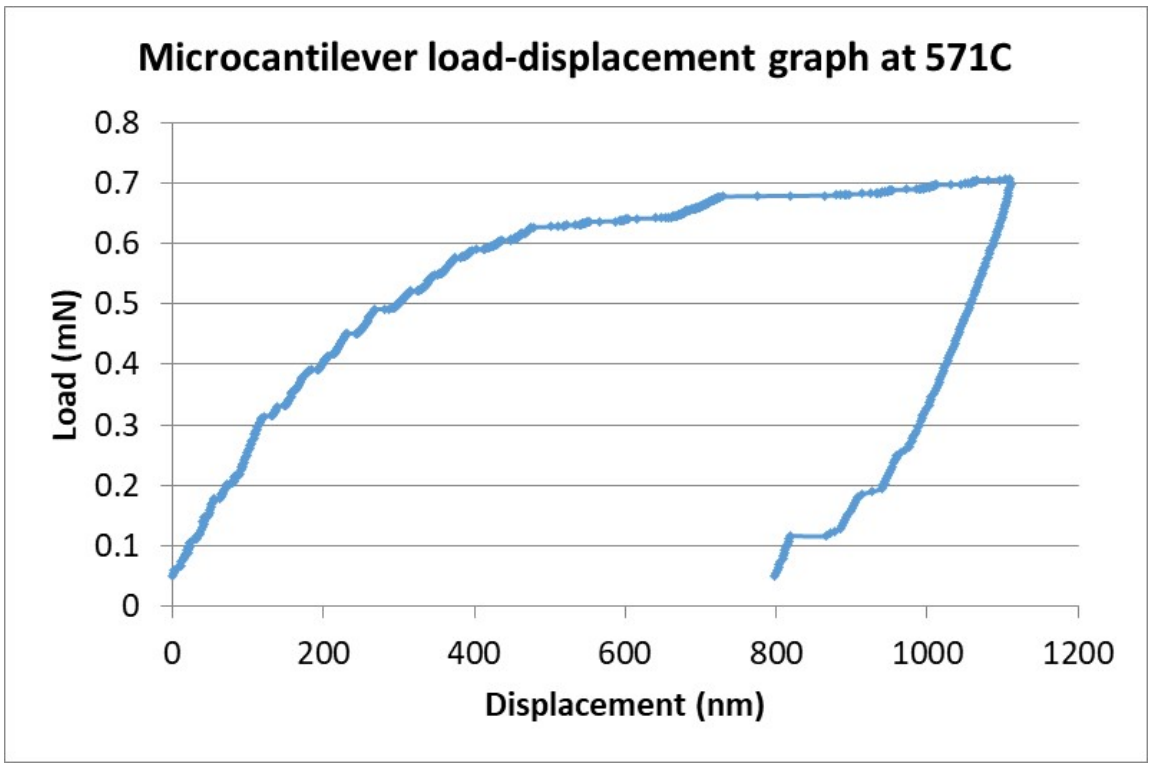


Figure 147: Load-displacement graph for a microcantilever bend test of single crystal Mo at 571°C showing short plateaus that suggest discrete strain bursts.

This is not a gradual displacement change so it is unlikely to have been caused by a thermal imbalance between the tip and sample. The initiation of these strain bursts most likely arose from the propagation of dislocation avalanches within the sample from dislocation sources [195] in response to the shear stress in the glide plane [270]. Large strain bursts and absence of strain hardening associated with dislocation elimination at the sample surface [196, 197] when local shearing occurs [198, 199] (as discussed on page 51) were not observed in any microcantilever bend tests apart from the 571°C graph [190].

Similarly to the four point bend graphs discussed on page 150, none of the load-displacement graphs showed evidence of bulk easy glide (slip on a single system), although the strain bursts are the equivalent on the micron scale with small occurrences of slip on a single system. These are small compared to strain bursts observed in other studies (such as those shown in figure 42). As there is no macro easy glide, it is unlikely this is due to cantilever beams being misorientated far from the $< 100 >$ directions.

Assuming the same reasoning as with the the four point bend specimens (page 146), the first active slip plane is likely to be one of type $\{112\}$. The two slip systems of this type subjected to a [100] compressive axis will be $(21\bar{1})[1\bar{1}1]$ and $(2\bar{1}\bar{1})[111]$, according to the stereogram shown in figure 133, both with Schmid factors of 0.47. The highest stress value is known to be compressive, near the fixed end of the beam, by observing the FEA model in figure 145. This

will be used in Section 6.3.2 for the calculation of dislocation flow stress.

6.3.2 Yield Behaviour

6.3.2.1 Defining the yield point As with four point bend tests, to define the yield point in a consistent way which removes user error or bias, the LINEST function in Microsoft Excel was used. At the point at which the slope drops by 2% or more from the measured elastic gradient, the sample is considered to have yielded. This corresponded to an outer fibre yield strain in the range 0.004 to 0.017.

Figure 148 shows the yield stress-temperature relationship of the single crystal Mo microcantilever bend tests calculated using simple beam theory and finite element analysis. The simple beam theory values are all 20 to 39% higher than the finite element values. The characteristic knee in yield stress is clearly present at approximately room temperature.

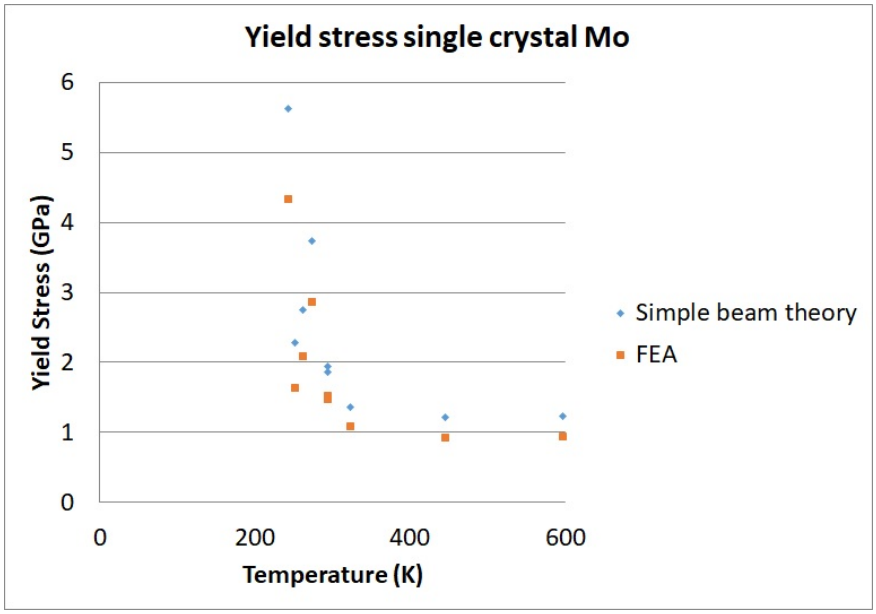


Figure 148: Yield stress calculated using simple beam theory and finite element analysis. The simple beam theory values are all 20 to 39% higher than the finite element values. The characteristic knee in yield stress is clearly present at approximately room temperature.

Figure 149 shows the microcantilever yield stresses (calculated using FEA) plotted with the single crystal four point bend test results. The microcantilevers had an average height of 4.32μm, whereas the four point bend specimens had an average height of 1160μm.

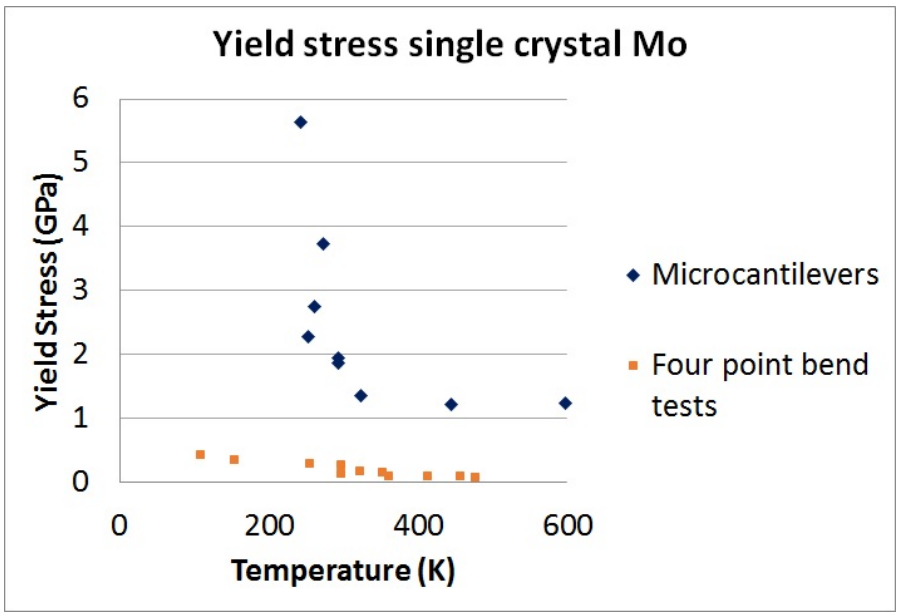


Figure 149: Microcantilever yield stresses (calculated using FEA) plotted with the single crystal four point bend test results.

6.4 Discussion

This chapter discussed microcantilever bend testing of single crystal Mo across a range of temperatures from -31 to 571°C. Although all bend tests (both bulk and microscale) were orientated normal to the {001} cleavage plane, there were no fractures even at the lowest temperatures. Previous work by Durrans [96] showed a strong brittle-ductile transition over this temperature range, with fractures readily occurring when the samples were notched. None of the bend specimens in this study were notched, so it is apparent that notching is essential to encourage Mo to fracture, despite the much reduced plasticity (higher stress required for dislocation motion) at low temperatures.

The comparison of yield stress values from the four point bend tests and microcantilever bend tests clearly reveal the presence of a size effect - smaller bend specimens required the application of much higher stresses to initiate dislocation movement. This was seen on figure 149. The four point bend test specimens were well within the bulk length scale of Mo. A quantitative size effect study would require the measurement of a large range of specimen dimensions, similar to the one carried out for indentation in this thesis. However, for FIB-milled microcantilevers, this would be extremely time consuming, especially when milling larger specimens.

The measured characteristic length scales for indentation (figure 110) suggest the depth at which size effect becomes significant increases from approximately 1μm at -30°C to approximately 2.5μm at 800°C. However, these results suggest that the characteristic length scales for bend testing must be much larger, as the microcantilever bend tests have clearly elevated yield stresses, and they are larger than the characteristic length scales at all temperatures (particu-

larly at low temperature).

It has previously been found by Wang [271] that strain gradient effects are significant when the beam thickness becomes comparable to the intrinsic material length, which would contradict this. However, Wang also suggested that the larger the beam thickness-to-length ratio, the larger the strain gradient effects, and beams with a length ten times the thickness will see a minimal size effect. The beams in this study had aspect ratios of 7.98 ± 1.5, and so according to Wang, they would not be strongly affected by strain gradient effects.

Additionally, the hardness-depth power law exponents measured from indentation in figure 114 showed that the indentation size effect increased with temperature up to the knee temperature. The divergence of micron scale and bulk scale yield stresses is very large below T_K, again disagreeing with the indentation results. A full size effect study into bend testing in Mo might help to explain this.

Motz et al. [187] suggested some additional mechanisms that might elevate the flow stress of small bend specimens that may explain the large flow stresses seen here. Firstly, a complex dislocation arrangement may have to accommodate the strain gradient, which results in a higher dislocation density and therefore in a higher flow stress. Secondly, a reduction of the number of available dislocation sources in the small deformed volume may hinder plastic deformation (the activity of these few sources has to be very high and due to the back stress of the emitted dislocations the source can become inactive. In this case a higher applied stress is necessary to re-activate the source again – the flow stress increases). Lastly, other dislocation arrangements such as pile-ups may cause high pile-up stresses shielding dislocation sources. In metallic single crystals, the defect density is commonly very small and this effect can become important. Thus, reducing the deformed volume decreases the probability of finding a sufficient number of dislocation sources and the strength of the material increases (dislocation starvation) [187]. In this study, although the microcantilever bend specimens were found to sustain higher stress, they were too large to meet the condition of dislocation starvation [212].

There are several differences between the microcantilever and four point bend tests other than size considerations that may affect the mechanical test results. Firstly, the four point bend tests use specimens with a rectangular cross-section and the microcantilevers have a pentagonal cross-section. The second moment of area does take this into account but this will not necessarily remove all errors. The matchstick specimens are measured at three places along their length and width by a screw gauge micrometer, and can be examined closely by eye from all directions to check for polishing asperities or irregularities that may influence their plastic behaviour. The microcantilevers are also measured in several places but this is carried out in an

SEM, with their height measured by tilting. If focus is not perfect or if the image is stigmated, this can lead to errors in measurement.

Due to the nature of a FIB-milled specimen (top of beam level with surface, material "dug" away to form testpiece), it is impossible to see the underside of a cantilever. A quick glance at the trenches around a cantilever will show regions of sputtered and redeposited metal, in characteristic uneven bands up the sides of the trench. On any microcantilever the state of the undercut sides is not fully known and there may be errors in the geometry used for analysis as a perfect, uniform pentagonal cross-section was assumed.

Additionally, FIB damage on the cantilever surface is unavoidable - Ga^+ ions go into solution with Mo, influencing surface properties [227]. Using a lower beam current helps to reduce the depth of damage but this is not always possible. Time on the FIB is restricted due to a high number of users and compromises of beam current size have to be made. On the other hand, four point bend matchstick specimens are polished using abrasive silicon carbide mats followed by diamond paste. This will result in cold work on all specimen surfaces, again potentially affecting plastic properties.

7 Overall Discussion

7.1 Thermal Dependence of Flow Stress

All four mechanical testing techniques covering temperatures from -196 to 880°C and from the nanoscale (in indentation) and the microscale (in bend testing) to the bulk scale resulted in data of the form 'flow stress vs temperature' after some data manipulation. All techniques showed a transition from a region of high thermal dependence of flow stress at low temperature to a low thermal dependence at high temperature, with this change occurring over a knee temperature T_K.

It is common to all four techniques that there are not enough data points around the transition from a strong to a weak thermal dependence to pinpoint a transition temperature from simple observation of the graph. However, most data sets have two distinctly different gradients at high and low temperature. A range of points away from the transition region was chosen from each separate behavioural regime, and a best-fit line calculated using the least squares fit method. This is demonstrated schematically in figure 150.

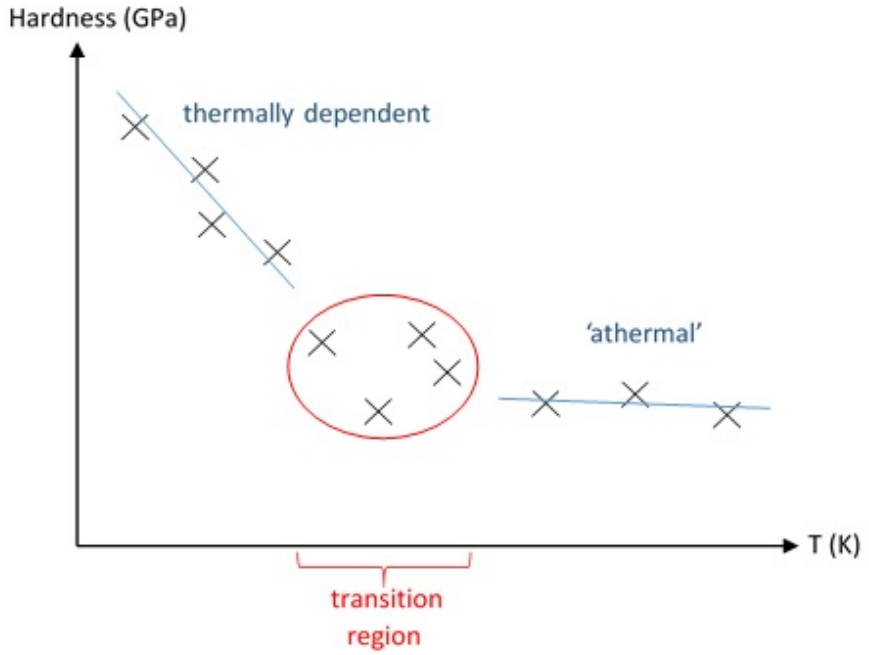


Figure 150: Schematic representation of a typical data point distribution, showing the thermally dependent region, the scatter around the transition and the 'athermal' region.

At temperatures above the knee temperature, T_k, a linear relationship was assumed. This appeared to be a good fit in all cases (R^2 values 0.47 to 0.98). At temperatures below T_k, Seeger [25] deduced the thermally-dependent component of flow stress in BCC metals (the 'apparent flow stress') had a squared relationship when strain rate was constant:

$$\sigma^* \propto (T_k - T)^2 \tag{70}$$

with the actual flow stress equal to the sum of the 'athermal' component and the apparent flow stress:

$$\sigma = \sigma_M + \sigma^* \tag{71}$$

As outlined in the literature review, the 'athermal' component was found by Seeger to only vary weakly with temperature and strain rate (presumably due to the temperature dependence of the elastic moduli). Above the knee temperature, the temperature is high enough to negate the difference in mobility between screw and non-screw dislocations.
However, in some cases, there were too few data points to fit to a quadratic curve satisfactorily, and so a straight line fit was also used for this region (R^2 range 0.44 to 1.0) to prevent any spurious relationships.
T_k is widely accepted to be the point below which a variation of flow stress with temperature sets in [272]. As such, it was calculated simply in this study as the point at which the two straight lines crossed. σ_M (athermal flow stress) is taken as the stress at the highest temperature measured towards which the hardness asymptotically descends with increasing temperature.

A flow stress approximation from microhardness data is shown in figure 151a, and an approximation from nanoindentation data in figure 151b. These calculations were performed on nanoindentations of load 300mN. The flow stress values were calculated from hardness using Tabor's hardness relation:

$$H_v = 3\sigma_f \tag{72}$$

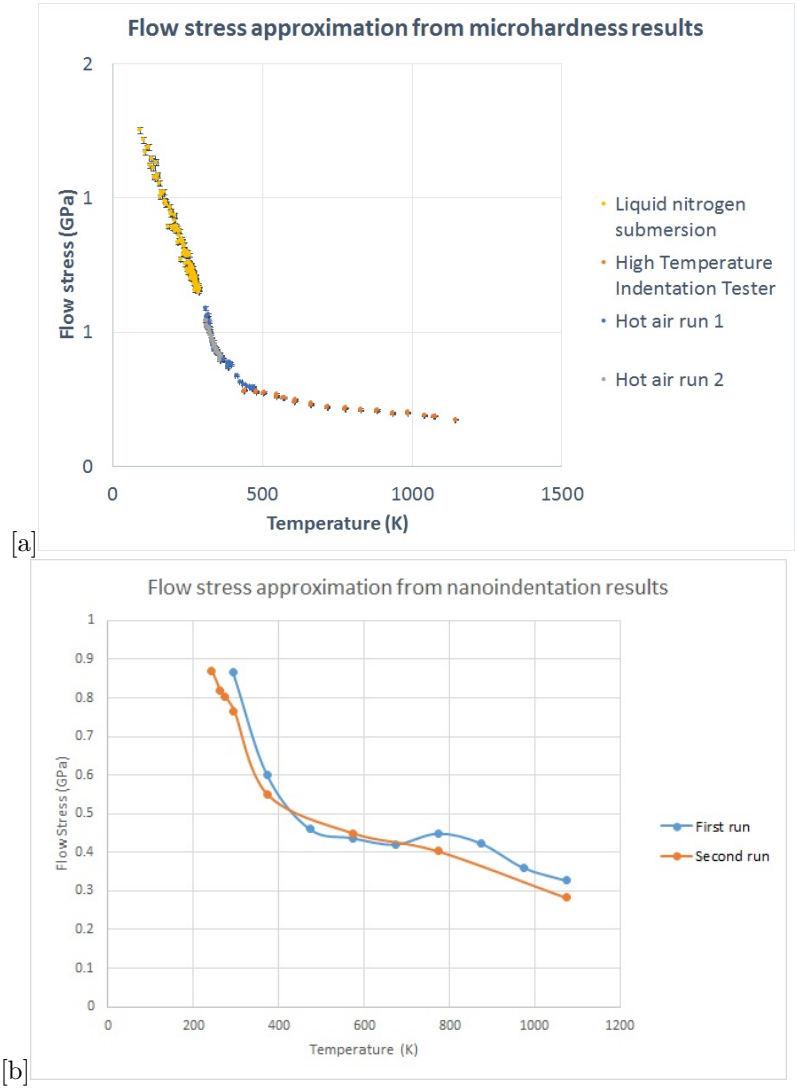
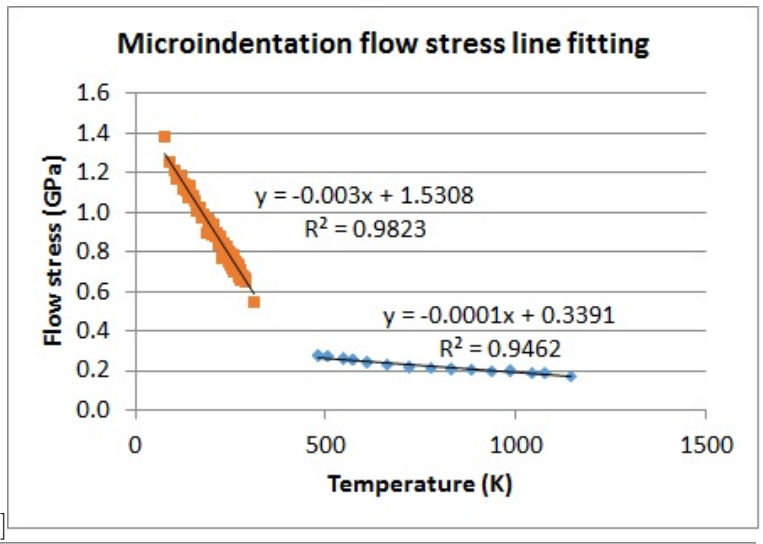


Figure 151: Flow stress approximation graphs for (a) microindentation and (b) nanoindentation.

Figure 152 shows flow stress approximation graphs for (a) microindentation and (b) nanoindentation with the points around the transition removed. A trend line has been fitted to the high and low temperature regimes. The trend line equations are shown next to each regime. Figure 153 shows the same for (a) single crystal four point bend tests, (b) polycrystalline four point bend tests and (c) microcantilever four point bend tests.

[a]


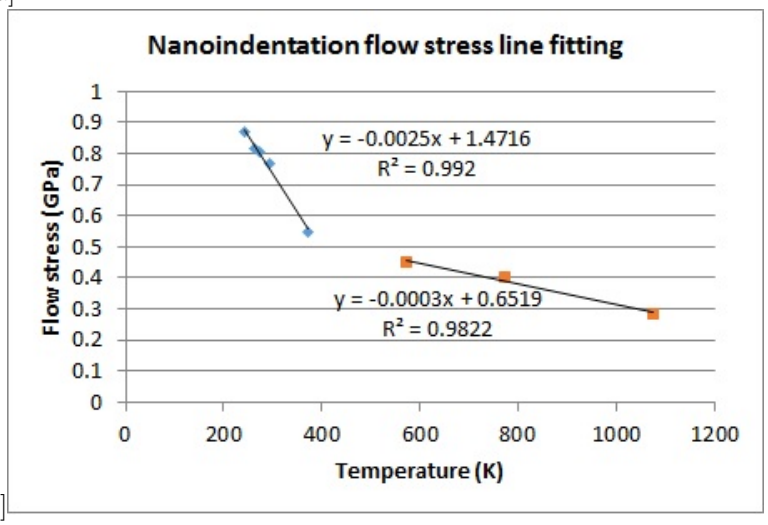
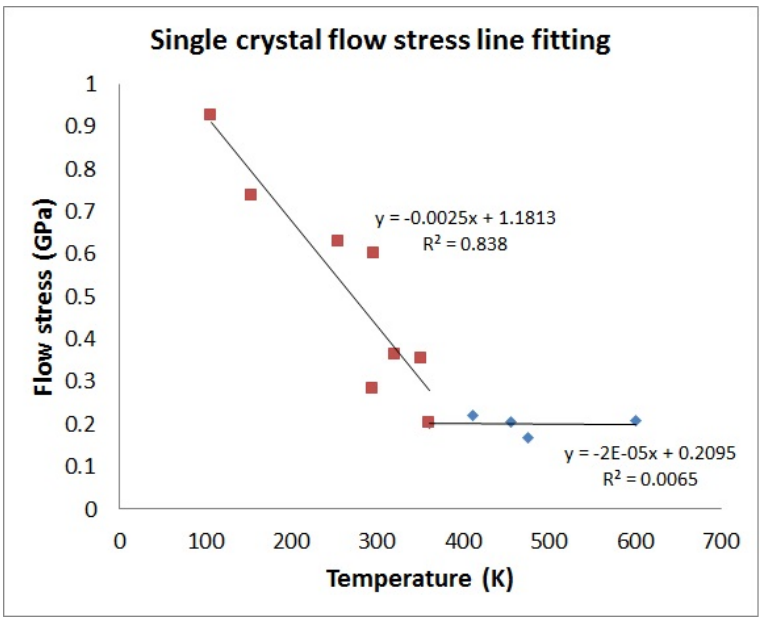
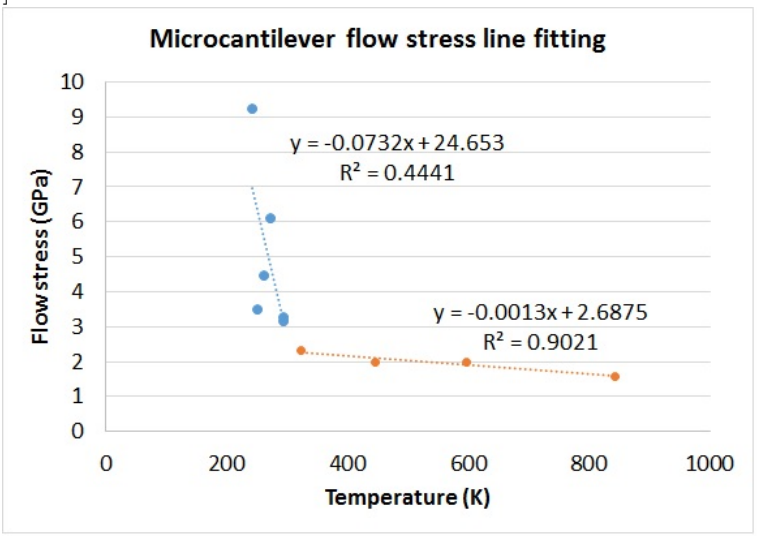
[b]


Figure 152: Flow stress approximation graphs with the points around the transition removed. A trend line has been fitted to the high and low temperature regimes. The trend line equations are shown next to each regime. (a) microindentation and (b) nanoindentation.



[a]



[b]

Figure 153: Flow stress graphs with the points around the transition removed. A trend line has been fitted to the high and low temperature regimes. The trend line equations are shown next to each regime. (a) single crystal four point bend tests and (c) microcantilever four point bend tests.

The flow stress-temperature relationships $\sigma_{flow} = f(T)$ for each technique above and below the knee temperature T_K are summarised in the following table along with the estimated value for T_K. The error on either side of the calculated knee arises because the change in gradient covers a temperature range. A small amount of error in the calculation of this point is to be expected due to the scatter around the best fit straight lines.

Table 6: Flow stress-temperature relationships $\sigma_{flow} = f(T)$ above and below the knee temperature T_K for all mechanical testing techniques on single crystal Mo

	T_K (K)	$\sigma_{flow} = f(T)$ below T_K	$\sigma_{flow} = f(T)$ above T_K
Microhardness testing	411 ± 85K	-0.003T+1.53	-0.0001T+0.34
Nanoindentation	375 ± 100K	-0.0025T+1.5	-0.0003T+0.65
Four point bend testing	395 ± 25K	-0.0025T+1.18	-0.00002T+0.21
Microcantilevers	306 ± 25K	-0.073T+24.7	-0.0013T+2.69

The T_K values are all within 105K for the four test techniques, although the microcantilever T_K may be considered an outlier as both indentation and the four point bend testing values are grouped together. Additionally, the thermal dependence of flow stress is considerably higher for microcantilever testing compared to the other techniques, and the athermal stress is also much higher. An elevated flow stress is to be expected as the microcantilevers will have been subject to size effect, as explained in the previous chapter.

The flow stress has a stronger thermal dependence above T_K for 300mN nanoindentations than microindentations, potentially as this load is still in the region affected by size dependence. A better measure of the athermal region would consider points of the same depth, not the same load, but this information would require further experimentation. It may also be possible that the nanoindentation data would show a relationship similar to the microcantilever data if the depth were to be kept constant, rather than the maximum load.

7.1.1 Estimation of Flow Stress at Absolute Zero

The value of the Peierls stress is generally assumed to be the intercept of the flow stress line extrapolated to absolute zero minus σ_M, the athermal flow stress [272], as the Peierls mechanism restricting kink-pair movement only acts beneath the knee temperature:

$$\sigma_P = \sigma(T)_{T=0} - \sigma_M \tag{73}$$

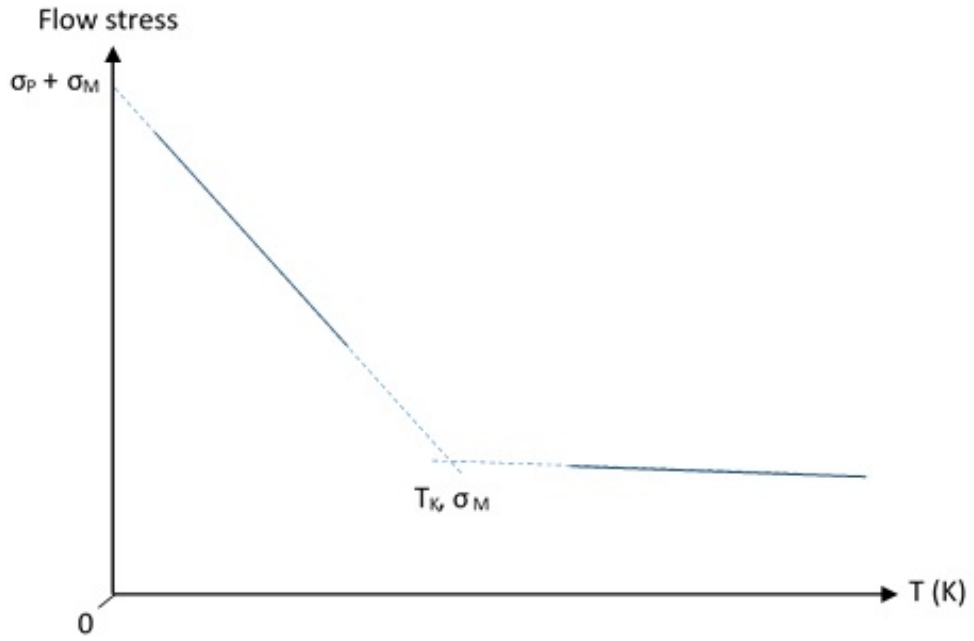


Figure 154: Flow stress at 0K (σ_M) calculated by extrapolating the temperature-dependent flow stress function to a temperature of 0K and subtracting the athermal component of stress (σ_M). T_K is the knee temperature, from which the athermal component of stress is collected.

As a measure of absolute zero flow stress that can be compared across indentation and bending experiments, the flow stress at absolute zero was estimated, as shown in figure 154. Two notable sources of error may be present when using this method - the trend line fitted to a small number of points, and the fact that a linear fitting function was used rather than quadratic. Any error in the line fit that could have been improved by performing repeat tests or additional test temperatures will lead to deviation from the true zero temperature flow stress. The magnitude of the athermal flow stress and the gradient of the thermal dependence will both have a large influence on this error.

The value of flow stress at 0K was found to be 1.53GPa for microindentation ('bulk' indentation). With an 'athermal' flow stress of 0.17GPa, that gives a value of 1.36GPa for zero temperature flow stress.
In the case of microhardness testing, a large number of data points were taken in both regimes, and the line fits are very close (R^2 values of 0.982 and 0.946). As an approximation, the errors in this line fit can be estimated as (100-98.2)%=1.8% using these R^2 values for the low temperature regime and (100-94.6)%=5.4% for the high temperature regime. 1.8% of 1.53 is 0.028GPa. 5.4% of 0.17 is 0.009GPa. Applying these errors to the zero temperature flow stress gives a value of 1.36±0.037GPa.

The value of flow stress at 0K was found to be 1.47GPa for nanoindentation. With an 'athermal' flow stress of 0.28GPa, that gives a value of 1.19GPa for zero temperature flow stress. In the case of nanoindentation testing, a small number of data points were taken in both regimes, although the line fits are very close (R^2 values of 0.992 and 0.982). As an approximation, the errors in this line fit can be estimated as (100-99.2)%=0.8% using these R^2 values for the low temperature regime and (100-98.2)%=1.8% for the high temperature regime. 0.8% of 1.47 is 0.012GPa. 1.8% of 0.28 is 0.005GPa. Applying these errors to the zero temperature flow stress gives a value of 1.19±0.017GPa.

The value of flow stress at 0K was found to be 1.18GPa for single crystal bend test samples. With an 'athermal' flow stress of 0.21GPa, that gives a value of 0.97GPa for zero temperature flow stress. Similarly to the polycrystalline four point bend tests, a small number of data points were taken in both regimes. Neither of the line fits are very close (R^2 values of 0.838 and 0.0065). As an approximation, the errors in this line fit can be estimated as (100-83.8)%=16.2% using these R^2 values for the low temperature regime and (100-0.65)%=99.35% for the high temperature regime. 16.2% of 1.18 is 0.19GPa. 99.35% of 0.21 is 0.21GPa. Applying these errors to the zero temperature flow stress gives a value of 0.97±0.40GPa.

The value of flow stress at 0K was found to be 24.7GPa for microcantilever bend tests. With an 'athermal' flow stress of 1.57GPa, that gives a value of 23.1GPa for zero temperature flow stress. In the case of microcantilever bend testing, a small number of data points were taken in both regimes. Neither of the line fits are very close (R^2 values of 0.444 and 0.902). As an approximation, the errors in this line fit can be estimated as (100-44.4)%=55.6% using these R^2 values for the low temperature regime and (100-90.2)%=9.8% for the high temperature regime. 55.6% of 24.7 is 13.7GPa. 53.4% of 1.57 is 0.15GPa. Applying these errors to the zero temperature flow stress gives a value of 23.1±13.85GPa.

These values are summarised in the following table:

Table 7: Zero temperature flow stress values for all mechanical testing techniques on single crystal Mo.

	Zero temperature flow stress σ_p (GPa)
Microhardness testing	1.36±0.037
Nanoindentation	1.19±0.017
Four point bend testing	0.97±0.40
Microcantilevers	23.1±13.85

It is notable that Durrans found the ductile-brittle transition in this strain rate range to

occur between -40 and 10°C for four point bend testing, as shown in figure 22. This fits with the condition that T_{DBT} is always less than T_K from [29]. As with the thermal dependence of flow stress, the microcantilever data is much different from the two indentation techniques and the bulk bend testing. As these values are an estimation of the zero temperature Peierls stress, they suggest that whichever mechanism elevates the flow stress at each test temperature may continue to act even if the specimen were to be cooled to absolute zero.

7.2 Activation Energy for Deformation

From the data acquired by mechanical testing over a temperature range, the apparent activation energy of deformation can be determined. This is the total activation energy from any of multiple mechanisms that can act during the deformation of the sample. Establishing values for the activation energies can give insight into the rate controlling mechanism.
The apparent activation energy can be calculated using the modulus-compensated hot hardness analysis of Sherby [273] and Armstrong [274].

$$\frac{H}{E} = G'.exp\left(\frac{Q_c}{nRT}\right) \tag{74}$$

A value of 8.31 $Jmol^{-1}K^{-1}$ for the gas constant R was used. As Young's modulus varies with temperature, temperature-dependent values were used. These were taken from Köster's analysis of elastic constants of various metals, including molybdenum [88]. These were extracted by Wheeler [275] and are shown in Section 1.2.4.

The gradient of a ln(H) vs 1/T plot (normalised using Young's modulus E and melting point T_m) can be used to find the activation energy of deformation [275]. The plot for micro-hardness testing to 4.9N of single crystal molybdenum is shown in figure 155 and the plot for nanoindentation testing to 0.3N is shown in figure 156.

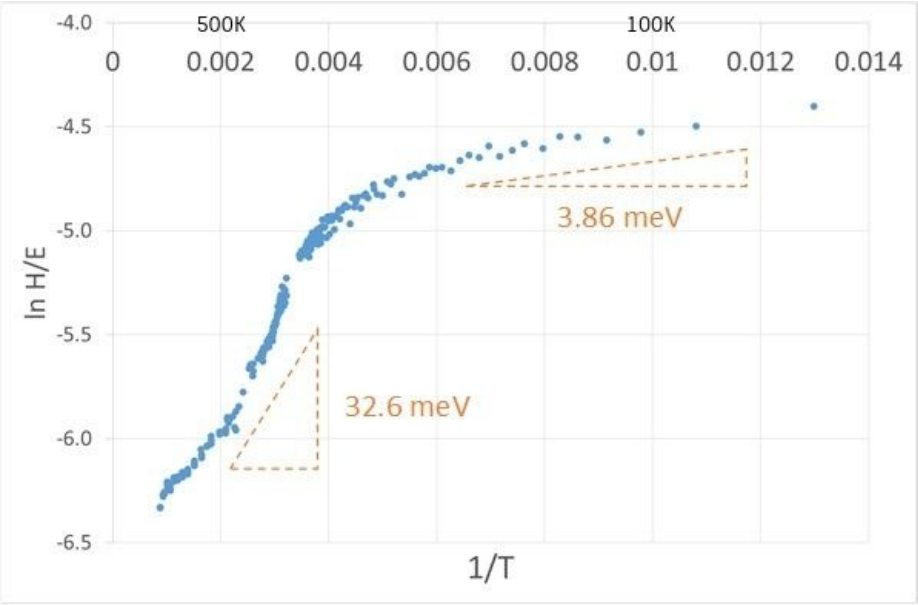


Figure 155: Arrhenius plot for the calculation of activation energy from a hardness - temperature graph, activation energy is equal to the gradient of ln(H/E) vs 1/T.

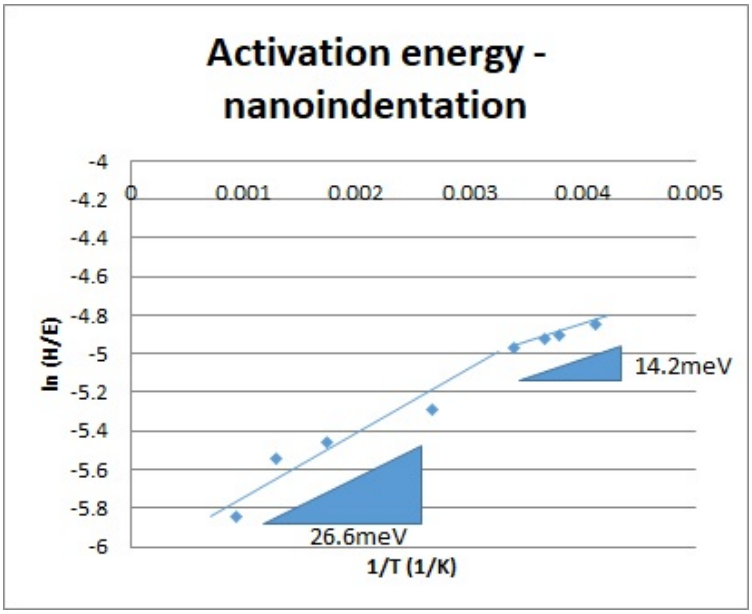


Figure 156: Arrhenius plot for the calculation of activation energy from a nanoindentation hardness - temperature graph, activation energy is equal to the gradient of ln(H/E) vs 1/T.

For consistency, the bend testing yield stress results were converted to hardness values. (The use of yield stress in this calculation would in fact not change the gradient of the graph - it would only cause a translation along the y-axis.) The Tabor relationship between yield stress and hardness was used [108]:

$$H \approx 3\sigma_y \tag{75}$$

The Meyer hardness values for four point bend tests are shown in figure 157, and those for microcantilever bend tests in figure 158.

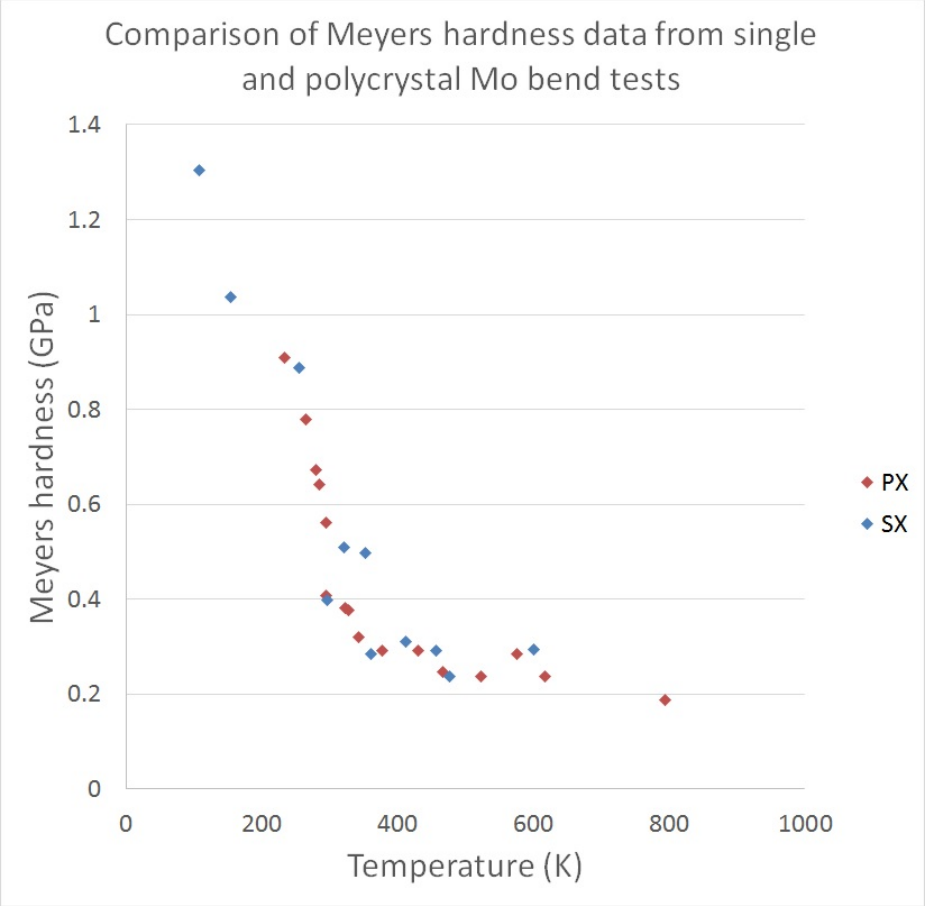


Figure 157: Meyer hardness approximation from bend test yield stress values for single crystal and polycrystalline molybdenum.

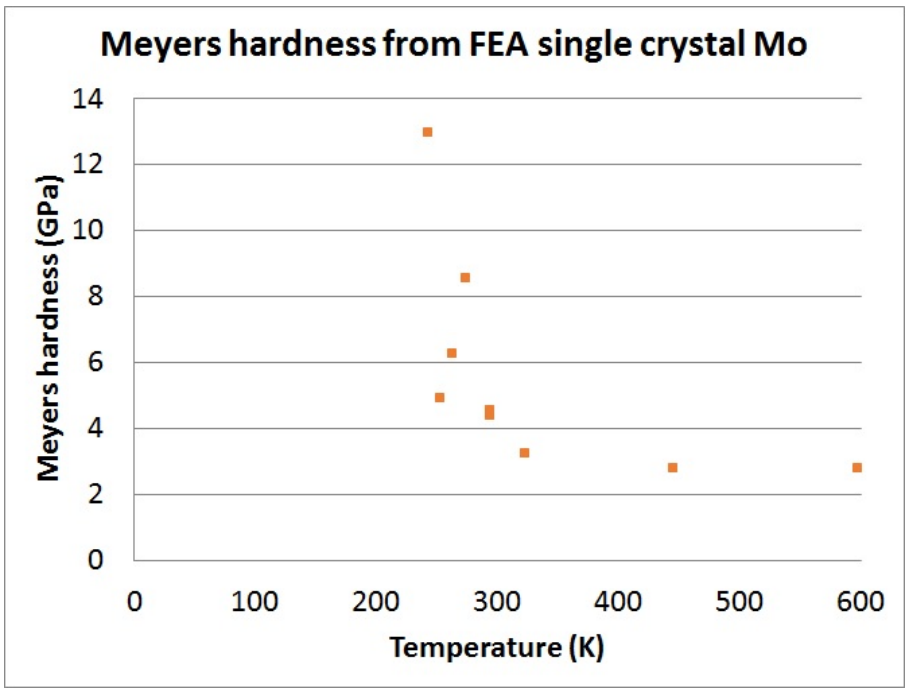


Figure 158: Meyer hardness approximation from cantilever bend test yield stress values.

The H vs 1/T plots for four point bend testing and microcantilever bend testing are shown in figures 159 and 160.

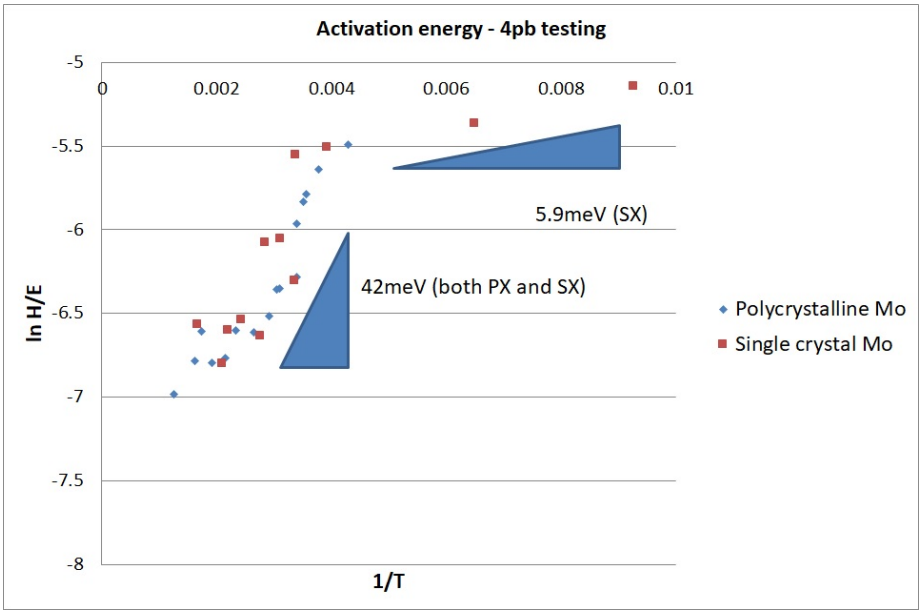


Figure 159: Arrhenius plot for the calculation of activation energy from the four point bend Meyer hardness - temperature graph, activation energy is equal to the gradient of ln(H/E) vs 1/T in each regime.

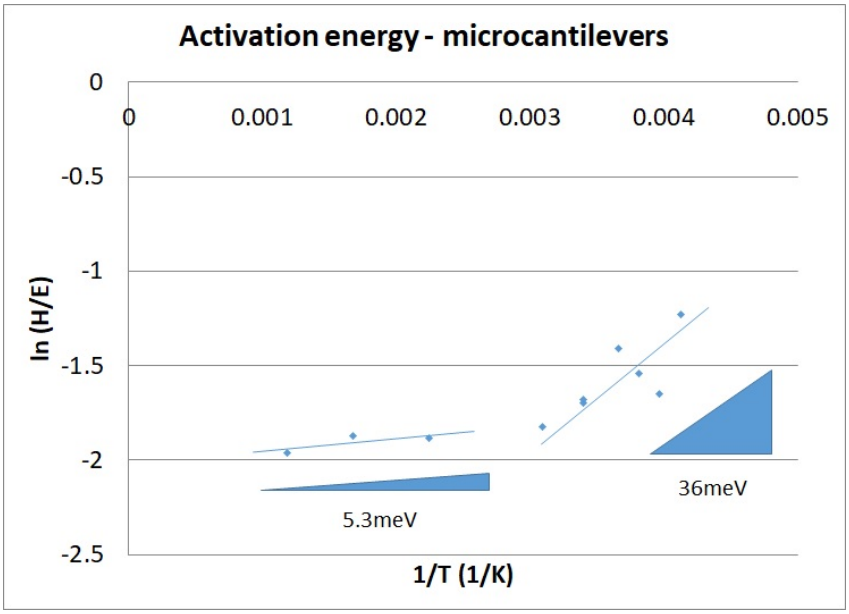


Figure 160: Arrhenius plot for the calculation of activation energy from the microcantilever bend Meyer hardness - temperature graph, activation energy is equal to the gradient of ln(H/E) vs 1/T in each regime.

The deformation in each case is separated into two regimes across this temperature range, made up of two straight lines on the hardness-temperature graph. As such, their differing gradients correspond to two different activation energies and are treated separately. One exception was the polycrystalline data from four point bend testing, for which there were not enough data

points far enough below T_K to resolve a second activation energy regime.

The following is used to extract the activation energy from the graph:

$$ln\left(\frac{H}{G'E}\right) = \frac{Q_c}{RT} \tag{76}$$

$$ln\left(\frac{H}{E}\right) + ln\left(\frac{1}{G'}\right) = \frac{Q_c}{R}\frac{1}{T} \tag{77}$$

$$ln\left(\frac{H}{E}\right) = \frac{Q_c}{R}\frac{1}{T} - ln\left(\frac{1}{G'}\right) \tag{78}$$

and so the gradient of a ln(H/E) vs 1/T graph is equal to $\frac{Q_c}{R}$, from which the activation energy Q_c can be extracted.

these activation energies are also a great deal lower than the literature data for activation energy of the kink-pair mechanism in molybdenum (510 - 630meV [99, 100, 96]). These are summarised in table 8.

Table 8: Activation energies for all mechanical testing techniques on single crystal Mo

	T_K (K)	Activation energy below T_K (meV)	Activation energy above T_K (meV)
Microhardness testing	411 ± 85K	3.86	32.6
Nanoindentation	375 ± 100K	14.2	26.6
Four point bend testing	395 ± 25K	42	5.9
Microcantilevers	306 ± 25K	36	5.3

Every activation energy value measured using this technique was a great deal lower than the literature data for activation energy of the kink-pair mechanism in molybdenum:

1. Prekel's work on high purity single crystal Mo found a kink-pair formation energy of 630meV [99], calculated using an etch-pitting technique to measure dislocation velocities at different strain rates in three-point-bend tests

2. Conrad's modelling work [100] based on macrostrain deformation dynamics gave a value of 640meV

3. Durrans [96] found an average value of 510meV for E_{DBT} of polycrystalline Mo.

.

This difference suggests that another factor may be the rate controlling deformation mechanism. The apparent activation energy of deformation is the total activation energy from any of multiple mechanisms that can act during the deformation of a metal, although in the case

of tensile deformation of BCC metals, the main contribution comes from the formation of a kink-pair.

However, the situation is slightly different for indentation (and bend) testing. Without a long hold period (non-creep), it is not simply the dislocation mobility in the form of kink pair formation and motion that controls the temperature dependence of indentation behaviour. During an indentation, the pressure on the sample falls with increasing penetration, until the work-hardened flow stress of the material beneath the indentation matches the indentation pressure. For an indenter with a sharp tip, the strain varies strongly between different locations in the deformation zone under the indenter. For large-scale Vickers hardness tests, an estimation is that hardness is related to uniaxial flow stress at about 8% strain[108]. As the average level of strain underneath the indentation is so high, there will be a large amount of work hardening, and the volume of work hardened material will increase as penetration increases. Therefore, it is possible that the strength of the interactions between dislocations responsible for the work hardening, and their temperature dependence, is the controlling phenomenon.

The stresses in the region under the indentation controlling the hardness are very high. They are high enough such that the stress to move a dislocation is not quite reached. There is, therefore, a considerable reduction in the energy barrier faced by any process controlling plasticity. This is due to the fact that the work is already taken up by the stress, which is pushing dislocations (in the form of kinks) up against the energy barrier. This considerably reduces the thermal component of energy required to move the dislocation over the barrier and down the other side.

This can be further explained using a dislocation mobility equation. Dislocations are moved over a small time-step, according to a screw dislocation velocity law based on the nucleation of kink pairs [46, 68]:

$$v_{dis} = v_0 exp\frac{-E_{kp}(\tau)}{kT}, E_{kp}(\tau) = 2H_{kp} - 2\alpha\tau^{1/2} \tag{79}$$

where v_{dis} is dislocation velocity, where $2\mathrm{H}_{kp}$ is the energy required to nucleate a kink pair at zero stress and τ is the stress on each dislocation.

It is possible to write the exponent in the velocity law, equation 79, in the form $E_{kp}(\tau) = 2\alpha\tau^{1/2} = 2H_{kp} - \tau V_a$ [276]

The activation volume, V_a can be understood as the activation area swept by a dislocation segment of given length over an activation distance of given length multiplied by the Burgers vector of the dislocation, or the work done by a stress field of the mechanism during a successful activation event [277].

In BCC metals it has been found to be equal to $2V_{kp}$ where V_{kp} is the activation volume of kink-pair formation [276]. Therefore, it can be expressed as $b.l.d$, where b is the magnitude of

the Burgers vector, l is the length of the dislocation segment involved in the thermal activation (the critical span between two kinks in a kink pair) and d is the obstacle thickness. The critical span between two kinks decreases with increasing stress.
This equation shows that the mobility of a dislocation will be increased by the application of a stress in a direction that tends to move the dislocation. The applied stress subtracts from the activation energy required to push the dislocation over the energy hill, or Peierls barrier.
It has also been proposed that at inertial effects play an increased role in the dynamics of dislocation motion at elevated stress, as the energetic barriers for kink nucleation are so reduced that a single nucleation event can trigger a series of subsequent nucleation events as the dislocation springs into motion. Such an avalanche of events would lead to an increased traversal distance per nucleation event and, therefore, a lower than expected activation energy for dislocation motion [278, 279].

As demonstrated in the explanation of the strain gradient plasticity model on page 119, the local strains under an indentation in a metal are greater with decreasing indentation size, as is the case in nanoindentation testing. Therefore, it might be expected that these result in higher stresses, increasing the proportion of the Peierls barrier taken up by the stress factor in equations 79 onwards and decreasing the thermal activation component. However, the thermal activation energy is only lower above the knee temperature. Below the knee temperature, it is significantly higher. One explanation for this might be the choice of constant load rather than constant depth as the maximum loading condition. The microhardness tests were all within the 'bulk' size range, and so size effect will not have had an effect. The nanoindentations were at the higher end of the 'size effected' range, with the higher temperature tests affected more strongly. It is perhaps not a fair test to perform the same calculation on one set of data that has no size effect, and another set that does, particularly when the calculation looks at the data points relative to each other.

The activation energies for bend testing are much higher than indentation below T_K but much lower above T_K. The bend testing activation energies for microscale and bulk samples are very similar to each other, so size does not appear to have a significant effect on activation energy. However, the stress state of a sample undergoing bend testing must have an effect on the thermal energy required to move a dislocation, or in this case, a pair of kinks.

8 Future Work

The work presented in this DPhil thesis has contributed to the understanding of the temperature dependence of the mechanical properties of molybdenum, particularly plastic behaviour. An area that was previously very sparse was the effect of deformation volume, or "size effect". It is recommended that any future testing of Mo on the micron scale (or below) spans a range of depths, particularly microcantilever bend testing, as it is challenging to infer any bulk behaviour from the results of a single beam width or indentation depth. This is applicable to the testing of thin irradiated layers.

The potential application of molybdenum as a first wall material necessarily means it will suffer radiation damage in service. The effect of radiation damage on the mechanical properties will likely depend on the the temperatures and fluences to which specimens are exposed. Similar work involving the production of radiation damaged specimens using self ion implantation [138] has used nanoindentation and microcantilevers as demonstrated in this thesis.

Iradiation of samples would also likely produce a high density of disslocations and dislocation sources. This provides an interesting enviroment in which to investigate the size effect and determine the extent to which it is dislocation source density dependent.

This work could be further expanded to cover the assessment of transmutation alloys of molybdenum. Parts subject to high neutron fluences will form new chemical elements [12], which act as alloying additions and may have significant effects on material properties. Investigation of transmutation alloys (carefully designed to simulate the chemcial makeup of molybdenum parts at various points in service lifetimes) which have additionally undergone self ion implantation could provide very valuable information about the suitability of molybdenum for fusion applications involving long lifetime components. Again nanoindentation and microcantilevers would be appropriate tools for carrying out this work.

Experimentation on samples that have undergone neutron irradiation would allow the most accurate characterisation possible, and also act as a way to compare the properties of genuinely irradiated samples and samples that have been designed to simulate irradiation (transmutation alloys and self ion). The high acivity levels of netron irradiated speciens would necessitate the use of small scale methods to reduce activity in test equipment.

By the use of isotopic refinement, nuclides that contribute to unwelcome transmutations can be removed, leaving behind a material composition designed to stay radioactive for a matter of decades rather than hundreds of thousands of years, reducing both decommissioning costs and environmental risks. Damage to molybdenum caused by radiation in the fusion reactor such as lattice displacements, hydrogen and helium implantation and transmutation can be simulated using either fission neutron irradiation or heavy ion irradiation.

Research expanding on the assessment of the temperature-dependent plasticity of molydbenum covered in this thesis to isotopically refined samples would go a long way to further the understanding of the suitability of the material for use in nuclear fusion. It would be useful to simulate the effect of fusion specific radiation on isotopically refined molybdenum, using self-ion and neutron irradiation. The application of the techniques used in this thesis and comparison with the information on pure, unirradiated Mo covered in this thesis applied to isotopically-refined, irradiated samples will give a clear, realistic picture of the mechanical properties of molybdenum used in the reactor.

References

[1] Webpage for the ITER organisation: 'The Divertor'. *http://www.iter.org/mach/divertor*, 2013.

[2] Culham Centre for Fusion Energy. JET's ITER-Like Wall. *http://www.ccfe.ac.uk/jet_ilw.aspx*, 2011.

[3] MI Budd. Estimated influence of neutron damage on the divertor protection material during the physics phase of net. *Journal of Nuclear Materials*, 170(2):129–133, 1990.

[4] N. Baluc. Materials for fusion power reactors. *Plasma Phys. Controlled Fusion*, page B165, 2006.

[5] R.D. Stambaugh P.C. Stangeby C.P.C. Wong A.W. Leonard, A.M. Garofolo and V.S. Chan. A fusion development facility to test divertor and pfc solutions for demo. *Submitted to the DOE ReNeW Process for Posting on the ReNeW Website*, 2009.

[6] ITER website. ITER iter. *https://www.iter.org/mag/3/22*, 2019.

[7] Marek Rubel. Fusion neutrons: Tritium breeding and impact on wall materials and components of diagnostic systems. *Journal of Fusion Energy*, pages 1–15, 2018.

[8] EFDA. Completion of irradiated divertor mock-ups and material sample testing, 2004.

[9] K. Gibson. Plasma-Materials Interactions. *York DTN Course*, 2013.

[10] JW Connor, A Kirk, and HR Wilson. Edge localised modes (elms): Experiments and theory. In *AIP Conference Proceedings*, volume 1013, pages 174–190. AIP, 2008.

[11] S; Barabash V; Amzallag C; Escourbiac F; Durocher A; Merola M; Linke J; Loewenhoff T; Pintsuk G Hirai, T; Panayotis et al. Use of tungsten material for the ITER divertor. *Nuclear Materials and Energy*, 9:616–622, 2016.

[12] M. Gilbert. Culham Centre for Fusion Energy. *Personal Correspondance*, 2013.

[13] C. Burrows. Oxford University Materials Department. *Personal Correspondance*, 2013.

[14] DK Murdoch, Ch Day, P Gierszewski, R-D Penzhorn, and CH Wu. Tritium inventory issues for future reactors: choices, parameters, limits. *Fusion engineering and design*, 46(2):255–271, 1999.

[15] BL Cox and FW Wiffen. The ductility in bending of molybdenum alloys irradiated between 425 and 1000c. *Journal of Nuclear Materials*, 85:901–905, 1979.

[16] Steve Fetter, ET Cheng, and FM Mann. Long-term radioactive waste from fusion reactors: Part ii. *Fusion Engineering and Design*, 13(2):239–246, 1990.

[17] NP Taylor, CBA Forty, DA Petti, and KA McCarthy. The impact of materials selection on long-term activation in fusion power plants. *Journal of Nuclear Naterials*, 283:28–34, 2000.

[18] Azom website. Azom molybdenum (Mo) - properties, applications. *https://www.azom.com/properties.aspx?ArticleID=616*, 2017.

[19] Azom website. Azom tungsten (W) - properties, applications. *https://www.azom.com/properties.aspx?ArticleID=614*, 2017.

[20] Blanchard. . 2012.

[21] A. Nemeth. *Masters Thesis*, K.I.T., 2013.

[22] E. Schmid. *Proceedings of the International Congress on Applied Mechanics*, Delft:342, 1924.

[23] University of Cambridge DoITPoMS, TLP Library. Slip geometry: the critical resolved shear stress, 2013.

[24] T Edahiro, K Kouzai, and HY Yasuda. Mechanical properties and hardening mechanism of Fe-Al-Ni single crystals containing NiAl precipitates. *Acta Materialia*, 2012.

[25] Alfred Seeger. Why anomalous slip in body-centred cubic metals? *Materials Science and Engineering: A*, 319:254–260, 2001.

[26] Bruch und sproed-duktil-uebergang in polykristallinem wolfram: Einuss der mikrostruktur und der lastrate.

[27] B Šesták and A Seeger. Gleitung und verfestigung in kubisch-raumzentrierten metallen und legierungen. *Z. Metallkde*, 69:195–202, 1978.

[28] Duesberry. Dislocations in solids. *Elsevier Science Publishers*, 1989.

[29] V Io Trefilov, Yu V Milman, and ON Grigoriev. Deformation and rupture of crystals with covalent interatomic bonds. *Progress in Crystal Growth and Characterization*, 16:225–277, 1988.

[30] V Vitek†. Core structure of screw dislocations in body-centred cubic metals: relation to symmetry and interatomic bonding. *Philosophical Magazine*, 84(3-5):415–428, 2004.

[31] M.I. Ripley. The deformation and fracture of molybdenum and its dilute alloys (dphil thesis. 1981.

[32] L Hollang, D Brunner, and A Seeger. Work hardening and flow stress of ultrapure molybdenum single crystals. *Materials Science and Engineering: A*, 319:233–236, 2001.

[33] L Hollang, M Hommel, and A Seeger. The flow stress of ultra-high-purity molybdenum single crystals. *Physica status solidi (a)*, 160(2):329–354, 1997.

[34] R. Arsenault. *H. Herman (Ed.) Advances in Materials Research, Interscience, New York*, 2:91, 1968.

[35] C.J. McMahon. *H. Herman (Ed.) Advances in Materials Research, Interscience, New York*, 2:121, 1968.

[36] Peter M Anderson, John P Hirth, and Jens Lothe. *Theory of dislocations*. Cambridge University Press, 2017.

[37] Derek Hull and David J Bacon. *Introduction to dislocations*. Butterworth-Heinemann, 2001.

[38] AHW Ngan and M Wen. Dislocation kink-pair energetics and pencil glide in body-centered-cubic crystals. *Physical Review Letters*, 87(7):075505, 2001.

[39] M.; Joseph T.D. Giannattasio, A.; Tanaka and S.G. Roberts. *Phys. Scripta*, T128:87, 2007.

[40] A Seeger, P Veyssiere, LP Kubin, and J Castaing. Dislocations 1984. *CNRS, Paris*, page 141, 1984.

[41] Alfred Seeger. Peierls barriers, kinks, and flow stress: Recent progress: Dedicated to professor dr. haël mughrabi on the occasion of his 65th birthday. *Zeitschrift für Metallkunde*, 93(8):760–777, 2002.

[42] A. Giannattasio and S.G. Roberts. Strain-rate dependence of the brittle-to-ductile transition temperature in tungsten. *Philosophical Magazine*, 87(17):2589–2598, 2007.

[43] L Hollang, Y Waseda, and M Isshiki. Purification process and characterization of ultra high purity metals, 2001.

[44] M Werner. Temperature and strain-rate dependence of the flow stress of ultrapure tantalum single crystals. *Physica status solidi (a)*, 104(1):63–78, 1987.

[45] Alfred Seeger and Uwe Holzwarth. Slip planes and kink properties of screw dislocations in high-purity niobium. *Philosophical Magazine*, 86(25-26):3861–3892, 2006.

[46] F Ackermann, H Mughrabi, and A Seeger. Temperature-and strain-rate dependence of the flow stress of ultrapure niobium single crystals in cyclic deformation. *Acta metallurgica*, 31(9):1353–1366, 1983.

[47] U Holzwarth and A Seeger. Temperature and strain-rate dependence of the flow stress of ultrapure niobium single crystals. *Strength of Metals and Alloys.*, 1:577–584, 1991.

[48] D Brunner, J Diehl, A Seeger, V Paidar, and L Lejcek. The structure and the properties of crystal defects. *Ed. V. Paider and L. Lejcek, Elsevier Publ. Co., Amsterdam/New York*, page 175, 1984.

[49] D Brunner and J Diehl. Strain-rate and temperature dependence of the tensile flow stress of high-purity α-iron above 250 k (regime i) studied by means of stress-relaxation tests. *Physica status solidi (a)*, 124(1):155–170, 1991.

[50] D Brunner and V Glebovsky. The plastic properties of high-purity w single crystals. *Materials Letters*, 42(5):290–296, 2000.

[51] A Seeger and L Hollang. The flow-stress asymmetry of ultra-pure molybdenum single crystals. *Materials Transactions, JIM*, 41(1):141–151, 2000.

[52] AJ Garratt-Reed and G Taylor. Optical and electron microscopy of niobium crystals deformed below room temperature. *Philosophical Magazine A*, 39(5):597–646, 1979.

[53] D Vesely. Dislocation structure in molybdenum single crystals after deformation at 293 and 400 k. *Philosophical Magazine*, 27(3):607–621, 1973.

[54] R Gröger, AG Bailey, and V Vitek. Multiscale modeling of plastic deformation of molybdenum and tungsten: I. atomistic studies of the core structure and glide of 1/2¡ 111¿ screw dislocations at 0k. *Acta Materialia*, 56(19):5401–5411, 2008.

[55] R Gröger, V Racherla, JL Bassani, and V Vitek. Multiscale modeling of plastic deformation of molybdenum and tungsten: Ii. yield criterion for single crystals based on atomistic studies of glide of 1/2¡ 111¿ screw dislocations. *Acta Materialia*, 56(19):5412–5425, 2008.

[56] R Gröger and V Vitek. Breakdown of the schmid law in bcc molybdenum related to the effect of shear stress perpendicular to the slip direction. In *Materials Science Forum*, volume 482, pages 123–126. Trans Tech Publ, 2005.

[57] Y Aono, E Kuramoto, D Brunner, and J Diehl. Plastic behavior of high-purity molybdenum single crystals in tension and compression. In *Strength of Metals and Alloys (ICSMA 8)*, pages 271–276. Elsevier, 1989.

[58] JA Planell and F Guiu. Cyclic deformation of molybdenum single crystals i. mechanical behaviour. *Philosophical Magazine A*, 54(3):325–342, 1986.

[59] J. Samuels and S.G. Roberts. The brittle-ductile transition in silicon. i. (experiments). *Proceedings of the Royal Society of London. Series A, Mathematical and Physical Sciences*, 421:1–23, 1989.

[60] S.G. Hirsch, P.B.; Roberts and J. Samuels. The Brittle-Ductile Transition in Silicon (2) Interpretation. *Proceedings of the Royal Society of London Series A - Mathematical, Physical and Engineering Sciences*, 421(1860):25–53, 1989.

[61] E. Tarleton and S.G. Roberts. Dislocation dynamic modelling of the brittle-ductile transition in tungsten. *Philosophical Magazine*, 89(31):2759–2769, 2009.

[62] F.C. Serbena and S.G. Roberts. The brittle-to-ductile transition in germanium. *Acta Metallurgica et Materialia*, 42:2505—2510, 1994.

[63] H.S. Roberts, S.G.; Kim and P.B. Hirsch. *Proceedings of the 9th international conference on the strength of metals and alloys, Haifa*, page 783, 1991.

[64] Z.; Tarleton E. Giannattasio, A.; Yao and S.G. Roberts. Brittle-ductile transitions in polycrystalline tungsten. *Philosophical Magazine*, 90(30):3947–3959, 2010.

[65] S.G. Hirsch, P.B.; Roberts. *Phil. Trans. Roy. Soc. Lond.*, A355:1991, 1997.

[66] PB Hirsch, AS Booth, M Ellis, and SG Roberts. Dislocation-driven stable crack growth by microcleavage in semi-brittle crystals. *Scripta Metallurgica et Materialia*, 27(12):1723–1728, 1992.

[67] K. Fujita, S.; Maeda and S. Hyodo. *Philosophical Magazine*, 65:13, 1992.

[68] Dieter Brunner. Comparison of flow-stress measurements on high-purity tungsten single crystals with the kink-pair theory. *Materials Transactions, JIM(Japan)*, 41(1):152–160, 2000.

[69] S Fujita, K Maeda, and S Hyodo. Dislocation-mobility-controlled cracking in gaas caused by constantrate indentation. *Philosophical Magazine A*, 65(1):131–147, 1992.

[70] Hyung-Sun Kim and Steve Roberts. Brittle–ductile transition and dislocation mobility in sapphire. *Journal of the American Ceramic Society*, 77(12):3099–3104, 1994.

[71] P Pirouz, M Zhang, J-L Demenet, and HM Hobgood. Yield and fracture properties of the wide band-gap semiconductor 4h-sic. *Journal of Applied Physics*, 93(6):3279–3290, 2003.

[72] AS Booth and SG Roberts. The brittle-ductile transition in γ-tial single crystals. *Acta Materialia*, 45(3):1045–1053, 1997.

[73] KF Ha, C Yang, and JS Bao. Effect of dislocation density on the ductile-brittle transition in bulk fe-3% si single crystals. *Scripta Metallurgica et Materialia*, 30(8):1065–1070, 1994.

[74] Richard W Hertzberg, Richard Paul Vinci, and Jason L Hertzberg. *Deformation and fracture mechanics of engineering materials*. John Wiley & Sons, Incorporated, 2012.

[75] André AN Németh, Jens Reiser, David EJ Armstrong, and Michael Rieth. The nature of the brittle-to-ductile transition of ultra fine grained tungsten (w) foil. *International Journal of Refractory Metals and Hard Materials*, 50:9–15, 2015.

[76] E Pink. Recrystallization diagrams for sintered molybdenum and tungsten. *Planseeber. Pulvermet.*, 13, 1965.

[77] S Primig, H Leitner, H Clemens, A Lorich, W Knabl, and R Stickler. On the recrystallization behavior of technically pure molybdenum. *International Journal of Refractory Metals and Hard Materials*, 28(6):703–708, 2010.

[78] T Fujii, R Watanabe, Y Hiraoka, and M Okada. Effects of rolling procedures on the development of annealing textures in molybdenum sheets. *Journal of the Less Common Metals*, 97:163–171, 1984.

[79] T Fujii, R Watanabe, Y Hiraoka, and M Okada. Preparation of a large-scale molybdenum single-crystal sheet by means of secondary recrystallization. *Journal of the Less Common Metals*, 96:297–304, 1984.

[80] Tadayuki Fujii, Ryoji Watanabe, Yutaka Hiraoka, and Masatoshi Okada. Effect of initial grain size on the secondary grain growth in molybdenum sheet. *Materials Science and Engineering*, 68(1):45–53, 1984.

[81] Yutaka Hiraoka, Masatoshi Okada, Tadayuki Fujii, and Ryoji Watanabe. Orientation dependence of the low temperature bend properties of molybdenum single crystals produced by the secondary recrystallization method. *Journal of the Less Common Metals*, 97:109–117, 1984.

[82] Tadayuki Fujii, Yutaka Hiraoka, and Ryoji Watanabe. Large crystal grains or single crystals of molybdenum and process for production thereof, January 1 1985. US Patent 4,491,560.

[83] Y Hiraoka, T Fujii, M Okada, and R Watanabe. Crack initiation and propagation characteristics of molybdenum single crystals. *J. Jpn. Inst. Met.*, 49(2):104–111, 1985.

[84] Yutaka Hiraoka, Masatoshi Okada, Tadayuki Fujii, and Ryoji Watanabe. Bend properties of molybdenum single-crystal sheets produced by the secondary recrystallization method (role of island grains). *Journal of the Less Common Metals*, 97:99–108, 1984.

[85] RL Barto and LJ Ebert. Deformation stress state effects on the recrystallization kinetics of molybdenum. *Metallurgical Transactions*, 2(6):1643–1649, 1971.

[86] JM Dickinson and PE Armstrong. Temperature dependence of the elastic constants of molybdenum. *Journal of Applied Physics*, 38(2):602–606, 1967.

[87] Frank H Featherston and JR Neighbours. Elastic constants of tantalum, tungsten, and molybdenum. *Physical Review*, 130(4):1324, 1963.

[88] Werner Koster. * die temperaturabhangigkeit des elastizitatsmoduls reiner metalle. *Zeitschrift fur Metallkunde*, 39(1):1–9, 1948.

[89] D Io Bolef and J De Klerk. Elastic constants of single-crystal mo and w between 77 and 500 k. *Journal of Applied Physics*, 33(7):2311–2314, 1962.

[90] MJ Druyvesteyn. Die elastische anisotropie von molybdän. *Physica*, 8(4):439–448, 1941.

[91] D Sander. The correlation between mechanical stress and magnetic anisotropy in ultrathin films. *Reports on Progress in Physics*, 62(5):809, 1999.

[92] AS Wronski, AC Chilton, and EM Capron. The ductile-brittle transition in polycrystalline molybdenum. *Acta Metallurgica*, 17(6):751–755, 1969.

[93] HA Johansen and JG Cleary. The ductile-brittle transition in tantalum carbide. *Journal of The Electrochemical Society*, 113(4):378–381, 1966.

[94] M. Ellis. The Ductile to Brittle Transition in BCC Metals (DPhil Thesis), Oxford University. 1991.

[95] J. Gibson. Part II Thesis, University of Oxford. 2011.

[96] L. Durrans. The Effect of Strain Rate on the Ductile-to-Brittle Transition Temperature of Polycrystalline Molybdenum Part II Thesis, University of Oxford. 2013.

[97] Peter Gumbsch, Joachim Riedle, Alexander Hartmaier, and Hellmut F Fischmeister. Controlling factors for the brittle-to-ductile transition in tungsten single crystals. *Science*, 282(5392):1293–1295, 1998.

[98] GR Odette, HJ Rathbun, M Hribernik, T Yamamoto, M He, and P Spätig. A multiscale approach to measuring and modeling cleavage fracture toughness in structural steels. In *Materials Issues for Generation IV Systems*, pages 203–226. Springer, 2008.

[99] HL Prekel, A Lawley, and H Conrad. Dislocation velocity measurements in high purity molybdenum. *Acta metallurgica*, 16(3):337–345, 1968.

[100] H Conrad and W Hayes. Thermally-activated deformation of the bcc metals at low temperatures. *Trans. Am. Soc. Metals*, 56, 1963.

[101] John E Dora and Stanley Rajnak. Conference proceedings: Nucleation of kink pairs and the peierls'mechanism of plastic deformation. 1963.

[102] IV Gorynin, VA Ignatov, VV Rybin, SA Fabritsiev, VA Kazakov, VP Chakin, VA Tsykanov, VR Barabash, and YG Prokofyev. Effects of neutron irradiation on properties of refractory metals. *Journal of Nuclear Naterials*, 191:421–425, 1992.

[103] A Hasegawa, K Abe, M Satou, K Ueda, and C Namba. Influence of heat-treatment on tensile behavior of neutron irradiated molybdenum. *Journal of Nuclear Naterials*, 233:565–569, 1996.

[104] V Chakin and V Kazakov. Radiation embrittlement of low-alloyed mo alloys. *Journal of Nuclear Naterials*, 233:570–572, 1996.

[105] J. Gibson. Tungsten alloys for fusion power (dphil thesis literature review. 2012.

[106] Horst Czichos, Tetsuya Saiato, and L Leslie R Smith. *Springer handbook of materials measurement methods*. Springer, 2006.

[107] William D Nix and Huajian Gao. Indentation size effects in crystalline materials: a law for strain gradient plasticity. *Journal of the Mechanics and Physics of Solids*, 46(3):411–425, 1998.

[108] D Tabor. The hardness and strength of metals. *J. Inst. Met*, 79(1):1–18, 1951.

[109] Anthony C Fischer-Cripps. *Nanoindentation*, volume 1. Springer, 2011.

[110] Abner Brenner. Microhardness tester for metals at elevated temperatures. *Journal of Research of the National Bureau of Standards*, 46(2):126–131, 1951.

[111] GS Pisarenki, VA Borisenko, and Yu A Kashtalyan. Effect of temperature on the hardness and modulus of elasticity of tungsten and molybdenum in the temperature range of 20 to 2700 c. *Sov. Powder Metall. Met. Ceram*, 5:371–372, 1962.

[112] ER Petty. A low temperature inflection in the temperature dependence of hardness of pure metals. *J Inst Metals*, 89:123, 1960.

[113] JH Westbrook. Temperature dependence of the hardness of pure metals. *ASM TRANS*, 45:221–243, 1953.

[114] Evan Robert Petty. *Hardness Properties of Metals and Alloys at Elevated Temperatures*. PhD thesis, University College of Swansea, 1958.

[115] Minyoung Lee and Donald G Flom. Hardness of polycrystalline tungsten and molybdenum oxides at elevated temperatures. *Journal of the American Ceramic Society*, 73(7):2117–2118, 1990.

[116] James SK-L Gibson, Steve G Roberts, and David EJ Armstrong. High temperature indentation of helium-implanted tungsten. *Materials Science and Engineering: A*, 625:380–384, 2015.

[117] M Darot, Y Gueguen, Z Benchemam, and R Gaboriaud. Ductile-brittle transition investigated by micro-indentation: results for quartz and olivine. *Physics of the Earth and Planetary Interiors*, 40(3):180–186, 1985.

[118] Shanling Wang and Pirouz Pirouz. Mechanical properties of undoped gaas. iii: Indentation experiments. *Acta Materialia*, 55(16):5526–5537, 2007.

[119] U Ramamurty and MC Kumaran. Mechanical property extraction through conical indentation of a closed-cell aluminum foam. *Acta materialia*, 52(1):181–189, 2004.

[120] SG Roberts, P Pirouz, and PB Hirsch. Doping effects on indentation plasticity and fracture in germanium. *Journal of Materials Science*, 20(5):1739–1747, 1985.

[121] M Sakai. Energy principle of the indentation-induced inelastic surface deformation and hardness of brittle materials. *Acta Metallurgica et Materialia*, 41(6):1751–1758, 1993.

[122] P Pirouz, S Wang, B Bayu-Aji, M Zhang, and J-L Démenet. The effect of dislocation core structure on the plastic and fracture behavior of GaAs and InP. *physica status solidi (c)*, 2(6):1973–1986, 2005.

[123] Takayoshi Suzuki and Takahito Ohmura. Ultra-microindentation of silicon at elevated temperatures. *Philosophical Magazine A*, 74(5):1073–1084, 1996.

[124] Christian Ullner, Jörg Beckmann, and Roger Morrell. Instrumented indentation test for advanced technical ceramics. *Journal of the European Ceramic Society*, 22(8):1183–1189, 2002.

[125] Christopher A Schuh. Nanoindentation studies of materials. *Materials Today*, 9(5):32–40, 2006.

[126] David EJ Armstrong, Angus J Wilkinson, and Steve G Roberts. Measuring anisotropy in young's modulus of copper using microcantilever testing. *J. Mater. Res*, 24(11):3268–3276, 2009.

[127] W Oliver and G Pharr. Improved technique for determining hardness and elastic modulus using load and displacement sensing indentation experiments. *Journal of Materials Research*, 7(6):1564–1583, 1992.

[128] JJ Williams, NC Chapman, and N Chawla. Mechanisms of sn hillock growth in vacuum by in situ nanoindentation in a scanning electron microscope (sem). *Journal of electronic materials*, 42(2):224–229, 2013.

[129] Benedikt Moser, Jakob Kuebler, Holger Meinhard, Walter Muster, and Johann Michler. Observation of instabilities during plastic deformation by in-situ sem indentation experiments. *Advanced Engineering Materials*, 7(5):388–392, 2005.

[130] Jeff TM De Hosson, Wouter A Soer, Andrew M Minor, Zhiwei Shan, Eric A Stach, SA Syed Asif, and Oden L Warren. In situ tem nanoindentation and dislocation-grain boundary interactions: a tribute to david brandon. *Journal of Materials Science*, 41(23):7704–7719, 2006.

[131] Eric A Stach, Tony Freeman, Andrew M Minor, Doug K Owen, John Cumings, Mark A Wall, Tomas Chraska, Robert Hull, JW Morris, A Zettl, et al. Development of a nanoindenter for in situ transmission electron microscopy. *Microscopy and Microanalysis*, 7(6):507–517, 2001.

[132] J Vlassak and WD Nix. Indentation modulus of elastically anisotropic half spaces. *Philosophical Magazine A*, 67(5):1045–1056, 1993.

[133] N Zaafarani, D Raabe, RN Singh, F Roters, and S Zaefferer. Three-dimensional investigation of the texture and microstructure below a nanoindent in a cu single crystal using 3d ebsd and crystal plasticity finite element simulations. *Acta Materialia*, 54(7):1863–1876, 2006.

[134] N Zaafarani, D Raabe, F Roters, and S Zaefferer. On the origin of deformation-induced rotation patterns below nanoindents. *Acta Materialia*, 56(1):31–42, 2008.

[135] TB Britton, H Liang, FPE Dunne, and AJ Wilkinson. The effect of crystal orientation on the indentation response of commercially pure titanium: experiments and simulations. *Proceedings of the Royal Society A: Mathematical, Physical and Engineering Science*, 466(2115):695–719, 2010.

[136] D Kiener, K Durst, M Rester, and AM Minor. Revealing deformation mechanisms with nanoindentation. *Jom*, 61(3):14–23, 2009.

[137] GB Viswanathan, Eunha Lee, Dennis M Maher, S Banerjee, and Hamish L Fraser. Direct observations and analyses alpha phase of an alpha/beta ti-alloy of dislocation substructures in the formed by nanoindentation. *Acta Materialia*, 53(19):5101–5115, 2005.

[138] J Bushby, S Roberts, and C Hardie. Nanoindentation investigation of ion-irradiated fe–cr alloys using spherical indenters. *Journal of Materials Research*, 27(01):85–90, 2012.

[139] W Oliver and G Pharr. Measurement of hardness and elastic modulus by instrumented indentation: Advances in understanding and refinements to methodology. *Journal of Materials Research*, 19(01):3–20, 2004.

[140] J Vlassak and WD Nix. Measuring the elastic properties of anisotropic materials by means of indentation experiments. *Journal of the Mechanics and Physics of Solids*, 42(8):1223–1245, 1994.

[141] WH Poisl, WC Oliver, and BD Fabes. The relationship between indentation and uniaxial creep in amorphous selenium. *Journal of Materials Research*, 10(8):2024–2032, 1995.

[142] James SK-L Gibson, Sebastian Schröders, Christoffer Zehnder, and Sandra Korte-Kerzel. On extracting mechanical properties from nanoindentation at temperatures up to 1000°c. *arXiv preprint arXiv:1709.07714*, 2017.

[143] Zhi Chao Duan and Andrea M Hodge. High-temperature nanoindentation: New developments and ongoing challenges. *JOM*, 61(12):32–36, 2009.

[144] Jonathan C Trenkle, Corinne E Packard, and Christopher A Schuh. Hot nanoindentation in inert environments. *Review of Scientific Instruments*, 81(7):073901–073901, 2010.

[145] DF Bahr, DE Wilson, and DA Crowson. Energy considerations regarding yield points during indentation. *J. Mater. Res*, 14(6):2269–2275, 1999.

[146] SA Syed Asif and JB Pethica. Nanoindentation creep of single-crystal tungsten and gallium arsenide. *Philosophical Magazine A*, 76(6):1105–1118, 1997.

[147] DE Kramer, KB Yoder, and WW Gerberich. Surface constrained plasticity: Oxide rupture and the yield point process. *Philosophical Magazine A*, 81(8):2033–2058, 2001.

[148] V Bhakhri and RJ Klassen. Investigation of high-temperature plastic deformation using instrumented microindentation tests. part ithe deformation of three aluminum alloys at 473 k to 833 k. *Journal of Materials Science*, 41(8):2259–2270, 2006.

[149] V Bhakhri and RJ Klassen. Investigation of high-temperature plastic deformation using instrumented microindentation tests. part ii: The deformation of al-based particulate reinforced composites at 473 k to 833 k. *Journal of Materials Science*, 41(8):2249–2258, 2006.

[150] JM Wheeler, DEJ Armstrong, W Heinz, and R Schwaiger. High temperature nanoindentation: The state of the art and future challenges. *Current Opinion in Solid State and Materials Science*, 19(6):354–366, 2015.

[151] Scopus. *SciVerse*. Elsevier, B.V., 2014.

[152] KV Rajulapati, MM Biener, J Biener, and AM Hodge. Temperature dependence of the plastic flow behavior of tantalum. *Philosophical Magazine Letters*, 90(1):35–42, 2010.

[153] A Sawant and S Tin. High temperature nanoindentation of a re-bearing single crystal ni-base superalloy. *Scripta Materialia*, 58(4):275–278, 2008.

[154] Hugh O Pierson. Handbook of carbon, graphite, diamonds and fullerenes: processing, properties and applications. *Noyes Publications, Park Ridge*, 1993.

[155] T.B.; Tarleton E.; Roberts S.G. Armstrong, D.E.J.; Britton and A.J. Wilkinson. High temperature micro-cantilever testing for elastic, plastic and fracture analysis. *Poster in hot nanoindenter room*, 421, 2013.

[156] Oxford Materials Department website. New High Temperature Nanotest Equipment. *http://www.materials.ox.ac.uk/blog/81/550/New-High-Temperature-Nanotest-Equipment.html*, 2012.

[157] X Qiu, Y Huang, WD Nix, KC Hwang, and H Gao. Effect of intrinsic lattice resistance in strain gradient plasticity. *Acta Materialia*, 49(19):3949–3958, 2001.

[158] Karsten Durst, Björn Backes, Oliver Franke, and Mathias Göken. Indentation size effect in metallic materials: Modeling strength from pop-in to macroscopic hardness using geometrically necessary dislocations. *Acta Materialia*, 54(9):2547–2555, 2006.

[159] M Fink, Th Fabing, M Scheerer, E Semerad, and B Dunn. Measurement of mechanical properties of electronic materials at temperatures down to 4.2 k. *Cryogenics*, 48(11):497–510, 2008.

[160] Jian Chen, Gerard A Bell, Hanshan Dong, James F Smith, and Ben D Beake. A study of low temperature mechanical properties and creep behaviour of polypropylene using a new sub-ambient temperature nanoindentation test platform. *Journal of Physics D: Applied Physics*, 43(42):425404, 2010.

[161] C Ascheron, C Haase, G Kühn, and H Neumann. Microhardness of sn-doped inp. *Crystal research and technology*, 24(2), 1989.

[162] B Vengatesan, N Kanniah, and P Ramasamy. Microhardness and crack patterns of cvt grown cdga 2 s 4 single crystals. *Journal of Materials Science letters*, 5(10):987–988, 1986.

[163] Ravender Tickoo, RP Tandon, KK Bamzai, and PN Kotru. Microindentation studies on samarium-modified lead titanate ceramics. *Materials chemistry and physics*, 80(2):446–451, 2003.

[164] J Guille and M Sieskind. Microindentation studies on bafcl single crystals. *Journal of Materials Science*, 26(4):899–903, 1991.

[165] George Z Voyiadjis and Amin H Almasri. Variable material length scale associated with nanoindentation experiments. *Journal of engineering mechanics*, 135(3):139–148, 2009.

[166] KW McElhaney, JJ Vlassak, and WD Nix. Determination of indenter tip geometry and indentation contact area for depth-sensing indentation experiments. *Journal of Materials Research*, 13(5):1300–1306, 1998.

[167] G Voyiadjis, A Almasri, and T Park. Experimental nanoindentation of bcc metals. *Mechanics Research Communications*, 37(3):307–314, 2010.

[168] GZ Voiadjis and RA Al-Rub. Determination of the material intrinsic length scale of gradient plasticity theory. In *IUTAM Symposium on Multiscale Modeling and Characterization of Elastic-Inelastic Behavior of Engineering Materials*, volume 114, pages 167–174.

[169] O Franke, J Trenkle, and C Schuh. Temperature dependence of the indentation size effect. *Journal of Materials Research*, 25(7):1225–1229, 2010.

[170] Oliver W Greer, J and W Nix. Size dependence of mechanical properties of gold at the micron scale in the absence of strain gradients. *Acta Materialia*, 53(6):1821–1830, 2005.

[171] Michael D Uchic, Dennis M Dimiduk, Jeffrey N Florando, and William D Nix. Sample dimensions influence strength and crystal plasticity. *Science*, 305(5686):986–989, 2004.

[172] T.; Pippan R. Motz, C.; Schoberl. Mechanical properties of micro-sized copper bending beam machined by the focussed ion beam technique). *Acta Materialia*, 53:4269–4279, 2005.

[173] Motz C Schöberl T Jenko M Kiener, D and G Dehm. Determination of mechanical properties of copper at the micron scale. *Advanced Engineering Materials*, 8(11):1119–1125, 2006.

[174] Jicheng Gong and Angus Wilkinson. Investigation of elastic properties of single-crystal α-ti using micro-cantilever beams. *Philosophical Magazine Letters*, 90(7):503–512, 2010.

[175] D Kiener, W Grosinger, G Dehm, and R Pippan. A further step towards an understanding of size-dependent crystal plasticity: In situ tension experiments of miniaturized single-crystal copper samples. *Acta Materialia*, 56(3):580–592, 2008.

[176] Michael D Uchic and Dennis M Dimiduk. A methodology to investigate size scale effects in crystalline plasticity using uniaxial compression testing. *Materials Science and Engineering: A*, 400:268–278, 2005.

[177] Julia Hütsch and Erica T Lilleodden. The influence of focused-ion beam preparation technique on micro-compression investigations: Lathe vs. annular milling. *Scripta Materialia*, 77:49–51, 2014.

[178] D. Di Maio and S.G. Roberts. Measuring fracture toughness of coatings using focused-ion-beam-machined microbeams. *J. Mater. Res.*, 20(2):299–3029, 2004.

[179] EO Hall. The deformation and ageing of mild steel: Iii discussion of results. *Proceedings of the Physical Society. Section B*, 64(9):747, 1951.

[180] NJ Petch. The cleavage strength of polycrystals. *J. Iron Steel Inst.*, 174:25–28, 1953.

[181] Wonmo Kang and M Taher A Saif. In situ study of size and temperature dependent brittle-to-ductile transition in single crystal silicon. *Advanced Functional Materials*, 2012.

[182] Jagannathan Rajagopalan, Jong H Han, and M Taher A Saif. Plastic deformation recovery in freestanding nanocrystalline aluminum and gold thin films. *Science*, 315(5820):1831–1834, 2007.

[183] JS Stölken and AG Evans. A microbend test method for measuring the plasticity length scale. *Acta Materialia*, 46(14):5109–5115, 1998.

[184] NA Fleck, GM Muller, MF Ashby, and JW Hutchinson. Strain gradient plasticity: theory and experiment. *Acta Metallurgica et Materialia*, 42(2):475–487, 1994.

[185] Stefan Wurster, Christian Motz, and Reinhard Pippan. Characterization of the fracture toughness of micro-sized tungsten single crystal notched specimens. *Philosophical Magazine*, 92(14):1803–1825, 2012.

[186] Jicheng Gong and Angus J Wilkinson. Micro-cantilever testing of¡ a¿ prismatic slip in commercially pure ti. *Philosophical Magazine*, 91(7-9):1137–1149, 2011.

[187] C Motz, T Schöberl, and R Pippan. Mechanical properties of micro-sized copper bending beams machined by the focused ion beam technique. *Acta materialia*, 53(15):4269–4279, 2005.

[188] A.J. Armstrong, D.E.J.; Wilkinson and S.G. Roberts. Measuring anisotropy in Young's modulus of copper using microcantilever testing. *J. Mater. Res.*, 24(11):3268–3276, 2009.

[189] PB Hirsch and SG Roberts. The brittle-ductile transition in silicon. *Philosophical Magazine A*, 64(1):55–80, 1991.

[190] AB Hagen, BD Snartland, and C Thaulow. Temperature and orientation effects on the deformation mechanisms of α-fe micropillars. *Acta Materialia*, 129:398–407, 2017.

[191] Rengen Ding, Jicheng Gong, Angus J Wilkinson, and Ian P Jones. Transmission electron microscopy of deformed ti–6al–4 v micro-cantilevers. *Philosophical Magazine*, 92(25-27):3290–3314, 2012.

[192] AS Schneider, CP Frick, BG Clark, PA Gruber, and E Arzt. Influence of orientation on the size effect in bcc pillars with different critical temperatures. *Materials Science and Engineering: A*, 528(3):1540–1547, 2011.

[193] Yinan Cui, Giacomo Po, and Nasr Ghoniem. Does irradiation enhance or inhibit strain bursts at the submicron scale? *Acta Materialia*, 132:285–297, 2017.

[194] EM Grieveson, DEJ Armstrong, Shuo Xu, and SG Roberts. Compression of self-ion implanted iron micropillars. *Journal of Nuclear Materials*, 430(1):119–124, 2012.

[195] Dennis M Dimiduk, Chris Woodward, Richard LeSar, and Michael D Uchic. Scale-free intermittent flow in crystal plasticity. *Science*, 312(5777):1188–1190, 2006.

[196] A Rinaldi, P Peralta, C Friesen, and K Sieradzki. Sample-size effects in the yield behavior of nanocrystalline nickel. *Acta Materialia*, 56(3):511–517, 2008.

[197] Frédéric Mompiou, Marc Legros, Andreas Sedlmayr, Daniel S Gianola, Daniel Caillard, and Oliver Kraft. Source-based strengthening of sub-micrometer al fibers. *Acta materialia*, 60(3):977–983, 2012.

[198] Won Seok Choi, Bruno C De Cooman, Stefanie Sandlöbes, and Dierk Raabe. Size and orientation effects in partial dislocation-mediated deformation of twinning-induced plasticity steel micro-pillars. *Acta Materialia*, 98:391–404, 2015.

[199] Motz C Weygand D Zaiser M Csikor, F and S Zapperi. Dislocation avalanches, strain bursts, and the problem of plastic forming at the micrometer scale. *Science*, 318(5848):251–254, 2007.

[200] R Gröger and V Vitek. Explanation of the discrepancy between the measured and atomistically calculated yield stresses in body-centred cubic metals. *Philosophical magazine letters*, 87(2):113–120, 2007.

[201] Oscar Torrents Abad, Jeffrey M Wheeler, Johann Michler, Andreas S Schneider, and Eduard Arzt. Temperature-dependent size effects on the strength of ta and w micropillars. *Acta Materialia*, 103:483–494, 2016.

[202] Loynachan C Wu Z Zhang Y Srolovitz D Gu, X and J Greer. Size-dependent deformation of nanocrystalline pt nanopillars. *Nano Letters*, 12(12):6385–6392, 2012.

[203] Jeffrey M Wheeler, Christoph Kirchlechner, Jean-Sébastien Micha, Johann Michler, and Daniel Kiener. The effect of size on the strength of fcc metals at elevated temperatures: annealed copper. *Philosophical Magazine*, 96(32-34):3379–3395, 2016.

[204] J Greer and J De Hosson. Plasticity in small-sized metallic systems: Intrinsic versus extrinsic size effect. *Progress in Materials Science*, 56(6):654–724, 2011.

[205] Michael D Uchic, Paul A Shade, and Dennis M Dimiduk. Plasticity of micrometer-scale single crystals in compression. *Annual Review of Materials Research*, 39:361–386, 2009.

[206] Oliver Kraft, Patric A Gruber, Reiner Mönig, and Daniel Weygand. Plasticity in confined dimensions. *Annual review of materials research*, 40:293–317, 2010.

[207] R Dou and B Derby. A universal scaling law for the strength of metal micropillars and nanowires. *Scripta Materialia*, 61(5):524–527, 2009.

[208] J Kim and J Greer. Tensile and compressive behavior of gold and molybdenum single crystals at the nano-scale. *Acta Materialia*, 57(17):5245–5253, 2009.

[209] AS Schneider, D Kaufmann, BG Clark, CP Frick, PA Gruber, R Mönig, O Kraft, and E Arzt. Correlation between critical temperature and strength of small-scale bcc pillars. *Physical review letters*, 103(10):105501, 2009.

[210] AS Schneider, CP Frick, E Arzt, WJ Clegg, and S Korte. Influence of test temperature on the size effect in molybdenum small-scale compression pillars. *Philosophical Magazine Letters*, 93(6):331–338, 2013.

[211] Verena Maier, Anton Hohenwarter, Reinhard Pippan, and Daniel Kiener. Thermally activated deformation processes in body-centered cubic cr–how microstructure influences strain-rate sensitivity. *Scripta Materialia*, 106:42–45, 2015.

[212] J Kim, D Jang, and J Greer. Tensile and compressive behavior of tungsten, molybdenum, tantalum and niobium at the nanoscale. *Acta Materialia*, 58(7):2355–2363, 2010.

[213] AS Schneider, BG Clark, CP Frick, PA Gruber, and E Arzt. Effect of orientation and loading rate on compression behavior of small-scale mo pillars. *Materials Science and Engineering: A*, 508(1):241–246, 2009.

[214] Triplicane A Parthasarathy, Satish I Rao, Dennis M Dimiduk, Michael D Uchic, and Dallas R Trinkle. Contribution to size effect of yield strength from the stochastics of dislocation source lengths in finite samples. *Scripta Materialia*, 56(4):313–316, 2007.

[215] D Kaufmann, R Mönig, CA Volkert, and O Kraft. Size dependent mechanical behaviour of tantalum. *International Journal of Plasticity*, 27(3):470–478, 2011.

[216] BRS Rogne and C Thaulow. Strengthening mechanisms of iron micropillars. *Philosophical Magazine*, 95(16-18):1814–1828, 2015.

[217] MA Haque and MTA Saif. Deformation mechanisms in free-standing nanoscale thin films: A quantitative in situ transmission electron microscope study. *Proceedings of the National Academy of Sciences of the United States of America*, 101(17):6335–6340, 2004.

[218] Yong Zhu and Horacio D Espinosa. An electromechanical material testing system for in situ electron microscopy and applications. *Proceedings of the National Academy of Sciences of the United States of America*, 102(41):14503–14508, 2005.

[219] Wonmo Kang and M Taher A Saif. In situ thermomechanical testing for micro/nanomaterials. *MRS Communications*, 1(01):13–16, 2011.

[220] Wonmo Kang and M Taher A Saif. A novel sic mems apparatus for in situ uniaxial testing of micro/nanomaterials at high temperature. *Journal of Micromechanics and Microengineering*, 21(10):105017, 2011.

[221] B Basnar, A Lugstein, H Wanzenboeck, H Langfischer, E Bertagnolli, and E Gornik. Focused ion beam induced surface amorphization and sputter processes. *Journal of Vacuum Science & Technology B: Microelectronics and Nanometer Structures*, 21(3):927–930, 2003.

[222] Aaron M Datesman, Jonathan C Schultz, Thomas W Cecil, Christine M Lyons, and Arthur W Lichtenberger. Gallium ion implantation into niobium thin films using a focused-ion beam. *Applied Superconductivity, IEEE Transactions on*, 15(2):3524–3527, 2005.

[223] H Gnaser, C Kallmayer, and H Oechsner. Focused-ion-beam implantation of ga in elemental and compound semiconductors. *Journal of Vacuum Science & Technology B: Microelectronics and Nanometer Structures*, 13(1):19–26, 1995.

[224] C Lehrer, L Frey, S Petersen, M Mizutani, M Takai, and H Ryssel. Defects and gallium-contamination during focused ion beam micro machining. In *Ion Implantation Technology, 2000. Conference on*, pages 695–698. IEEE, 2000.

[225] P Roediger, HD Wanzenboeck, S Waid, G Hochleitner, and E Bertagnolli. Focused-ion-beam-inflicted surface amorphization and gallium implantation—new insights and removal by focused-electron-beam-induced etching. *Nanotechnology*, 22(23):235302, 2011.

[226] S Rubanov and PR Munroe. Fib-induced damage in silicon. *Journal of Microscopy*, 214(3):213–221, 2004.

[227] S Shim, Hongbin Bei, Michael K Miller, George Mathews Pharr, and Easo P George. Effects of focused ion beam milling on the compressive behavior of directionally solidified micropillars and the nanoindentation response of an electropolished surface. *Acta Materialia*, 57(2):503–510, 2009.

[228] M. M. Yovanovich. Micro and macro hardness measurements, correlations, and contact models - 44th aiaa aerospace sciences meeting and exhibit, 9 - 12 january 2006, reno, nevada. *http://www.mhtl.uwaterloo.ca/pdf$_p$apers/mhtl*06 − 2.*pdf*, *accessed*2015.

[229] NM Everitt. Indentation creep on single crystal magnesium oxide. Journal of Hard Materials(UK), *3(3):269–284, 1991.*

[230] Nicola Mary Everitt. Indentation creep and anisotropy in magnesium oxide and germanium. *PhD thesis, University of Oxford, 1990.*

[231] nikon imaging software nis-elements. http://www.nikon.com/products/instruments/lineup/bioscience /img$_s$oft/key$_f$eatures.htm. Accessed : 2015 − 05 − 29.

[232] Mikhail Grigorevich Lozinskii. High temperature metallography. *Elsevier, 2013.*

[233] Panayiotis J Karditsas and M-J Baptiste. Thermal and structural properties of fusion related materials. Technical report, UKAEA Government Division, Fusion, Culham (United Kingdom), 1995.

[234] H Hashizume, K Miya, M Seki, and K Ioki. Thermomechanical behavior of the first wall subjected to plasma disruption. Fusion engineering and design, *5(2):141–154, 1987.*

[235] H Shinno, M Kitajima, and M Okada. Thermal stress analysis of high heat flux materials. Journal of Nuclear Materials, *155:290–294, 1988.*

[236] Frank P Incropera. Fundamentals of heat and mass transfer. *John Wiley & Sons, 2011.*

[237] Yu V Milman. Plasticity characteristic obtained by indentation. Journal of Physics D: Applied Physics, *41(7):074013, 2008.*

[238] Yu V Milman, BA Galanov, and SI Chugunova. Plasticity characteristic obtained through hardness measurement. Acta Metallurgica et Materialia, *41(9):2523–2532, 1993.*

[239] NA Stelmashenko, MG Walls, LM Brown, and Yu V Milman. Microindentations on w and mo oriented single crystals: an stm study. Acta Metallurgica et Materialia, *41(10):2855–2865, 1993.*

[240] NA Stilwell and D Tabor. Elastic recovery of conical indentations. Proceedings of the Physical Society, *78(2):169, 1961.*

[241] IJ McColm. Ceramic hardness' plenum. New York, *1990.*

[242] C. Tromas. Nanomechanics gradschool, Autrans. Conference presentation, *2014.*

[243] Micromaterials website. micromaterials nanotest xtreme. http://www.micromaterials.co.uk/nanotest-xtreme/, *2014.*

[244] J. Gibson. Dphil thesis, university of oxford. 2015.

[245] Xiaodong Li and Bharat Bhushan. A review of nanoindentation continuous stiffness measurement technique and its applications. Materials characterization, *48(1):11–36, 2002.*

[246] B. Beake. The nanoindenter – using EPSRC funding to connect engineering disciplines, Birmingham University. Conference presentation*, 2014.*

[247] Webpage for CalTech Materials Science: 'History of Thermoelectrics'. http://thermoelectrics.caltech.edu/thermoelectrics/history.html*, 2015.*

[248] Webpage for Horizon Press: 'PCR Troubleshooting and Optimization'. http://www.horizonpress.com/hsp/supplementary/pcr-troubleshooting/c6f1.html*, 2015.*

[249] Mark P D'Evelyn and Kornelija Zgonc. Elastic properties of polycrystalline cubic boron nitride and diamond by dynamic resonance measurements. Diamond and Related Materials*, 6(5-7):812–816, 1997.*

[250] Jin S Zhang, Jay D Bass, Takashi Taniguchi, Alexander F Goncharov, Yun-Yuan Chang, and Steven D Jacobsen. Elasticity of cubic boron nitride under ambient conditions. Journal of Applied Physics*, 109(6):063521, 2011.*

[251] M Dao, N v Chollacoop, KJ Van Vliet, TA Venkatesh, and S Suresh. Computational modeling of the forward and reverse problems in instrumented sharp indentation. Acta materialia*, 49(19):3899–3918, 2001.*

[252] Jack C Hay, A Bolshakov, and GM Pharr. A critical examination of the fundamental relations used in the analysis of nanoindentation data. Journal of Materials Research*, 14(06):2296–2305, 1999.*

[253] Feodor M Borodich and Leon M Keer. Evaluation of elastic modulus of materials by adhesive (no–slip) nano–indentation. In Proceedings of the Royal Society of London A: Mathematical, Physical and Engineering Sciences*, volume 460, pages 507–514. The Royal Society, 2004.*

[254] RB King. Elastic analysis of some punch problems for a layered medium. International Journal of Solids and Structures*, 23(12):1657–1664, 1987.*

[255] Anthony C Fischer-Cripps. Critical review of analysis and interpretation of nanoindentation test data. Surface and coatings technology*, 200(14):4153–4165, 2006.*

[256] SC Storer, ME Fitzpatrick, SV Hainsworth, and MA Rist. Experimental study of room-temperature indentation viscoplastic 'creep'in zirconium. Philosophical Magazine*, 96(24):2547–2563, 2016.*

[257] George Z Voyiadjis, Danial Faghihi, and Cheng Zhang. Analytical and experimental determination of rate-and temperature-dependent length scales using nanoindentation experiments. Journal of Nanomechanics and Micromechanics*, 1(1):24–40, 2011.*

[258] George M Pharr, Erik G Herbert, and Yanfei Gao. The indentation size effect: a critical examination of experimental observations and mechanistic interpretations. Annual Review of Materials Research*, 40:271–292, 2010.*

[259] William D Nix. Elastic and plastic properties of thin films on substrates: nanoindentation techniques. Materials Science and Engineering: A*, 234:37–44, 1997.*

[260] Yu V Milman, Golubenko, and SN Dub. Indentation size effect in nanohardness. Acta Materialia*, 59(20):7480–7487, 2011.*

[261] Y Huang, F Zhang, KC Hwang, WD Nix, GM Pharr, and G Feng. A model of size effects in nano-indentation. Journal of the Mechanics and Physics of Solids*, 54(8):1668–1686, 2006.*

[262] *Ilze Manika and Janis Maniks. Size effects in micro-and nanoscale indentation.* Acta Materialia, *54(8):2049–2056, 2006.*

[263] *Dabiao Liu and DJ Dunstan. Material length scale of strain gradient plasticity: A physical interpretation.* International Journal of Plasticity, *98:156–174, 2017.*

[264] *George Z Voyiadjis and Rashid K Abu Al-Rub. Gradient plasticity theory with a variable length scale parameter.* International Journal of Solids and Structures, *42(14):3998–4029, 2005.*

[265] *E. Tarleton. Dphil thesis. 2009.*

[266] *S. Dewsbury. Part ii thesis, university of oxford. 2008.*

[267] *JM Gere. Mechanics of materials, 5th si edition, nelson thornes ltd. Technical report, ISBN 0-7487-6675-8, Cheltenham, UK, 2002.*

[268] *Louis L Bucciarelli.* Engineering mechanics for structures. *Dover, 2009.*

[269] *Stephen Timoshenko.* Strength of materials Part 1. *D. Van Nostrand Co., Inc, 1940.*

[270] *S Brinckmann, J Kim, and J Greer. Fundamental differences in mechanical behavior between two types of crystals at the nanoscale.* Physical review letters, *100(15):155502, 2008.*

[271] *W Wang, Y Huang, KJ Hsia, KX Hu, and A Chandra. A study of microbend test by strain gradient plasticity.* International Journal of Plasticity, *19(3):365–382, 2003.*

[272] *Takayoshi Suzuki, Hirokazu Koizumi, and Helmut OK Kirchner. Plastic flow stress of bcc transition metals and the peierls potential.* Acta Metallurgica et Materialia, *43(6):2177–2187, 1995.*

[273] *OD Sherby and PM Burke. Progress in materials science, vol. 13, 1967.*

[274] *OD Sherby and PE Armstrong. Prediction of activation energies for creep and self-diffusion from hot hardness data.* Metallurgical and Materials Transactions B, *2(12):3479–3484, 1971.*

[275] *JM Wheeler, V Maier, K Durst, M Göken, and J Michler. Activation parameters for deformation of ultrafine-grained aluminium as determined by indentation strain rate jumps at elevated temperature.* Materials Science and Engineering: A, *585:108–113, 2013.*

[276] *Z.; Tarleton E. Giannattasio, A.; Yao and S.G. Roberts. Brittle-ductile transitions in polycrystalline tungsten.* Philosophical Magazine, *90(30):3947–3959, 2010.*

[277] *G Taylor. Thermally-activated deformation of bcc metals and alloys.* Progress in materials science, *36:29–61, 1992.*

[278] *Takayoshi Suzuki and Hirokazu Koizumi. Inertial motion and multi-kink pair formation of dislocations on the peierls potential.* Philosophical Magazine A, *67(5):1153–1160, 1993.*

[279] *PA Gordon, T Neeraj, Y Li, and J Li. Screw dislocation mobility in bcc metals: the role of the compact core on double-kink nucleation.* Modelling and Simulation in Materials Science and Engineering, *18(8):085008, 2010.*